

Measurement of the inclusive $t\bar{t}$ cross section and search for additional scalars in $t\bar{t}$ final states at the CMS experiment

Dissertation

zur Erlangung des Doktorgrades
an der Fakultät für Mathematik, Informatik und Naturwissenschaften
Fachbereich Physik
der Universität Hamburg

von

Laurids Jeppe

Hamburg
2025

| | |
|---|--|
| Gutachter der Dissertation: | Prof. Dr. Christian Schwanenberger Dr. Alexander Grohsjean |
| Zusammensetzung der Prüfungskomission: | Prof. Dr. Christian Schwanenberger Dr. Alexander Grohsjean TBD TBD TBD |
| Vorsitzender der Prüfungskommission: | TBD |
| Datum der Disputation: | TBD |
| Vorsitzender Fach-Promotionsausschuss Physik: | Prof. Dr. Wolfgang J. Parak |
| Leiter des Fachbereichs Physik: | Prof. Dr. Markus Drescher |
| Leiter der Fakultät MIN: | Prof. Dr.-Ing. Norbert Ritter |

Abstract

Several measurements of top quark pair ($t\bar{t}$) production at the CMS experiment are presented. The inclusive $t\bar{t}$ production cross section $\sigma_{t\bar{t}}$ is measured for the first time at $\sqrt{s} = 13.6$ TeV, using 1.21 fb^{-1} of early LHC Run 3 data. By combining the dilepton and lepton+jets ($\ell+\text{jets}$) decay channels of $t\bar{t}$ and constraining the lepton and b tagging efficiencies in a likelihood fit, a precision of 3.4% comparable to previous $\sigma_{t\bar{t}}$ measurements is achieved.

Following this, a study of off-shell $t\bar{t}$ production and $t\bar{t}/tW$ interference is performed using the Monte Carlo (MC) generator **bb41**, which is validated for the first time in CMS simulation and compared to other MC generators, finding a significantly improved description of the data.

Finally, a search for spin-0 states decaying to $t\bar{t}$ in the dilepton channels is presented, using 138 fb^{-1} of LHC Run 2 data at $\sqrt{s} = 13$ TeV. The invariant $t\bar{t}$ mass ($m_{t\bar{t}}$) is combined with spin correlation observables to gain sensitivity to the spin and \mathcal{CP} structure of possible new states. A statistically significant excess of events over the $t\bar{t}$ continuum background is observed at low values of $m_{t\bar{t}}$, consistent with pseudoscalar spin correlations. It is interpreted in terms of a pseudoscalar $t\bar{t}$ bound state η_t , and its cross section is measured to be $\sigma(\eta_t) = 8.7 \pm 1.1\text{ pb}$ using a simplified model inspired by non-relativistic quantum chromodynamics.

The same data is further interpreted in terms of generic additional pseudoscalar or scalar bosons, and exclusion regions on their coupling to the top quark are derived both for the dilepton channels alone as well as in a combination with a separate analysis of the $\ell+\text{jets}$ channels. As a third interpretation of the data, Axion-Like Particles (ALPs) decaying to $t\bar{t}$ are considered in the limiting case of vanishing tree-level ALP-gluon couplings, while the more generic case is studied phenomenologically in simulation.

Zusammenfassung

Es werden mehrere Messungen der Produktion von Top-Quark-Paaren ($t\bar{t}$) am CMS-Experiment vorgestellt. Der inklusive $t\bar{t}$ -Produktionsquerschnitt $\sigma_{t\bar{t}}$ wird zum ersten Mal bei $\sqrt{s} = 13.6$ TeV gemessen, unter Verwendung von frühen LHC Run 3-Daten mit integrierter Luminosität von 1.21 fb^{-1} . Durch Kombination der Dilepton- und Lepton+Jets ($\ell+\text{jets}$)-Zerfallskanäle von $t\bar{t}$ und simultane Bestimmung der Lepton- und b-tagging-Effizienzen in einem Likelihood-Fit wird eine mit früheren $\sigma_{t\bar{t}}$ -Messungen vergleichbare Präzision von 3.4% erreicht.

Anschließend wird Produktion von off-shell $t\bar{t}$ und $t\bar{t}/tW$ -Interferenz mit dem Monte Carlo (MC)-Generator `bb41` untersucht, der zum ersten Mal in der CMS-Simulation validiert und mit anderen MC-Generatoren verglichen wird und dabei zu einer deutlich verbesserten Beschreibung der Daten führt.

Schließlich wird eine Suche für nach $t\bar{t}$ zerfallende Spin-0-Zustände in den Dilepton-Kanälen mit Daten von LHC Run 2, einer integrierten Luminosität von 138 fb^{-1} und $\sqrt{s} = 13$ TeV vorgestellt. Die invariante Masse von $t\bar{t}$ ($m_{t\bar{t}}$) wird mit Spinkorrelations-Observablen kombiniert, um die Sensitivität gegenüber dem Spin und der \mathcal{CP} -Struktur möglicher neuer Zustände zu erhöhen. Ein statistisch signifikanter Überschuss von Ereignissen im Vergleich zum $t\bar{t}$ -Kontinuums-Hintergrund bei geringen Werten von $m_{t\bar{t}}$, konsistent mit pseudoskalaren Spinkorrelationen, wird beobachtet. Der Überschuss wird als pseudoskalarer gebundener $t\bar{t}$ -Zustand η_t interpretiert, und dessen Produktionsquerschnitt wird mithilfe eines vereinfachten, von nichtrelativistischer Quantenchromodynamik inspirierten Modells zu $\sigma(\eta_t) = 8.7 \pm 1.1 \text{ pb}$ gemessen.

Die selben Daten werden weiterhin als generische zusätzliche pseudoskalare oder skalare Bosonen interpretiert, und Ausschlussregionen hinsichtlich ihrer Kopplungen zum Top-Quark werden sowohl für die Dilepton-Kanäle allein als auch für eine Kombination mit einer separaten Analyse der $\ell+\text{jets}$ -Kanäle berechnet. Als eine dritte Interpretation der Daten werden zu $t\bar{t}$ zerfallende Axion-Like Particles (ALPs) im Grenzfall verschwindender ALP-Gluon-Kopplungen betrachtet, während der allgemeinere Fall auf phänomenologische Weise in Simulationsdaten untersucht wird.

Contents

| | | |
|----------|---|-----------|
| 1 | Introduction | 9 |
| 2 | Theoretical framework | 11 |
| 2.1 | Standard Model | 11 |
| 2.1.1 | Top quark | 12 |
| 2.1.2 | Higgs mechanism | 13 |
| 2.2 | The $p p \rightarrow t\bar{t}$ process | 14 |
| 2.2.1 | Spin state of the $t\bar{t}$ system | 16 |
| 2.2.2 | Spin density matrix | 19 |
| 2.2.3 | Bound state effects in $t\bar{t}$ | 21 |
| 2.3 | Beyond the Standard Model | 24 |
| 2.3.1 | Heavy scalars in $t\bar{t}$ production | 25 |
| 2.3.2 | Two-Higgs Doublet Model | 28 |
| 2.3.3 | Axion-Like Particles | 28 |
| 3 | Monte Carlo event generation | 31 |
| 3.1 | Matrix Element generators | 31 |
| 3.2 | Parton showers and matching | 34 |
| 3.3 | Multi-parton interactions | 35 |
| 3.4 | Hadronization | 35 |
| 3.5 | Pileup | 36 |
| 3.6 | Detector and trigger simulation | 36 |
| 4 | Experimental methods | 38 |
| 4.1 | The Large Hadron Collider | 38 |
| 4.2 | The CMS experiment | 39 |
| 4.3 | Object reconstruction | 41 |
| 4.4 | Statistical interpretation | 43 |
| 5 | Measurement of the inclusive $t\bar{t}$ cross section at $\sqrt{s} = 13.6$ TeV | 48 |
| 5.1 | Introduction | 48 |
| 5.2 | Datasets and event selection | 49 |
| 5.2.1 | Datasets | 49 |
| 5.2.2 | Object definition | 50 |
| 5.2.3 | Channel definition | 51 |

| | | |
|----------|---|-----------|
| 5.3 | Corrections | 52 |
| 5.3.1 | Experimental corrections | 53 |
| 5.3.2 | Data-driven background estimation | 57 |
| 5.4 | Control distributions | 63 |
| 5.5 | Systematic uncertainties | 67 |
| 5.6 | Fit results | 72 |
| 5.6.1 | Statistical checks | 74 |
| 5.6.2 | Top quark mass dependence | 74 |
| 5.7 | Summary and Outlook | 75 |
| 6 | Simulation of on- and off-shell $t\bar{t}$ production with bb4l | 78 |
| 6.1 | Introduction | 78 |
| 6.2 | The Monte Carlo generator bb4l | 78 |
| 6.3 | Other $t\bar{t}$ Monte Carlo generators | 79 |
| 6.3.1 | hvq | 80 |
| 6.3.2 | ST_wtch | 80 |
| 6.3.3 | ttb_NLO_dec | 80 |
| 6.4 | Technical setup | 81 |
| 6.4.1 | Parton shower matching | 81 |
| 6.4.2 | Same-flavor leptons | 82 |
| 6.5 | Results | 82 |
| 6.5.1 | Comparison between generators | 82 |
| 6.5.2 | Comparison of FSR matching settings | 89 |
| 6.5.3 | Recoil in top decay | 90 |
| 6.6 | Summary and Outlook | 91 |
| 7 | Search for heavy scalar or pseudoscalar bosons in $t\bar{t}$ final states | 93 |
| 7.1 | Introduction | 93 |
| 7.2 | Analysis setup | 94 |
| 7.2.1 | Datasets | 94 |
| 7.2.2 | Object definition | 97 |
| 7.2.3 | Event selection | 97 |
| 7.2.4 | Experimental corrections | 98 |
| 7.2.5 | Reconstruction of the $t\bar{t}$ system | 100 |
| 7.2.6 | Sensitive observables | 103 |
| 7.3 | Higher-order corrections in $t\bar{t}$ | 104 |
| 7.3.1 | NNLO QCD corrections | 105 |
| 7.3.2 | NLO EW corrections | 105 |
| 7.4 | Matrix element reweighting for A/H signals | 107 |
| 7.4.1 | Principle of the method | 107 |
| 7.4.2 | Combination of multiple origin samples | 109 |
| 7.4.3 | Validation | 110 |

| | | |
|----------|--|------------|
| 7.5 | Systematic uncertainties | 110 |
| 7.5.1 | Theory uncertainties | 110 |
| 7.5.2 | Experimental uncertainties | 112 |
| 7.5.3 | Uncertainty smoothing | 113 |
| 7.5.4 | Differences between MC generators | 114 |
| 7.6 | Pre-fit distributions | 116 |
| 7.7 | Interpretation of the excess | 121 |
| 7.7.1 | Extraction of $t\bar{t}$ bound state effects | 121 |
| 7.7.2 | Parity of the excess | 122 |
| 7.7.3 | Checks of the result | 122 |
| 7.7.4 | Interpretation in terms of A and H | 129 |
| 7.8 | Limits on A/H bosons | 130 |
| 7.9 | Combination with the $\ell+$ jets channels | 132 |
| 7.9.1 | Analysis strategy in the $\ell+$ jets channel | 137 |
| 7.9.2 | A/H limits | 138 |
| 7.9.3 | Simultaneous A+H exclusion contours | 138 |
| 7.10 | Comparison to other results | 145 |
| 7.10.1 | ATLAS $A/H \rightarrow t\bar{t}$ search | 145 |
| 7.10.2 | Other $t\bar{t}$ measurements | 146 |
| 7.11 | Summary and Outlook | 147 |
| 8 | Investigation of Axion-Like Particles decaying to $t\bar{t}$ | 149 |
| 8.1 | Introduction | 149 |
| 8.2 | Translation of experimental limits | 149 |
| 8.3 | Phenomenological setup | 151 |
| 8.4 | Comparison of ALP and A | 153 |
| 8.5 | Projected limits for ALPs | 155 |
| 8.6 | Summary and Outlook | 157 |
| 9 | Summary and Conclusions | 159 |
| A | Bibliography | 161 |

¹ 1 Introduction

² It has always been the goal of high-energy physics to decipher the fundamental rules
³ of nature. The most recent triumph in this journey was undoubtably the discovery of
⁴ the Higgs boson at the ATLAS and CMS experiments of the Large Hadron Collider
⁵ (LHC) in 2012 [1–3], thus completing the Standard Model of particle physics (SM).
⁶ Since then, the SM has been measured with ever-growing precision in the hope
⁷ of finding and characterizing possible deviations from its predictions, and searches
⁸ for new phyiscs beyond the Standard Model (BSM) have been performed in many
⁹ possible phase spaces and for many SM extensions. So far, no significant discrepancy
¹⁰ has been found.

¹¹ One promising avenue for searches for new physics is the top quark, which is
¹² the most massive fundamental particle in the SM. It is thus relevant for possible
¹³ new particles with Yukawa couplings, i.e. couplings proportional to the particle
¹⁴ mass, such as extended Higgs sectors. It is also of interest within the context of
¹⁵ the SM: as the only colored particle that decays before hadronizing, it allows for
¹⁶ measurements of spin properties, and poses challenges for its precision modeling in
¹⁷ quantum chromodynamics (QCD).

¹⁸ In this thesis, different aspects of top quark pair ($t\bar{t}$) production in proton-proton
¹⁹ collisions at the LHC are studied. It has been performed as part of the Compact
²⁰ Muon Solenoid (CMS) experiment [4], which is one of the two large general-purpose
²¹ LHC experiments. The first topic is a measurement of the inclusive $t\bar{t}$ production
²² cross section, performed at a center-of-mass energy of $\sqrt{s} = 13.6$ TeV [5]. This world-
²³ record energy was reached by the LHC for the first time in 2022 at the start of LHC
²⁴ Run 3, after three years of shutdown and technical upgrades. The measurement
²⁵ performed here uses only 1.21 fb^{-1} of data, taken directly at the start of Run 3 in
²⁶ July and August 2022, to achieve a precision on the $t\bar{t}$ cross section comparable with
²⁷ previous LHC measurements. This was made possible by designing a strategy aimed
²⁸ at estimating needed experimental corrections directly as part of the measurement.
²⁹ In addition to confirming the SM at a new energy, the result was the first public
³⁰ result of LHC Run 3 and showed the high quality of the then-fresh collision data.

³¹ Second, the modeling of $t\bar{t}$ production in off-shell regions of phase space as well
³² as the interference between $t\bar{t}$ and tW production at CMS is studied [6]. This is
³³ done using the Monte Carlo (MC) event generator **bb41** [7], which computes the full
³⁴ $pp \rightarrow b\bar{b}\ell^+\ell^-\nu_\ell\bar{\nu}_\ell$ matrix element for the dilepton decay channel of $t\bar{t}$, thus naturally
³⁵ including off-shell and interference effects. **bb41** is validated for the first time in
³⁶ the CMS simulation setup, and compared to other MC generators for $t\bar{t}$ production,

37 preparing its use in future precision $t\bar{t}$ measurements at CMS.

38 Finally, a search for new spin-0 states decaying to $t\bar{t}$ is performed, using the
39 full CMS Run 2 dataset with a luminosity of 138 fb^{-1} [8, 9]. The dilepton decay
40 channel of $t\bar{t}$ is considered, and besides the invariant $t\bar{t}$ mass ($m_{t\bar{t}}$), spin correlation
41 observables constructed from the leptons and top quarks are used to distinguish
42 different spin states of the $t\bar{t}$ system, giving sensitivity to the \mathcal{CP} structure of possible
43 new states. Excitingly, a statistically significant excess is observed in the data
44 compared to the standard SM predictions, which is located at low $m_{t\bar{t}}$ values and
45 prefers pseudoscalar spin states. The excess is interpreted to be consistent with a
46 pseudoscalar $t\bar{t}$ (quasi-)bound state, which is expected to exist in the SM according
47 to non-relativistic QCD calculations, though its modeling remains a challenge. This
48 constitutes the first time such a $t\bar{t}$ bound state is experimentally observed.

49 Alternatively, the results are interpreted in terms of generic additional pseu-
50 doscalar or scalar bosons, as expected e.g. in a Two-Higgs-Doublet Model. The
51 interference of these new bosons decaying to $t\bar{t}$ and SM $t\bar{t}$ production is taken into
52 account, leading to complex signatures in the $m_{t\bar{t}}$ spectrum. In addition to an inter-
53 pretation of the same low- $m_{t\bar{t}}$ excess, exclusion regions are derived for the presence
54 of either one or two such new bosons in terms of their couplings to the top quark.
55 For this purpose, the analysis of the dilepton decay channel of $t\bar{t}$ is further combined
56 with a separate analysis of the lepton+jets decay channel.

57 As a third interpretation, heavy Axion-Like Particles (ALPs) decaying to $t\bar{t}$ are
58 considered for the first time [10]. After explicitly translating the experimental results
59 for generic pseudoscalars to ALPs in the limiting case of no explicit gluon couplings,
60 the general case is studied in simulated events. Sensitivity estimates for heavy
61 ALPs coupling to top quarks, and for the possibility to distinguish them from other
62 pseudoscalars, are derived for the currently available luminosity as well as future
63 projections.

64 The thesis is organized as follows. In Chapters 2 to 4, the framework used for
65 the analyses is outlined. In particular, Chapter 2 describes aspects of the SM and
66 BSM theories relevant for this work, Chapter 3 briefly discusses the machinery of
67 Monte Carlo generators as used for all relevant studies, and Chapter 4 describes the
68 LHC and the CMS detector as well as object reconstruction and statistical inference
69 techniques. Following that, Chapters 5 to 8 each discuss one of the experimental
70 or phenomenological results that comprise this work: the inclusive $t\bar{t}$ cross section
71 measurement in Chapter 5, the study of off-shell $t\bar{t}$ production and $t\bar{t}/tW$ inter-
72 ference in Chapter 6, the search for spin-0 states in $t\bar{t}$, including its interpretation
73 as a $t\bar{t}$ bound state, in Chapter 7, and the investigation of ALPs decaying to $t\bar{t}$
74 in Chapter 8. Chapters 5 and 6 fully consist of work done as part of this thesis,
75 while in Chapters 7 and 8 the major contributions from this thesis are summarized
76 at the beginning of the chapters. Finally, a short summary and outlook is given in
77 Chapter 9.

⁷⁸ 2 Theoretical framework

⁷⁹ This chapter gives an outline of the theoretical concepts and models used in this
⁸⁰ thesis. It is split into two parts: First, the Standard Model of elementary particle
⁸¹ physics is discussed, with a heavy emphasis on the top quark. Secondly, several
⁸² hypothesized extensions of the Standard Model, relevant for the searches presented
⁸³ in Chapters 7 and 8, are briefly introduced and compared.

⁸⁴ 2.1 Standard Model

⁸⁵ The Standard Model of elementary particle physics, often simply called the Stan-
⁸⁶ dard Model or SM, is, at the time of writing, the most successful theory describing
⁸⁷ the fundamental particles making up our universe. It is the result of a steady pro-
⁸⁸ gression of increasingly complex models, starting with the introduction of quantum
⁸⁹ mechanics in the early 20th century and ending - for now - with the discovery of the
⁹⁰ Higgs boson at the LHC in 2012. The model has been extensively tested at many
⁹¹ different experiments, most importantly the large collider experiments like LEP, the
⁹² Tevatron, and the LHC. So far, it has survived all these tests with excellence.

⁹³ The SM is formulated as a relativistic quantum field theory (QFT). That is, its
⁹⁴ most fundamental objects are fields acting on four-dimensional spacetime which,
⁹⁵ after a quantization procedure, yield physically observable particles as fundamental
⁹⁶ excitations. By the usual counting scheme, there exist seventeen different such fields,
⁹⁷ which can be classified into different groups, as schematically shown in Fig. 2.1.

⁹⁸ The first group consists of the twelve fermions, which have spin $\frac{1}{2}$ and make up
⁹⁹ all visible matter. They are further split into the leptons, consisting of three elec-
¹⁰⁰ trically charged leptons - electron, muon, and tau lepton - and three corresponding
¹⁰¹ electrically neutral neutrinos, as well as the quarks, of which there are six differ-
¹⁰² ent flavors, called up, down, strange, charm, bottom, and top. The quarks have
¹⁰³ fractional electric charge, and in addition carry color charge as their defining prop-
¹⁰⁴ erty. Of note is that the fermions are also split into three generations, with each
¹⁰⁵ generation consisting of a charged lepton, a neutrino, and two quarks. The only fun-
¹⁰⁶ damental differences between the particles of different generations are their masses,
¹⁰⁷ though the resulting physically observable properties, such as the lifetime, might be
¹⁰⁸ dramatically different.

¹⁰⁹ The second group of particles are the bosons, which have integer spin. Here,
¹¹⁰ the four gauge bosons with spin 1 act as the force carriers of the four fundamental
¹¹¹ interactions described by the SM: the photon, for the electromagnetic interaction

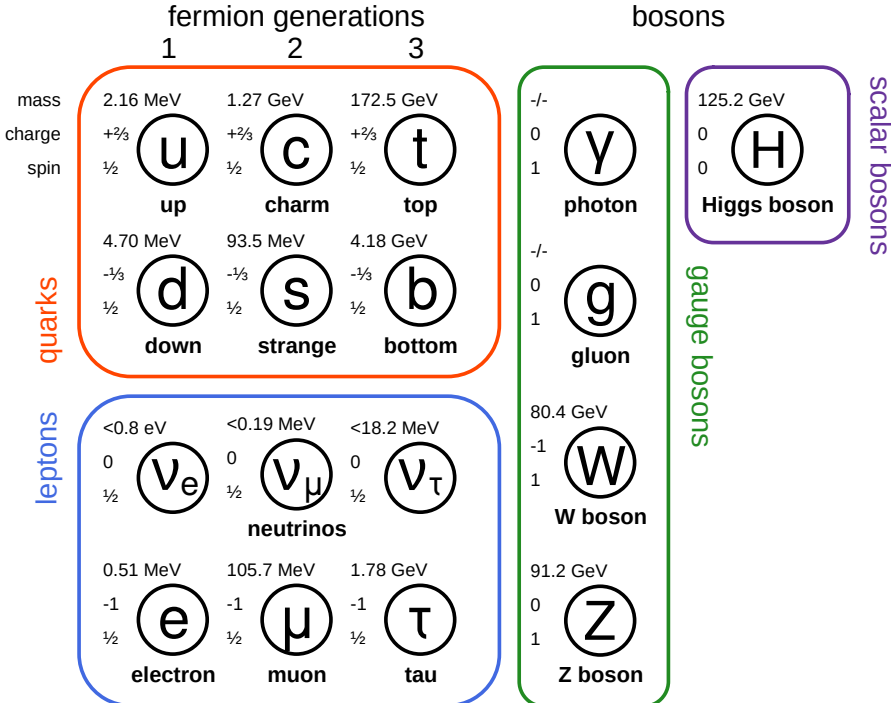


Figure 2.1: **The Standard Model.** A schematic depiction of the particle content of the SM, showing the seventeen fundamental particles, split into six quarks, six leptons, four gauge bosons, and the Higgs boson. The masses, electromagnetic charges, and spin of the particles is given next to the labels. Mass information is taken from Ref. [11].

with coupling strength α_{elm} ; the W and Z bosons, for the weak interaction with coupling strength α_W ; and the gluon, for the strong interaction with coupling strength α_S . At high enough energies, the electromagnetic and weak interaction unify into the electroweak interaction (coupling strength α_{EW}). The last and final particle is the Higgs boson, which has spin 0. Its most important role in the SM is to give mass to the fermions, as well as the W and Z bosons, through the so-called Higgs mechanism [12, 13], which is briefly outlined in Sec. 2.1.2.

2.1.1 Top quark

All results presented as part of this thesis focus on one particular fundamental particle: the top quark. As such, it will be described in further detail in this section. The top quark was first discovered in 1995 at the Tevatron by the CDF and D0 experiments [14, 15]. With a rest mass of $m_t \approx 172.5 \text{ GeV}$, the top quark is the most massive known fundamental particle, and as a result it has unique properties compared to the other quarks: Its extremely short lifetime of $\sim 5 \times 10^{-25} \text{ s}$ is lower

126 than the typical time needed for a quark to hadronize under the strong interaction,
 127 making it the only bare quark - that is, the only quark which, via its decay products,
 128 is observable outside of hadrons. Among others, a consequence of this is that it fully
 129 preserves spin information during its decay, while such information is typically lost
 130 for other quarks during hadronization. More details on this are found in Sec. 2.2.2.

131 A second important property of the top quark that follows from its high mass is
 132 its large Yukawa coupling to the SM Higgs boson, which is of order one. As a result,
 133 the Higgs boson couples preferentially to the top quark of all SM fermions, and the
 134 study of both the SM Higgs boson and hypothetical additional Higgs bosons (see
 135 Sec. 2.3) is tightly connected to the top quark.

136 In the SM, the top quark decays to a bottom quark and a W boson with a branch-
 137 ing ratio (BR) of almost 100% (to the degree that all other decays are commonly
 138 neglected). The W boson, in turn, can decay either to a charged lepton (e , μ or τ)
 139 and the corresponding neutrino with a BR of $\sim 32.6\%$, or to a pair of quarks (one
 140 up- and one down-type) with a BR of $\sim 67.4\%$. This results in different final states
 141 for top production processes, which are discussed more in Sec. 2.2.

142 2.1.2 Higgs mechanism

143 The Higgs boson is the most recently discovered particle of the SM. Its existence was
 144 confirmed in 2012 at the LHC by the ATLAS and CMS collaborations [1–3], firmly
 145 establishing the SM in its current form as the accepted description of elementary
 146 particle physics. While this work does not focus on the SM Higgs boson as it
 147 does on the top quark, a short discussion of its role in the SM - the so-called Higgs
 148 mechanism - is relevant for possible SM extensions to additional Higgs bosons, which
 149 are searched for in Chapters 7 and 8.

150 In the SM Lagrangian, the Higgs boson appears as a complex doublet ϕ in the
 151 form

$$\mathcal{L}_{\text{SM}} \subset (D_\mu \phi)^\dagger D^\mu \phi + V(\phi) \quad (2.1)$$

152 where D_μ is the covariant derivative, containing the minimal coupling to the gauge
 153 fields, and the Higgs potential $V(\phi)$ is

$$V(\phi) = \mu^2 \phi^\dagger \phi - \lambda (\phi^\dagger \phi)^2. \quad (2.2)$$

154 Here, μ^2 and λ are free parameters of the model. If both parameters are positive,
 155 this potential (known as the “Mexican hat potential”) has a minimum at a non-zero
 156 value of

$$|\phi| = \frac{\mu}{\sqrt{2\lambda}} \equiv \frac{v}{\sqrt{2}} \quad (2.3)$$

157 with the vacuum expectation value $v = \mu/\sqrt{\lambda}$. On the other hand, the minimum -

158 corresponding to the vacuum state - is degenerate with respect to the three phases
159 (i.e. the $SU(2)$ symmetry) of the complex doublet.

160 In the Higgs mechanism, this symmetry is now spontaneously broken in the transi-
161 tion from the high-energy state of the early universe (where the minimum is at
162 $|\phi| = 0$) to the low-energy state observed today. The physical particles after sym-
163 metry breaking are then described by fluctuations around the new vacuum state.
164 If the Higgs field were to be considered on its own, this would lead to one massive
165 (corresponding to fluctuations in the $|\phi|$ direction) and three massless degrees of
166 freedom (corresponding to the phases).

167 However, the interaction with the electroweak gauge fields encoded within D_μ
168 leads to the massless degrees of freedom being absorbed into the gauge fields. This
169 turns three of the four massless spin-1 gauge fields of the electroweak Lagrangian
170 (with two degrees of freedom each) into massive fields instead (which have an ad-
171 ditional longitudinal polarization, and thus three degrees of freedom). These three
172 massive gauge fields are identified with the W and Z bosons, while the remaining
173 massless field is identified with the photon. Finally, the leftover massive degree of
174 freedom from the Higgs doublet ϕ is identified with the spin-0 boson observed at
175 the LHC.

176 The resulting masses of the Z, W and Higgs bosons can be predicted as a function
177 of μ^2 , λ and the electroweak couplings and thus used to test the Higgs mechanism.
178 In addition to the electroweak bosons, the Higgs mechanism can also give masses to
179 fermions (charged leptons and quarks) by including a Yukawa interaction term in the
180 Lagrangian. This results in couplings between the SM Higgs boson and the different
181 fermions that are proportional to the respective fermion mass, leading to the largest
182 coupling to the top quark. In possible extensions of the SM, this proportionality
183 might be modified, making Yukawa coupling measurements attractive as tests of the
184 SM.

185 2.2 The $p p \rightarrow t \bar{t}$ process

186 In proton-proton collisions at the LHC, the dominant production mode of top quarks
187 is the production of a top-antitop quark pair ($t\bar{t}$). The different parts of this thesis all
188 focus on this process in different ways, and so this chapter gives a detailed overview
189 of relevant effects.

190 At LO in QCD, there are three diagrams (up to permutations of initial and final
191 states) contributing to $t\bar{t}$ production, which can be seen in Fig. 2.2. They differ in
192 their initial states: the first two diagrams are induced by gluon fusion, while the
193 last one is induced by quark fusion (mostly from $u\bar{u}$ and $d\bar{d}$). The fraction of these
194 is determined by the corresponding parton densities; at a center-of-mass energy of
195 $\sqrt{s} \geq 13$ TeV, gluon fusion dominates with a fraction of roughly 90%.

196 At NLO in QCD, many more diagrams become relevant, including those induced

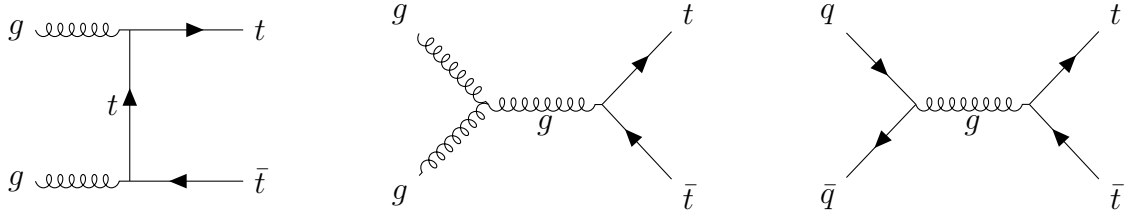


Figure 2.2: **Feynman diagrams for $pp \rightarrow t\bar{t}$.** The three diagrams (up to permutations) that contribute to the $pp \rightarrow t\bar{t}$ process at LO in QCD.

197 by the fusion of one quark and one gluon, while radiating a real quark. Similarly,
 198 real emissions of gluons can take place in gg or $q\bar{q}$ fusion diagrams. These effects change
 199 the kinematic properties of the produced top quarks, leading to NLO corrections for
 200 predicted distributions.

201 After production, both the top quark and antiquark in the $t\bar{t}$ pair decay into a W
 202 boson and a b (anti)quark each. This leads to three different decay channels of the
 203 $t\bar{t}$ pair depending on the decays of the two W bosons, which are classified according
 204 to their number of leptons: The dilepton channel, with final state $b\bar{b}\ell^+\ell^-\nu\bar{\nu}$; the
 205 lepton+jets channel, with final state $b\bar{b}\ell\nu q\bar{q}$; and the all-hadronic channel, with final
 206 state $b\bar{b}qq\bar{q}\bar{q}$. Here, q stands in for any light quark (u, d, s or c).

207 The three channels differ greatly in their experimental challenges: The dilepton
 208 channel has the lowest branching ratio of $\sim 10.6\%$, which is further reduced to \sim
 209 5.1% when excluding τ leptons due to then being experimentally hard to reconstruct.
 210 It also suffers from the fact that the two produced neutrinos escape the detector
 211 unobserved and are only measured as missing transverse momentum, losing both
 212 information in the forward direction as well as the ability to disentangle the two
 213 neutrinos. On the other hand, the final state of two opposite-sign charged leptons,
 214 two b jets, and missing transverse momentum does not have many other contributing
 215 processes in the SM, leading to very pure selections (particularly when the two
 216 leptons are an electron and a muon). All results in this thesis make use of this
 217 channel prominently.

218 By contrast, the lepton+jets channel has a large BR of $\sim 43.9\%$ ($\sim 30.3\%$ when
 219 excluding τ leptons), leading to high data statistics, and allows for easier interpre-
 220 tation of the missing transverse momentum due to only one neutrino. However, it
 221 can suffer from contamination by W+jets and multijet QCD background (the latter
 222 with non-prompt or fake leptons), from issues with combinatorics (i.e. the assign-
 223 ment of experimentally measured jets to the decay products) and from hadronic jet
 224 uncertainties, which can be large. This decay channel is employed for the result in
 225 Chapter 5 as well as in the combination in Chapter 7.

226 Finally, the all-hadronic channel, with a similar BR of $\sim 45.4\%$, is typically
 227 difficult to isolate from the background of QCD multijet production, and in addition
 228 suffers even more strongly from combinatorics and jet uncertainties than the

| Term symbol | Spin multiplicity | \mathcal{P} | \mathcal{C} |
|-------------|-------------------|---------------|---------------|
| 1S_0 | singlet | -1 | +1 |
| 3P_0 | triplet | +1 | +1 |
| 3S_1 | triplet | -1 | -1 |
| 1P_1 | singlet | +1 | -1 |
| 3P_1 | triplet | +1 | +1 |
| 3D_1 | triplet | -1 | -1 |

Table 2.1: **Spin states of $t\bar{t}$.** Overview of the possible angular momentum states of the $t\bar{t}$ system with $J \leq 1$, including the spin multiplicity, the parity \mathcal{P} and the charge-parity \mathcal{C} .

229 lepton+jets channel. As a result, it is in many cases the least precise of the three
 230 channels, and is not studied further in this work.

231 2.2.1 Spin state of the $t\bar{t}$ system

232 As fermions with spin $\frac{1}{2}$, top quarks have two possible spin states. As a result, the
 233 relative spins of the $t\bar{t}$ system can be either aligned, leading to a total vector state
 234 with spin $S = 1$, or anti-aligned, leading to a scalar state with spin $S = 0$. Further-
 235 more, the $t\bar{t}$ system as a whole can have orbital angular momentum L , where L is a
 236 non-negative integer. In analogy to atomic orbitals, the total angular momentum is
 237 then $\vec{J} = \vec{L} + \vec{S}$, and for any chosen basis the set of quantum numbers $\{S, L, J, J_z\}$
 238 consists of conserved quantities. The angular momentum state is commonly written
 239 using a term symbol $^{2S+1}L_J$, where $2S+1$ denotes the multiplicity of the spin state,
 240 and the orbital angular momentum L is written using spectroscopic notation (S for
 241 $L = 0$, P for $L = 1$, D for $L = 2$ etc). An overview of the lowest possible states
 242 ($J \leq 1$) is given in Tab. 2.1, including also the parities and charge-parities \mathcal{P} and
 243 \mathcal{C} , which can be inferred from the intrinsic parities of top and antitop as well as the
 244 orbital angular momentum. In proton-proton collisions, a mixture of all these states
 245 is produced, with the ratio depending on the production mode (gg , $q\bar{q}$ or gq) as well
 246 as the energy.

247 In practice, the spins of the top (anti)quarks cannot be observed directly, and
 248 instead must be inferred from their decay products. The way in which the spin
 249 information is passed to the decay products is determined by the maximally parity-
 250 violating nature of the weak interaction together with conservation of angular mo-
 251 mentum. This is illustrated in Fig. 2.3 for the leptonic decay of the top (anti)quark:
 252 Since the b quark is light compared to the top quark and will thus be ultra-
 253 relativistic, as a fermion its helicity is determined by its chirality. As a result,
 254 for the decay $t \rightarrow W^+ b$ the b quark - left-handed due to the weak interaction - has
 255 negative helicity (spin opposite to its direction of flight), leading to two possibilities

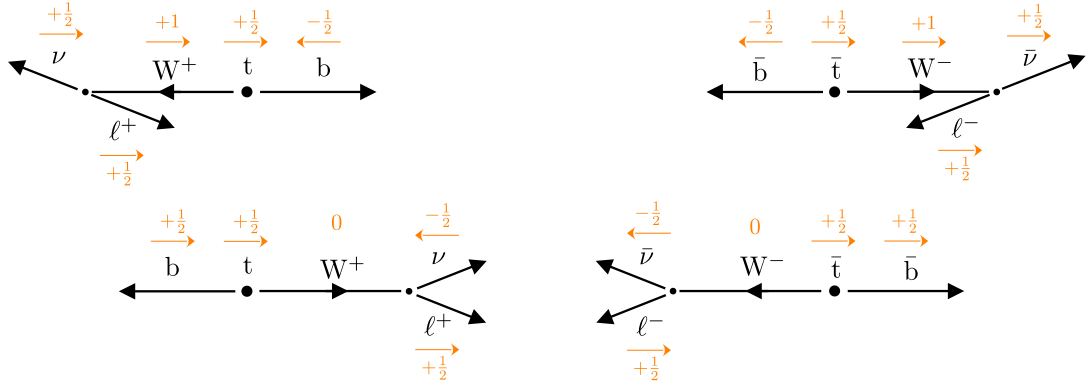


Figure 2.3: **Helicity in top decays.** Sketch of the allowed helicity configurations in a top quark (left) and antiquark decay (right) in the rest frame of the quark, involving either a transversely (top, $S_z = 1$) or longitudinally polarized W boson (bottom, $S_z = 0$). The z axis corresponds to the spin of the top (anti)quark, and the orange arrows and numbers illustrate the spin in the z direction of the respective particles. It can be seen that, due to conservation of angular momentum and the parity-violating nature of the weak interaction, the ℓ^+ is preferred to be emitted in the direction of the t spin, while the ℓ^- is preferred to be emitted opposite to the direction of the \bar{t} spin.

for the W boson through conservation of angular momentum: transversely polarized (spin 1, top left in Fig. 2.3) or longitudinally polarized (spin 0, bottom left in Fig. 2.3).

Since the decay of the W^+ into $\ell^+\nu$ is again mediated by the weak interaction, and both decay products are nearly massless, the helicities of ℓ^+ and ν must be positive and negative, respectively. Applying again conservation of angular momentum, one then finds from the sketch that in both cases, the charged lepton is emitted preferably in the direction of the top quark spin.

Repeating the same line of arguments for the decay of the antitop (Fig. 2.3 on the right), one finds that the opposite holds there: the charged lepton is emitted preferably opposite to the antitop spin. As a result, the direction of flight of the charged lepton in the center-of-mass system of its parent (anti)top can be used as a proxy for the (anti)top spin (or, equivalently, its polarization). It should be noted that this property of the top quark is unique among the quarks of the SM, since all other quarks hadronize via the helicity-ignorant strong interaction and thus lose the largest part of their spin information¹.

Returning to the full $t\bar{t}$ system, and applying the above observation to both

¹See e.g. Ref. [16] for the greatly reduced possibilities of measuring spin correlations in $b\bar{b}$ or $c\bar{c}$ systems at the LHC.

273 top and antitop, one can now define observables to probe the $t\bar{t}$ spin state, or
 274 equivalently, the spin correlation between t and \bar{t} . A simple such variable is the
 275 azimuthal difference $\Delta\phi_{\ell\ell}$ between the two leptons in a dileptonic decay. Assuming
 276 that the top and antitop are emitted back-to-back, a state with the top and antitop
 277 spins aligned (i.e. $S = 1$) will cause the two leptons to be emitted preferably in
 278 opposite directions, leading to large $\Delta\phi_{\ell\ell}$, while anti-aligned spins ($S = 0$) will
 279 lead preferably to parallel leptons and thus small $\Delta\phi_{\ell\ell}$. While this variable has
 280 the advantage of being easy to define and experimentally clean to measure, it is
 281 suboptimal in that it is also strongly affected by the kinematics of the $t\bar{t}$ production,
 282 including higher-order corrections in QCD, and is heavily sculpted when selecting
 283 certain areas of $t\bar{t}$ phase space. Thus, it is afflicted with large modeling uncertainties.

284 A more powerful variable can be defined by employing suitable reference systems
 285 as follows: the lepton and antilepton are first Lorentz boosted into the center-of-
 286 mass frame of the $t\bar{t}$ system, and then further boosted into the center-of-mass frame
 287 of their parent (anti)tops. Then, a correlation variable c_{hel} is defined as the scalar
 288 product of their direction unit vectors in these reference frames²:

$$c_{\text{hel}} = \hat{\ell}_t^+ \cdot \hat{\ell}_{\bar{t}}^- \quad (2.4)$$

289 It can be shown that, irrespective of the mode of production of the $t\bar{t}$ system and
 290 inclusive in the rest of the phase space, the distribution of this observable always
 291 follows a straight line [18], i.e.

$$\frac{1}{\sigma} \frac{d\sigma}{dc_{\text{hel}}} = \frac{1}{2} (1 - D c_{\text{hel}}) \quad (2.5)$$

292 The slope D depends on the spin and angular momentum of the produced $t\bar{t}$
 293 state. At LO in QCD, it can be shown that $D = -1$ for pure singlet states (anti-
 294 aligned spins, e.g. 1S_0 , 1P_1) and $D = +\frac{1}{3}$ for pure triplet states (aligned spins, e.g.
 295 3S_1 , 3P_0) [19, 20]. Higher-order corrections in QCD can slightly reduce these slopes
 296 through emissions of real gluons in the decay, which weaken the correlations, but
 297 these effects are on the order of 0.2% at NLO for leptons [21, 22].

298 In practice, any observed ensemble of $t\bar{t}$ pairs will be a mixture of the different spin
 299 states depending on the production mechanism and underlying theory, which can
 300 be probed by measuring the slope D . As will be discussed in Sec. 2.3, extensions
 301 of the SM can change the predicted slope, making measurements of D attractive
 302 tests for new physics. The value of D has been measured e.g. in Refs. [23–25], as
 303 well as more recently as a proxy variable in the context of measurements of quantum
 304 entanglement in $t\bar{t}$ production [26, 27].

²In this work, the naming convention from Ref. [17] is followed for c_{hel} . In e.g. Ref. [18], this variable is instead called $\cos\varphi$.

305 **2.2.2 Spin density matrix**

306 A more detailed way to quantify the spin properties of the $\text{t}\bar{\text{t}}$ system, respective
307 to an arbitrary spin basis, is the production spin density matrix \mathbf{R} , which (when
308 averaged over initial spins and colors, and summed over final colors) can be written
309 as [19, 20, 28]

$$\mathbf{R} = A \mathbb{1} \otimes \mathbb{1} + B_i^1 \sigma_i \otimes \mathbb{1} + B_i^2 \mathbb{1} \otimes \sigma_i + C_{ij} \sigma_i \otimes \sigma_j. \quad (2.6)$$

310 Here, $\mathbb{1}$ is the two-dimensional identity matrix, σ_i with $i = 1, 2, 3$ are the Pauli
311 matrices, and the first and second components of the tensor product refer to the
312 spin of the top quark and antiquark, respectively. The scalar coefficient A describes
313 the overall amplitude (i.e. the cross section) of $\text{t}\bar{\text{t}}$ production, the vectors \vec{B}^1 and
314 \vec{B}^2 describe the polarization of the top quark and antiquark, and the matrix \mathbf{C}
315 describes the correlation between their spins. All of them are, in general, functions
316 of the partonic center-of-mass energy and the scattering angle of the top quark
317 relative to the incoming partons.

318 As explained in Sec. 2.2.1, in a dileptonic decay the spin information is transferred
319 almost completely to the charged leptons. Defining the lepton directions of flight in
320 their parent frames $\hat{\ell}_t^+$ and $\hat{\ell}_{\bar{t}}^-$ as in Eq. (2.4), the resulting differential cross section
321 in terms of the lepton angles is [28]

$$\frac{1}{\sigma} \frac{d\sigma}{d\Omega} = 1 + \vec{B}^1 \cdot \hat{\ell}_t^+ + \vec{B}^2 \cdot \hat{\ell}_{\bar{t}}^- + (\hat{\ell}_t^+)^T \mathbf{C} \hat{\ell}_{\bar{t}}^- \quad (2.7)$$

322 By integrating out the remaining angles, it can be shown from this that irrespec-
323 tive of the chosen basis the slope D as defined in Eq. (2.5) can be recovered from
324 the matrix \mathbf{C} as [18, 29]

$$D = -\frac{1}{3} \text{Tr} [\mathbf{C}] \quad (2.8)$$

325 As discussed in Sec. 2.2.1, D is maximally negative for pure singlet states, and thus
326 is ideal for separating those in a mixed ensemble. One can define similar separating
327 observables for other states using the spin density matrix by choosing a suitable spin
328 basis. In this work, the so-called helicity basis proposed in Ref. [30] is used. The
329 three axes of this basis, denoted \hat{k} , \hat{r} and \hat{n} , are defined as follows: \hat{k} is simply the
330 direction of flight of the top quark in the center-of-mass frame of the $\text{t}\bar{\text{t}}$ system, such
331 that the top quark spin with respect to \hat{k} is equal to the helicity. The second axis,
332 \hat{r} , is orthogonal to \hat{k} in the scattering plane of the $\text{pp} \rightarrow \text{t}\bar{\text{t}}$ process. Finally, the
333 third axis \hat{n} is orthogonal on both \hat{k} and \hat{r} , oriented such that the $\{\hat{k}, \hat{r}, \hat{n}\}$ system
334 is left-handed. If \hat{p} denotes the beam axis and θ_t^* the top scattering angle, the latter
335 two axes are given by

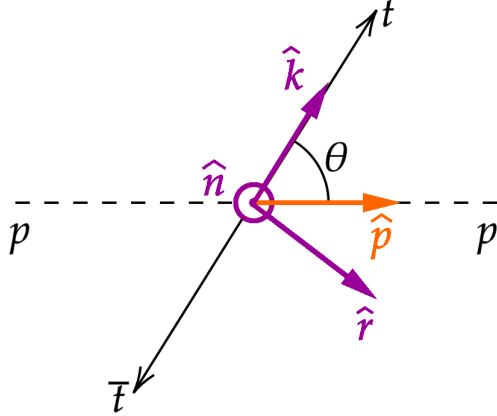


Figure 2.4: **Helicity basis.** Sketch of the helicity basis used to define the top and antitop quark spins. The unit vectors \hat{k} , \hat{r} and \hat{n} define the right-handed basis, while the beam axis is given by \hat{p} and the top quark scattering angle by θ . *Figure taken from Ref. [19].*

$$\hat{r} = \frac{\hat{p} - \cos \theta_t^* \hat{k}}{|\hat{p} - \cos \theta_t^* \hat{k}|} \quad \text{and} \quad \hat{n} = \hat{r} \times \hat{k} = \frac{\hat{p} \times \hat{k}}{|\hat{p} \times \hat{k}|}. \quad (2.9)$$

This coordinate system is visualized in Fig. 2.4. It is used, among others, in Refs. [24, 25] to measure both the polarizations \vec{B}^1 and \vec{B}^2 and spin correlation coefficients C_{ij} ($i, j = k, r, n$). In this work, only the spin correlation is considered. Particularly, in addition to c_{hel} , the following observable is defined:

$$c_{\text{han}} = (\hat{\ell}_t^+)_k (\hat{\ell}_{\bar{t}}^-)_k - (\hat{\ell}_t^+)_r (\hat{\ell}_{\bar{t}}^-)_r - (\hat{\ell}_t^+)_n (\hat{\ell}_{\bar{t}}^-)_n \quad (2.10)$$

where $(\hat{\ell}_i)_i$, $i = k, r, n$ refers to the i -th component of the respective vector in the $\{k, r, n\}$ basis. This observable, like c_{hel} , has the advantage of always being linear in the absence of phase space cuts, i.e.

$$\frac{1}{\sigma} \frac{d\sigma}{dc_{\text{han}}} = \frac{1}{2} (1 + D^{(k)} c_{\text{han}}) \quad (2.11)$$

where [19]

$$D^{(k)} = -\frac{1}{3} (C_{kk} - C_{rr} - C_{nn}). \quad (2.12)$$

From Eq. (2.12), it can be seen that the slope $D^{(k)}$ is maximal when the top and antitop spins are anti-correlated along the top direction of flight ($C_{kk} = -1$) and correlated along the orthogonal directions ($C_{rr} = C_{nn} = +1$). The (unpolarized) state described by these correlations is a pure triplet state ($S = 1$) [19]. Particularly,

348 the 3P_0 state of $t\bar{t}$ always corresponds to this spin state: It has no total angular
 349 momentum, and its total spin and orbital angular momentum must be anti-aligned.
 350 Since the orbital angular momentum is always exactly zero in the direction of flight
 351 of the top quarks, $L_k = 0$, it follows that also $S_k = 0$, i.e. the total spin is in an
 352 eigenstate in the \hat{k} direction. Together with $S = 1$ overall, this implies $C_{kk} = -1$ as
 353 well as $C_{rr} = C_{nn} = +1$.

354 2.2.3 Bound state effects in $t\bar{t}$

355 When predicting distributions of observables for hard scattering processes such as
 356 $t\bar{t}$ production, one usually employs perturbative calculations at a fixed order in the
 357 strong coupling constant α_S , possibly matched to a parton shower (see Chapter 3).
 358 However, at low energy scales (or equivalently, long distances) the strong interaction
 359 becomes non-perturbative, leading to effects that can not be captured in the usual
 360 perturbative expansion irrespective of the order in α_S (though they might or might
 361 not be captured in expansions or resummations with other parameter choices).

362 In the $pp \rightarrow t\bar{t}$ process, such effects might play a role in the vicinity of the
 363 $t\bar{t}$ production threshold, i.e. for $m_{t\bar{t}} \sim 2m_t$, where the relative velocities of the
 364 produced top quarks become small. In particular, one possible class of effects not
 365 included in simple expansions in α_S are $t\bar{t}$ bound states (“toponium”). Such states
 366 (also called quarkonia) are well-known in $c\bar{c}$ and $b\bar{b}$ production, where they lead to
 367 composite particles such as J/ψ , η_c or Υ . When translating this knowledge to $t\bar{t}$,
 368 however, there is a significant difference: due to the large top quark mass, the lifetime
 369 of the top quark is expected to be shorter than the (formal) lifetime of any possible
 370 $t\bar{t}$ bound state. As a result, the state would in the majority of cases not decay e.g.
 371 to photons, gluons or hadrons like the lighter quarkonia, but instead disassociate
 372 by one of the constituent top quarks decaying normally to Wb . This phenomenon,
 373 sometimes called a “quasi-bound state” or a “virtual bound state”, would lead to a
 374 possible peak in the $m_{WWb\bar{b}}$ spectrum slightly below the $t\bar{t}$ threshold.

375 Calculations of the $m_{WWb\bar{b}}$ spectrum at the $t\bar{t}$ threshold including the effects
 376 from a possible bound state have been performed independently in Refs. [31–35].
 377 All of these calculations work in the framework of non-relativistic QCD (NRQCD),
 378 which treats the slowly moving ($v \ll c$) top (anti)quarks as non-relativistic particles.
 379 This approach can be seen as a low-energy effective field theory (EFT) of the SM
 380 where high-energy modes have been integrated out, or alternatively, as an alternate
 381 perturbative expansion in the ratio α_S/β , where β is the top quark velocity. The
 382 result is a non-relativistic Schrödinger equation for the wavefunction of the $t\bar{t}$ system,
 383 with the interaction between the top quarks described by the low-energy limit of
 384 the QCD Coulomb potential, representing the exchange of soft gluons. At LO, it is
 385 given by [32]

$$V_{\text{QCD}}^{[1,8]}(q) = -\frac{4\pi\alpha_S C^{[1,8]}}{q^2}, \quad (2.13)$$

where the color factor is $C^{[1]} = 4/3$ for color-singlet and $C^{[8]} = -1/6$ for color-octet states. As a result, only $t\bar{t}$ systems in a color-singlet state feel an attractive force and can possibly form a bound state, while color-octet states are instead repulsed. At the LHC, $t\bar{t}$ bound states can thus at LO be produced only from gg initial states, since $q\bar{q}$ systems are always color-octets. From this, the spin state of the produced bound state can be inferred: Since both of the top quarks have low velocity, states with orbital angular momentum $L \neq 0$ will be strongly suppressed (beyond NLO in NRQCD [32]). Furthermore, the gg initial state in $t\bar{t}$ production close to the $t\bar{t}$ threshold always has spin $S = 0$ (and thus total angular momentum $J = 0$), with $S = 2$ contributions suppressed by powers of the top velocity [20], so that the resulting $t\bar{t}$ system must be in the ${}^1S_0^{[1]}$ state. At NLO in QCD, also ${}^3S_1^{[1]}$ states can be produced; however, the contribution is very small (less than 0.1% of the total cross section [32]).

Refs. [32–35] agree that the binding energy of the $t\bar{t}$ bound state, defined as the difference of the peak position in the $m_{WWb\bar{b}}$ spectrum to $2m_t$, is around -2 GeV, resulting in a “mass” of 343 GeV for the $t\bar{t}$ bound state for a top mass of 172.5 GeV. The exact lineshape of the peak is less well known. However, the experimental resolution of $m_{WWb\bar{b}}$ is expected to be much larger than the bound state width of order $\sim 2\Gamma_t$ (see Sec. 7.2.5), making the details of the spectrum irrelevant to an experimental search.

The existing NRQCD calculations predict only certain differential distributions and cannot be directly compared to experimental data on a per-event level. Because of this, a simplified model for the $t\bar{t}$ bound state is introduced following Refs. [19, 36–38]. Instead of a first-principles calculation, the bound state effects are modeled as an additional state spin-0 state η_t , which is added to the conventional perturbative QCD (pQCD) calculation of $t\bar{t}$. η_t is defined to couple directly to gluons and top quarks via the Lagrangian

$$\mathcal{L}_{\eta_t} = -\frac{1}{4}g_{gg\eta_t}\eta_t G_{\mu\nu}^a \tilde{G}^{a\mu\nu} - ig_{t\bar{t}\eta_t}\eta_t \bar{t}\gamma_5 t \quad (2.14)$$

where $G_{\mu\nu}^a$ is the gluon field strength tensor, $\tilde{G}_{\mu\nu}^a$ its dual, and $g_{gg\eta_t}$ as well as $g_{t\bar{t}\eta_t}$ are arbitrary coupling strengths. The resulting model has three free parameters: the binding energy $E_b = m(\eta_t) - 2m_t$, the total width $\Gamma(\eta_t)$ and the production cross section $\sigma(\eta_t)$ (the latter determining the couplings $g_{gg\eta_t}$ and $g_{t\bar{t}\eta_t}$). In Ref. [37], they are determined by fitting them to the NRQCD calculation from Ref. [33], yielding

$$E_b = -2 \text{ GeV} \implies m(\eta_t) = 343 \text{ GeV}, \quad \Gamma(\eta_t) = 7 \text{ GeV}, \quad \sigma(\eta_t) = 6.43 \text{ pb} \quad (2.15)$$

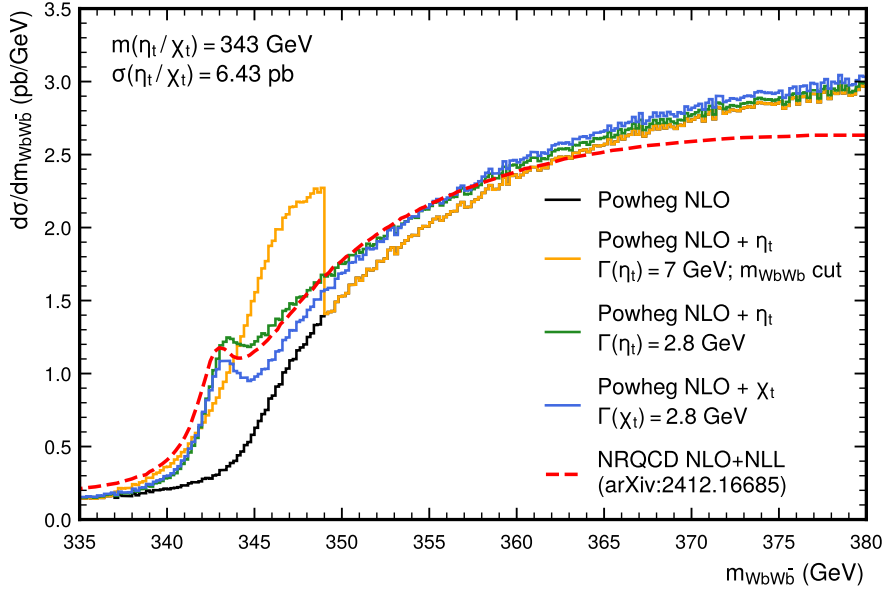


Figure 2.5: **Lineshape of η_t and χ_t .** The $m_{WWb\bar{b}}$ distribution close to the $t\bar{t}$ threshold, as predicted by the η_t and χ_t models stacked on top of a pQCD $t\bar{t}$ prediction from Powheg hvq (see Sec. 3.1). For the orange line, the η_t width is chosen to be 7 GeV, and a cut on $|m_{WWb\bar{b}} - m(\eta_t)|$ is applied (Eq. (2.15)), while for the green line, the η_t width is chosen as 2.8 GeV, and no further cuts are made (Eq. (2.16)). The blue line shows χ_t for a width of 2.8 GeV. All models are compared to an NRQCD prediction from Ref. [35].

418 In the generation of events, the top quarks are allowed to be fully off-shell by
 419 calculating the full amplitude $pp \rightarrow \eta_t \rightarrow W^+W^-b\bar{b}$, thus making sure that the
 420 phase-space region $m_{WWb\bar{b}} < 2m_t$ is populated. Furthermore, Ref. [37] recommends
 421 that the contribution of η_t should be restricted to the region $|m_{WWb\bar{b}} - m_{\eta_t}| \leq 6 \text{ GeV}$
 422 so that the bulk of the $t\bar{t}$ phase space, in which the pQCD calculation is expected
 423 to be accurate while the NRQCD calculation misses relativistic corrections, is not
 424 affected.

425 However, Refs. [36, 38] recommend instead

$$E_b = -2 \text{ GeV} \implies m(\eta_t) = 343 \text{ GeV}, \quad \Gamma(\eta_t) = 2\Gamma_t = 2.8 \text{ GeV}. \quad (2.16)$$

426 and no cut on $|m_{WWb\bar{b}} - m(\eta_t)|$.

427 The resulting $m_{WWb\bar{b}}$ distribution for the combination of pQCD $t\bar{t}$ and η_t is shown
 428 in Fig. 2.5 at the level of hard scattering for both parametrizations, and compared to
 429 an NRQCD prediction from Ref. [35]. At the level of hard scattering, the lower width

of $\Gamma(\eta_t) = 2\Gamma_t$ agrees much better with the predicted NRQCD spectrum and avoids an unphysical discontinuity due to the $m_{WWb\bar{b}}$ cutoff. Thus, this parametrization will be used in this work wherever possible, i.e. in Secs. 7.7 and 7.8, though the parametrization of Eq. (2.15) is retained for the sake of consistency with other results in Sec. 7.9. For more details, see these sections.

In the final stages of this work, a more involved model for $t\bar{t}$ bound states was published in Ref. [39]. There, instead of simulating an additional pseudoscalar state η_t , the bound state effects are included in leading-order color-singlet $t\bar{t}$ production by directly reweighting produced events with the ratio of Green's functions. This model is in principle fully predictive, i.e. it does not require fitting parameters to external calculations. However, it could not be validated in time for inclusion in the results of Chapter 7, it does not explicitly distinguish between $t\bar{t}$ spin states, and it is also unclear on how to match it to the $t\bar{t}$ continuum. Because of this, it is not further considered here and its investigation left for future work.

While NRQCD predicts any possible $t\bar{t}$ bound state contribution in pp collisions to be dominated by the $^1S_0^{[1]}$ state, with contributions from excited states strongly suppressed, experimentally it will still be useful to compare this spin state to other possibilities. To this end, a second toy model, denoted χ_t , is defined in analogy to η_t by the interaction Lagrangian

$$\mathcal{L}_{\chi_t} = -\frac{1}{4}g_{gg\chi_t}\chi_t G_{\mu\nu}^a \tilde{G}^{a\mu\nu} - g_{t\bar{t}\chi_t}\chi_t \bar{t}t \quad (2.17)$$

where $g_{gg\chi_t}$ and $g_{t\bar{t}\chi_t}$ are again arbitrary couplings. This Lagrangian contains a \mathcal{CP} -even coupling to the top quark, compared to the \mathcal{CP} -odd coupling in Eq. (2.14). It thus produces $t\bar{t}$ systems in the $^3P_0^{[1]}$ state, which is the only other possible state with $J=0$ (cf. Tab. 2.1). The free parameters of this model are again cross section, mass, and width; they are set here to the same values as for η_t in all cases³. The resulting $m_{WWb\bar{b}}$ lineshape is also seen in Fig. 2.5; it looks qualitatively similar to η_t , showing a similar small peak at ~ 343 GeV. In Sec. 7.7.2, it will be used in conjunction with η_t to probe the spin state of the observed excess. Other possible states, such as the vector state $^3S_1^{[1]}$, are not considered here and instead left for future work.

2.3 Beyond the Standard Model

The Standard Model, greatly successful as it is at describing the results of collider experiments so far, is nonetheless known to be incomplete. In fact, there exist

³Based on analogies to $c\bar{c}$ and $b\bar{b}$ quarkonia [40], it is likely that a true 3P_0 bound state would have a slightly higher mass, though it is unknown whether this would be noticeable even in the hard-scattering level spectrum due to the large smearing from the top width. It is anyway expected to be irrelevant within the experimental resolution.

462 several experimental results which can not be explained by SM predictions, such
 463 as the observation of dark matter in many astrophysical contexts or the observed
 464 masses of the neutrinos.

465 In addition, the SM is plagued by several theoretical challenges that will likely not
 466 be overcome without major modifications to the theory. Chief among these is the
 467 unification of the forces of the SM - the electroweak and strong interactions - with
 468 gravity as described by General Relativity, which is not included in the SM at all.
 469 Doing so has proven extremely challenging, and no fully consistent unified theory
 470 of all forces is known yet. Further open questions are, for example, the hierarchy
 471 problem or the strong \mathcal{CP} problem.

472 In order to solve these problems in a satisfactory manner, a more general theory
 473 will have to be found, which should include the SM as its low-energy limit. In
 474 many cases, this will result in additional as of yet undiscovered particles. There is
 475 a multitude of such Beyond the Standard Model (BSM) extensions, each attacking
 476 different parts of the problems, and one of the major tasks of particle physics is to
 477 explore which parts of the parameter space of these models can be probed with the
 478 current experiments.

479 This work, in particular, aims to probe models predicting new, heavy spin-0 states
 480 coupling strongly to the top quark. Such states can be searched for in the $pp \rightarrow t\bar{t}$
 481 process, as outlined in a generic fashion in Sec. 2.3.1. Following that, two explicit
 482 realizations of such models are discussed, namely the Two-Higgs Doublet Model
 483 (2HDM) (Sec. 2.3.2) and Axion-Like Particle (ALP) models (Sec. 2.3.3).

484 2.3.1 Heavy scalars in $t\bar{t}$ production

485 Consider an unspecified BSM extension predicting (possibly among others) a massive
 486 spin-0 state Φ coupling to top quarks via a Yukawa interaction. In the absence of
 487 couplings to other particles, the Lagrangian of such a state can be written as [19]

$$\mathcal{L}_\Phi = \frac{1}{2}(\partial_\mu \Phi)(\partial^\mu \Phi) + \frac{m_\Phi^2}{2}\Phi^2 + g_{\Phi\bar{t}t} \frac{m_t}{v} \bar{t}\Phi (\cos \alpha + i\gamma_5 \sin \alpha) t. \quad (2.18)$$

488 where m_Φ is the mass of the new state and $g_{\Phi\bar{t}t}$ is a coupling modifier, scaled to
 489 the SM Higgs-top Yukawa coupling with the SM Higgs vacuum expectation value v .
 490 The phase α is a free parameter determining the \mathcal{CP} structure of the $\Phi\bar{t}t$ coupling:
 491 For $\alpha = 0$, the coupling is purely \mathcal{CP} -even or scalar, while for $\alpha = \pi/2$, the coupling
 492 is purely \mathcal{CP} -odd or pseudoscalar. Intermediate values for α will cause \mathcal{CP} -mixed
 493 couplings, which in general will result in \mathcal{CP} violation in processes involving top
 494 quarks. Possible experimental indicators of such \mathcal{CP} violation in $pp \rightarrow t\bar{t}$ are e.g.
 495 discussed in Ref. [29].

496 In the scope of this work, only the limiting \mathcal{CP} -conserving cases of Φ are consid-
 497 ered. For convenience, the pure pseudoscalar case will in the following be called A,
 498 while the pure scalar case will be called H.

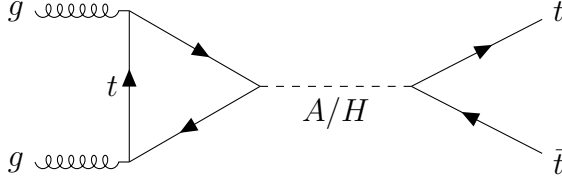


Figure 2.6: **Feynman diagram for $gg \rightarrow A/H \rightarrow t\bar{t}$.** Only the leading-order gluon fusion diagram is shown, with a top quark running in the loop.

Similar to the SM Higgs boson, the most important production channel of either state at the LHC will be through loop-induced gluon fusion, followed by associated production with either $t\bar{t}$ or a single top quark. Only the former is considered here; experimental searches for the latter case can be found e.g. in Ref. [41]. Furthermore, the decay of the new state will depend on its mass: For low masses, the particle will decay either through loop-induced couplings to e.g. gg or $\gamma\gamma$ or, if present, through couplings to other SM or BSM particles than the top quark. For masses of $m_{A/H} > 2m_t$, however, the decay to $t\bar{t}$ is kinematically allowed and will in many cases be dominant due to the large Yukawa coupling. In this case, the process $gg \rightarrow A/H \rightarrow t\bar{t}$ will lead to the same final state as SM $t\bar{t}$ production, as illustrated in Fig. 2.6. This process will be considered in more detail in the rest of this chapter, and one of the main results of this thesis is an experimental search for such a signature (Chapter 7).

Fig. 2.7 shows the predicted differential cross sections of this model, in form of the difference to the SM, for different masses in terms of $m_{t\bar{t}}$, the invariant mass of the $t\bar{t}$ pair, at the level of the hard scattering and at LO in QCD. It can be seen that the total effect of A and H is a very distinct peak-dip structure around the A/H mass. This is because the $gg \rightarrow A/H \rightarrow t\bar{t}$ production channel interferes with SM $gg \rightarrow t\bar{t}$ production, which leads to deficits in certain regions of phase space due to destructive interference. For high A/H masses, there is an additional broad peak at low masses of $m_{t\bar{t}}$. This originates in the gluon PDF, which is steeply falling for rising partonic center-of-mass energy and thus compensates the suppression by the off-shell A/H at low $m_{t\bar{t}}$ for the A/H-SM interference.

A further consequence of the interference is that the differential cross section scales non-linearly with the coupling modifiers $g_{At\bar{t}}$ and $g_{Ht\bar{t}}$. The dependence (for arbitrary observables) can be parameterized as

$$d\sigma = d\sigma^{\text{SM}} + g_{A/Ht\bar{t}}^2 d\sigma^{\text{int}} + g_{A/Ht\bar{t}}^4 d\sigma^{\text{res}} \quad (2.19)$$

where the superscripts “SM”, “int” and “res” refer to the SM, SM-A/H interference, and resonant A/H contributions, respectively.

In addition to the $m_{t\bar{t}}$ spectrum, an A/H contribution is also expected to modify the spin state of the $t\bar{t}$ system. As a single particle, an intermediate A/H resonance

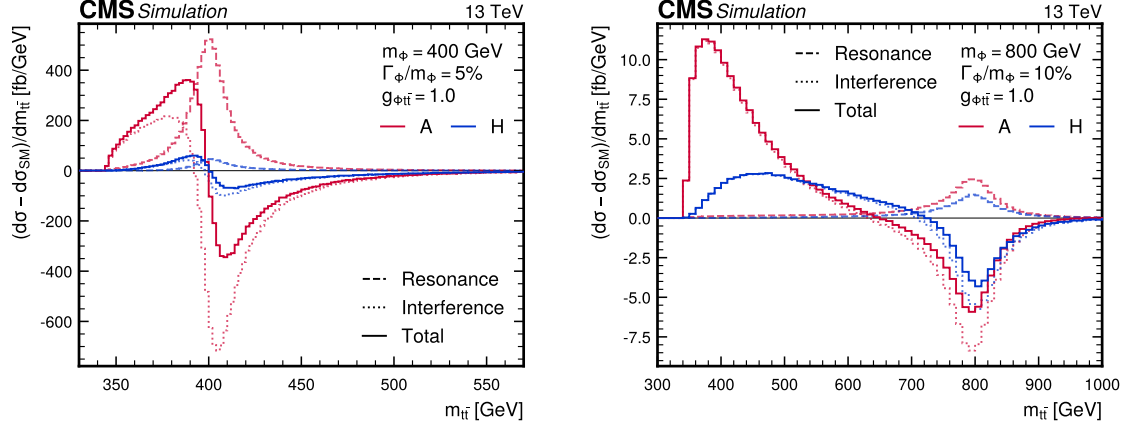


Figure 2.7: **Differential cross sections for $A/H \rightarrow t\bar{t}$.** The hadronic differential cross section as a function of the invariant $t\bar{t}$ mass, with the SM prediction subtracted, for $m_{A/H} = 400 \text{ GeV}$ (left) and $m_{A/H} = 800 \text{ GeV}$ (right) as well as for A (red) and H (blue), at a coupling modifier of $g_{A/Ht\bar{t}} = 1$. The resonance and interference components as well as their sum are shown as dashed, dotted and solid lines, respectively. They are calculated from same the Monte Carlo simulation samples described in Sec. 7.2.1.

529 has neither spin nor orbital angular momentum. Due to conservation of angular
 530 momentum, this implies that the $t\bar{t}$ system will be produced in a state with $J = 0$,
 531 which leaves only the 1S_0 and 3P_0 states (compare Tab. 2.1).

532 Furthermore, the spin-0 intermediate state has positive intrinsic parity and is
 533 charge-neutral. This implies that for H , whose interaction with the top quark is
 534 separately \mathcal{C} - and \mathcal{P} -conserving, the $t\bar{t}$ system will have quantum numbers of $\mathcal{C} = +1$
 535 and $\mathcal{P} = +1$, which is true for the 3P_0 state. For A , on the other hand, the
 536 interaction is maximally \mathcal{P} -violating, leading to quantum numbers of $\mathcal{C} = +1$ and
 537 $\mathcal{P} = -1$, which matches the 1S_0 state. As a result, the process $gg \rightarrow A \rightarrow t\bar{t}$ will
 538 always produce the 1S_0 spin singlet state, while $gg \rightarrow H \rightarrow t\bar{t}$ will produce the 3P_0
 539 spin triplet state.

540 As explained in Secs. 2.2.1 and 2.2.2, the observable c_{hel} has maximal slope D for
 541 spin-singlet states, making it a good discriminator between A and the SM. For H ,
 542 it can be shown that the produced triplet state instead maximizes the slope $D^{(k)}$ of
 543 the observable c_{han} , as defined in Eq. (2.10) [19]. Consequently, both c_{hel} and c_{han}
 544 will be used in the experimental search for such states presented in Chapter 7.

545 2.3.2 Two-Higgs Doublet Model

546 A common class of models predicting additional scalars as discussed in Sec. 2.3.1
 547 are Two-Higgs-Doublet Models (2HDMs) [42, 43]. In these models, there are two
 548 complex Higgs doublets with eight degrees of freedom in total (as opposed to a
 549 single doublet in the SM), which after electroweak symmetry breaking results in five
 550 physical states (compare Sec. 2.1.2). Such a structure for the Higgs sector arises,
 551 for example, in many supersymmetric models [44] or axion models [45].

552 In general, 2HDMs can include \mathcal{CP} -violating interactions (similar to Sec. 2.3.1)
 553 as well as flavor-changing neutral currents (FCNCs). Both of these phenomena are
 554 experimentally well constrained, and so it makes sense to restrict oneself to \mathcal{CP} -
 555 and flavor-conserving limits. Doing so leads to definite quantum numbers of the
 556 five physical scalar states of the 2HDM: two neutral scalar (\mathcal{CP} -even) states h and
 557 H , a neutral pseudoscalar (\mathcal{CP} -odd) state A , and two charged states H^+ and H^- .
 558 Usually, the state h is identified with the SM Higgs boson at a mass of 125 GeV.
 559 Then, the two other neutral states H and A - if massive enough - could play the role
 560 of additional Higgs bosons decaying to $t\bar{t}$ as discussed in Sec. 2.3.1.

561 Depending on the nature of the discrete symmetry that is used to impose flavor
 562 conservation, there can be different types of 2HDMs, which differ in the structure of
 563 the couplings to the SM. No particular 2HDM type is assumed in this work, and the
 564 results of Chapter 7 are instead presented in terms of the generic model of Sec. 2.3.1.

565 2.3.3 Axion-Like Particles

566 Another very generic class of BSM scalars relevant to the $pp \rightarrow t\bar{t}$ process are
 567 axions and Axion-Like Particles (ALPs), denoted here as a . Axions were originally
 568 conceived as solutions to the strong \mathcal{CP} problem [46–49], which is a result of the
 569 non-trivial vacuum structure of QCD: when deriving the effective QCD Lagrangian,
 570 the presence of certain classes of topological solutions to the classical Yang-Mills
 571 equations leads to an additional \mathcal{CP} -violating term [50]

$$\mathcal{L}^{QCD} \supset \theta \frac{\alpha_S}{8\pi} G_{\mu\nu} \tilde{G}^{\mu\nu}, \quad (2.20)$$

572 where $G_{\mu\nu}$ is the gluon field strength and $\tilde{G}_{\mu\nu}$ its dual. The coefficient θ of this
 573 term is a free parameter in the range $[0, 2\pi)$, with no particular value preferred from
 574 first principles. However, experimentally, no \mathcal{CP} violation in pure QCD has been
 575 observed, and θ is strongly bounded at $|\theta| \leq 10^{-10}$ (the strongest bounds coming
 576 from measurements of the electromagnetic dipole moment of the neutron [50–52]).
 577 The strong \mathcal{CP} problem thus consists of explaining why the \mathcal{CP} -violating $G_{\mu\nu} \tilde{G}^{\mu\nu}$
 578 term vanishes.

579 The most prominent way to solve the strong \mathcal{CP} problem is by introducing a new
 580 real scalar field a , the axion field, with a Lagrangian [50]

$$\mathcal{L}^{\text{ax}} = \frac{1}{2}\partial_\mu a\partial^\mu a + \frac{\alpha_S}{8\pi} \frac{a}{f_a} G_{\mu\nu} \tilde{G}^{\mu\nu} + \text{interaction terms} \quad (2.21)$$

where f_a is called the axion scale, and all other interaction terms with SM fields are required to be invariant under a shift $a \rightarrow a + \kappa f_a$ with arbitrary κ . It can be shown that this Lagrangian, when added to the SM QCD Lagrangian including the term in Eq. (2.20), leads to a global minimum at $a/f_a + \theta = 0$, so that after a field shift the \mathcal{CP} -violating term is absorbed in the axion-gluon coupling and no \mathcal{CP} violation is expected in QCD alone. This is known as the Peccei-Quinn mechanism.

In Eq. (2.21), the axion-gluon interaction term has dimension 5 and is thus non-renormalizable, with the cutoff scale given by f_a . The axion must thus be necessarily be seen as an low-energy EFT description of different physics at the higher scale f_a . Many different UV-complete models including axions exist [50, 53–56], which lead to different interaction terms with other SM particles such as photons, electroweak bosons or massive fermions.

In this work, a focus is placed upon models which predict couplings to SM fermions, particularly the top quark, and the EFT Lagrangian is parametrized in a model-independent approach as [57]

$$\begin{aligned} \mathcal{L}^{\text{ALP}} = & \frac{1}{2}\partial_\mu a\partial^\mu a + \frac{m_a}{2}a^2 - \frac{a}{f_a}c_G \frac{a}{f_a} G_{\mu\nu} \tilde{G}^{\mu\nu} - \frac{a}{f_a}c_B \frac{a}{f_a} B_{\mu\nu} \tilde{B}^{\mu\nu} \\ & - \frac{a}{f_a}c_W \frac{a}{f_a} W_{\mu\nu} \tilde{W}^{\mu\nu} - \frac{\partial^\mu a}{f_a} \sum_f c_f \bar{\Psi}_f \gamma_\mu \Psi_f, \end{aligned} \quad (2.22)$$

where the index f runs over the SM fermions, Ψ_f are the fermion fields, $B_{\mu\nu}$ and $W_{\mu\nu}$ are the EW boson fields before symmetry breaking, and the free parameters are the scale f_a , the mass m_a , and the couplings to gluons c_G , to EW bosons c_B and c_W and to fermions c_f (where no flavor mixing was assumed). This Lagrangian, depending on the choice of the free parameters, might or might not correspond to a UV-complete model and solve the strong \mathcal{CP} problem. Because of this, the field a is here called an Axion-Like Particle. Even when it does not correspond to a true axion, it might be a physically well-motivated extension of the SM, e.g. as a dark matter candidate or mediator.

In the ALP-fermion interaction term in Eq. (2.22), the shift symmetry of a is directly manifest since it only depends on the derivative of a . However, by employing the equations of motion for a as well as the Higgs mechanism, one can rewrite Eq. (2.22) with a Yukawa-like interaction instead. Dropping the EW bosons and fermions other than the top quark leads to

$$\mathcal{L}^{\text{ALP}} = \frac{1}{2}\partial_\mu a\partial^\mu a + \frac{m_a}{2}a^2 - \frac{a}{f_a}c_{\tilde{G}} \frac{a}{f_a} G_{\mu\nu} \tilde{G}^{\mu\nu} + i c_t m_t \frac{a}{f_a} \bar{t} \gamma^5 t. \quad (2.23)$$

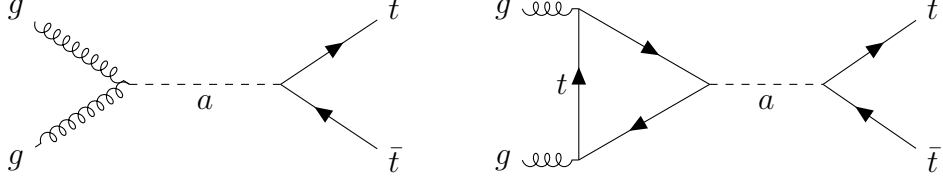


Figure 2.8: **Feynman diagrams for $gg \rightarrow a \rightarrow t\bar{t}$.** The left diagram corresponds to the gluon-ALP contact interaction and scales with $c_{\tilde{G}}c_t$, while the right diagram shows the top quark loop and scales with c_t^2 .

610 Performing this basis change includes an additional ALP-gluon coupling term (in
 611 general dependent on the other SM couplings), which was absorbed by redefining
 612 the Wilson coefficient from c_G to $c_{\tilde{G}}$. This basis will be used in the remainder of
 613 this work.

614 It can be seen by comparing Eq. (2.23) to Eq. (2.18) that the ALP-top coupling
 615 has the exact same structure as the generic \mathcal{CP} -odd boson introduced in Sec. 2.3.1.
 616 Thus, if the ALP is heavy enough to be produced at the LHC and decay to $t\bar{t}$, it
 617 can be searched for in $t\bar{t}$ final states similarly to the generic pseudoscalar A . Such
 618 heavy ALP masses can be reached naturally and serve as solutions to the strong \mathcal{CP}
 619 problem e.g. in UV models containing extra non-abelian gauge groups, resulting in
 620 containing forces with large containment scales [58–61].

621 If, in addition, the ALP couplings also satisfy $c_{\tilde{G}} = 0$, the two Lagrangians in
 622 Eqs. (2.18) and (2.23) are identical, and all conclusions drawn on A can be directly
 623 transferred to the ALP. On the other hand, if $c_{\tilde{G}} \neq 0$, an additional production
 624 diagram involving a gluon contact interaction becomes available, as depicted in
 625 Fig. 2.8. A phenomenological study characterizing both cases in detail forms the
 626 core of Chapter 8 of this work.

627 3 Monte Carlo event generation

628 In order to test the Standard Model or extract any of its parameters at the LHC, one
629 requires a prediction which can be compared to the experimental data recorded by
630 the detectors in the form of collision events. This is, in general, a very complex task
631 consisting of many different subprocesses and physical scales. The generation starts
632 with the hard parton scattering, then continues with the emission of additional
633 radiation, underlying event effects, hadronization, and pileup, and ends with the
634 simulation of the different subdetectors and triggers. Many of these processes are not
635 only probabilistic, but intractable through direct analytical or numeric integration
636 due to the large phase space and the complexity of the problems involved.

637 Instead, the Monte Carlo (MC) method is used for this purpose. Here, it amounts
638 to randomly sampling an event from the phase space of the starting distribution - in
639 this case, the hard scattering - and then passing it through a chain of simulation tools
640 for the remaining steps until one arrives at an event that is directly comparable to
641 events recorded experimentally. This method is advantageous in that the numerical
642 error in an arbitrary region of phase space always scales with $1/\sqrt{N}$, where N is
643 the total number of events produced, independently of the dimensionality of the
644 problem. Thus, getting a numerically accurate prediction is mostly a matter of
645 producing a sufficient number of MC events.

646 In this chapter, the different tools used in the CMS simulation chain are discussed.
647 A focus is laid on the hard scattering or matrix element generators (Sec. 3.1) as well
648 as the parton showering (Sec. 3.2) since these are the focus of the studies presented
649 in Chapter 6, while underlying event effects (Sec. 3.3), hadronization (Sec. 3.4),
650 pileup (Sec. 3.5), as well as the detector and trigger simulation (Sec. 3.6) are only
651 briefly touched upon.

652 3.1 Matrix Element generators

653 At the LHC, protons are collided with large center-of-mass energies of multiple
654 TeV. Because protons are not fundamental particles, but bound states of QCD
655 which cannot be perturbatively described from first principles, providing accurate
656 predictions for proton-proton collisions is generally a very challenging task. For the
657 specific case of hard scattering processes, i.e. processes in which the particles in
658 the final state X have large transverse momenta, one can employ the factorization
659 theorem of QCD [62]:

$$\sigma(pp \rightarrow X) = \int_0^1 dx_1 \int_0^1 dx_2 \sum_{a,b} f_a(x_1, \mu_F) f_b(x_2, \mu_F) \hat{\sigma}(a(x_1 P) + b(x_2 P) \rightarrow X) \quad (3.1)$$

where P is the incoming momentum of the protons, assumed to be purely longitudinal and thus $P = \sqrt{s}/2$, and the sum runs over all possible combinations a, b of initial state partons (quarks and gluons). This formula factorizes the total hadronic cross section into two parts: The partonic cross section $\hat{\sigma}(a + b \rightarrow X)$ describes the scattering of two partons at high energies, and can be computed perturbatively in α_S due to asymptotic freedom of QCD. The functions $f_a(x, \mu_F)$ on the other hand are the parton distribution functions (PDFs) and describe the probability of finding a parton of type a with momentum fraction $p_a/P = x$ in the proton structure. Since they probe low momentum scales where α_S is large, they cannot be computed perturbatively and instead need to be measured experimentally. In addition to x , they also depend on the factorization scale μ_F , which is the energy scale defining the separation between hard (perturbative) and soft (non-perturbative) QCD. It is typically set to be equal to the characteristic energy of the incoming partons, e.g. half the partonic invariant mass. In contrast to the dependence on x , the dependence on μ_F is a prediction of QCD and follows from the DGLAP equations [63, 64].

The partonic cross section can further be written differentially as [62]

$$d\hat{\sigma}(ab \rightarrow X) = \frac{1}{2\hat{s}} \left(\prod_f \frac{d^3 p_f}{(2\pi)^3} \frac{1}{2E_f} \right) |\mathcal{M}(ab \rightarrow X)|^2 (2\pi)^4 \delta^{(4)} \left(\sum_f p_f \right) \quad (3.2)$$

where $\hat{s} = x_1 x_2 s$ is the partonic center-of-mass energy squared, the term in the brackets refers to the integral over the final state phase space and depends only on the number and masses of the final state particles f , the δ function encodes momentum conservation, and only the scattering matrix element \mathcal{M} depends on the details of the process considered.

Events are now generated by drawing randomly from the full kinematically allowed final state phase space, as well as from the PDFs characterizing the initial state, and keeping them with a probability proportional to the corresponding hadronic cross section according to Eq. (3.1). The partonic cross section here might be known analytically for simple processes, or might need to be integrated numerically for complex processes (especially at NLO or higher). The PDFs, based on fits to experimental data, are usually tabulated and interpolated; in this work, the NNPDF 3.1 PDF set is most commonly used for this purpose [65]. In practice, codes usually employ an adaptive sampling algorithm to enhance the fraction of events that pass and thus

691 speed up the calculation, see e.g. Ref. [66].

692 ME generators exist at LO, NLO, and (approximate) NNLO in QCD, all of which
 693 are used at different points in this work. For NLO and NNLO processes, care must
 694 be taken to cancel ultraviolet (UV) as well as infrared (IR) divergences that often
 695 appear in the integration of the matrix element. The former is done in the framework
 696 of renormalization, which usually introduces a dependence on an additional scale,
 697 the renormalization scale μ_R . Similar to μ_F , it is typically set to the energy scale
 698 of the process, and, since the dependence is expected to vanish at infinite order in
 699 QCD, variations of μ_R and μ_F are often used to assess the size of uncertainties due
 700 to missing higher orders [67]¹.

701 IR divergences, on the other hand, arise when the momenta of massless particles
 702 in loop diagrams, such as gluons or light quarks, approach zero. They need to
 703 be canceled with corresponding divergent diagrams containing the emission of a
 704 real particle, which occur when the emission is soft or collinear with respect to the
 705 emitter. As a result, NLO calculations for the final state X will always need to also
 706 take into account the final state $X + j$, where j can be a gluon or light quark [69].

707 In this work, two different ME generators are used. The first is MG5_AMC@NLO,
 708 a general-purpose ME generator that can work both at LO and NLO [70]. It features
 709 fully automated computation of arbitrary processes in the SM or BSM, where new
 710 BSM models can be specified in the Universal FeynRules Output (UFO) format [71].
 711 It is used in this work for both SM and BSM processes.

712 The second ME generator used is POWHEG (short for Positive Weighted Hardest
 713 Emission Generator), which is a generic framework for NLO and approximate NNLO
 714 generators [72–74]. In contrast to MG5_AMC@NLO, it is not automated, and re-
 715 quires the manual implementation of each process. Many processes are publicly
 716 available as part of the POWHEG Box collection, and several are used in this work.
 717 Importantly, $pp \rightarrow t\bar{t}$ is generated at NLO with the POWHEG Box process `hvq` [75]
 718 in Chapters 5, 7 and 8. POWHEG has the advantage that it generates (almost) only
 719 events with positive weights, while the subtraction procedure in MG5_AMC@NLO
 720 leads to a significant fraction of negative weights at NLO, possibly leading to nu-
 721 matical instability in certain regions of phase space.

¹Using μ_R and μ_F variations as estimates of missing higher order uncertainties, while common, can only give a rough estimate of the magnitude of missing higher order contributions and does not truly give information about shape deficiencies in differential distributions. A recent, more thorough approach are *theory nuisance parameters* quantifying the uncertainty in specific parts of the theory calculation [68]. This method has however not yet been extended to $t\bar{t}$ production and is thus not considered here.

3.2 Parton showers and matching

The output of ME generators are events whose final states typically involve quarks and gluons with high momenta. Formally, such computations are accurate to some fixed order in α_S at which the calculation was performed, and all further emissions of gluons, as well as splittings of gluons into quark-antiquark-pairs, is suppressed by additional powers of α_S . However, one finds that, again due to IR singularities, such emissions and splittings are in fact proportional to $\alpha_S \log(\hat{s}/\Lambda_{\text{QCD}}^2)$, where $\Lambda_{\text{QCD}} \approx 250 \text{ MeV}$ is the scale at which QCD becomes nonperturbative. This term is of order 1 and thus leads to large corrections [62, 64].

A way to incorporate these corrections is by using parton showers. The idea of a parton shower is to successively generate all real emissions and splittings down to the scale of Λ_{QCD} , where every splitting happens with a probability proportional to α_S and the corresponding logarithm. To do this, one needs to define an ordering variable which determines in which order the splittings are performed. Two common choices are the transverse momentum of the emission (p_T -ordered shower) or the emission angle respective to the emitting particle (angular-ordered shower). The result of either choice is an effective resummation of the logarithms associated to each emission, which is why parton showers are said to be leading-log (LL) accurate for certain observables.

The main parton shower used in this work is a p_T -ordered dipole shower, included as part of the PYTHIA multi-purpose event generator [76, 77]. It works by collecting quark-antiquark pairs into color dipoles, which radiate gluons together so that the recoil is distributed between the quarks. Here, it is mostly used by matching it to the ME generators described in Sec. 3.1. This is usually trivial at LO: the parton shower simply starts from the final state as given by the ME generator. At NLO or higher, however, the additional emissions in the final state of the ME generator that need to be inherently included to regularize IR singularities would lead to double-counting if the parton shower is run in a naive way. To prevent this, the most common strategy in PYTHIA is to start both initial state and final state parton showers at the scale of the ME-level emission (sometimes called “wimpy shower”).

This approach assumes that the scale definitions in the ME generator and the parton shower are identical, which in general will not always be the case. In particular, for the important case of POWHEG matched to PYTHIA, used in this work for the simulation of $\text{pp} \rightarrow t\bar{t}$, there is a mismatch in the scales which might lead to double-counting. A more refined approach here is to use a vetoed shower: the shower is started at the kinematically allowed limits and evolved downwards as usual, ordered by the scale as defined by PYTHIA. For the first emission the scale is then recomputed according to the POWHEG definition, and it is vetoed and reshowered if this scale is higher than the one in the ME.

More complicated procedures have to be invoked in the case that the ME contains more than one real emission. This case is studied in detail for the ME generator **bb41**

763 in Chapter 6. Furthermore, besides PYTHIA, multi-purpose generator HERWIG [78,
764 79] is considered in parts of Chapter 7, and briefly described there.

765 3.3 Multi-parton interactions

766 In addition to the hard scattering, additional soft QCD interactions might occur
767 in a scattering event between the other partons in the two colliding protons. This
768 is referred to as multi-parton interactions (MPI) or underlying event (UE). It is
769 handled by PYTHIA based on heuristic models, interleaved with the parton shower.
770 In general, MPI parameters need to be tuned to experimental data. This was done
771 by the PYTHIA authors, such as the different versions of the Monash tune [80], and
772 building on top of this by the CMS collaboration in the form of the CP tune family,
773 most recently the CP5 tune [81]. Both tunes are based on a large dataset of e^+e^- ,
774 ep , $p\bar{p}$, and pp collision data from many different experiments. The CP5 tune will
775 be used in all parts of this work.

776 3.4 Hadronization

777 The result of the MPI-interleaved parton shower consists of a collection of bare
778 quarks and gluons at energies of $\mathcal{O}(\Lambda_{\text{QCD}})$, at which QCD becomes non-perturbative.
779 The hadronization of these quarks and gluons into hadrons as well as their subse-
780 quent decays thus need to be described heuristically.

781 For most of this work, this is done using the Lund string fragmentation model [82,
782 83], again implemented in PYTHIA. In this model, the strong force between a quark
783 and an antiquark of opposite color is modeled as a string in space-time, standing in
784 for e.g. a three-dimensional flux tube. The energy stored in the string is proportional
785 to its length, consistent with the long-distance behavior of QCD observed e.g. in
786 lattice QCD. Hard gluons can be accommodated in this model as kinks in the string,
787 i.e. for a $q\bar{q}g$ state, the q and \bar{q} are connected through the gluon instead of directly.

788 As the quarks move apart, the energy stored in the string increases, until it is large
789 enough that the string fragments by creating an additional $q\bar{q}$ pair from the vacuum.
790 If the energy in the resulting strings is still large enough, the procedure repeats.
791 Otherwise, the low-mass $q\bar{q}$ pair is considered a meson, based on the flavors of its
792 constituents. In its purest form, this model has only two free parameters (usually
793 denoted a and b) which parametrize the distribution of the momentum fraction
794 of the $q\bar{q}$ pair in each fragmentation. However, in order to correctly describe e.g.
795 flavor composition and p_T spectra of jets, many more parameters usually have to be
796 introduced. For more detail on string fragmentation in PYTHIA, see e.g. Ref. [77].
797 Similar to MPI, hadronization parameters need to be tuned to data, and are also
798 included in the Monash and CP5 tunes.

799 One shortcoming of the default MPI and hadronization models are that both
800 work in the leading color (LC) approximation, i.e. in the limit of a large number
801 of QCD colors ($N_c \rightarrow \infty$). This simplifies the models greatly because the chance
802 of two unrelated color lines sharing the same color becomes infinitesimally small.
803 Corrections to this approximation are typically of order $1/N_c^2 = 1/9$, and can be done
804 via color reconnection (CR), for which different models exist, see e.g. Refs. [84, 85].
805 The difference between different models is often considered a source of uncertainty
806 in measurements, such as in Secs. 5.5 and 7.5.

807 Finally, decays of produced unstable hadrons, including possible decay chains,
808 are also handled by PYTHIA. Branching ratios are taken from experimental mea-
809 surements where available, and predicted from heuristic models where not, see e.g.
810 Ref. [77].

811 3.5 Pileup

812 At the currently achieved instantaneous luminosities, the proton bunches colliding at
813 the LHC contain more than 10^{11} protons on average. Because of this large number, it
814 is expected that a single collision event contains interactions between more than one
815 pair of protons from the two colliding bunches. This is known as pileup. It differs
816 from MPI, in which the different interactions are between multiple partons in the
817 same proton and are thus correlated from a QFT perspective, while different pileup
818 interactions are in principle independent from each other. In Run 2, the average
819 number of pileup interactions per bunch crossing ranged from 23-32 depending on
820 the era of datataking [86], while it is 40 or higher in Run 3.

821 In simulation, pileup interactions are considered by mixing the generated hard
822 interaction process with a dedicated sample of purely soft-QCD interactions, also
823 generated in PYTHIA. The probability distribution of the number of pileup interac-
824 tions is an input to this procedure, and is typically corrected after the generation
825 is finished by reweighting in a suitable variable. In Sec. 5.3.1, an experimental ap-
826 proach to this problem is taken by correcting experimentally accessible pileup-related
827 parameters directly to data. In Sec. 7.2.4, on the other hand, the distribution of
828 the true number of interactions is instead reweighted based on a theory prediction
829 given the total inelastic cross section [87].

830 3.6 Detector and trigger simulation

831 After the simulation of the interaction processes, the resulting collection of particles
832 produced in an event is propagated to a full physics-based detector simulation using
833 the program GEANT4 [88]. Based on the output of this simulation, the two tiers of
834 trigger systems are similarly simulated using in-house tools. The result is a set of

835 detector information from all subdetectors as well as the outputs of different triggers,
836 similar to true experimental data, and so it can be passed to the different object
837 reconstruction algorithms (cf. Sec. 4.3) in the same way as the data. Events are then
838 analyzed by comparing the reconstructed objects and quantities between data and
839 simulation, ensuring a one-to-one comparison. Possible residual differences between
840 data and simulation are often corrected for by applying calibration factors measured
841 using well-known processes. The details of such calibrations will be explained in
842 Chapters 5 and 7 where relevant.

843 **4 Experimental methods**

844 **4.1 The Large Hadron Collider**

845 At the time of writing, the Large Hadron Collider [89] is the largest and most
846 powerful particle accelerator in the world. Located underground at the border of
847 France and Switzerland close to Geneva, it consists of two circular beamlines of
848 roughly 27 km circumference, in which proton bunches are accelerated and collided.
849 Superconducting magnets, cooled with liquid helium at around 4 K temperatures,
850 generate magnetic fields of over 8 T to keep the protons on their circular orbit,
851 and similarly superconducting electromagnetic radio-frequency cavities accelerate
852 the protons to beam energies up to 7 TeV. When operating as designed, around
853 2800 proton bunches per beam containing 3×10^{14} protons total are present in the
854 beamline simultaneously, revolving with a frequency of about 11.245 kHz. From
855 this, peak instantaneous luminosities of about $20 \text{ kHz} \mu\text{b}^{-1}$ can be reliably reached.
856 Alternatively, the LHC can also collide heavy ions, such as lead or oxygen, instead
857 of protons.

858 There are four large experiments making use of the colliding beams at the LHC,
859 located at the four interaction points. The two larger of these are ATLAS [90]
860 and CMS [4], both of which are general-purpose experiments intended to study
861 all aspects of the Standard Model in proton-proton collisions. The work of thesis
862 was performed as part of the CMS collaboration, and so the CMS experiment is
863 described in Sec. 4.2 in more detail. The two smaller experiments, on the other
864 hand, are specialized for certain tasks, namely the study of B physics and exotic
865 hadrons for LHCb [91] and the study of heavy-ion collisions for ALICE [92].

866 The data taken at the LHC so far can be divided into three Runs. Run 1 lasted
867 from 2010–2012, during which the LHC operated at center-of-mass energies of 7 and
868 8 TeV, significantly below the original target values, and yielded a total integrated
869 luminosity of about 29 fb^{-1} . It is this data that led to the original discovery of the
870 Higgs boson. Following this, after two years of pause, Run 2 resumed in 2015 with
871 a center-of-mass energy of 13 TeV and lasting to 2018. Around 140 fb^{-1} of data was
872 collected during this time. This complete dataset, save for the small contribution
873 from 2015, is analyzed in Chapter 7 of this thesis.

874 Finally, Run 3 of the LHC started in 2022 after another three years of pause, and
875 is planned to last until 2026 at the time of writing. The center-of-mass energy was
876 again increased slightly to 13.6 TeV, and in the years 2022–2024 around 196 fb^{-1}
877 have been recorded, already surpassing Run 2. In Chapter 5 of this thesis, the very

878 first data of Run 3, corresponding to 1.21 fb^{-1} taken in July and August 2022 at
879 CMS, are analyzed in the context of a $t\bar{t}$ cross section measurement.

880 In the future, it is planned to upgrade the LHC to be able to run at higher
881 instantaneous luminosities as well as a further increased energy of 14 TeV [93]. The
882 CMS detector will similarly be upgraded to replace aging components and deal
883 with the increased pileup conditions [94, 95], and a total integrated luminosity of
884 around 3 ab^{-1} is expected to be collected. In Chapter 8, among others, sensitivity
885 projections for this luminosity are made for Axion-Like Particles decaying to $t\bar{t}$.

886 4.2 The CMS experiment

887 The Compact Muon Solenoid experiment [4, 95], located at Interaction Point 5 of
888 the LHC close to Cessy, France, is a general-purpose particle detector targeting a
889 broad range of SM and BSM phenomena. Its main feature is a superconducting
890 solenoid magnet creating a strong magentic field of 3.8 T. CMS is a hermetic detec-
891 tor, covering almost the full solid angle in space, and is split into a *barrel*, covering
892 pseudorapidities of $|\eta| \lesssim 1.5$, and two forward *endcaps*, covering high $|\eta|$ values. It
893 consists of several subdetectors, which are geared towards different particle types
894 and properties.

895 **Subdetectors** The innermost part of CMS is the *tracker*, which is a silicon detec-
896 tor comprised of several layers of silicon pixel and strip sensors [97, 98]. These record
897 interactions with particles (“tracker hits”) shooting outwards from the interaction
898 point in the center in three-dimensionsial space. Through reconstruction of the par-
899 ticle tracks and fits of the curvature due to the magenetic field, the tracker thus
900 allows for the measurement of particle momenta. Furthermore, extrapolating the
901 tracks back to their origin allows for the determination of the point of interaction,
902 and thus for discrimination between particles arising from different proton-proton
903 interactions. Due to the presence of the beampipe, the tracker covers only pseu-
904 dorapidities of $|\eta| < 2.5$, enabling high precision momentum determination in this
905 range only.

906 The second-to-innermost subdetector is the *electromagnetic calorimeter* (ECAL),
907 which is intended to measure the energy of electrons and photons [99, 100]. It
908 consists of transparent lead tungstate cells, in which incoming electrons or pho-
909 tons create electromagnetic showers leading to avalanches of electron-positron pairs
910 and photon radiation. These are then recorded by photodiodes, and the energy of
911 the incoming particle can be reconstructed from the amount of measured photons.
912 Pseudorapidities of $|\eta| < 1.48$ and $1.65 > |\eta| < 3$ are covered for the barrel and the
913 endcaps, respectively. The majority electrons and photons are fully stopped in the
914 ECAL and do not interact with the further subdetectors.

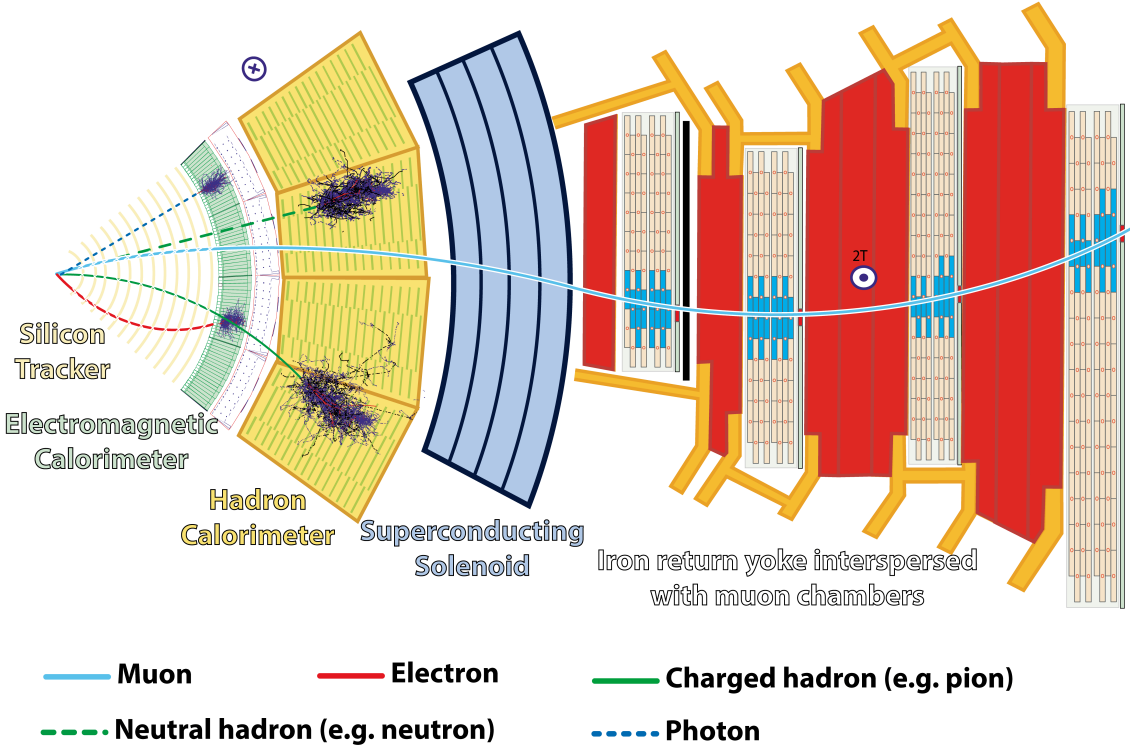


Figure 4.1: **The CMS detector.** A cross section view of the different CMS subdetectors, with the trajectories of example particles and their interactions. *Figure taken from Ref. [96].*

Following the ECAL, and similar in functionality, the *hadronic calorimeter* (HCAL) measures the energy of charged or neutral hadrons [101, 102]. It consists of interleaved absorber plates, which initiate hadronic showers through the strong interaction with the nuclei of the material, and scintillators, which transmute the hadronic showers into photons to be detected by photodetectors. The HCAL covers $|\eta| < 1.4$ and $1.4 < |\eta| < 3$ for the barrel and endcaps, respectively, and additionally features a forward section ranging up to $|\eta| < 5$, though the latter is not used anywhere in this work.

Surrounding the HCAL lies the superconducting solenoid, followed by the final subdetector: the *muon chambers* [103, 104]. They are interspersed with four layers of the iron return yoke of the magnet, which confines the magnetic field. Since muons interact only sparsely with matter, they escape the calorimeters and the solenoid unhindered, and are detected in four muon subsystems working in accord at different pseudorapidities: the drift tubes ($|\eta| < 1.2$), cathode strip chambers ($0.9 < |\eta| < 2.4$), resistive plate chambers ($|\eta| < 1.9$) and gas electron multipliers ($1.6 < |\eta| < 2.4$). All of them are gas detectors, which are sensitive to the ionization of a gas when a muon passes through it, and record hits of the muon trajectory,

thus allowing for a momentum measurement similar to the tracker.

Trigger system Besides the different subdetectors, a crucial part of the CMS experiment is the *trigger system* [105]. It is necessary due to the large number of bunch crossings at the LHC, which, if they were all recorded, would produce data rates far in excess of the computational bandwidth and storage capacities available. To combat this, only events which are of physical interest should be recorded. It is the task of the trigger system to determine what these events should be.

The trigger system is split into two parts. The first is the low-level or level-one trigger (L1T) [106], which is a hardware trigger consisting of custom electronics and whose inputs are directly the output signals of several of the subdetectors. It is designed to trigger on signatures consistent with specific objects, such as electrons, muons or hadronic jets, with significant energy. Since it needs to take a decision for every collision event, it only has a time interval of around $4\mu\text{s}$ to do so, requiring purpose-build low-latency electronics. Its target is a output event rate of 100 kHz, which can be adjusted by prescaling certain trigger paths so that only a fraction of passing events is recorded.

The second part of the trigger system is the high-level trigger (HLT) [107, 108]. It is a software trigger, running on a GPU-accelerated server farm directly in the CMS service cavern, on which a dedicated, speed-optimized version of the standard CMS object reconstruction algorithm is executed for each event passing the L1T. Specific triggers are then implemented as decisions based on these reconstructed trigger objects, allowing large freedom in selecting events based on the desired physics program. Typical triggers require, for example, the presence of different numbers or combinations of electrons, muons, photons, hadronic jets or missing transverse momentum. The transverse momentum thresholds and further requirements on these objects need to be adjusted so that the total trigger rate is reduced to an average of around 400 Hz. Only these events are then saved to hard drives, and kept for further analysis.

4.3 Object reconstruction

In order to interpret the physics behind a collision event, the outputs of the subdetectors have to be translated into physics objects which can be mapped to the underlying physical particles. At CMS, this is done with a single unifying method, the Particle Flow (PF) algorithm [109], which is designed to combine the information from the several subdetectors to build physics objects (called PF candidates) as appropriate. The physics objects relevant to this work are listed in the following.

Charged particle tracks are obtained from the tracker by fitting recorded tracker hits using a χ^2 minimization, and their momentum and charge are estimated from

4 Experimental methods

their curvature as described above [97]. By extrapolating the tracks back to their origin, the position of vertices in space can also be determined.

From the tracks, the *primary vertices* (PVs) can be determined, which are the locations of the proton-proton interactions that caused the tracks in the first place. By contrast, secondary vertices arise from the decays of particles with long enough lifetime that they move a significant distance from the PV. PVs are determined by a likelihood fit to all tracks of sufficient quality [97]. In each event, the PV whose tracks show the largest p_T sum is designated the hard-scattering PV, assumed to correspond to the physical process of interest, while further PVs are due to soft-QCD pileup interactions. The number of PVs per event is thus a good measure of the amount of pileup.

The other main ingredient besides tracks and vertices are *calorimeter clusters* from either the ECAL or the HCAL. A clustering algorithm is required here because particles typically deposit their energy in more than one calorimeter crystal.

By matching the positions of calorimeter clusters and charged particle tracks, *electrons* (for the ECAL) and *charged hadrons* (for the HCAL) can be constructed. The combined measurements of the momentum (from the curvature) and the deposited energy (from the calorimeter) allows for the reconstruction of the mass, and thus the identification of the particle. For electrons, the effect of bremsstrahlung originating in the tracker volume has to be considered, usually resulting in multiple calorimeter clusters per electron (called a supercluster) which need to be combined together. Isolation criteria on the clusters are also required to veto electrons that are part of a hadronic jet. By contrast, calorimeter clusters which do not have charged tracks are assigned to *photons* (for the ECAL) or *neutral hadrons* (for the HCAL). CMS furthermore employs algorithms to remove hadrons that are believed to originate from pileup instead of the hard-scattering vertex. In Run 2, the Charged Hadron Subtraction (CHS) method [109] was used for this purpose, while in Run 3, the better performing PUPPI method [86, 110] was used instead.

Muons interact only very rarely with the calorimeter, and are instead built by directly combining charged tracks with hits in the muon chambers. In this work, muons are only considered if they match to hits in both subdetectors.

From these definitions, further high-level objects can be built. The first are *hadronic jets*, which are clustered from all other PF candidates using the anti- k_T algorithm with a distance parameter of $\Delta R = 0.4$ [111] (referred to as AK4 jets). This algorithm is infrared- and collinear-safe, i.e. it is not strongly sensitive to soft nonperturbative QCD effects [64], and has the advantage that the resulting jets are approximately circular in the $\varphi-\eta$ plane. Since leptons or photons can be created from electroweak decays of hadrons, these also need to be included in the jet clustering; to ensure that they are not double-counted, leptons and photons that are included in jets are removed from further consideration through isolation criteria.

Hadronic jets can further be *b tagged*, that is, identified as originating from a B hadron. Since the strong interaction is flavor-conserving, the decay of B hadrons

1011 to hadrons of other flavors has to be mediated by the flavor-mixing in the weak
 1012 interaction, leading to comparatively long lifetimes. B hadrons can thus be identified
 1013 through secondary vertices corresponding to the B hadron decay, which can be
 1014 displaced from the PV by several millimeters. In practice, machine learning-based
 1015 classifiers like the DEEPJET algorithm [112] are used, which take more properties
 1016 of the jet into account besides the displacement of the secondary vertex.

1017 Finally, the *missing transverse momentum* \vec{p}_T^{miss} can be calculated as the negative
 1018 of the vectorial sum of all transverse momenta in the event [113]. Since the initial
 1019 state of a collision at the LHC has negligible transverse momentum, \vec{p}_T^{miss} represents
 1020 the total transverse momentum of the particles that left the detector unobserved.
 1021 In the SM, this is the case for neutrinos, but it could also be BSM particles such as
 1022 e.g. dark matter candidates.

1023 4.4 Statistical interpretation

1024 In experimental particle physics, results are typically extracted by comparing detector-
 1025 level predictions, for example obtained using MC simulation, to the observed data
 1026 for suitably chosen observables. The measured data here are necessarily afflicted
 1027 by statistical uncertainties, both due to the inherent randomness of quantum me-
 1028 chanics and the probabilistic behaviour of the detector. They should thus be seen
 1029 as a sample drawn from a random distribution, and in order to extract underlying
 1030 parameters of any model, statistical methods are required.

1031 In this work, all statistical interpretation is performed in the framework of *binned*
 1032 *profile maximum likelihood fits*. This method follows the Frequentist approach of
 1033 considering physical properties that should be extracted to be fixed, if unknown,
 1034 quantities, which enter the random distribution of the observed data as parameters.
 1035 In order to estimate the desired properties, the observed datapoints are sorted into
 1036 orthogonal bins according to one or more sensitive observables, and each bin is
 1037 treated as an independent counting experiment where the observed number of events
 1038 is given by a Poissonian distribution.

1039 **Likelihood definition** Denoting the set of physical properties to be estimated
 1040 (the parameters of interest or POIs) collectively as $\vec{\mu}$, the likelihood of $\vec{\mu}$ for bin i ,
 1041 given that N_i events were observed, is [114]

$$L_i(\vec{\mu}, \vec{\theta}) = \text{Pois}\left(N_i | n_i(\vec{\mu}, \vec{\theta})\right). \quad (4.1)$$

1042 Here, Pois refers to the Poissonian distribution, and $n_i(\vec{\mu}, \vec{\theta})$ is the mean expected
 1043 number of events in bin i as predicted by the physics model under consideration.
 1044 The set of parameters $\vec{\theta}$ are *nuisance parameters* (NPs), which encode the effects

4 Experimental methods

of different sources of systematic uncertainty affecting the measurement. The full likelihood of the measurement is now given as the product of all bins:

$$L(\vec{\mu}, \vec{\theta}) = \prod_i L_i(\vec{\mu}, \vec{\theta}) \cdot G(\vec{\theta}). \quad (4.2)$$

The function $G(\vec{\theta})$ represents the *constraint terms* of the NPs, encoding any possible prefit uncertainties on them. For example, an experimental source of uncertainty (e.g. a scale factor) f might be measured with a mean value of \hat{f} and standard deviation σ_f . Then, the corresponding NP would be normalized as $\theta_f = (f - \hat{f})/\sigma_f$, and the constraint terms $G(\vec{\theta})$ would include a factor $\mathcal{N}(\theta_f | 0, 1)$, i.e. the standard normal distribution for θ_f . This way, the range $\theta_f = \pm 1$ corresponds to one standard deviation of the corresponding systematic uncertainty source.

In practice, the functional form of the expectation n_i must be given by the physics model studied in the experiment. In this work, the events are modeled as a sum of signal and background processes. An important case is a linear signal, where the only POI is the *signal strength* μ and the expectation for bin i is

$$n_i(\mu, \vec{\theta}) = \mu s_i(\vec{\theta}) + b_i(\vec{\theta}). \quad (4.3)$$

The functions s_i and b_i are the signal and background expectations, respectively, which both can be influenced by NPs.

To extract a best-fit value of the POI (or multiple POIs), one now maximizes the full likelihood simultaneously over both the POIs $\vec{\mu}$ and the NPs $\vec{\theta}$, giving the *maximum likelihood estimator* for $\vec{\mu}$. In practice, usually the function $-2 \ln L$ is minimized instead to have numerically tractable quantities.

Confidence intervals In the Frequentist approach to statistics, an uncertainty can be assigned to the estimate in the form of *confidence intervals*. To do so, a *test statistic* has to be defined, which usually takes the form of a *profile likelihood ratio*, e.g. [114]

$$\lambda(\vec{\mu}) = -2 \ln \frac{\hat{L}(\vec{\mu})}{\max_{\vec{\mu}'} \hat{L}(\vec{\mu}')} \quad \text{with} \quad \hat{L}(\vec{\mu}) = \max_{\vec{\theta}} L(\vec{\mu}, \vec{\theta}). \quad (4.4)$$

$\hat{L}(\vec{\mu})$ is the profile likelihood, i.e. the likelihood maximized over the NPs, and the ratio is taken between the probed POI values $\vec{\mu}$ and the best-fit values $\vec{\mu}'$. Small values of $\lambda(\vec{\mu})$ now signalize good agreement with the data for the POI values $\vec{\mu}$. The value of the test statistic λ depends on the observed data N_i , and can thus be seen as a random variable with a probability density $f(\lambda|\vec{\mu})$, which again depends on the POIs as parameters. Then, given an observed value of the test statistic λ^{obs} , a set of POIs $\vec{\mu}$ is excluded at confidence level (CL) α if

$$P(\lambda(\vec{\mu}) < \lambda^{\text{obs}}) = \int_0^{\lambda^{\text{obs}}} f(\lambda|\vec{\mu}) d\lambda > \alpha. \quad (4.5)$$

1075 The probability density $f(\lambda|\vec{\mu})$ can be evaluated numerically using toy datasets.
 1076 Alternatively, for simple signal models like the linear signal given in Eq. (4.3), it
 1077 can be analytically shown that λ is approximately χ^2 -distributed, with the degrees
 1078 of freedom equaling the number of POIs [115, 116].

1079 In particular, for the case of one POI μ with best-fit value $\hat{\mu}$, a two-sided confi-
 1080 dence interval at $\sim 68\%$ CL (corresponding to one standard deviation of the normal
 1081 distribution) is then simply given as [114]

$$\lambda(\hat{\mu} \pm \Delta\mu) = -2(\ln \hat{L}(\hat{\mu} \pm \Delta\mu) - \ln \hat{L}(\hat{\mu})) = 1. \quad (4.6)$$

1082 That is, the uncertainty corresponds to a change in negative profile log-likelihood
 1083 $-2 \ln \hat{L}$ by 1 with respect to the best-fit point.

1084 **Significance** The framework of confidence intervals can also be used to define the
 1085 *significance* of an observed signal. To do so, a hypothesis test is performed, with the
 1086 background-only case as the null hypothesis to be rejected. For an observed value
 1087 of the test statistic λ^{obs} (defined again by Eq. (4.4)), the probability to make this
 1088 observation under the background-only hypothesis (the *p-value*) is

$$p_0 = \int_0^{\lambda^{\text{obs}}} f(\lambda|\vec{\mu} = 0) d\lambda. \quad (4.7)$$

1089 To translate this into a significance, the *p*-value is compared to the area under
 1090 the curve of a standard normal distribution: a significance of 2 standard deviations,
 1091 giving $\approx 95\%$ probability under the normal distribution, corresponds to a *p*-value
 1092 of 0.05. Similar to the case described above, the *p*-value can be obtained from
 1093 analytical approximate distributions in the case of a simple linear signal.

1094 **Exclusion limits** A different application of confidence intervals are *exclusion limits*,
 1095 used in experiments where no or little signal was observed. Here, for a POI that
 1096 is bounded from below (usually by zero, e.g. a signal strength), an upper limit μ^{up}
 1097 is sought such that all values $\mu > \mu^{\text{up}}$ are excluded at a certain CL. At the LHC,
 1098 the CL_s method [117, 118] is commonly used for this purpose. The test statistic is
 1099 modified from Eq. (4.4) to be

$$q(\mu) = \begin{cases} \lambda(\mu), & \hat{\mu} \leq \mu \\ 0, & \hat{\mu} > \mu \end{cases} \quad (4.8)$$

1100 where $\hat{\mu}$ again refers to the best-fit value of μ . The point of this modification is that
 1101 a certain value of μ should not be seen as excluded if the data is more compatible

4 Experimental methods

1102 with a higher μ value; thus, the test statistic is set to zero in this case.

1103 Following that, for an observed test statistic q^{obs} , the CL_s value is defined as

$$\text{CL}_s(\mu) = \frac{p_{s+b}(\mu)}{1 - p_b} \quad (4.9)$$

1104 with

$$p_{s+b}(\mu) = \int_0^{q^{\text{obs}}} f(q|\mu) dq \quad \text{and} \quad p_b = \int_0^{q^{\text{obs}}} f(q|\mu = 0) dq. \quad (4.10)$$

1105 p_{s+b} and p_b are the probabilities to observe a test statistic of q^{obs} under the
1106 signal+background and background-only hypotheses, respectively, defined similarly
1107 as in Eq. (4.7). The ratio of the two probabilities is used instead of p_{s+b} directly to
1108 prevent exclusion of small signals in the case that the data is not well compatible
1109 with neither the background-only or the signal+background hypothesis (particularly
1110 if the experiment is not very sensitive to a certain kind of signal and p_{s+b} and p_b are
1111 thus similar). The exclusion limit at CL α is then simply given by $\text{CL}_s(\mu^{\text{up}}) = 1 - \alpha$.
1112 A common choice, used in this work, is $\alpha = 95\%$ (corresponding to a p -value of 0.05).

1113 **Nuisance parameter diagnostics** Real maximum likelihood fits used in analy-
1114 ses at the LHC are often very complex, with more NPs than there are bins. In such
1115 underconstrained fits, the behaviour of the different NPs - encoding the different
1116 sources of uncertainty - is often not intuitively clear a priori, and it is thus impor-
1117 tant to investigate their postfit behaviour to check whether the fit is healthy and
1118 numerically stable.

1119 To do so, first, the *pulls and constraints* of the NPs are defined as their best-
1120 fit values and profiled postfit uncertainties, similar as for the POIs above, relative
1121 to their prefit uncertainties. To have a NP pulled means that its best-fit value is
1122 different from the prefit expectation. Similarly, to have it constrained means that its
1123 estimated postfit uncertainty is smaller than the assumed prefit value. Both of these
1124 effects are not necessarily a sign of an unhealthy fit: If the observables considered in
1125 the fit are sensitive to a particular physical or experimental parameter as encoded
1126 by the NP in question, a constraint, and possibly a pull, are expected, and simply
1127 show the power of the fit to measure that particular parameter.

1128 If, on the other hand, a strong constraint or pull (beyond what is expected from
1129 statistical fluctuations) is seen in a NP to which no sensitivity is expected, it might
1130 be a sign of problems with the fit, such as spurious constraints from noisy inputs,
1131 missing degrees of freedom to describe the data, or too small prefit uncertainties.
1132 Whether this casts doubt on the result or not needs to be gauged on a case-by-case
1133 basis, and depends on the relevance of the NP in question.

1134 The relevance of individual NPs to the result can be quantified using *impacts*.
1135 The impact of a NP θ with best-fit value $\hat{\theta}$ and postfit uncertainty $\Delta\theta$ is defined by

repeating the maximum likelihood fit at values of $\hat{\theta} \pm \Delta\theta$, with θ then held fixed in the maximization of Eq. (4.4). The shift in the resulting POI values with respect to the best-fit POI is the impact on that particular POI. In a fit with a single POI, the impacts can be used to rank the NPs and the systematic uncertainties they encode in order of importance to the fit result. In particular, NPs with very small impact can be considered irrelevant for the fit result. However, it should be kept in mind that this procedure does not fully account for possible correlations between the NPs.

Uncertainty breakdown Related but not identical to the concept of impacts is an *uncertainty breakdown*, which can be used to quantify the contribution from different sources of uncertainty to the total postfit uncertainty on the POI. To do so, either a single NP or a group of NPs originating from the same source (e.g. all NPs corresponding to a certain correction) are frozen at their postfit values, and the fit is repeated with the POI and remaining parameters left untouched. The result will yield the same best-fit value for the POI, but with a possibly reduced uncertainty (as estimated from the likelihood). The uncertainty due to the frozen NP or NP group is then defined as the quadratic difference to the nominal uncertainty. This method does not account for correlations between different uncertainty sources (though it does consider correlations between the NPs in a certain group). As a result, the uncertainties obtained in this way will in general not sum up in quadrature to the original uncertainty.

A further use of this method is to define the statistical component of the uncertainty on a POI: it is simply the remaining uncertainty when all considered NPs are frozen to their postfit values simultaneously. Conversely, the quadratic difference between the total and the statistical uncertainty can be considered the systematic uncertainty.

Technical implementation In this work, two different tools are used to implement the methods described above. In Chapters 5 and 7, where experimental data is analyzed, the CMS general-purpose statistics tool `combine` is used [119]. In Chapter 8, on the other hand, the Python-based tool `pyhf` [120] is employed for the purpose of calculating expected significances and limits.

1166 5 Measurement of the inclusive $t\bar{t}$ cross 1167 section at $\sqrt{s} = 13.6$ TeV

1168 5.1 Introduction

1169 In July 2022, the LHC officially resumed collecting data after over three years of
1170 shutdown, thereby starting LHC Run 3. It did so at a new, unprecedented center-
1171 of-mass energy of $\sqrt{s} = 13.6$ TeV, inviting the experiments to measure physical
1172 observables at the new energy frontier.

1173 One important such observable is the inclusive $t\bar{t}$ production cross section. It is,
1174 in essence, the total rate of top quark pair production at the LHC, integrated over
1175 the kinematic distributions of the particles produced. As mentioned in Chapter 2,
1176 the top quark has a special place in the standard model as the heaviest known
1177 elementary particle, as well as the only colored particle that usually decays before
1178 hadronizing. It is thus important for many potential BSM scenarios, such as models
1179 with additional Higgs bosons, which might couple strongly to the top quark. As such,
1180 measurements of top quark-related observables at the highest possible energies are
1181 attractive tests of the SM. The inclusive $t\bar{t}$ production cross section, as one of the
1182 simplest top quark observables, is well suited for a first measurement at the new
1183 center-of-mass energy.

1184 Simultaneously, restarting such a large experiment as CMS after a three-year
1185 shutdown poses many experimental challenges. Due to the change in energy, as
1186 well as physical changes in the accelerator and detector, new calibrations as well as
1187 validations of some previous calibrations are required to ensure that the detector
1188 performance is understood. An early measurement of the inclusive $t\bar{t}$ cross section
1189 is well suited to serve as such a cross-check: Because of the decay chain of the top
1190 quark, a top quark measurement involves many of the different objects reconstructed
1191 at CMS, which allows for a check of a wide landscape of calibrations.

1192 The measurement described in this chapter was designed specifically with these
1193 motivations in mind, and as such exhibits several novel features. Firstly, it com-
1194 bines events from both the dilepton and ℓ +jets decay channels of $t\bar{t}$, categorized
1195 by lepton flavor content, combining the higher statistics of the ℓ +jets channel with
1196 the high purity of the $e\mu$ channel and allowing to constrain uncertainties on the
1197 lepton identification efficiency directly from the data. This is done using a sim-
1198 taneous maximum likelihood fit to the event yields in the different categories, with
1199 experimental and theoretical uncertainties treated as nuisance parameters.

1200 Secondly, the events are additionally categorized by their number of b-tagged jets,
1201 which similarly allows for an in-situ measurement of the b-tagging efficiencies. This
1202 averts needing to wait for external b-tagging calibrations, allowing for a measure-
1203 ment as early as possible.

1204 The results of this work were first presented as a Physics Analysis Summary in
1205 September 2022 [121], only two months after the start of datataking, as the first
1206 public physics result of LHC Run 3. It was later published in *JHEP* as Ref. [5],
1207 again representing the first published Run 3 result. A similar result by ATLAS was
1208 later published in Ref. [122].

1209 This chapter is structured as follows: In Sec. 5.2, the used datasets, object def-
1210 initions, and event selection criteria are described, followed by the derivation and
1211 application of needed corrections in Sec. 5.3, and the resulting data-MC agreement
1212 is shown in Sec. 5.4. The considered systematic uncertainties are listed in Sec. 5.5,
1213 and the fit results are presented in Sec. 5.6. The chapter is concluded by a short
1214 summary and outlook in Sec. 5.7.

1215 5.2 Datasets and event selection

1216 In this section, the choice of datasets for experimental data and for simulation, as
1217 well as the choice of triggers, is described. Following that, the object and event se-
1218 lection procedure is outlined and several event categories to be used in the likelihood
1219 fit are defined.

1220 5.2.1 Datasets

1221 **Experimental data** The measurement is performed on data recorded during the
1222 period between July 27th and August 02nd 2022, corresponding to an integrated lu-
1223 minosity of 1.21 fb^{-1} . This amount of data is chosen as a balance between sensitivity
1224 and speed for the early measurement: It roughly corresponds to the point where the
1225 measurement precision is no longer primarily limited by the quantity of the data,
1226 while at the same time restricting to a dataset where beam and detector conditions
1227 were stable and comparable to the data-taking in Run 2.

1228 Both single-lepton and dilepton triggers were used to select events used in this
1229 measurement during detector operation, identifying leptons in the range of $|\eta| < 2.5$.
1230 The p_T requirements of the triggers are summarized in Tab. 5.1.

1231 **Simulation** To compare the data with predictions, Monte Carlo (MC) simula-
1232 tion is used to simulate both the $t\bar{t}$ signal as well as most important background
1233 processes, specifically single-top quark production in the t -channel, associated tW
1234 production, $Z+jets$ production, $W+jets$ production, and diboson (WW , WZ and
1235 ZZ) production. The MC generator POWHEG v2 [72–74] is used to generate $t\bar{t}$,

| Trigger | Lepton requirement |
|---------------------|---|
| e+jets | $e(p_T > 32 \text{ GeV})$ |
| $\mu + \text{jets}$ | $\mu(p_T > 27 \text{ GeV})$ |
| ee | $e(p_T > 23 \text{ GeV}) \text{ and } e(p_T > 12 \text{ GeV})$ |
| $\mu\mu$ | $\mu(p_T > 17 \text{ GeV}) \text{ and } \mu(p_T > 8 \text{ GeV})$ |
| $e\mu$ | $e(p_T > 23 \text{ GeV}) \text{ and } \mu(p_T > 8 \text{ GeV}) \text{ or }$ $e(p_T > 12 \text{ GeV}) \text{ and } \mu(p_T > 23 \text{ GeV})$ |

Table 5.1: **Trigger definitions** as used for the $t\bar{t}$ cross section measurement. The leptons are required to be isolated and in the pseudorapidity range $|\eta| < 2.5$.

single-top, and tW events at next-to-leading order (NLO) in perturbative QCD, while the generators MADGRAPH5_AMC@NLO [70] and PYTHIA 8 [76] are used to generate Z+jets/W+jets and diboson events, respectively, at leading order (LO). For t -channel single-top, MADSPIN is used to simulate the top decay.

All of the generated events are interfaced to PYTHIA 8 for parton showering and hadronization, using the MLM prescription in the case of the samples produced with MADGRAPH, and further processed in a full simulation of the CMS detector as described in Chapter 3. The proton structure in the matrix element calculation is described by the NNPDF3.1 parton distribution function (PDF) set at NNLO. Note that another background contribution, from QCD-produced multijet events with fake or non-prompt leptons, is not simulated, but estimated from data (see Sec. 5.3.2).

Theoretical predictions, as well as the measured integrated luminosity, are used to normalize the cross sections of the signal and background samples as follows: The $t\bar{t}$ signal, is normalized to a cross section of 921^{+29}_{-37}pb computed at NNLO+NLL in QCD [123], which is also used as a prediction for comparison with the SM. For the other backgrounds, the following orders in QCD and methods or programs are used: MCFM [124] (NNLO) for single-top, DYTURBO [125] (NNLO) for W+jets and Z+jets, MATRIX [126] (NLO) for diboson, and an NNLO calculation from Ref. [127] for tW.

5.2.2 Object definition

Leptons Electrons or muons are considered for the analysis if they have $p_T > 10$ GeV and $|\eta| < 2.4$. For electrons, the range $1.44 < |\eta| < 1.57$, corresponding to the transition region between barrel and endcaps in the ECAL, is removed. Furthermore, additional identification criteria (ID) are applied to remove non-prompt or fake (i.e. wrongly reconstructed) leptons and enrich the selection with $t\bar{t}$ events.

For electrons, the “tight” working point of the cut-based ID described in Ref. [100]

is applied, which includes information from both the details of the electromagnetic shower in the ECAL and the track, as well as the matching between the two. It also includes a requirement for the electron to be isolated from other particles such as hadrons, which is implemented in the form of the relative isolation variable I_{rel} . It is defined as the scalar p_T sum of all particles in a cone around the lepton in question, divided by the lepton p_T . Here, $\Delta R = \sqrt{(\Delta\eta)^2 + (\Delta\varphi)^2} < 0.3$ is used for the radius of the cone. Additional corrections accounting for pileup particles are applied.

For muons, a similar cut-based ID is used as described in Ref. [128], also at the tight working point. Here, criteria on the compatibility of tracks in the inner tracker, the muon detectors and the reconstructed primary vertex are employed. Again, a cut on I_{rel} is used, defined equivalently but with a cone size of $\Delta R < 0.4$.

Jets The anti- k_T algorithm [111] is used to cluster reconstructed particles into jets with a distance parameter of 0.4. In order for a jet to be considered, it is required to have $p_T > 30$ GeV and $|\eta| < 2.4$, and jets overlapping with any considered leptons (i.e. fulfilling the above criteria) are removed.

Tagging of b jets A special role is played by jets originating from the showering and hadronization of b quarks. Naively, two such jets are expected per $t\bar{t}$ event from the two top decays, although in practice one or both jets may fall out of acceptance of the detector or otherwise not be identified. Furthermore, additional b quarks may be produced by radiation at higher orders in QCD. Correctly tagging these jets as such can greatly improve signal purity by cutting away backgrounds such as Z+jets, W+jets and QCD multijet events.

Here, the DEEPJET algorithm [112, 129], which is based on a deep neural network (DNN) classifier, is used to identify (“tag”) b jets. A working point with an identification efficiency of more than 75% is used, with misidentification rates of around 17% for charm jets and around 1% for other jets from light quarks or gluons.

5.2.3 Channel definition

Events are selected with either one or two leptons, corresponding respectively to the ℓ +jets and dilepton decay channels of $t\bar{t}$. They are categorized into separate channels by their lepton flavor content, and additional requirements are applied for the different channels.

Dilepton channels Events with exactly two leptons, required to have opposite electric charge, are sorted into three dilepton channels ($e\mu$, ee , and $\mu\mu$). The presence of at least one jet is required, and in the same-flavor channels (ee and $\mu\mu$), at least one jet is required to be b tagged in order to reject Z+jets and QCD multijet

1298 background. In the much purer e μ channel, on the other hand, events without b
1299 tags are retained to later help constrain the b tagging efficiency in the fit to data.

1300 In order to reject even more Z+jets background, events in the same-flavor channels
1301 with an invariant dilepton mass of $|m_{\ell\ell} - m_Z| < 15$ GeV, where m_Z is the Z boson
1302 mass, are removed.

1303 **ℓ +jets channels** Events with exactly one lepton are sorted into the e+jets or
1304 μ +jets channels based on their flavor. At least three jets are required, of which
1305 at least one needs to be b tagged. Note that regardless of these selections, there
1306 is still non-negligible background from QCD multijet events where the lepton is
1307 non-prompt or fake, which is estimated from data (see Sec. 5.3.2).

1308 **p_T requirement** In all channels, the considered leptons are required to have $p_T >$
1309 35 GeV. This requirement is needed in the ℓ +jets channels in order to stay above the
1310 single-lepton trigger p_T thresholds (compare Tab. 5.1). In this measurement, the
1311 choice is made to apply the same p_T requirement also both leptons in the dilepton
1312 channels to ensure consistency between the lepton definitions. This is done to help
1313 constrain the lepton ID scale factors using the combination of lepton flavor channels,
1314 which otherwise might not be accurate since the scale factors for different lepton
1315 definitions might differ. In particular it opens up the possibility to extract a result
1316 on the cross section without any prior knowledge on the lepton ID efficiencies, which
1317 was done in the first published version of this analysis [121].

1318 **b tag and jet categorization** In practice, the efficiency of the b tagging algo-
1319 rithm used might be different between simulation and data, necessitating a correc-
1320 tion to prevent bias. In this analysis, this efficiency is measured simultaneously with
1321 the cross section directly in the data. To do so, the lepton flavor channels are ad-
1322 ditionally split into categories based on the number (exactly 0, 1, or 2) of b tagged
1323 jets. Since only the e μ channel allows events with 0 b tags, this results in 11 cate-
1324 gories total. To gain further sensitivity to the b tagging efficiency and to increase
1325 possible separation between $t\bar{t}$ signal and background, the selected events are finally
1326 coarsely binned into the number of accepted jets for the eventual fit, giving a total
1327 number of 40 bins.

1328 5.3 Corrections

1329 While the simulation used in CMS tries to describe as many physics and detector
1330 effects as possible, in practice it should always be expected that not all observables
1331 agree with the experimental data perfectly. This is especially true for an early
1332 analysis such as this, as the detector conditions might have changed significantly

1333 during the long shutdown between LHC Runs 2 and 3, and the simulation had not
1334 been recalibrated at the time of the measurement.

1335 Because of this, the analysis setup is designed to either directly measure or cross-
1336 check as many required experimental calibration and correction factors as possible.
1337 This includes pileup corrections, efficiency scale factors for triggers, electrons, muons
1338 and b tags, as well as jet energy corrections, all of which are briefly described in this
1339 section.

1340 In addition to these experimental corrections, background processes might also
1341 be imperfectly described by the simulation because of theoretical shortcomings. In
1342 this case, ways have to be found to correct them directly from the experimental
1343 data. Here, two such cases are relevant and will be presented in the latter half of
1344 this section: The Z+jets background in the dilepton channels and in the presence
1345 of b tagged jets, for which the normalization is taken from data; and the QCD
1346 background in the ℓ +jets channels, which uses a fully data-driven estimation and
1347 foregoes simulation entirely.

1348 5.3.1 Experimental corrections

1349 **Pileup reweighting** The simulation samples used in this analysis were generated
1350 before the start of Run 3 datataking using a projected estimate of the average pileup.
1351 As a result, the pileup distribution in the simulation does not match the one observed
1352 in data, which could influence mostly jet-related variables such as the number of jets
1353 and the jet p_T .

1354 Since at the time of the measurement, no theory-based calculation for the cor-
1355 rect pileup distribution were available, an experimental approach was taken. Three
1356 experimental observables that are strongly correlated with pileup were identified:

- 1357 • The number of well-reconstructed primary vertices per event n_{PV} ;
- 1358 • The median p_T density in the calorimeter, calculated from calorimeter-only
1359 jets as $\rho^{\text{calo}} = \text{med}(p_T/A)$, where A is the jet area defined in the φ - η plane
1360 and the median is taken over all jets in the event;
- 1361 • The median p_T density in the tracker ρ^{trk} , defined equivalently as ρ^{calo} , but
1362 for jets calculated only from tracker information.

1363 A binned reweighting from simulation to data is derived for each observable based
1364 on the full data sample, and the average of the three weights is applied to the
1365 simulation, so that approximate agreement is achieved in all three variables. The
1366 distributions before and after reweighting can be seen in Fig. 5.1.

5 Measurement of the inclusive $t\bar{t}$ cross section at $\sqrt{s} = 13.6$ TeV

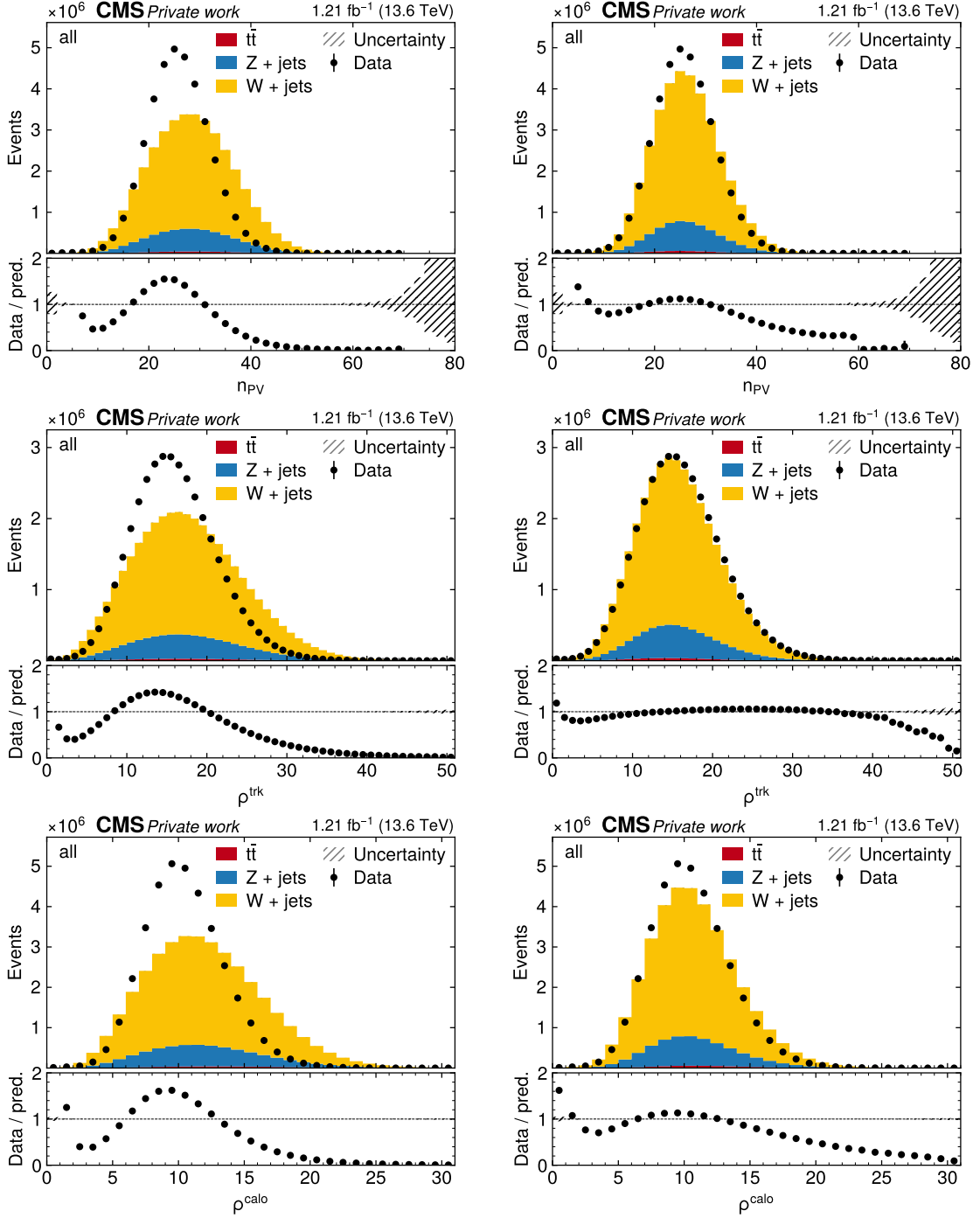


Figure 5.1: Pileup reweighting. Pileup-related distributions in MC and data in before (left) and after reweighting (right). From top to bottom: number of primary vertices as well as the mean energy densities ρ^{trk} (calculated using tracker input) and ρ^{calo} (calculated using calorimeter input).

1367 **Trigger scale factors** The trigger efficiency, i.e. the probability for an event
1368 falling into the selection phase space to be triggered by the low- and high-level
1369 triggers, can differ between simulation and data. In principle, both dilepton and
1370 single-lepton triggers are used for this measurement and should be considered for
1371 the efficiency calculation. However, due to the high offline p_T requirements for the
1372 two leptons applied in all channels, the fraction of events that are triggered only
1373 by the dilepton triggers is negligibly small, and can be neglected for the purpose of
1374 determining the scale factor. Thus, only the single-lepton triggers are considered in
1375 this section for simplicity.

1376 The efficiency measurement is performed by the so-called tag-and-probe (T&P)
1377 method, using $Z \rightarrow e^+e^-$ and $Z \rightarrow \mu^+\mu^-$ events. They are selected using the same
1378 definitions presented above, including the lepton identification, except for requiring
1379 their invariant mass to fulfill $|m_{\ell\ell} - m_Z| < 20$ GeV. At least one of the leptons
1380 is required to pass the relevant single-lepton trigger and is then designated the
1381 tag, while the other lepton might or might not pass the trigger and is designated
1382 the probe. Assuming the probability for the two leptons to pass the trigger to be
1383 independent of each other, the trigger efficiency, given by probability of the probe
1384 to pass, can be written as

$$\epsilon_{\text{tr}} = \frac{N(\text{Probe passes})}{N(\text{Probe passes}) + \frac{1}{2}N(\text{Probe fails})} \quad (5.1)$$

1385 where N is the observed event yield, and the combinatoric factor $\frac{1}{2}$ comes from
1386 the fact that either one or the other lepton can fail to pass the trigger.

1387 The efficiency is measured in this way in coarse bins of lepton p_T and $|\eta|$, separately
1388 for muons and electrons, in both simulation and experimental data. It is then applied
1389 to simulation in the following way: For $\ell+\text{jets}$ events, a simple ratio $\epsilon_{\text{tr,data}}/\epsilon_{\text{tr,sim}}$
1390 is applied to each simulation event as a scale factor, which is displayed in Fig. 5.2.
1391 For dilepton events, on the other hand, the fact that only one lepton needs to pass
1392 the single-lepton trigger needs to be taken into account. This leads to a per-event
1393 efficiency given by

$$\epsilon_{\text{tr},\ell\ell} = \epsilon_{\text{tr},\ell 1} + \epsilon_{\text{tr},\ell 2} - \epsilon_{\text{tr},\ell 1}\epsilon_{\text{tr},\ell 2} \quad (5.2)$$

1394 where $\epsilon_{\text{tr},\ell 1}$ and $\epsilon_{\text{tr},\ell 2}$ are the efficiencies evaluated at the p_T and $|\eta|$ of the two
1395 leptons, respectively. Again, the ratio of this event efficiency in data and simulation
1396 is applied to the simulation.

1397 **Lepton scale factors** Similarly to the triggers, the reconstruction and identifi-
1398 cation of leptons can exhibit different efficiencies between simulation and data, and
1399 thus require scale factors. The efficiencies are measured with a similar tag-and-
1400 probe method as for the triggers, and the simulation is corrected to the data. This
1401 is the standard approach commonly taken in CMS, detailed in Refs. [100, 128] for

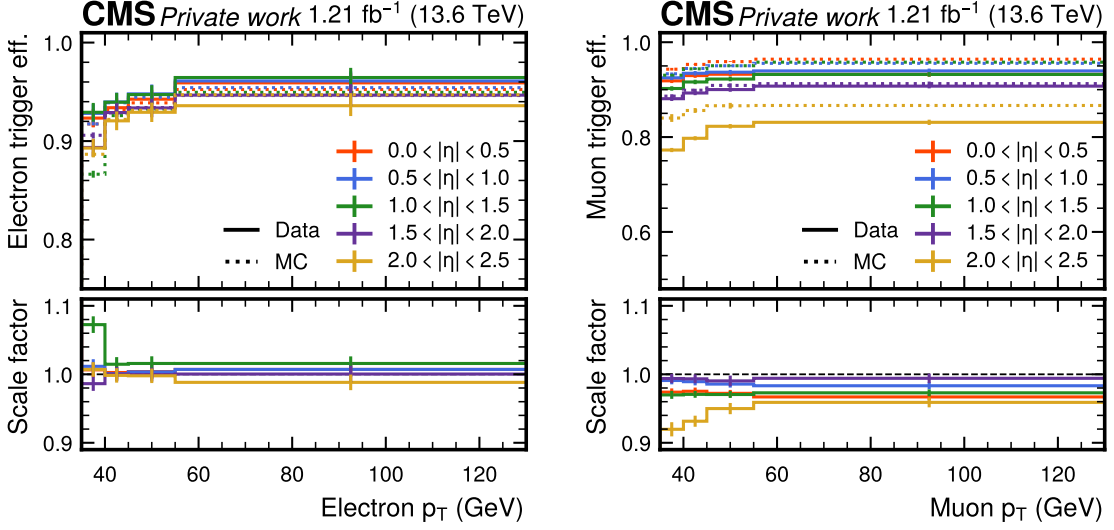


Figure 5.2: **Trigger scale factors.** Single-lepton trigger efficiencies in data and MC (top) and scale factors (bottom) for electrons (left) and muons (right) as a function of lepton p_T and $|\eta|$, calculated using a tag-and-probe-method. The error bars designate both statistical and systematic uncertainties.

¹⁴⁰² electrons and muons, respectively. The efficiency measurement was not performed as
¹⁴⁰³ part of this thesis, but is still shown in Figs. 5.3 and 5.4 for reference. The muon
¹⁴⁰⁴ scale factors are split into a reconstruction and an identification part, while these
¹⁴⁰⁵ are combined for the electron scale factors.

¹⁴⁰⁶ **b tagging scale factors** The performance of b tagging algorithms, including
¹⁴⁰⁷ the DEEPJET algorithm used here, is also well-known to have differences between
¹⁴⁰⁸ simulation and data, and requires correction. This is especially true since the multi-
¹⁴⁰⁹ variate classifier underlying DEEPJET had at the time of the measurement not been
¹⁴¹⁰ re-trained on Run 3 data, and the calibration from Run 2 was used instead.

¹⁴¹¹ However, no external calibration of the b tagging efficiencies in Run 3 was available
¹⁴¹² at the timescale of this work. Instead, the b tagging efficiency in data is measured
¹⁴¹³ simultaneously with the $t\bar{t}$ cross section in a single likelihood fit, which is described
¹⁴¹⁴ in more detail in Sec. 5.5. No b tagging scale factors are applied at the level of
¹⁴¹⁵ object selection.

¹⁴¹⁶ **Jet energy corrections** Another observable that often differs significantly be-
¹⁴¹⁷ tween observed data and simulation is the measured energy response of the jets.
¹⁴¹⁸ It is usually corrected by empirical methods, i.e. comparing simulation to data for
¹⁴¹⁹ well-known resonances like the Z boson. The jet energy correction (JEC) is not
¹⁴²⁰ measured as part of this thesis, and instead centrally provided by CMS following

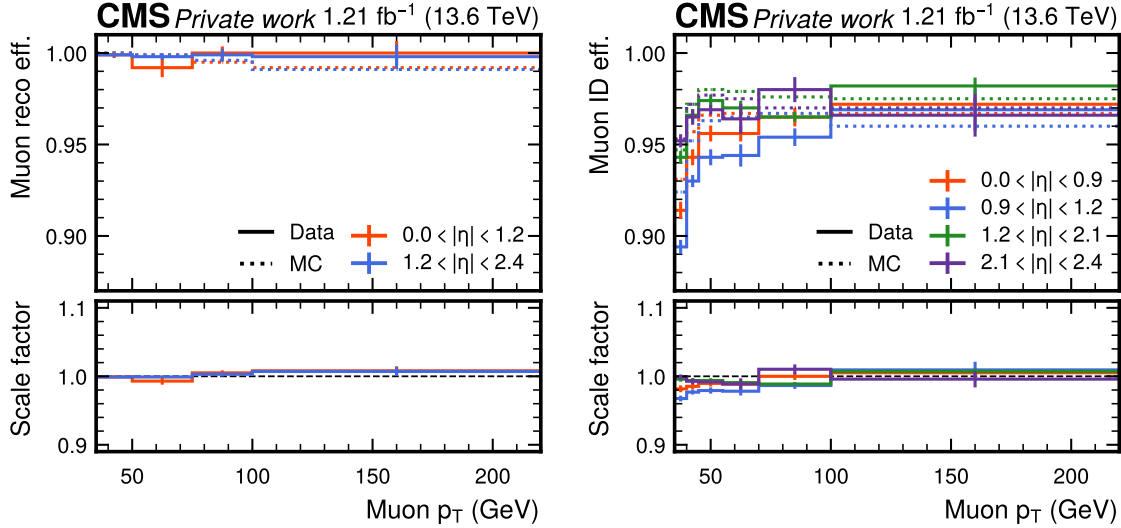


Figure 5.3: **Muon scale factors.** Muon efficiencies in data and MC (top) and scale factors (bottom), split into reconstruction (left) and identification (right) and shown as a function of lepton p_T and $|\eta|$, calculated using a tag-and-probe-method. The error bars designate both statistical and systematic uncertainties.

the methods of Ref. [130].

5.3.2 Data-driven background estimation

QCD background A significant background contribution in the $\ell + \text{jets}$ channels, especially in the categories with only one b tag, is given by QCD multijet events with one reconstructed lepton. The lepton in question might be non-prompt, e.g. from radiated photons splitting into leptons or weakly decaying hadrons created during hadronization, or it might be fake, i.e. a different particle (such as a photon or pion in the case of electrons) misidentified as a lepton.

It is often not practical to estimate this background using MC simulation as is done for the other backgrounds in this analysis. The reason is that, due to the large cross section of QCD multijet events at the LHC but low ratio of events with a fake or non-prompt lepton, very large MC datasets are needed to achieve significant statistics in the selected phase space, requiring excessive computing power. In addition to that, fake leptons are known not to be consistently well-described well by the simulation.

Instead, a fully data-driven approach is taken to estimate the QCD background in the $\ell + \text{jets}$ channels. For this, multiple control regions (CRs) orthogonal to the signal region (SR) are defined. In the first CR, denoted ‘‘QCD CR’’, the same cuts as in the SR are applied, except that the requirement for the single lepton

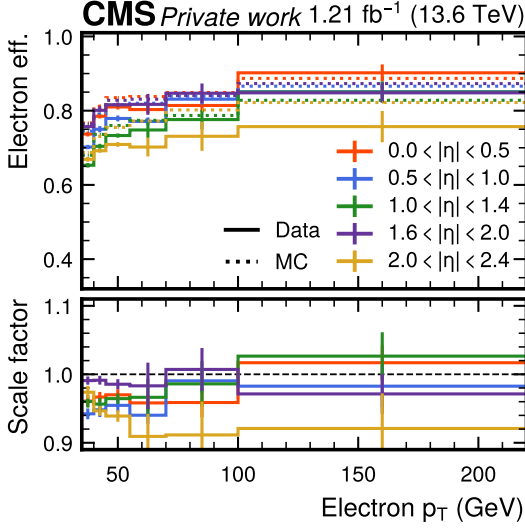


Figure 5.4: **Electron scale factors.** Combined electron efficiencies in data and MC (top) and scale factors (bottom) as a function of lepton p_T and $|\eta|$, calculated using a tag-and-probe-method. The error bars designate both statistical and systematic uncertainties.

to be isolated from other particles (I_{rel} , see Sec. 5.2.2) is inverted. It is expected that QCD events that fall in either the QCD CR or the SR show similar shapes in observable distributions, as long as said observables are uncorrelated with the lepton isolation. Thus, the shape of the QCD background can be extracted from the CR and applied in the SR. Figs. 5.5 and 5.6 show some control distributions in the $\mu+\text{jets}$ and $e+\text{jets}$ channels, respectively, with the difference between data and MC in this region considered QCD background.

The normalization of the QCD background is fixed through the so-called *ABCD method* [131, 132], for which an additional CR (the “1-jet CR”) is defined. It again contains events that pass the main selection, except for requiring exactly one jet (as opposed to at least three jets in the SR or QCD CR). These events are enriched with QCD events and contain negligible amounts of $t\bar{t}$ signal. They are used to measure the ratio f_{fake} of QCD events that pass or fail the lepton isolation requirement, given by

$$f_{\text{fake}} = \frac{N_{1\text{ jet}, \text{ pass}}^{\text{data}} - N_{1\text{ jet}, \text{ pass}}^{\text{MC}}}{N_{1\text{ jet}, \text{ fail}}^{\text{data}} - N_{1\text{ jet}, \text{ fail}}^{\text{MC}}} \quad (5.3)$$

where $N_{1\text{ jet}, \text{ pass}}$ and $N_{1\text{ jet}, \text{ fail}}$ denote 1-jet-events that pass and fail the lepton isolation requirement, respectively; “data” refers to the experimental data, and “MC” refers to the sum of all non-QCD processes, which are estimated by MC simulation. Here, this ratio is measured in four coarse bins of lepton p_T and $|\eta|$ to accurately

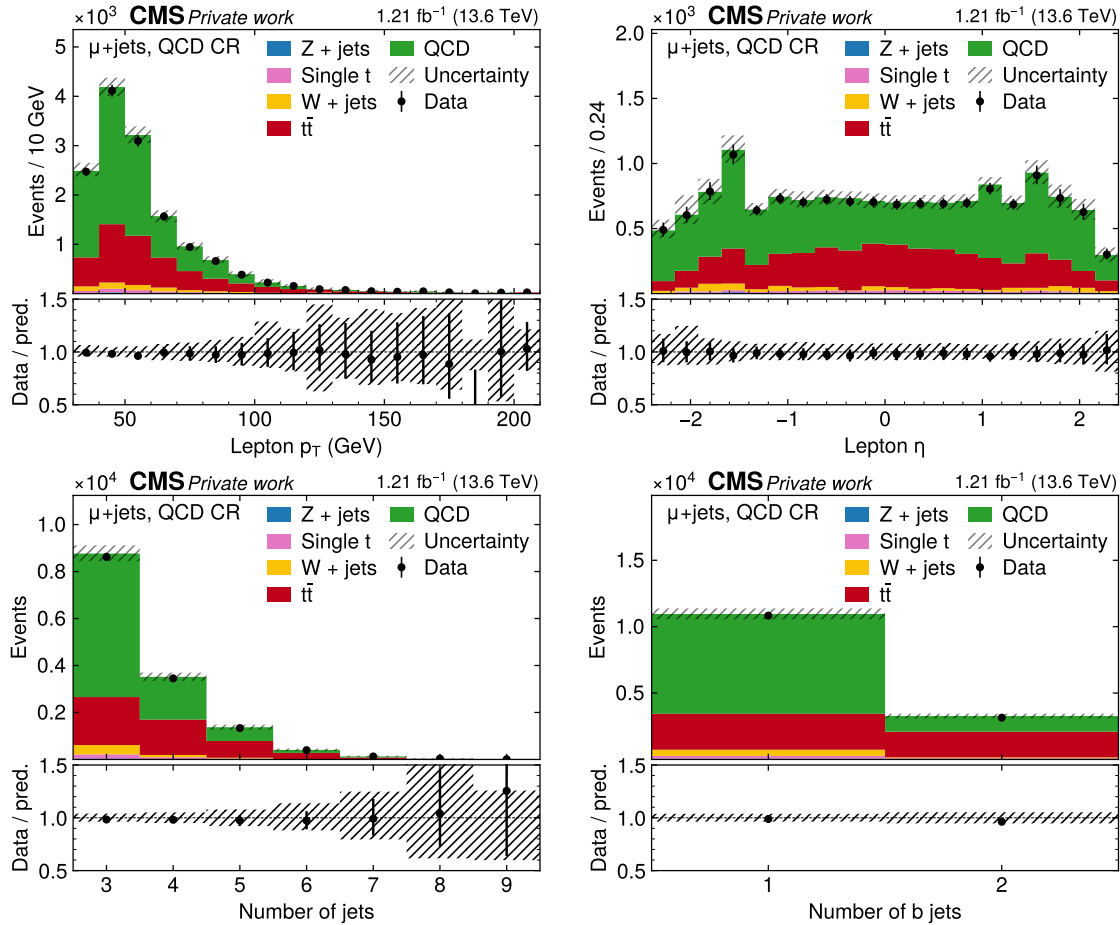


Figure 5.5: **QCD control region for $\mu + \text{jets}$.** Distributions in the QCD CR for the $\mu + \text{jets}$ channel. From top left to bottom right: p_T of the lepton, η of the lepton, the number of jets, and the number of b-tagged jets. The uncertainty bands include MC statistical and systematic uncertainties. The difference between data and MC prediction is considered QCD background and shown in green.

¹⁴⁵⁷ model lepton-related distributions; it can be seen in Fig. 5.7.

¹⁴⁵⁸ Naively, the full distribution of the QCD background in the SR for any observable
¹⁴⁵⁹ can then be written as

$$N_{\text{SR}}^{\text{QCD}} = (N_{\text{CR}}^{\text{data}} - N_{\text{CR}}^{\text{MC}}) \times f_{\text{fake}} \quad (5.4)$$

¹⁴⁶⁰ where $N_{\text{CR}}^{\text{data}}$ and $N_{\text{CR}}^{\text{MC}}$ refer to the total data and non-QCD MC yields in the QCD
¹⁴⁶¹ CR.

¹⁴⁶² In practice, this is complicated by the fact that a non-negligible amount of $t\bar{t}$
¹⁴⁶³ signal is present in the QCD CR, whose cross section, as the parameter of interest

5 Measurement of the inclusive $t\bar{t}$ cross section at $\sqrt{s} = 13.6$ TeV

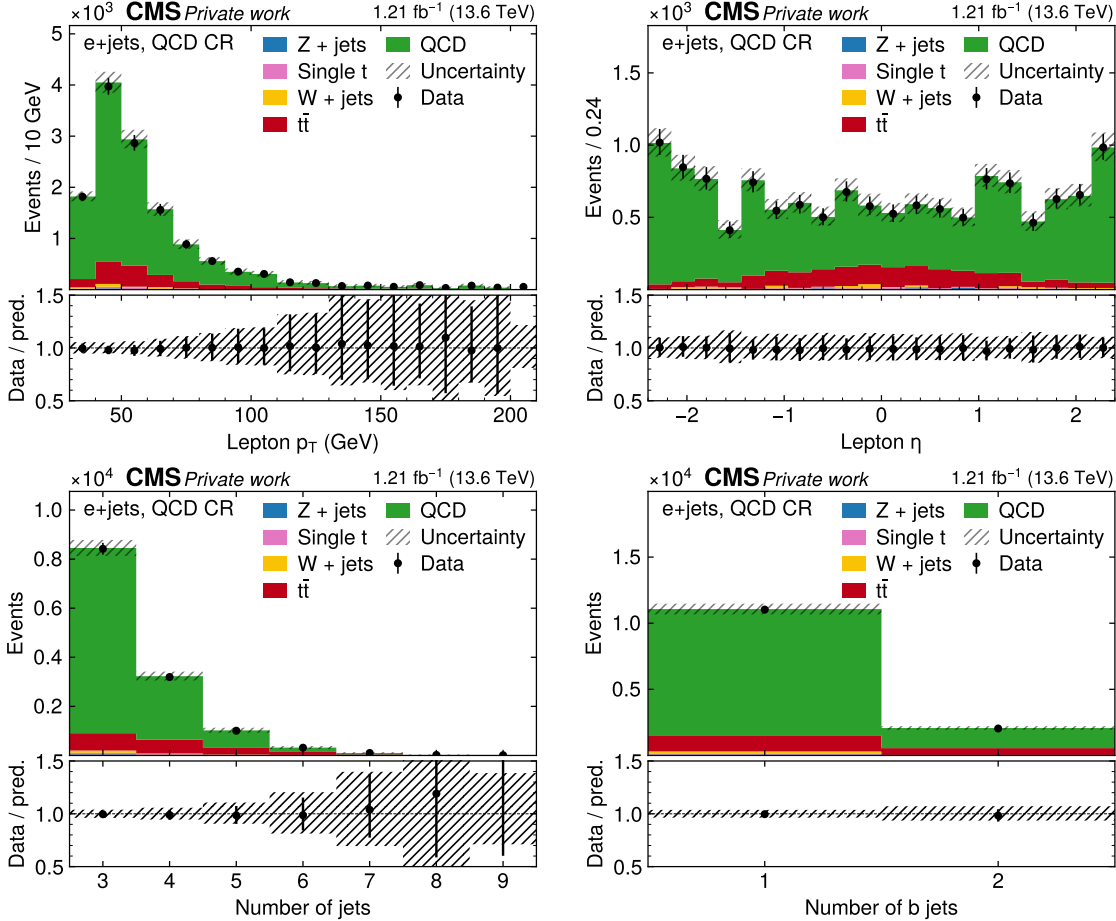


Figure 5.6: **QCD control region for e+jets.** Distributions in the QCD CR for the e+jets channel, same as in Fig. 5.5. The difference between data and MC prediction is considered QCD background and shown in green.

in the measurement, is not known *a priori*. To circumvent this problem, a modified method is introduced, which is agnostic about the prediction for the $t\bar{t}$ cross section. One sets for the SR

$$N_{\text{SR}}^{\text{data}} = N_{\text{SR}}^{t\bar{t}} + N_{\text{SR}}^{\text{MC,BG}} + N_{\text{SR}}^{\text{QCD}} \quad (5.5)$$

and similarly for the QCD CR

$$N_{\text{CR}}^{\text{data}} = N_{\text{CR}}^{t\bar{t}} + N_{\text{CR}}^{\text{MC,BG}} + N_{\text{CR}}^{\text{QCD}}, \quad (5.6)$$

where N^{data} is the total data yield, $N^{t\bar{t}}$ is the $t\bar{t}$ signal contribution, $N^{\text{MC,BG}}$ is the contribution of non-QCD backgrounds as predicted by MC, and N^{QCD} is the QCD contribution. It is assumed that the ratio f_{sig} of signal events in the SR and QCD

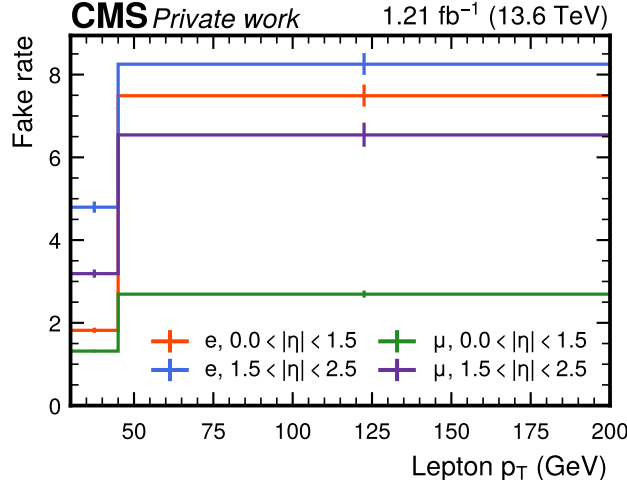


Figure 5.7: **QCD fake rate.** The fake rate for the QCD background estimated in the 1 jet bin, separately for electrons and muons as, a function of lepton p_T and $|\eta|$. The error bars designate statistical uncertainties only.

1471 CR (but not necessarily the normalization) is correctly predicted by MC:

$$f_{\text{sig}} := \frac{N_{\text{CR}}^{\text{t}\bar{t}}}{N_{\text{SR}}^{\text{t}\bar{t}}} = \frac{N_{\text{CR}}^{\text{t}\bar{t}, \text{MC}}}{N_{\text{SR}}^{\text{t}\bar{t}, \text{MC}}} \quad (5.7)$$

1472 Furthermore, one sets similar to Eq. (5.4)

$$N_{\text{SR}}^{\text{QCD}} = N_{\text{CR}}^{\text{QCD}} \times f_{\text{fake}} \quad (5.8)$$

1473 where f_{fake} is still given by Eq. (5.3), which is unaffected since the $t\bar{t}$ signal contam-
1474 ination in the 1-jet CR is negligible.

1475 Combining all these equations, one can first replace $N_{\text{CR}}^{\text{t}\bar{t}}$ in Eq. (5.6) by $f_{\text{sig}} N_{\text{SR}}^{\text{t}\bar{t}}$
1476 according to Eq. (5.7), then eliminate $N_{\text{SR}}^{\text{t}\bar{t}}$ in favour of $N_{\text{SR}}^{\text{data}}$, i.e. the total data
1477 yield in the SR, and get

$$N_{\text{SR}}^{\text{QCD}} = f_{\text{fake}} \left(N_{\text{CR}}^{\text{data}} - N_{\text{CR}}^{\text{MC,BG}} - f_{\text{sig}} \left(N_{\text{SR}}^{\text{data}} - N_{\text{SR}}^{\text{MC,BG}} - N_{\text{SR}}^{\text{QCD}} \right) \right). \quad (5.9)$$

1478 Solving this equation for $N_{\text{SR}}^{\text{QCD}}$ finally yields the corrected QCD contribution in
1479 the SR:

$$N_{\text{SR}}^{\text{QCD}} = \left(N_{\text{CR}}^{\text{data}} - N_{\text{CR}}^{\text{MC,BG}} - f_{\text{sig}} (N_{\text{SR}}^{\text{data}} - N_{\text{SR}}^{\text{MC,BG}}) \right) \times \frac{f_{\text{fake}}}{1 - f_{\text{sig}} f_{\text{fake}}} \quad (5.10)$$

1480 The resulting QCD distributions from this method are further treated in the same
1481 way as the MC backgrounds, and can be seen together with them in Figs. 5.8 to 5.10.

1482 **Z+jets background** In contrast to the QCD background, the Z+jets background,
1483 which is relevant mostly in the ee and $\mu\mu$ channels, is in most respects well-described
1484 by MC simulation. However, in the phase space used in the analysis, there can be
1485 problems related to the requirement of at least one reconstructed b jet. In Z+jets
1486 events, b quarks can in principle be produced as real emissions through higher-
1487 order corrections in QCD. However, in the LO simulation used here this is done by
1488 the parton shower, which might lead to poor modeling of the b quark properties
1489 compared to data. This in turn could influence the acceptance of Z+jets events,
1490 leading to an incorrect normalization in events with one or more b tags.

1491 Here, a data-driven normalization is derived for Z+jets events with one or two b
1492 tags in the dilepton channels, following the method of Ref. [41]. This is important
1493 especially in the same-flavor channels, where Z+jets is a dominant background.

1494 The normalization is derived using a CR in which the cut on $m_{\ell\ell}$ is inverted, i.e.
1495 in events with $|m_{\ell\ell} - m_Z| < 15$ GeV (“inside the Z window”), which are strongly
1496 enriched in Z+jets contributions. It is assumed that the Z+jets contribution in the
1497 $e\mu$ channel (which stems mostly from $Z \rightarrow \tau\tau$ events) is negligible compared to the
1498 ee and $\mu\mu$ channels, and that all other backgrounds (including $t\bar{t}$) are approximately
1499 equal in the three dilepton channels up to combinatorics, in the sense that their
1500 differences are small compared to the Z+jets event yield. Then, said Z+jets yield
1501 in the Z window in the same-flavor channels can be estimated directly from data by
1502 subtracting the $e\mu$ channel – and with it, the other backgrounds – from the ee and
1503 $\mu\mu$ channels. This results in

$$N_{ee/\mu\mu}^{Z+jets} = N_{ee/\mu\mu, in}^{\text{data}} - \frac{1}{2} N_{e\mu, in}^{\text{data}} k_{ee/\mu\mu, in} \quad (5.11)$$

1504 where $N_{\ell\ell, in}^{\text{data}}$ refers to the number of observed events inside the Z window for the
1505 respective channel, and $k_{ee} = k_{\mu\mu}^{-1} = \sqrt{N_{ee, in}^{\text{data}}/N_{\mu\mu, in}^{\text{data}}}$ is a efficiency factor to correct
1506 for the different acceptance of electrons and muons.

1507 To translate this yield from the CR to the SR, the ratio $R_{in/out} = N_{in}^{Z+jets}/N_{out}^{Z+jets}$
1508 (referring to *inside* and *outside* of the Z window) of event numbers between those
1509 two regions has to be estimated. This could in principle be done by directly using
1510 the MC simulation (as done in e.g. Refs. [17, 133]). However, since this ratio
1511 might by itself be mismodeled in MC, a more cautious approach is taken here. A
1512 second CR is defined from events with 0 b tags (which are not considered in the
1513 main measurement in the same-flavor channels) and used to construct to construct
1514 a more loose assumption:

| ee | ep | $\mu\mu$ |
|-----------------|-----------------|-----------------|
| 1.36 ± 0.04 | 1.32 ± 0.03 | 1.28 ± 0.03 |

Table 5.2: **Z+jets scale factors.** Ratio of the Z+jets event yields estimated in data using the method described in Sec. 5.3.2 to the prediction by the MC simulation. Uncertainties are statistical only.

$$\frac{R_{\text{in/out}}^{\text{data}}(\geq 1 \text{ b tag})}{R_{\text{in/out}}^{\text{MC}}(\geq 1 \text{ b tag})} = \frac{R_{\text{in/out}}^{\text{data}}(0 \text{ b tags})}{R_{\text{in/out}}^{\text{MC}}(0 \text{ b tags})} \quad (5.12)$$

1515 This equation means that the *ratio of ratios* $R_{\text{in/out}}(\geq 1 \text{ b tag})/R_{\text{in/out}}(0 \text{ b tags})$
 1516 is assumed to be well described by MC. It can be solved for the Z+jets yield outside
 1517 of the Z window in the same-flavor channels, yielding

$$\begin{aligned} N_{\text{out}}^{\text{Z+jets}} &= \frac{N_{\text{in}}^{\text{Z+jets}}}{R_{\text{in/out}}^{\text{data}}(\geq 1 \text{ b tag})} \\ &= \frac{R_{\text{in/out}}^{\text{MC}}(0 \text{ b tags})}{R_{\text{in/out}}^{\text{data}}(0 \text{ b tags})} \frac{N_{\text{in}}^{\text{Z+jets}}}{R_{\text{in/out}}^{\text{MC}}(\geq 1 \text{ b tag})} \end{aligned} \quad (5.13)$$

1518 where $N_{\text{in}}^{\text{Z+jets}}$ is given by Eq. (5.11). In practice, this yield is quoted as a scale factor
 1519 compared to the nominal MC prediction. For the ep channel (in which Z+jets is
 1520 much less important), the scale factor is simply assumed to be the geometric mean
 1521 of the ee and $\mu\mu$ scale factors.

1522 The final scale factors can be seen in Tab. 5.2.

1523 5.4 Control distributions

1524 The agreement between simulation and data in several control distributions is pre-
 1525 sented in Figs. 5.8 to 5.10. All corrections described in the previous section are
 1526 applied in these figures. In addition, they are scaled by the b tagging efficiency scale
 1527 factors obtained in the final likelihood fit (Sec. 5.6) to better reflect the estimates
 1528 for essential calibrations.

1529 Good agreement between data and simulation within the full uncertainties is seen
 1530 in all distributions.

5 Measurement of the inclusive $t\bar{t}$ cross section at $\sqrt{s} = 13.6$ TeV

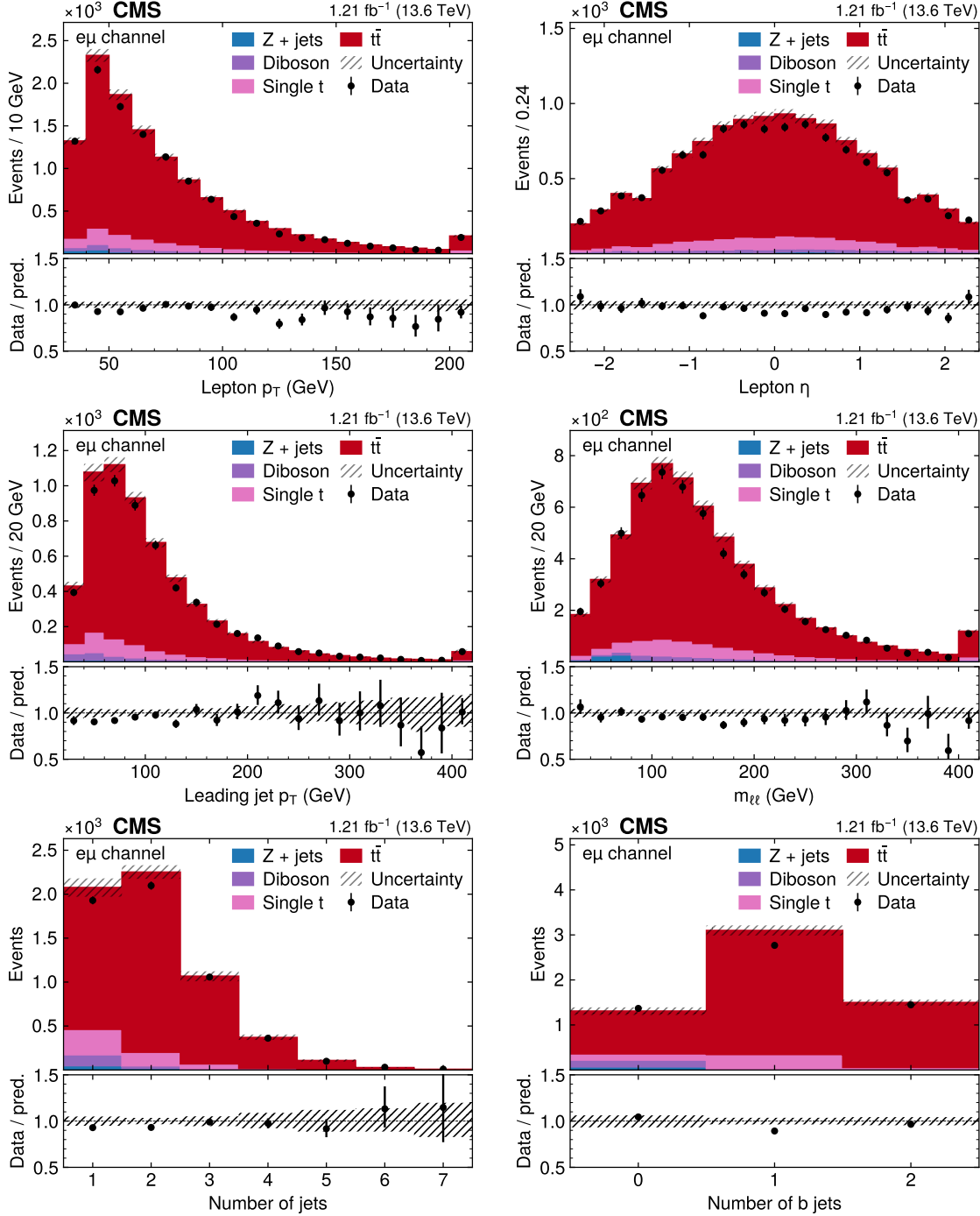


Figure 5.8: Control distributions in the $e\mu$ channel. Shown are (from top left to bottom right) the distributions of p_T of both leptons, $|\eta|$ of both leptons, p_T of the leading jet, the invariant lepton mass $m_{\ell\ell}$, the number of jets and the number of b jets. All figures show both data (black dots) and different simulated background processes (colored bars). For the latter, all corrections described in Sec. 5.3 as well as post-fit b tagging scale factors (Sec. 5.6) are applied, and the shaded area covers both statistical and systematic uncertainties. *Figure taken from Ref. [5].*

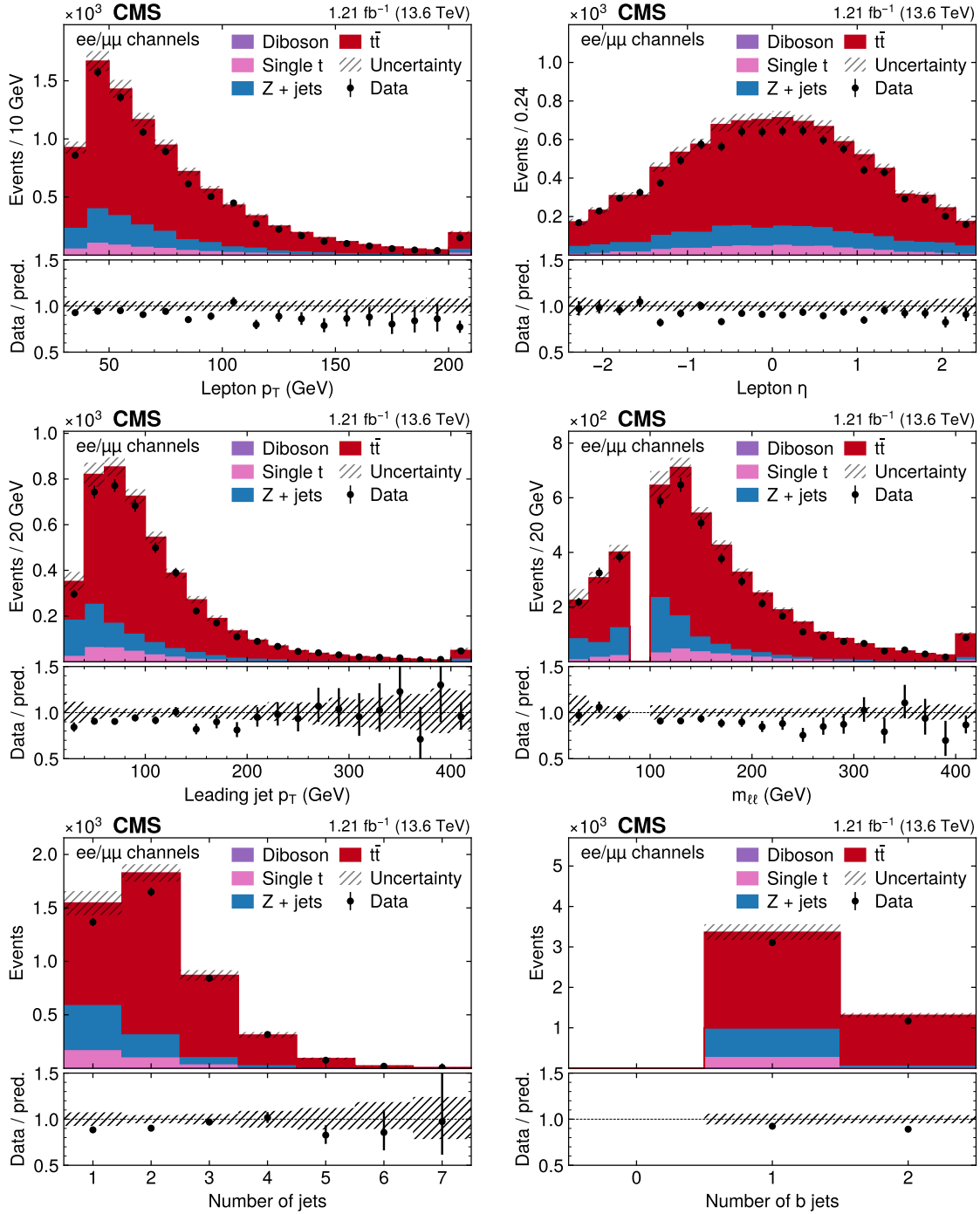


Figure 5.9: **Control distributions in the ee and $\mu\mu$ channels.** The distributions are shown in the same manner as in Fig. 5.8. *Figure taken from Ref. [5].*

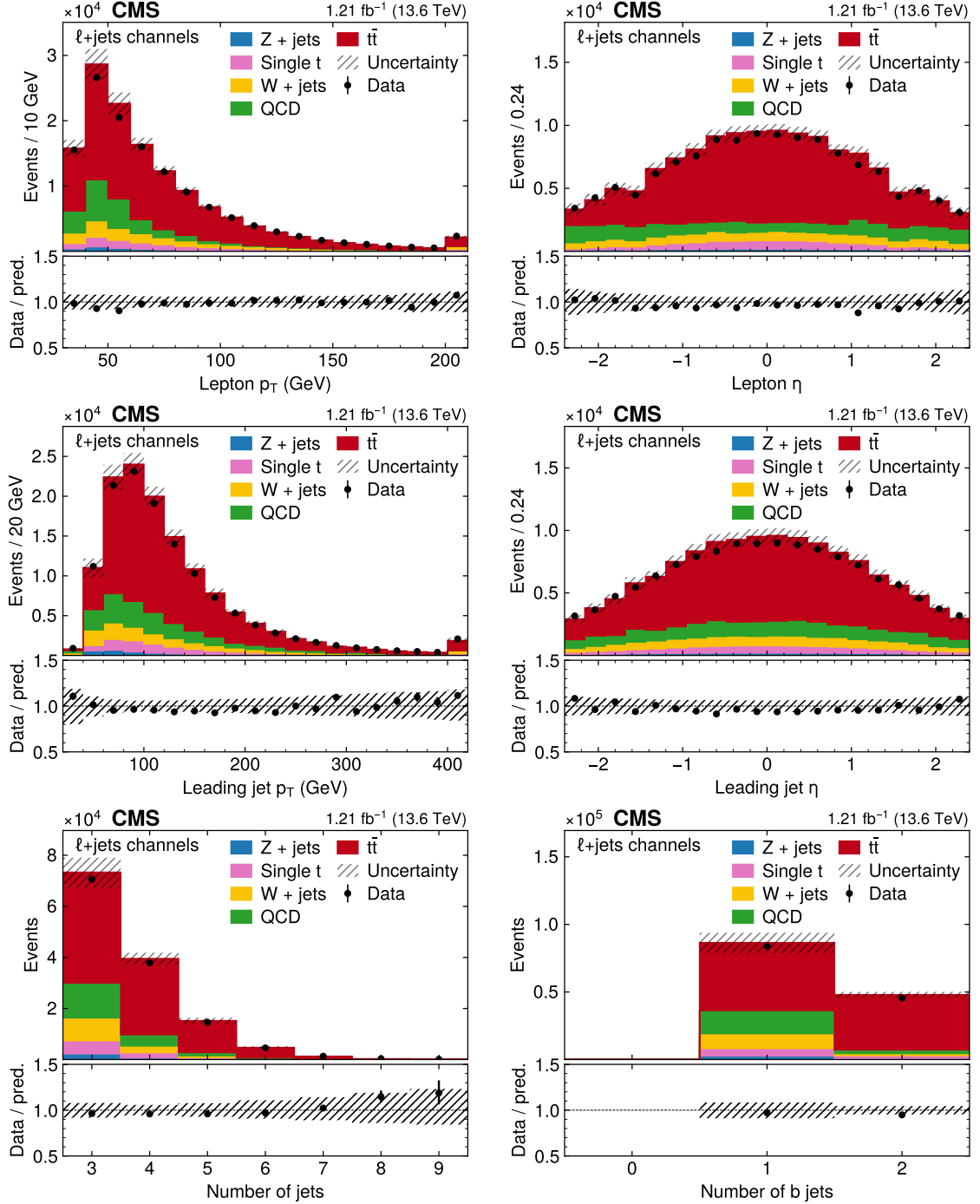


Figure 5.10: **Control distributions in the $\ell + \text{jets}$ channels.** The distributions are shown in the same manner as in Fig. 5.8, except for the center-right figure, which here shows $|\eta|$ of the leading jet. *Figure taken from Ref. [5].*

1531 5.5 Systematic uncertainties

1532 In order to translate the distribution of observed and expected events into a result
1533 for the inclusive $t\bar{t}$ cross section while taking into account all relevant sources of
1534 systematic uncertainties, a binned profile maximum likelihood fit as described in
1535 Sec. 4.4 is performed using the tool `combine` [119]. The parameter of interest (POI)
1536 used for this fit is the signal strength $r = \sigma_{t\bar{t}}/\sigma_{t\bar{t}}^{\text{pred}}$, i.e. the inclusive $t\bar{t}$ cross section
1537 normalized to its theoretical prediction. A linear signal model is used as defined in
1538 Eq. (4.3), and the $t\bar{t}$ cross section is extracted using its maximum likelihood estimate
1539 and uncertainty.

1540 This section describes the considered systematic uncertainties, which can be di-
1541 vided into experimental uncertainties, arising from incomplete knowledge of the
1542 details of the detector and resulting differences between data and simulation, and
1543 theoretical uncertainties, which concern imperfect modeling of the underlying phys-
1544 ical processes in the different event generators.

1545 All systematic uncertainties are included in the fit as nuisance parameters (NPs) as
1546 discussed in Sec. 4.4. In practice, NPs which encode shape effects on the considered
1547 observables are implemented using *template morphing*, i.e. a smooth polynominal
1548 interpolation between the nominal shape and the shapes encoding the variations
1549 by ± 1 standard deviations. NPs that encode only normalization effects are instead
1550 implemented as simple log-normal uncertainties. Both definitions can be found in
1551 detail in Ref. [119].

1552 Special attention is given in this section to some experimental uncertainties which
1553 are important to this measurement. This includes the luminosity, which is the
1554 dominating uncertainty, as well as the b tagging uncertainties due to the special
1555 way they are treated in the fit.

1556 **Luminosity uncertainty** In order to translate event yields into a result on any
1557 cross section, the total integrated luminosity is required as a calibration constant.
1558 Any experimental error on the luminosity will be directly transferred to the total
1559 error on the measurement, and thus minimizing the luminosity uncertainty is crucial
1560 for any cross section measurement.

1561 For the dataset used in this analysis, the total integrated luminosity was measured
1562 by the CMS Collaboration with an estimated uncertainty of 2.3%. Of this number,
1563 2.1% is due to the calibration of the integrated luminosity, using the methods pre-
1564 sented in Ref. [87].

1565 The agreement in the absolute scale is checked by comparing different indepen-
1566 dently calibrated luminosity measurements, and the integrated luminosity measured
1567 with the hadronic forward (HF) calorimeter and the silicon pixel detector is found to
1568 agree at a level of better than 0.8%. Taking additional contributions due to residual
1569 differences in the time-stability and linearity between the luminosity detectors into
1570 account leads to the full figure of 2.3%. The preliminary estimate of the integrated

luminosity at the time of publication was further cross-checked by using the yield of reconstructed Z bosons decaying into pairs of muons [134], corrected for efficiencies and normalized to the fiducial cross section prediction calculated at NNLO with next-to-NNLL corrections applied, which also showed good agreement.¹

In contrast to all other uncertainties described below, the uncertainty in the integrated luminosity is not directly included in the likelihood fit, but rather treated as an external uncertainty and added in quadrature afterwards, since it is expected to factorize completely from all other uncertainties. The impact of varying the normalization of the backgrounds estimated from simulation by the integrated luminosity uncertainty was found to be negligible.

b tagging uncertainty As mentioned in Sec. 5.3.1, the efficiency for correctly identifying a jet originating from a b quark (b tagging) is expected to be different in data and simulation. At the time of this measurement, directly after the start of Run 3, no general-purpose b tagging studies had been available. Thus, the approach adopted here is to consider the b tagging efficiency in data to be completely unknown and measure it concurrently with the cross section in the likelihood fit.

For this purpose, the probability for an event with n_{jet} selected jets to have n_{btag} correctly identified b jets, depending on the assumed b tagging efficiency ϵ_b , is assumed to be a multinomial of the form

$$P(n_{\text{btag}}|n_{\text{jet}}) \propto \epsilon_b^{n_{\text{btag}}} (1 - \epsilon_b)^{n_{\text{no tag}}} \quad (5.14)$$

Here, $n_{\text{no tag}}$ is the number of true b jets in the event which fall into the acceptance of the selection, but fail to be tagged by DEEPJET. It is estimated from MC simulation.

By taking the ratio of eq. 5.14 in data and simulation, one can derive a per-event weight which corrects the number of b tags in MC:

$$w_b = \frac{(\epsilon_b^{\text{data}})^{n_{\text{btag}}} (1 - \epsilon_b^{\text{data}})^{n_{\text{no tag}}}}{(\epsilon_b^{\text{MC}})^{n_{\text{btag}}} (1 - \epsilon_b^{\text{MC}})^{n_{\text{no tag}}}} = (f_b)^{n_{\text{btag}}} \left(\frac{1 - f_b \epsilon_b^{\text{MC}}}{1 - \epsilon_b^{\text{MC}}} \right)^{n_{\text{no tag}}} \quad (5.15)$$

Here, $f_b = \epsilon_b^{\text{data}} / \epsilon_b^{\text{MC}}$ is the unknown b tagging scale factor. It is left freely floating in the likelihood fit. This is technically implemented by producing shape templates from MC with f_b varied up and down by a fixed value and interpolating inbetween. This shape template can be seen in Fig. 5.11, where it is evident that the categorization in the number of b tags gives significant constraining power for f_b . In the 1b categories, the shape with respect to the number of jets deviates significantly from a flat variation proportional to f_b as naively expected. This is because of out-of-acceptance jets, corresponding to the second factor in Eq. (5.15).

¹Since publication of this result, a more precise luminosity measurement for 2022 data has become available in Ref. [135].

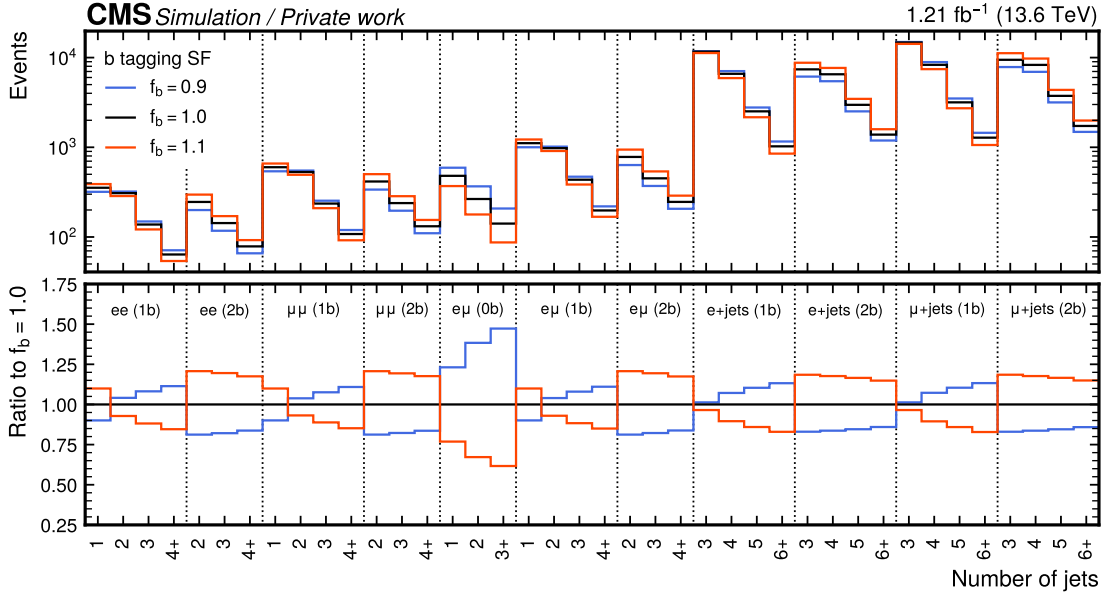


Figure 5.11: **b tagging scale factor variation.** The effect of varying the b tagging scale factor f_b in $t\bar{t}$ MC by an arbitrary value of ± 0.1 , shown for the number of jets in the 11 fit categories.

1603 Note that, since f_b is taken to be a single number, this method only corrects the
 1604 overall b jet efficiency and does not consider any dependence of ϵ_b on jet kinematics.
 1605 Because this measurement uses the same jet quality requirements (particularly the
 1606 same p_T cuts) in all channels, and assuming the b jet p_T and η spectra in the different
 1607 channels are roughly similar, any kinematic dependence is effectively integrated
 1608 out in the overall efficiency scale factor f_b . The fact that the spectrum itself is
 1609 not corrected is not considered an issue here since the likelihood fit does not use
 1610 kinematic information directly.

1611 **Lepton identification uncertainty** The uncertainty assumed on the lepton iden-
 1612 tification scale factors comes from two different sources: First, an inherent un-
 1613 certainty originating in the tag-and-probe method (as described in Sec. 5.3.1) is con-
 1614 sidered. It consists of statistical uncertainties from both data and simulation, a
 1615 systematic uncertainty derived from a comparison with a different Z+jets simu-
 1616 lation sample produced at NLO in QCD, and another systematic uncertainty due
 1617 to the choice of fitting function. Together, they make up for an uncertainty of
 1618 $\sim 0.8\%$ (0.5%) on the electron (muon) scale factors in the bulk of the phase space,
 1619 and can rise up towards $\sim 5\%$ for high lepton p_T .

1620 Secondly, it is taken into account that the scale factor between data and simula-
 1621 tion might be slightly different in the Z+jets selection used for the T&P method and

the $t\bar{t}$ selection used for the measurement of the cross section. The most important reason for this is the requirement of (b tagged) jets in almost all considered categories, as well as the requirement for at least three jets in the lepton+jets channels. This effect has been studied at CMS in the past and the difference found to be less than 0.5% for muons and 1.0% for electrons. Taking a conservative approach, these values are used as an additional component in the respective uncertainties.

In the first, preliminary version of this measurement [121], the dedicated lepton efficiency scale factors as measured with the T&P method were not yet available, and a different approach was taken. Similar to the b tagging efficiency, the lepton efficiency scale factors were kept freely floating the likelihood fit. Due to the different dependency on the lepton efficiencies in the different lepton flavor channels, the fit was able to constrain the efficiencies to a precision of 2% [5]. The resulting scale factors were later found to be in good agreement with those obtained from the T&P method, serving as a valuable cross-check. However, this method ultimately led to less precision and was thus not used in the final result.

Pileup uncertainty As described in Sec. 5.3.1, three different pileup-related variables are employed to reweight the simulation to the observed data, and the average of the three weights is used as the nominal value. This method is repeated using only one of the variables - the number of good reconstructed vertices n_{PV} - and the difference in expected yields treated as an uncertainty. This procedure was compared to the usual estimation of pileup-related uncertainties in CMS. There, the theoretical expectation for the number of interactions is derived as a function of total inelastic proton-proton cross section, and the latter is than varied by its experimental unceratinty. It was found that the heuristic method used here leads to larger uncertainties, and can thus be considered more conservative.

Jet energy uncertainties Uncertainties in the jet energy calibration are split into 26 different sources concerning different experimental and theoretical effects, following the standard CMS procedure outlined in Ref. [130]. 17 of these sources are found to be non-negligible and included in the fit. These sources include, among others, uncertainties due to jet p_T resolution and jet flavour composition, statistical uncertainties in the derivations of the energy corrections, and residual differences between data and simulation.

Trigger uncertainties Since the trigger scale factors are derived using the tag-and-probe method in the same way as the lepton scale factors, similar uncertainties are applied, including the extrapolation uncertainties of 0.5% for muons and 1.0% for electrons. The only difference is that in the dilepton channels the uncertainties need to be propagated according to Eq. (5.2). This has the effect of greatly reducing the impact of the trigger uncertainties in those channels compared to the lepton ID

1660 uncertainties, since the nominal per-event trigger efficiency is already very close to
1661 one.

1662 **Matrix element scale uncertainties** The theoretical predictions of both sig-
1663 nal and background are calculated using matrix elements at either LO or NLO in
1664 perturbative QCD, matched to a parton shower. Since this effectively means trun-
1665 cating the perturbative expansion of the scattering amplitude at a given power in
1666 the strong and electroweak coupling constants, the effect of higher-order terms is
1667 neglected in the calculation.

1668 At the same time, the necessity of renormalization of divergent diagrams and
1669 factorization of non-perturbative contributions introduces non-physical parameters
1670 into the prediction in the form of the renormalization and factorization scales μ_R
1671 and μ_F (cf. Sec. 3.1). These parameters are usually set to typical energy scales of
1672 the considered process, and might also depend on the event kinematics (dynamic
1673 scales).

1674 To estimate possible errors due to these missing terms as well as due to the choice
1675 of scales, the scales μ_R and μ_F are varied separately by a factor of 2 up and down, and
1676 the resulting change in simulation is taken as an uncertainty in the form of shape
1677 templates [136]. In order to not double-count uncertainties in the cross section
1678 prediction for the backgrounds (see below), but keep possible rate variations due to
1679 acceptance effects, the templates are normalized to the nominal cross section values
1680 before any selection cuts are applied. Different physical processes are considered to
1681 be uncorrelated since they are produced with different generators and at different
1682 orders.

1683 **PDF uncertainties** The parton distribution functions (PDFs) used to evaluate
1684 the non-perturbative contribution of the proton-proton collision have systematic
1685 uncertainties attached. They are estimated by independently reweighting the sim-
1686 ulation to 100 different replicas of the used NNPDF 3.1 PDF set and taking the
1687 envelope of the resulting changes, following the recommendations of the PDF4LHC
1688 working group [137]. Additionally, the effect of the choice of the strong coupling con-
1689 stant in the PDF is assessed using a similar reweighting, and attached as a separate
1690 nuisance parameter. Analogously to the matrix element uncertainties, the resulting
1691 variations are normalized before any selection cuts to keep acceptance and shape
1692 effects while not double-counting cross section changes.

1693 **Parton shower uncertainties** The parton shower model used for the predictions
1694 is only accurate (at most) at leading-log (LL) as well as leading color (LC) in QCD
1695 (cf. Sec. 3.2) and thus requires appropriate uncertainties. For this purpose, the
1696 scales at which the strong coupling constant is evaluated are varied up and down by

¹⁶⁹⁷ a factor 2 separately for initial and final state radiation and for different processes,
¹⁶⁹⁸ and the resulting changes propagated to the fit as shape templates.

¹⁶⁹⁹ **ME/PS matching uncertainty** For the simulation of the $t\bar{t}$ signal, an additional
¹⁷⁰⁰ uncertainty concerning the matching between matrix element simulation in POWHEG
¹⁷⁰¹ and parton showering in PYTHIA is considered. This is done by varying the h_{damp}
¹⁷⁰² parameter in POWHEG controlling the amount of radiation generated at matrix
¹⁷⁰³ element level, following Ref. [138].

¹⁷⁰⁴ **Background cross section uncertainties** For the cross sections of the different
¹⁷⁰⁵ processes, log-normal rate uncertainties are assigned based on the process and order
¹⁷⁰⁶ at which it was calculated. A 15% uncertainty is used for the single- t background
¹⁷⁰⁷ since it is generated fully at NLO with a NNLO prediction for the cross section,
¹⁷⁰⁸ while for W+jets and Diboson, 30% is used since these samples are only generated
¹⁷⁰⁹ at LO. For Z+jets, this is reduced to 20% due to the data-driven estimation of the
¹⁷¹⁰ normalization. Additionally, for the fully data-driven QCD background, two sepa-
¹⁷¹¹ rate nuisance parameters for the e+jets and μ +jets channels are defined, covering a
¹⁷¹² conservative uncertainty of 30% each.

¹⁷¹³ **Background statistical uncertainties** Finally, since the background in this
¹⁷¹⁴ measurement is estimated either using MC simulation or data-driven methods, an
¹⁷¹⁵ independent statistical uncertainty needs to be attached to each bin, reflecting the
¹⁷¹⁶ finite number of events it contains. This is done using the so-called *Barlow–Beeston*
¹⁷¹⁷ *light* method [139]. For MC backgrounds, these uncertainties are minuscule. How-
¹⁷¹⁸ ever, for the data-driven QCD background, they also contain the propagated statis-
¹⁷¹⁹ tical uncertainty due to the limited number of data events in the CRs, which is in
¹⁷²⁰ general non-negligible.

¹⁷²¹ 5.6 Fit results

¹⁷²² Performing the fit yields a $t\bar{t}$ signal strength of $r = 0.958 \pm 0.025$, where the un-
¹⁷²³ certainty includes statistical and all systematic contributions, except for the 2.1%
¹⁷²⁴ uncertainty on the luminosity. This corresponds to an inclusive $t\bar{t}$ cross section of

$$\sigma_{t\bar{t}} = 882 \pm 23 \text{ (stat+syst)} \pm 20 \text{ (lumi) pb.}$$

¹⁷²⁵ The result is in good agreement with the standard model prediction of $\sigma_{t\bar{t}}^{\text{pred}} =$
¹⁷²⁶ 921^{+29}_{-37} pb.

¹⁷²⁷ Fig. 5.12 shows the agreement between data and simulation before and after the
¹⁷²⁸ fit. It can be immediately seen that the fit greatly reduces the uncertainty on the

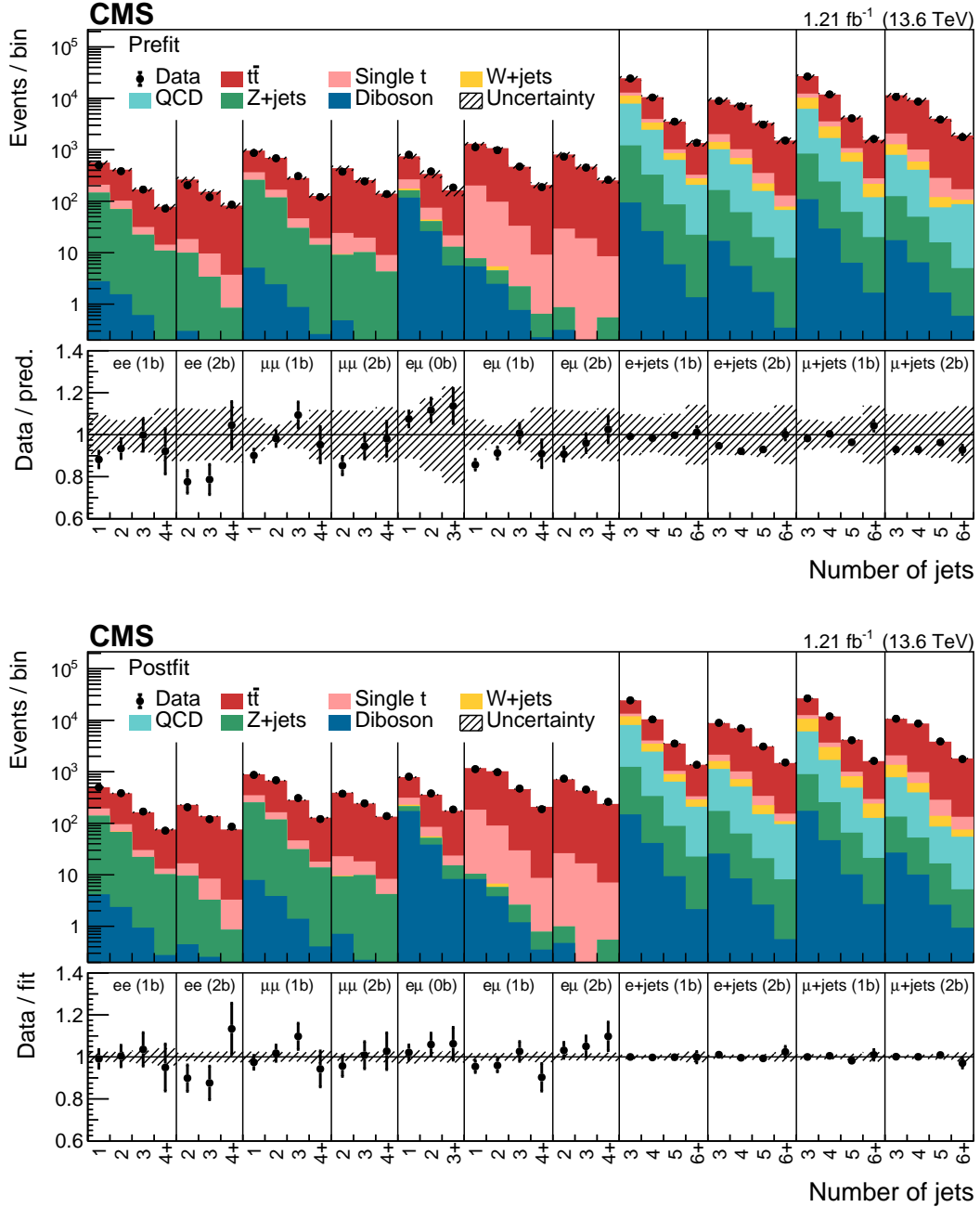


Figure 5.12: Comparison of data and simulation before and after the fit.

The distribution of the number of jets in the different fit categories is shown for data and simulation before (top) and after the likelihood fit (bottom). The fit greatly improves the agreement and strongly constrains the background uncertainties. *Figure taken from Ref. [5].*

1729 prediction by constraining systematic uncertainties and simultaneously improves the
1730 agreement compared to the data.

1731 Of particular note here is the free-floating b tagging efficiency (compare sec. 5.5),
1732 whose effect can be directly read off from the categorization in the number of b jets:
1733 Before the fit (Fig. 5.12 top), the event yield for two or more b jets is overestimated in
1734 the simulation, while the yield for zero b jets is underestimated. This suggests that
1735 the b tagging efficiency is slightly lower in the data than assumed in the simulation.
1736 Indeed, the fit confirms this: the b tagging scale factor between data and simulation
1737 in the phase space of this measurement is measured to be $f_b = 0.980 \pm 0.009$. As a
1738 result, after the fit (Fig. 5.12 bottom), the event yields agree in all b jet categories.

1739 5.6.1 Statistical checks

1740 To better understand the sources of systematic uncertainty, as well as the contribu-
1741 tions of the different measurement channels, the fit is repeated twice, restricted
1742 to either the dilepton or the $\ell + \text{jets}$ channels. For both cases as well as the combi-
1743 nation, the contribution of different groups of nuisance parameters is calculated as
1744 explained in Sec. 4.4. The results can be found in Tab. 5.3, where it can be seen
1745 how the combination of channels helps to reduce the total uncertainty.

1746 Furthermore, the nuisance parameter pulls, constraints and impacts, as defined
1747 in Sec. 4.4, are shown in Fig. 5.13. One can see here especially how the electron
1748 identification scale factors, which are the leading impact, are constrained by the
1749 combination of channels, while the same is not true of the muon identification scale
1750 factors due to their lower pre-fit uncertainty.

1751 5.6.2 Top quark mass dependence

1752 An additional source of uncertainty that has not been considered so far is the choice
1753 of top quark mass in the $t\bar{t}$ MC simulation. It affects the selection efficiency indi-
1754 rectly via the p_T cuts on leptons and jets, with higher top quark mass values leading
1755 to harder spectra and thus to larger efficiencies.

1756 Contrary to other uncertainty sources, the top quark mass is not profiled in the
1757 likelihood fit. Instead, the dependence of the extracted $t\bar{t}$ cross section is explicitly
1758 quantified as a function of the top quark mass by shifting its value in simulation by
1759 ± 3 GeV from its default of $m_t = 172.5$ GeV. The extraction of $\sigma_{t\bar{t}}$ is then repeated
1760 and the dependence on m_t extracted through a simple linear fit. This strategy has
1761 been taken in previous CMS and ATLAS $t\bar{t}$ cross section measurements [140, 141],
1762 and thus facilitates comparison with previous results.

1763 For an upwards shift of $\Delta m_t = 1$ GeV, the $t\bar{t}$ cross section is found to shift down-
1764 wards by 8.5 pb, and vice versa. If one takes the current experimental uncertainty of
1765 0.3 GeV [11] as an allowed range for m_t , this would lead to an additional uncertainty
1766 on $\sigma_{t\bar{t}}$ of 0.3%.

| Source | Full measurement | dilepton only | $\ell+$ jets only |
|-------------------------|------------------|---------------|-------------------|
| Lepton ID efficiencies | 1.6 | 2.4 | 1.0 |
| Trigger efficiency | 0.4 | 0.0 | 0.5 |
| JES | 0.7 | 0.7 | 1.0 |
| b tagging efficiency | 1.0 | 0.4 | 1.8 |
| Pileup reweighting | 0.5 | 0.0 | 1.0 |
| ME scale, $t\bar{t}$ | 0.5 | 0.4 | 0.6 |
| ME scale, backgrounds | 0.1 | 0.1 | 0.3 |
| ME/PS matching | 0.2 | 0.2 | 0.4 |
| PS scales | 0.4 | 0.9 | 0.6 |
| PDF and α_S | 0.3 | 0.4 | 0.4 |
| Single t background | 1.1 | 1.2 | 0.8 |
| Z+jets background | 0.3 | 0.1 | 0.0 |
| W+jets background | 0.0 | 0.0 | 0.1 |
| Diboson background | 0.4 | 0.4 | 0.0 |
| QCD multijet background | 0.3 | 0.0 | 0.5 |
| Statistical uncertainty | 0.5 | 1.2 | 0.5 |
| Combined uncertainty | 2.6 | 3.3 | 3.0 |
| Integrated luminosity | 2.3 | 2.3 | 2.3 |

Table 5.3: **Sources of systematic uncertainty.** The relative per-cent contribution of different groups of sources of systematic uncertainty for the full measurement as well as for restrictions to the dilepton and $\ell+$ jets channels only. They are calculated according to Sec. 4.4 and do not take correlations between the different groups into account.

1767 5.7 Summary and Outlook

1768 In this chapter, the inclusive $t\bar{t}$ cross section is measured for the first time at a center-
 1769 of-mass energy of $\sqrt{s} = 13.6$ TeV. Data corresponding to an integrated luminosity of
 1770 1.21 fb^{-1} from the beginning of LHC Run 3 are analyzed. Despite this comparatively
 1771 small amount of data, a total precision of ca. 3% with respect to the inclusive cross
 1772 section is achieved.

1773 Fig. 5.14 compares the result of this chapter to other inclusive $t\bar{t}$ cross section
 1774 measurements performed by CMS at other center-of-mass energies [140, 142–148],
 1775 as well as to the SM prediction [149]. The precision is comparable to other measure-
 1776 ments at $\sqrt{s} = 7, 8$, and 13 TeV, some of them with significantly higher integrated
 1777 luminosities. All results are in agreement with the SM.

1778 This measurement was designed specifically for the earliest data of Run 3, in

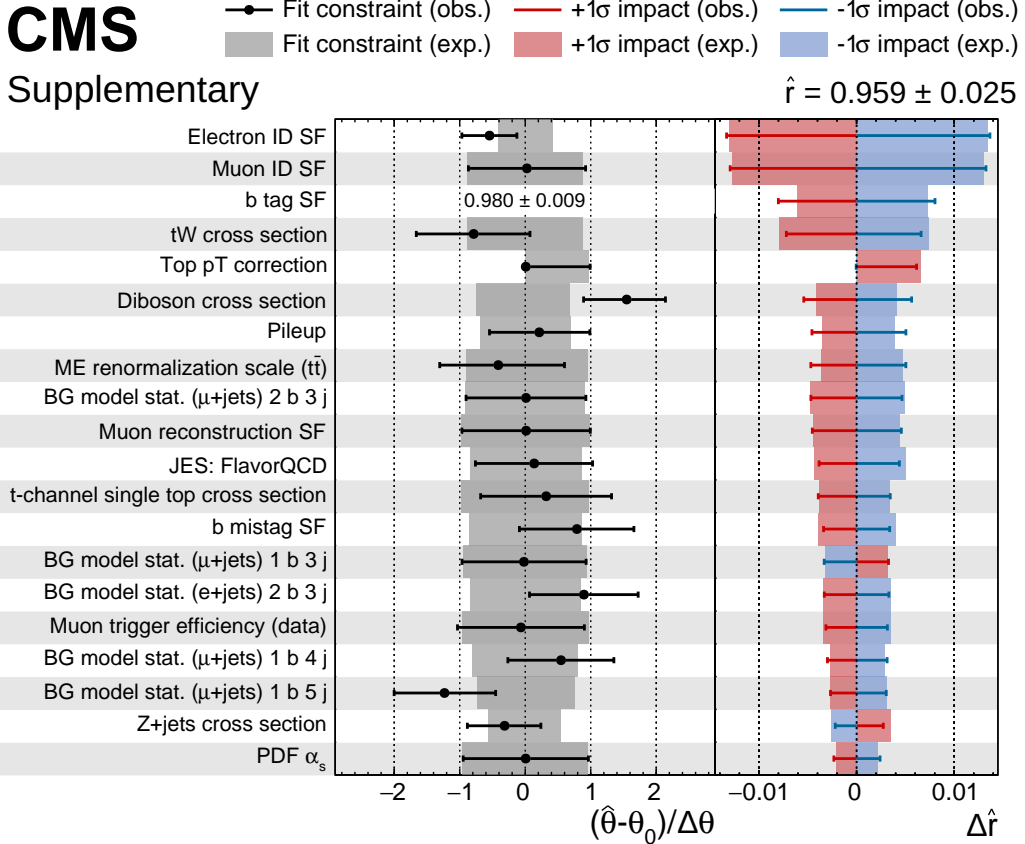


Figure 5.13: **Nuisance parameter pulls, constraints and impacts.** The expected and observed values are shown as shaded bands and error bars, respectively. Nuisance parameters are sorted by their observed impact on the signal strength r . For the b tagging scale factor, for which no pre-fit uncertainty is defined, the post-fit uncertainty is shown instead of the pull. *Figure taken from the supplementary material of Ref. [5].*

order to achieve high precision without relying on a full suite of calibrations being available. In particular, b tagging and lepton efficiencies can be constrained in situ using the combination of dilepton and $\ell+jets$ channels as well as the categorization by number of b-tagged jets. No large inconsistencies for any of the considered physics objects were found. The measurement was made public in September of 2022 just two months after the start of Run 3 and constituted the first public physics result of LHC Run 3. At the time, it provided a valuable first proof that CMS data taken in Run 3 were of high quality and ready for physics.

The next step for this result would be to transfer the technique developed in this work to well-understood data and high integrated luminosities in order to achieve the highest precision possible for $\sigma_{t\bar{t}}$. Such a measurement will certainly be domi-

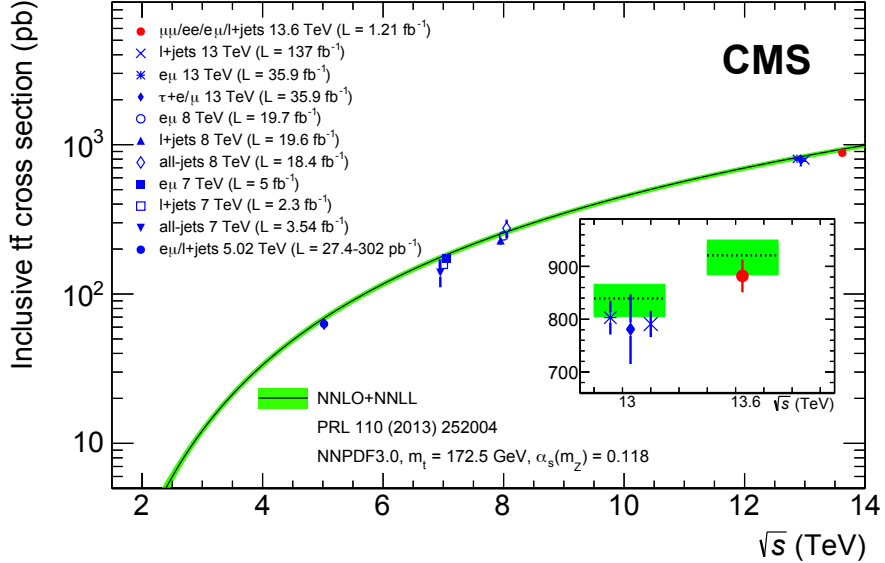


Figure 5.14: **Summary of $\sigma_{t\bar{t}}$ measurements.** An overview of inclusive $t\bar{t}$ cross section measurements at CMS at different center-of-mass energies [140, 142–148] as well as comparison to the SM prediction [149]. This measurement is displayed as the red dot. *Figure taken from Ref. [5].*

nated by systematic uncertainties, most importantly the luminosity and the lepton identification efficiencies (as already partly the case here). The channel combination method developed here could potentially help reduce the latter of these through an in situ constraint, while the former is orthogonal to the analysis strategy and its reduction requires more precise luminosity measurements. It will likely also be necessary to study the different sources of uncertainty in more detail, and investigate whether some of them can be reduced through more careful calibrations.

Additionally, one could try to use such a high-precision $t\bar{t}$ cross section measurement to indirectly measure the top quark mass, one of the fundamental parameters of the Standard Model, by comparing the measured value to SM predictions for different top quark masses. For this purpose, it would be important to reduce the dependence on the top quark mass in simulation (c.f. Sec. 5.6.2), for example by reducing the p_T requirements on leptons and jets as much as experimentally feasible. All of this leaves multiple parts for future studies to tread, which will be exciting to follow in the coming years as larger parts of the Run 3 dataset are analyzed at CMS.

1806 **6 Simulation of on- and off-shell $t\bar{t}$**
1807 **production with `bb41`**

1808 **6.1 Introduction**

1809 The accurate modeling of top quark production processes at the LHC is of crucial
1810 importance for precision measurement of top quark properties. In particular, the
1811 fact the top quark is an unstable colored resonance with a short lifetime presents
1812 challenges for correctly modeling its mass lineshape as used for top mass and width
1813 measurements [150–152]. Typically, the modeling is done with full NLO MC sim-
1814 ulations matched to a parton shower (NLO+PS), and multiple such generators are
1815 available with different features and degrees of accuracy.

1816 In this chapter, the predictions of some of these generators from the POWHEG
1817 framework [72, 73] are compared to each other, as well as to unfolded data mea-
1818 sured in Ref. [153], for different variables relevant to top mass and/or width mea-
1819 surements. A particular focus is the generator `bb41` [7], which specifically improves
1820 the treatment of the unstable top resonance and of the interference between $t\bar{t}$ and
1821 tW , and is described in detail in Sec. 6.2. In this work, `bb41` is implemented and
1822 validated for the first time in the CMS simulation setup. The comparison is done
1823 at the generator level, i.e. including parton showering and hadronization but not
1824 detector simulation and experimental reconstruction.

1825 The results of this work have been published in a CMS public note as Ref. [6].
1826 Since the publication of this note, a new version of `bb41` has been made avail-
1827 able [154], leading to small differences as discussed below. In this thesis, updated
1828 results including both versions will be shown.

1829 **6.2 The Monte Carlo generator `bb41`**

1830 `bb41` [7, 154] is a full NLO+PS MC generator for the process $pp \rightarrow b\bar{b}\ell^+\ell^-\nu_\ell\bar{\nu}_\ell$,
1831 including all off-shell contributions. This includes the dilepton decay channel of
1832 both $t\bar{t}$ and tW production, as well as non-resonant contributions involving Z or
1833 Higgs bosons, as shown in Fig. 6.1. Since these processes all lead to the same
1834 final state at NLO in QCD, they interfere with each other and can not be easily
1835 separated. `bb41` includes this interference by construction since it computes the full
1836 amplitude including all diagrams at once.

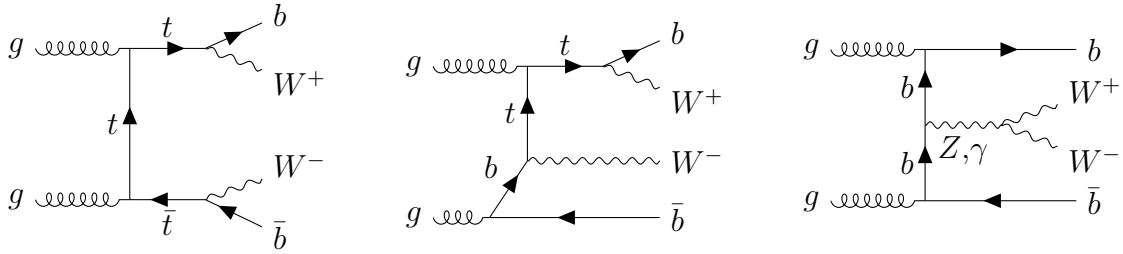


Figure 6.1: **Feynman diagrams for bb41.** Examples of Feynman diagrams for the $pp \rightarrow b\bar{b}W^+W^-$ process as described by bb41, including double-resonant (left), single-resonant (center) and non-resonant contributions (right). The decay of the W bosons into leptons is not shown for brevity.

1837 In addition, by considering the full amplitude instead of splitting it into production
 1838 and decay parts, bb41 fully treats the top quark as an unstable resonance without
 1839 approximations. It is implemented in the “resonance-aware” version of POWHEG,
 1840 called POWHEG vRES [155], which includes hard QCD radiation also for unstable
 1841 resonances - such as top quarks - in addition to the initial state radiation always
 1842 provided by POWHEG. As a result, an event generated by bb41 can have up to
 1843 three hard emissions at matrix element level. The correct description of these FSR
 1844 emissions is relevant e.g. for observables related to the mass of the top quark, and
 1845 can be challenging for parton showers, leading to large uncertainties.

1846 This work investigates two different versions of bb41. The first version is the one
 1847 originally published in Ref. [7] and publically available on the POWHEG website [156].
 1848 In the following, it will be referred to as bb41 v1.

1849 The second version of bb41 was recently published in Ref. [154]. Its most promi-
 1850 nent feature compared to the previous version is the addition of the lepton+jets
 1851 decay channel of $t\bar{t}$, i.e. the $b\bar{b}\ell\nu_{\ell}q\bar{q}'$ final state. In addition, it includes several
 1852 improvements to the dilepton final state, such as avoidance of spurious finite width
 1853 effects and improved resonance history projectors (see Ref. [154] for details). At the
 1854 time of writing this thesis, the new code is not publically available. A preview ver-
 1855 sion was made available to the CMS collaboration by the authors, and the dilepton
 1856 final state of this version - referred to as bb41 v2 - is shown in this work. The lep-
 1857 ton+jets final state, on the other hand, was not ready for validation in the preview
 1858 version, and so could not be included.

1859 6.3 Other $t\bar{t}$ Monte Carlo generators

1860 The distributions predicted by bb41 are compared to three other MC generators
 1861 for the $t\bar{t}/tW$ final state, which are briefly presented in this section. All of these
 1862 are implemented in POWHEG v2, and as such do not contain explicit treatment of

1863 radiation in unstable resonances.

1864 6.3.1 **hvq**

1865 **hvq** [75], standing for *heavy quark*, is the standard code used, at the time of writing, by both the ATLAS and CMS collaborations for producing $t\bar{t}$ MC events. It 1866 applies the narrow-width approximation (NWA) to generate stable $t\bar{t}$ pairs at NLO 1867 in QCD, with up to one additional ISR emission. The top quarks are then randomly 1868 smeared according to the top quark width, giving an approximate treatment 1869 of finite-width effects. Following this, the top quarks are decayed - in this case, in 1870 the dilepton channel for all lepton flavors - using internal POWHEG routines [157]. 1871 These routines work at tree level with NLO matrix element corrections and preserve 1872 spin correlations. Further ISR emissions as well as all FSR emissions are handled 1873 by the matching to the parton shower. 1874

1875 6.3.2 **ST_wtch**

1876 Since **hvq** generates only the double-resonant $t\bar{t}$ amplitude, a second generator has to 1877 be used alongside it for the single-resonant tW and $t\bar{t}/tW$ interference contributions. 1878 Here, **ST_wtch** [158] is used for this purpose. It works very similar to **hvq**, also 1879 generating a stable tW pair in the NWA, smearing with the top width and decaying 1880 the particles using the same routines.

1881 However, in order to at least approximately recover the full $b\bar{b}W^+W^-$ amplitude, 1882 it is necessary to select a scheme for the treatment of the $t\bar{t}/tW$ interference to 1883 prevent double-counting. Since the separation between $t\bar{t}$ and tW is not well defined 1884 at NLO, such schemes will to some degree always be ad-hoc and ambiguous. Two 1885 such schemes are implemented for **ST_wtch**, and both are compared in this work: 1886 in the first, called diagram removal (DR), all terms involving the square of double- 1887 resonant diagrams are simply removed from the squared amplitude. This is the 1888 most intuitive choice, but has the disadvantage of not being gauge invariant [159]. 1889 The second method, diagram subtraction (DS), keeps double-resonant diagrams in 1890 the squared amplitude, and subtracts a gauge invariant counter-term to remove the 1891 double counting [158–160]. For both schemes, the prediction of **ST_wtch** is added 1892 to the one of **hvq** (together called $t\bar{t} + tW$) to produce distributions that can be 1893 compared to **bb41**.

1894 6.3.3 **ttb_NLO_dec**

1895 The generator **ttb_NLO_dec** [161], similar to **hvq**, works in the NWA and thus 1896 generates stable $t\bar{t}$ pairs with ad-hoc smearing. However, unlike **hvq**, it is fully 1897 NLO-accurate not only in the production, but also in the decay of the top quarks.

| Parameter | Value |
|---------------------------|------------------|
| POWHEG settings | |
| Top quark mass | 172.5 GeV |
| Top quark width | 1.33 GeV |
| h_{damp} | $1.38 m_t$ [138] |
| PDF set | NNPDF 3.1 [65] |
| PYTHIA settings | |
| PYTHIA version | 8.307 |
| PYTHIA tune | CP5 [81] |
| PowhegHooks settings [77] | |
| POWHEG:veto | on |
| POWHEG:pThard | 0 |
| POWHEG:pTdef | 1 |

Table 6.1: **Generator settings.** An overview of the settings for POWHEG and PYTHIA, as well as the matching between them, for all considered generators.

1898 This means that, like `bb41`, it generates up to one hard FSR emission per decaying
 1899 top quark, leading to up to three hard emissions in the final state.

1900 It also provides an LO-accurate treatment of the $t\bar{t}/tW$ interference by reweighting
 1901 the generated $t\bar{t}$ events to the full off-shell LO amplitude. Thus, like `bb41`, it can
 1902 be used on its own and does not need to be added together with e.g. `ST_wtch`, but
 1903 is expected to work at a lower accuracy since it includes more approximations.

1904 6.4 Technical setup

1905 For all generators, LHE events were generated and then showered and hadronized
 1906 with the multi-purpose generator PYTHIA. Wherever possible, the same settings
 1907 were used for the different generators, an overview of which can be found in Tab. 6.1.
 1908 They are mostly identical to the default settings used by CMS for MC generation,
 1909 as discussed in Ref. [81].

1910 6.4.1 Parton shower matching

1911 Special care has to be taken regarding the matching of the POWHEG ME gener-
 1912 ators to the parton shower as provided by PYTHIA. For `hvq` and `ST_wtch`, this
 1913 is accomplished here using a shower veto as described in Sec. 3.2, and technically
 1914 implemented using the PowhegHooks module of PYTHIA. By default, this module
 1915 can only handle one ISR emission at matrix element level, and thus needs to be
 1916 extended for `bb41` and `ttb_NLO_dec`, which also contain FSR emissions in the top

1917 decay. This was implemented by the **bb41** authors in the **PowhegHooksBB4L** module
1918 as described in detail in Ref. [162]. A updated form of this module compatible with
1919 **bb41** v2 is used here. Similarly to the ISR case, it is possible to directly start the
1920 shower at the energy scale of the POWHEG emission, or alternatively employ a veto
1921 for emissions above this scale. The latter is used as the default option, and compared
1922 to the former in Sec. 6.5.2.

1923 6.4.2 Same-flavor leptons

1924 By default, both versions of **bb41** generate only dilepton final states with opposite-
1925 flavor leptons (electrons, muons or τ leptons). This is because, in principle, there
1926 are additional diagrams contributing to the $b\bar{b}\ell^+\ell^-\nu_\ell\bar{\nu}_\ell$ amplitude for same-flavor
1927 leptons, such as $b\bar{b}ZZ$ with $ZZ \rightarrow \ell^+\ell^-\nu_\ell\bar{\nu}_\ell$, that are not included in **bb41**.

1928 In practice, the effect of these diagrams will be small, especially in experimental
1929 analyses where a cut is applied to reject resonant same-flavor lepton pairs close to
1930 the Z boson mass (compare Sec. 5.2.3). To make sure that **bb41** can be used in CMS
1931 for experimental analyses involving all lepton flavors, a relabeling procedure already
1932 included in **bb41** is extended to also produce same-flavor lepton final states, neglect-
1933 ing the aforementioned diagrams. This procedure is used for all **bb41** distributions
1934 shown in this chapter.

1935 6.5 Results

1936 6.5.1 Comparison between generators

1937 In this section, the two **bb41** versions are compared against each other, as well as
1938 to the alternative generators introduced in Sec. 6.3, for different observables. All of
1939 these comparisons are done after parton showering and hadronization, but without
1940 any detector simulation.

1941 The package **RIVET** [163] was used to analyze the events. For some observables,
1942 publically available analysis packages were employed, which is stated in the captions
1943 of the figures where applicable. Furthermore, some observables include distributions
1944 at the jet level, which are obtained by running an anti- k_T algorithm with distance
1945 parameter $\Delta R = 0.4$ (AK4) [111].

1946 **Lepton observables** To begin the comparison, events with at least two leptons of
1947 opposite sign satisfying $p_T > 20$ GeV and $|\eta| < 2.4$ are selected. Photons surround-
1948 ing the leptons in a small cone of $\Delta R < 0.1$, originating from photon radiation,
1949 are clustered together with the leptons (“dressed leptons”). The p_T distributions of
1950 the leading and subleading of these two leptons are shown in Fig. 6.2. They show

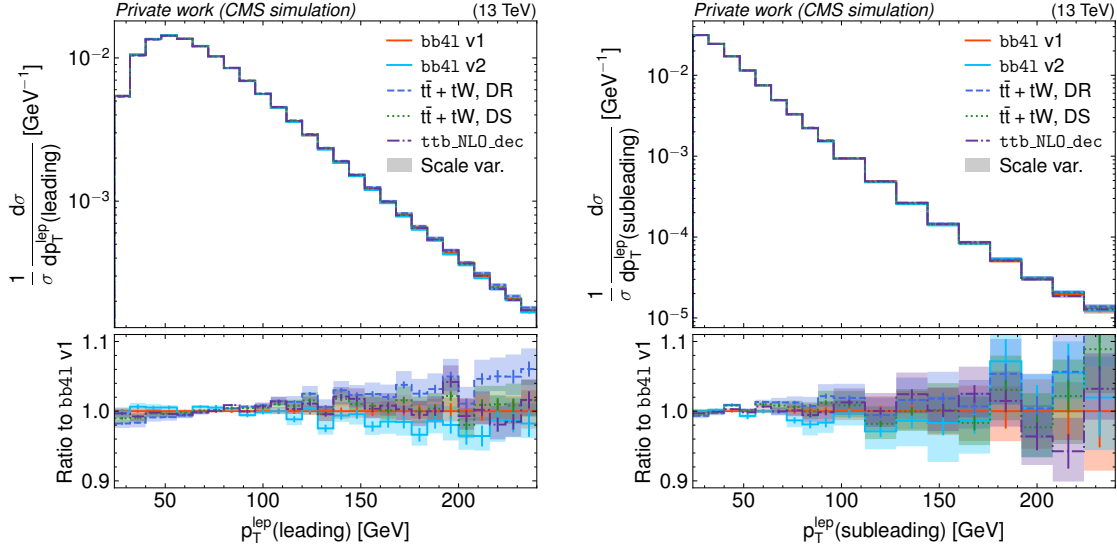


Figure 6.2: **Distributions of lepton p_T** of the leading (left) and subleading (right) lepton for bb41 v1 (red), v2 (aqua), $t\bar{t} + tW$ with the DR (blue) and DS scheme (green), as well as ttb_NLO_dec (magenta). The shaded bands show the uncertainty due to scale variations, while the error bars show the statistical uncertainty. *Figure adapted from Ref. [6].*

good agreement between the generators within the scale uncertainties, with $t\bar{t} + tW$ predicting a slightly harder lepton spectrum than the others.

The same trend can be seen in Fig. 6.3 for the invariant lepton mass $m_{\ell\ell}$, both inclusively and split by lepton flavor channels. The per-channel distributions are all comparable within statistical uncertainties, which validates the extension to same-flavor leptons for bb41 presented in Sec. 6.4.2.

Jet observables Next, some selected AK4 jet observables are compared. Jets containing a B hadron are identified as b jets using a ghost association technique [164, 165].

Fig. 6.4 shows the inclusive number of jets and the p_T of the leading b jet for the different cases. Several differences are observable here both between the two versions of bb41 and between bb41 and the other generators. For the number of jets, these are mostly covered by the scale uncertainties, while for the b jet p_T , there is an uncovered discrepancy at very low p_T . It is interesting to note that the number of jets agrees well between $t\bar{t} + tW$ and bb41 v2, while bb41 v1 and ttb_NLO_dec disagree and predict a larger number of jets. The origin of these discrepancies, especially between the bb41 versions, is not yet understood.

Next, Fig. 6.5 shows the b quark fragmentation, defined as the fraction of energy of the central B hadron in a jet compared to the total jet energy, as well as the average

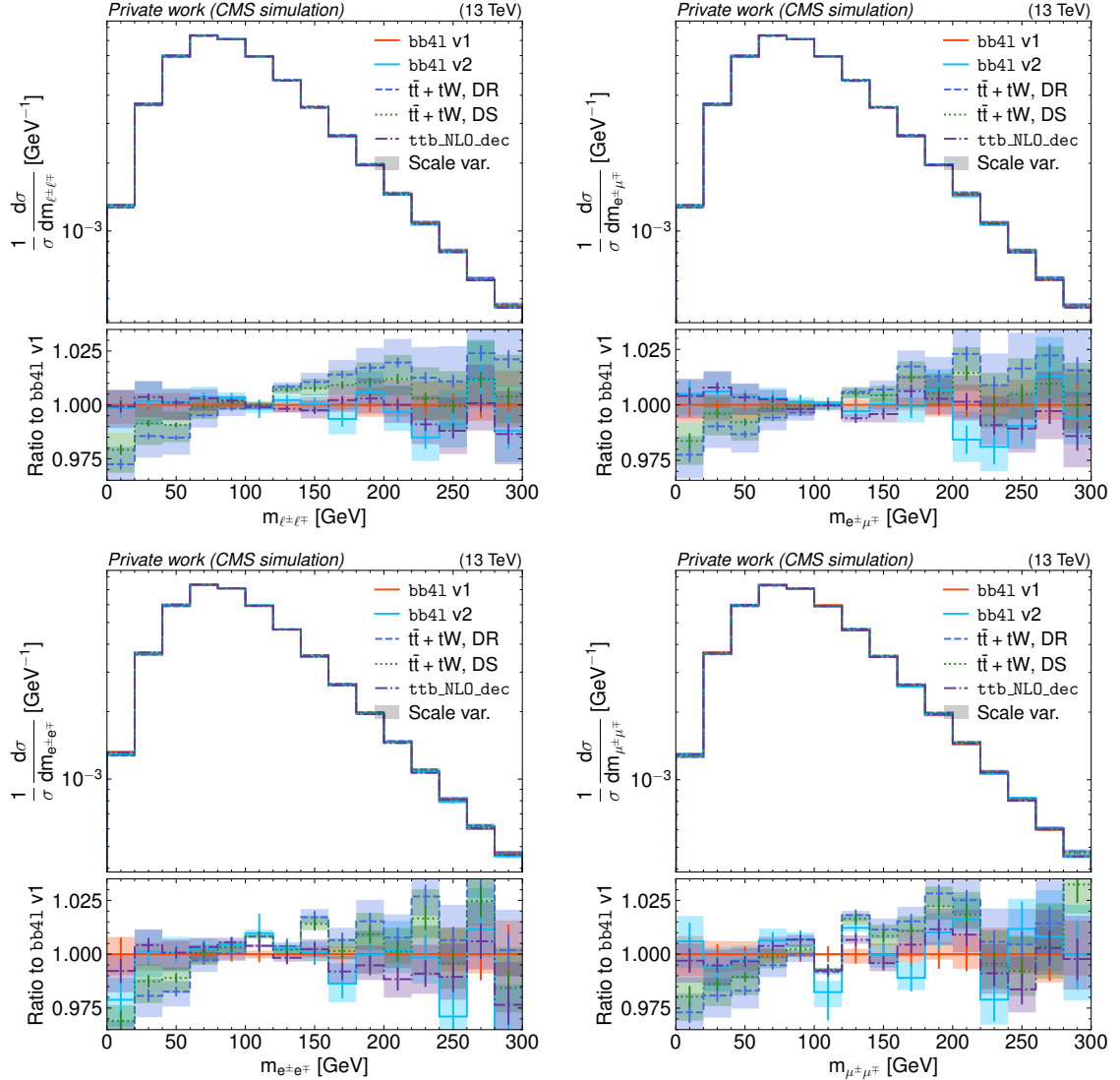


Figure 6.3: **Distributions of $m_{\ell\ell}$** for all lepton flavors combined (upper left) as well as in the $e\mu$ (upper right), ee (lower left) and $\mu\mu$ channels (lower right), shown in the same manner as in Fig. 6.2. *Figure adapted from Ref. [6].*

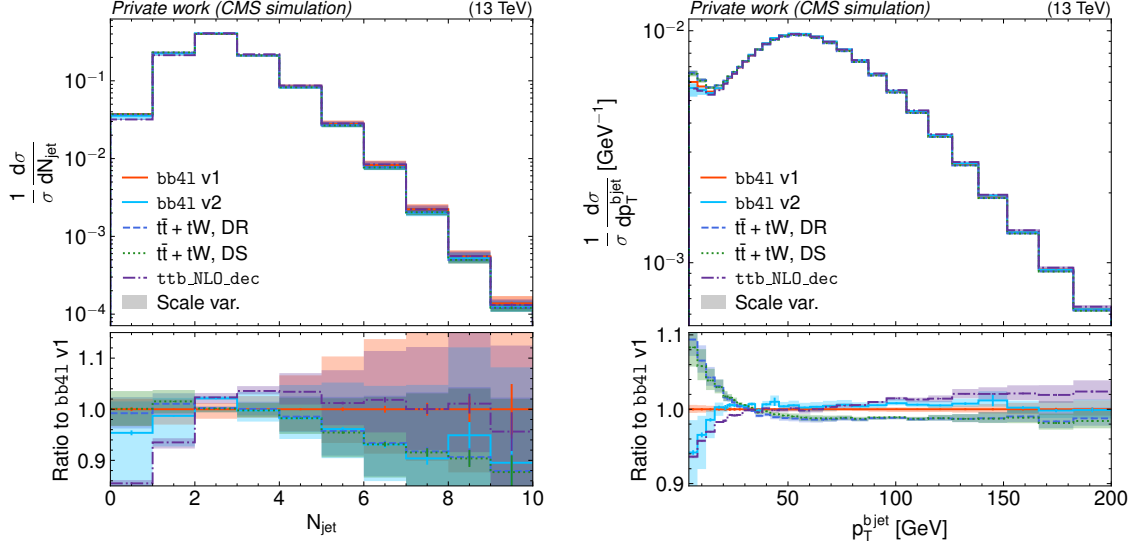


Figure 6.4: **Number of jets and b jet p_T .** Distributions of the inclusive number of AK4 jets (left) and the p_T of the leading b jet (right, RIVET analysis MC_HFJETS), shown in the same manner as in Fig. 6.2. *Figure adapted from Ref. [6].*

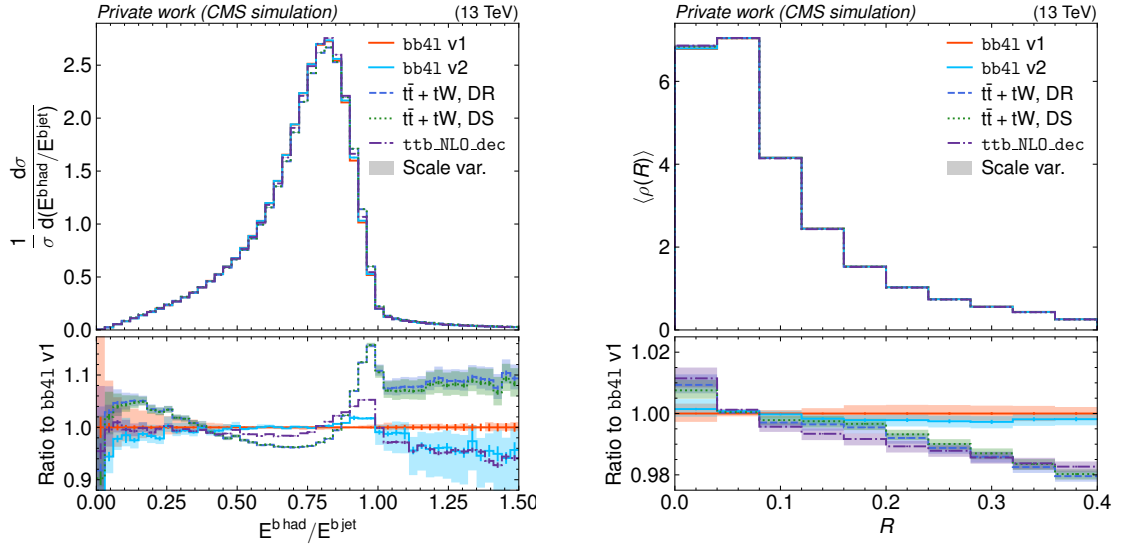


Figure 6.5: **b fragmentation and jet shape.** Distributions of the b quark fragmentation (left, RIVET analysis MC_HFJETS) and the average differential b jet shape (right, RIVET analysis MC_HFDECAYS), shown in the same manner as in Fig. 6.2. *Figure adapted from Ref. [6].*

1970 differential b jet shape $\langle \rho(R) \rangle$, which is the density of particles making up the b
 1971 jet as a function of its radius R . Both of these variables are sensitive to final-state
 1972 radiation from the top decay, and are thus expected to be affected by the full NLO
 1973 calculation performed by **bb41**. It can be seen that both versions of **bb41** predict
 1974 softer b jet spectra and wider jets than both $t\bar{t} + tW$ and **ttb_NLO_dec**, which can
 1975 be interpreted as more FSR emissions being generated. Notably, this effect cannot
 1976 be solely due to the inclusion of hard FSR emissions in **bb41** since these are also
 1977 present in **ttb_NLO_dec**.

1978 In general, all of these trends for **bb41** (softer lepton and b jet spectra as well
 1979 as wider jets) agree with what was observed in Refs. [162, 166], but differ from the
 1980 results initially reported in Ref. [7].

1981 **Invariant $b\ell$ mass** A common proxy observable to use for measurements of the
 1982 top quark mass in dilepton events is the invariant mass $m_{b\ell}$ of a b jet and a lepton.
 1983 To do so, a procedure is needed to unambiguously assign the leptons and b jets (of
 1984 which there might be varying numbers per event depending on the event selection)
 1985 to each other. Here, exactly two b jets per event are required, and the so-called
 1986 minimax mass is used, defined as

$$m_{b\ell}^{\text{minimax}} = \min [\max(m_{b_1\ell_1}, m_{b_2\ell_2}), \max(m_{b_1\ell_2}, m_{b_2\ell_1})]. \quad (6.1)$$

1987 This prescription amounts to maximizing over the two $b\ell$ pairs in the event,
 1988 and then minimizing over the two possible assignments of b jets and leptons. It
 1989 is notable in that, for double-resonant $t\bar{t}$ events, it shows a kinematic cutoff at a
 1990 value of $\sqrt{m_t^2 - m_W^2} \approx 150$ GeV. As a result, the tail above this cutoff is sensitive to
 1991 single-resonant tW events as well as $t\bar{t}/tW$ interference and thus to the top quark
 1992 width.

1993 Fig. 6.6 shows the distribution of $m_{b\ell}^{\text{minimax}}$, again for all considered cases. It can
 1994 be seen that both versions of **bb41** are in good agreement with each other, and are also
 1995 in agreement with **ttb_NLO_dec** except for the lowest bin. Unfolded ATLAS data
 1996 taken from Ref. [153] is overlaid on top of the predictions, and shows good agreement
 1997 for both **bb41** and **ttb_NLO_dec**. In the tail, the two interference handling schemes
 1998 for $t\bar{t} + tW$ show significant differences as expected, with **bb41** and **ttb_NLO_dec**
 1999 lying between them. Since **bb41** is expected to provide a more accurate prediction
 2000 of the interference than either scheme, this validates that using the difference of
 2001 the schemes as an uncertainty covers the true values, as is done in many CMS and
 2002 ATLAS measurements. Going forward, such uncertainties could be dropped from
 2003 future measurements by using **bb41** predictions directly.

2004 **Top quark reconstruction** Finally, in order to directly study the effects on top
 2005 quark observables, a simple generator-level top quark reconstruction is performed.
 2006 To do so, two dressed leptons and two b jets are selected as before, while the two

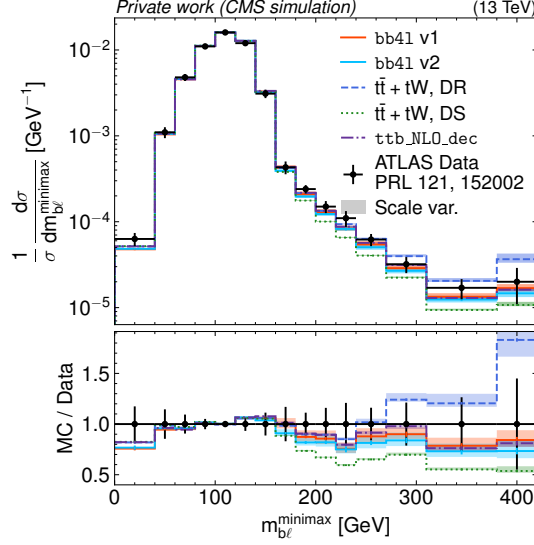


Figure 6.6: **Distribution of $m_{b\ell}^{\text{minimax}}$** , shown in the same manner as in Fig. 6.2. ATLAS data from Ref. [153] is overlaid as black dots, and the RIVET routine from said reference was used to obtain the distributions. *Figure adapted from Ref. [6].*

neutrinos in the dileptonic top decay are taken from truth-level information. The W bosons are reconstructed from the neutrinos and charged leptons according to the lepton charge, and then combined with the b jets to form two possible assignments of b-W pairs, which are taken as top quark and antiquark candidates again depending on the lepton charge. The ambiguity in assignments is resolved by choosing the pairs for which the difference Δm_t between the invariant masses is minimized.

This reconstruction procedure is not equivalent to a full experimental reconstruction, in which the neutrinos are only measured as missing transverse momentum and can thus not be directly assigned to the leptons. It also does not include any detector resolution effects. However, it does take into account the effects of FSR in the top decay by considering the full b jets instead of parton-level b quarks, which is why it was chosen for the comparison.

Fig. 6.7 shows the resulting distributions for the top quark mass and p_T . It can be seen that the different generators show different lineshapes for the top quark mass: **bb41** predicts a small shift towards lower values compared to $t\bar{t} + tW$ for both interference handling schemes as well as **ttb_NLO_dec**, and also predicts significantly lower amounts of off-shell tops with masses below the pole mass compared to $t\bar{t} + tW$. Both of these facts are important for precision top mass measurements, in which such shifts can influence the final fit results. The presence of these differences is expected: due to the use of the NWA for both $t\bar{t} + tW$ and **ttb_NLO_dec**, the top lineshape can only be modeled approximately in these generators, while **bb41**

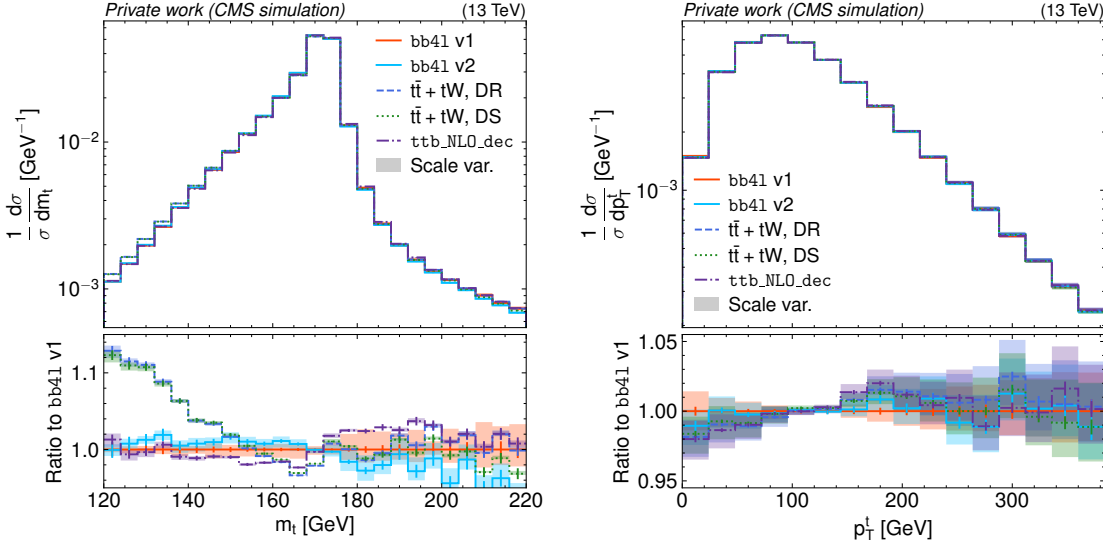


Figure 6.7: **Top quark lineshape and p_T .** Distributions of the reconstructed top quark mass (left) and p_T (right), summed for both top quark and antiquark, shown in the same manner as in Fig. 6.2. *Figure adapted from Ref. [6].*

provides a true NLO-accurate description. It can furthermore be seen that the two **bb41** versions are not in perfect agreement with each other, though the difference is within the scale uncertainties by 1 standard deviation.

For the top quark p_T , on the other hand, any trend in the comparison between the generators is covered by the scale uncertainties, though **bb41** does seem to again predict softer p_T spectra than the other generators, consistent with the trends observed for the lepton p_T and $m_{\ell\ell}$.

Lastly, the invariant mass and p_T distributions of the $t\bar{t}$ system as a whole are shown in Fig. 6.8. For $m_{t\bar{t}}$, no clear trend can be seen for any of the considered generators. The p_T of the $t\bar{t}$ system, on the other hand, shows significant differences both between the two **bb41** versions and between **bb41** and the other generators (which agree with each other). It should be noted that, since the initial state of the $pp \rightarrow t\bar{t}$ process has negligible p_T ¹, this variable is exactly zero at LO in QCD, and consequently determined only by emissions at NLO and beyond. As a result, it is expected to be sensitive to the NLO calculation and matching between matrix element and parton shower.

¹Non-zero p_T of the incoming partons can be modeled with transverse momentum distributions [167], but this is not considered here.

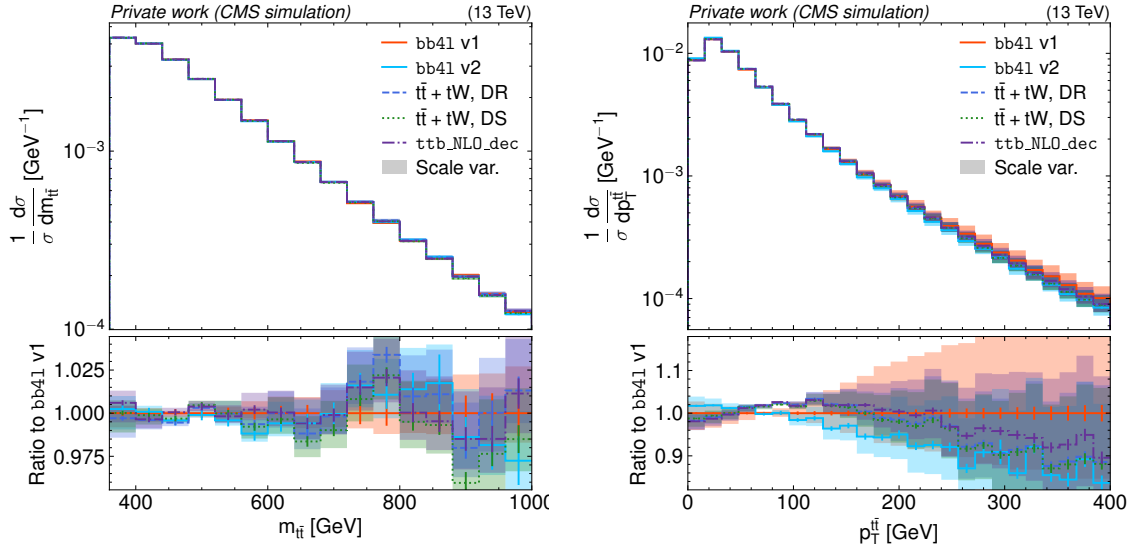


Figure 6.8: **Kinematics of the $t\bar{t}$ system.** Distributions of the reconstructed invariant mass (left) and p_T (right) of the $t\bar{t}$ system, shown in the same manner as in Fig. 6.2. *Figure adapted from Ref. [6].*

2044 6.5.2 Comparison of FSR matching settings

2045 Complementary to the previous generator comparisons, this section investigates the
 2046 effect of the matching between matrix element and parton shower for FSR in **bb41**.
 2047 As explained in Sec. 6.4.1, two principal options are available to match **bb41** to
 2048 PYTHIA in the used module **PowhegHooksBB4L**: In the first and nominal approach
 2049 (denoted “FSR veto”), the parton shower is started at the kinematic limit, and
 2050 FSR emissions that lie above the POWHEG energy scale of the relevant emission
 2051 from the top decay as generated by POWHEG are vetoed. In the second approach
 2052 (“Res. scale”), the shower is directly started at the energy scale of the POWHEG
 2053 FSR emission, neglecting the mismatch between scale definitions in POWHEG and
 2054 PYTHIA.

2055 In order to demonstrate the importance of correct parton shower matching, a third
 2056 case (“Kin. limit”) is considered, in which the parton shower for FSR emissions
 2057 is started naively at the kinematic limit without any veto procedure specifically
 2058 directed at **bb41**. This approach is thus expected to double-count FSR emissions.

2059 The comparison in this section has been performed with **bb41 v1**. The matching
 2060 for ISR emissions, done by **PowhegHooks**, is left identical between the three cases,
 2061 as given in Tab. 6.1.

2062 Fig. 6.9 shows the distributions of the top quark mass, reconstructed the same as
 2063 before, and the b fragmentation for the different matching choices. Both of these
 2064 observables were chosen for their sensitivity to FSR effects. It can be seen that

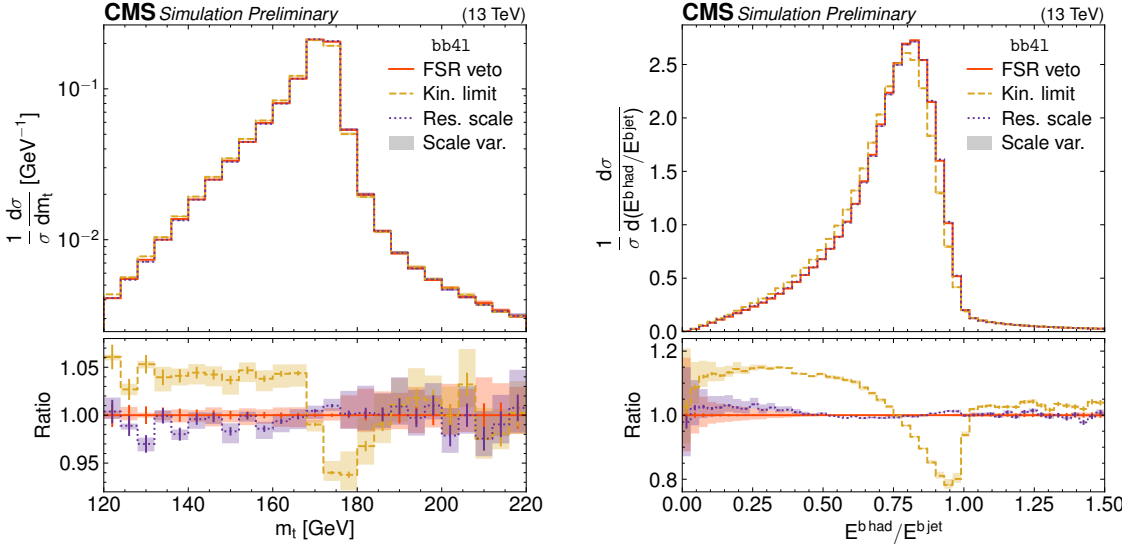


Figure 6.9: **Comparison of FSR matching settings.** Distributions of the reconstructed top quark mass (left, same as in Fig. 6.7) and the b quark fragmentation (right, same as in Fig. 6.5), for **bb41** with different FSR matching settings as explained in the text (Sec. 6.5.2). The shaded bands show scale uncertainties. *Figure taken from Ref. [6].*

the options “FSR veto” and “Res. scale” agree reasonably well with each other, with the top mass lineshape showing a small shift between them within the scale uncertainties. This implies that the mismatch between the POWHEG and PYTHIA energy scale definitions has a subleading effect in practice. On the other hand, the naive “Kin. limit” approach shows a large discrepancy due to its double-counting of FSR emissions, highlighting the importance of correct matching FSR matching procedures for NLO generators.

6.5.3 Recoil in top decay

In the simple parton shower in PYTHIA, there is a well-known problem affecting the virtualities of heavy unstable colored resonances, such as the top quark, in the treatment of FSR emissions in the resonance decay [168]. In particular, when performing a gluon emission off the decaying top quark and thus changing a $t \rightarrow Wb$ configuration to $t \rightarrow Wbg$, there is an ambiguity on how to distribute the recoil imposed by the gluon between the top decay products (W and b quark) such that the four-momentum of the Wbg system is conserved.

PYTHIA 8.307, which is the version used for the previous studies in this chapter, offers two different treatments for this problem, which amount to assigning the recoil to only the W (“recoil to W”) or only to the b quark (“recoil to b”). Both of these

2083 are approximations, since a true treatment would distribute the recoil between the
 2084 W and b quark in some form. CMS, and thus the studies previously shown in this
 2085 chapter, use the “recoil to b” option.

2086 Since PYTHIA 8.310, a third option (“recoil to top”) has been made available
 2087 via the setting `TimeShower:recoilStrategyRF`. For this option, the W is chosen
 2088 as the recoiler at first, but the emissions are then reweighted in such a way as to
 2089 approximate the radiation pattern expected in a true resonance-aware shower [168].
 2090 It has been found in Ref. [169] that the difference between this improved method
 2091 and the old ones can have a substantial impact on top mass proxy observables and
 2092 consequently measured top mass values, and there have been discussions on whether
 2093 such a difference should be included as a systematic uncertainty.

2094 This problem, in its core, is an issue of the parton shower and not the ME gen-
 2095 erator. Nonetheless, `bb4l` is expected to alleviate some of the ambiguities since it
 2096 always includes the hardest gluon emission in each top decay at the ME level, where
 2097 no question of assigning the recoil is raised. For subsequent and thus subleading
 2098 emissions, the issue in principle still persists.

2099 To estimate the effect of the top recoil in `bb4l` and compare it to $t\bar{t} + tW$, events
 2100 from both generators are re-showered in PYTHIA 8.310 with the two choices of setting

```
TimeShower:recoilStrategyRF = 1 ("recoil to b") and
TimeShower:recoilStrategyRF = 2 ("recoil to top").
```

2101 `bb4l` v2 is used for this comparison, and all other settings are kept at the nominal.
 2102 For $t\bar{t} + tW$, only the DR scheme is considered for the interference handling.

2103 The results are shown in Fig. 6.10 for the reconstructed top mass and the b
 2104 quark fragmentation. Large differences are visible between the two recoil strategies
 2105 for $t\bar{t} + tW$, as expected from Refs. [168, 169]. For `bb4l`, on the other hand, the
 2106 differences are very small, and lie within the scale uncertainties for the top quark
 2107 mass. This implies that the effect of the recoil in subleading emissions is negligible
 2108 in `bb4l` for the shown observables. As a result, `bb4l` circumvents the problem of
 2109 top recoil that can otherwise be significant for $t\bar{t}$ analyses. **TODO** After discussion
 2110 with Afiq I am not really convinced whether these results are actually correct... In
 2111 particular, are we sure that the recoil strategy option in pythia works correctly when
 2112 matched to bb4l? Simone is unfortunately no longer around to ask. Should I remove
 2113 it?

2114 6.6 Summary and Outlook

2115 In this chapter, several generator-level studies of the MC generator `bb4l`, which
 2116 generates the full $b\bar{b}\ell^+\ell^-\nu_\ell\bar{\nu}_\ell$ final state including $t\bar{t}/tW$ interference and off-shell
 2117 top effects at NLO in QCD, have been presented. `bb4l` has been compared to

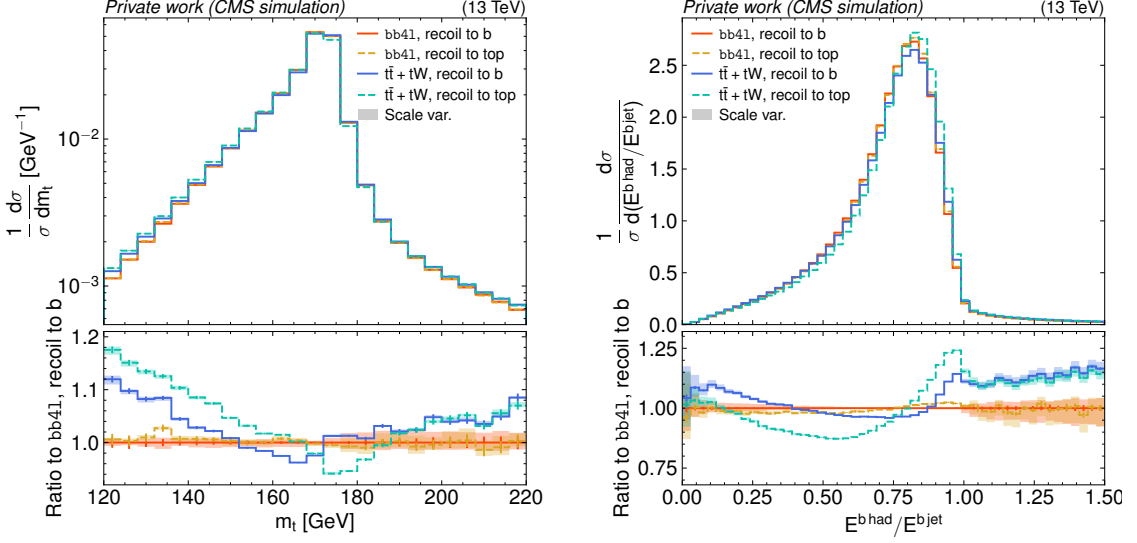


Figure 6.10: **Comparison of top recoil strategies.** Distributions of the reconstructed top quark mass (left, same as in Fig. 6.7) and the b quark fragmentation (right, same as in Fig. 6.5), for **bb41** and $t\bar{t} + tW$ with two different recoil treatments, as defined in the text (Sec. 6.5.3). The shaded bands show scale uncertainties.

other common $t\bar{t}$ generators, namely **hvq**, **ST_wtch** (with two interference handling schemes) and **ttb_NLO_dec**, for different lepton, (b) jet and reconstructed top quark observables. For $m_{bl}^{\min\max}$, **bb41** agrees well with ATLAS data from Ref. [153], improving greatly upon the two interference handling schemes DR and DS for $t\bar{t} + tW$. For the reconstructed top quark mass, **bb41** shows a significant shift compared to $t\bar{t} + tW$. In addition, two different **bb41** versions have been compared, finding slight differences within scale uncertainties, and the matching of ME and parton shower as well as the treatment of the top recoil in **bb41** have been studied further.

These studies represent valuable information for the choice of $t\bar{t}$ MC generator in upcoming CMS measurements. For analyses in which $t\bar{t}$ and tW are major backgrounds, **bb41** can help reduce uncertainties originating in the $t\bar{t}/tW$ interference treatment, and provide a more accurate description when off-shell regions of phase space are probed. This is briefly explored in Sec. 7.5.4 in the context of a search for $t\bar{t}$ bound state effects, which are naturally located in an off-shell-region. Furthermore, **bb41** will be of use when the $pp \rightarrow t\bar{t}$ process is instead the signal of a measurement. In particular, for future work it would be interesting to perform a simultaneous top mass and width measurement using MC templates generated with **bb41**, as originally proposed in Ref. [162], in CMS, or alternatively perform an differential $t\bar{t} + tW$ cross section measurement, where **bb41** could be used to unfold the data to generator level.

2138 **7 Search for heavy scalar or pseudoscalar**
2139 **bosons in $t\bar{t}$ final states**

2140 **7.1 Introduction**

2141 Additional spin-0 particles are predicted in many attractive extensions of the Stan-
2142 dard Model, and can be searched for in $t\bar{t}$ final states at the LHC if the new states are
2143 heavy (i.e. have a mass larger than $2m_t$), electrically neutral, and exhibit Yukawa-
2144 like couplings to fermions (see Sec. 2.3.1). A generic model for such states with either
2145 pseudoscalar (A) or scalar (H) couplings to top quarks was given in Eq. (2.18).

2146 In addition, $t\bar{t}$ bound state effects are expected in the SM in several calculations,
2147 with a pseudoscalar component dominating at the LHC as discussed in Sec. 2.2.3.
2148 Since the experimental invariant mass resolution for the $t\bar{t}$ final state is rather coarse,
2149 additional BSM particles and bound state effects are expected to lead to similar
2150 experimental signatures, and it thus makes sense to search for them for using the
2151 same methods.

2152 This chapter presents such a search for new spin-0 states with either scalar or
2153 pseudoscalar interactions with the top quark, using the full Run 2 dataset with an
2154 integrated luminosity of 138 fb^{-1} at the CMS experiment. It follows up on a similar
2155 search done using only 35.9 fb^{-1} of data taken in 2016 [17]. Similar searches have
2156 also been published by ATLAS, one with 20.3 fb^{-1} of data taken at $\sqrt{s} = 8 \text{ TeV}$ [170]
2157 and one with 140 fb^{-1} of data taken at $\sqrt{s} = 13 \text{ TeV}$ [171].

2158 The work done as part of this thesis focused on the dilepton decay channel of $t\bar{t}$,
2159 which is thus described in detail in Secs. 7.2 to 7.6. A significant excess of events
2160 is observed at invariant masses close to the $t\bar{t}$ threshold, which is interpreted either
2161 as a pseudoscalar $t\bar{t}$ bound state (Secs. 7.7.1 to 7.7.3) or as an additional scalar
2162 or pseudoscalar boson (Sec. 7.7.4). For the latter interpretation, exclusion limits
2163 for a large mass range are also presented in Sec. 7.8. Following this, the dilepton
2164 channel is combined with a similar analysis of the $\ell+\text{jets}$ decay channel, which is
2165 discussed in Sec. 7.9, and exclusion regions are provided for the presence of either
2166 one or two additional bosons. Finally, the results of this work are briefly compared
2167 in Sec. 7.10 to those of Ref. [171], in which no excess was observed, as well as to
2168 other $t\bar{t}$ measurements, and a summary and outlook are given in Sec. 7.11.

2169 The results presented here were first made public as a Physics Analysis Sum-
2170 mary [8], and later submitted to *Reports on Progress in Physics* in an updated form
2171 focusing solely on the interpretation of a $t\bar{t}$ bound state [9]. A further submission

focusing on the interpretation in terms of additional bosons is in preparation. They are the continuation of a previous PhD thesis [172], in which the analysis strategy of the dilepton channels as well as the procedure of obtaining exclusion limits for additional bosons was designed. Following up on this, the contribution of the work at hand consists of the implementation of matrix element reweighting for the signal simulation (Sec. 7.4), the simulation of the $t\bar{t}$ bound state signal (Sec. 2.2.3), the interpretation of the observed excess in terms of $t\bar{t}$ bound states or additional bosons including all corresponding cross-checks (Sec. 7.7), the comparison to other results (Sec. 7.10), and the preparation of the results for publication in Refs. [8] and [9].

7.2 Analysis setup

This section describes the analysis strategy in the dilepton channels, consisting of the considered datasets, object definitions, event selection criteria, corrections and reconstruction algorithms.

7.2.1 Datasets

Experimental data The analysis is performed using the full CMS Run 2 ultra-legacy (UL) dataset, which is the final, re-reconstructed and recalibrated dataset recommended by CMS for physics analyses. It is split into the three datataking years of Run 2: 2016, 2017 and 2018, where 2016 is further split into two parts, denoted “2016pre” and “2016post”, because of a modification of the APV readout chip settings that affects the efficiency of the track hit reconstruction during the 2016 data-taking period [173].

A similar combination of dilepton and single-lepton triggers as in Sec. 5.2.1 is used for all years, with the p_T thresholds varying slightly between datataking eras, as shown in Tab. 7.1.

Background simulation Since the final state of the signals considered in this analysis are the same as in the SM $t\bar{t}$ background, it is clear that a large irreducible background is expected. As a result, it is essential that the SM Monte Carlo simulation is as both theoretically precise and has sufficient statistics, and that any remaining imprecisions are covered by the systematic uncertainty model.

The SM $t\bar{t}$ background is again simulated at NLO in QCD with the `hvq` process from the MC generator package `POWHEG v2` and interfaced to `PYTHIA 8` for showering. Similar settings as in Sec. 5.2.1 have been used. To achieve the necessary precision, the NLO simulation is reweighted to higher orders in both QCD and electroweak (EW) processes, which is described in Sec. 7.3.

In addition, several minor backgrounds are included, a summary of which can be found in Tab. 7.2. Of note here is the Z+jets background, which is simulated at

| Trigger | Year | Lepton p_T requirement |
|---------------|------|--|
| single-e | 2016 | e ($p_T > 27 \text{ GeV}$) |
| | 2017 | e ($p_T > 35 \text{ GeV}$) |
| | 2018 | e ($p_T > 32 \text{ GeV}$) |
| single- μ | 2016 | μ ($p_T > 24 \text{ GeV}$) |
| | 2017 | μ ($p_T > 27 \text{ GeV}$) |
| | 2018 | μ ($p_T > 24 \text{ GeV}$) |
| e μ | all | e ($p_T > 12 \text{ GeV}$) and μ ($p_T > 23 \text{ GeV}$) or e ($p_T > 23 \text{ GeV}$) and μ ($p_T > 8 \text{ GeV}$) |
| ee | all | e ₁ ($p_T > 23 \text{ GeV}$) and e ₂ ($p_T > 12 \text{ GeV}$) |
| $\mu\mu$ | all | μ_1 ($p_T > 17 \text{ GeV}$) and μ_2 ($p_T > 8 \text{ GeV}$) |

Table 7.1: **Trigger p_T thresholds.** Overview of the used triggers in the three datataking years, as well as their lepton p_T thresholds.

NNLO in QCD using the MiNNLO method in POWHEG v2. It was found here that the higher-order corrections are relevant to the analysis especially for low values of the invariant dilepton mass $m_{\ell\ell}$. Most processes are normalized to cross sections predicted at higher orders of QCD where available, which can be found in Tab. 7.3.

Signal simulation The signal for the general A/H model described in Sec. 7.1 is generated at LO in QCD using MADGRAPH 5 with a custom Universal FeynRules Output (UFO) model. The $pp \rightarrow A/H \rightarrow t\bar{t}$ resonance and the A/H-SM interference are simulated separately, and both are again showered with PYTHIA 8. In order to cover the phase space of the A/H model, the signals are generated for all combinations of the following values of the A/H masses and widths:

$$\begin{aligned} m_{A/H} &\in \{365, 400, 500, 600, 800, 1000\} \text{ GeV} \\ \Gamma_{A/H}/m_{A/H} &\in \{2.5, (5), 10, 25\} \% \end{aligned} \quad (7.1)$$

Samples with a width of 5% were generated only for a mass of 400 GeV, which leads to 38 signal points total. In addition, samples for the pseudoscalar case only were generated with

$$m_A \in \{450, 550, 700, 900\} \text{ GeV}, \quad \Gamma_A/m_A = 9 \%. \quad (7.2)$$

All of these samples were combined and used reweighted at matrix element level to obtain also phase space points between these mass and width values, as described further in Sec. 7.4.

Furthermore, signal samples for possible $t\bar{t}$ bound state effects are generated using the color-singlet η_t and χ_t models as defined in Sec. 2.2.3, using custom UFO models

| Process | QCD order | ME Generator |
|----------------------------|-----------|------------------------------|
| $t\bar{t}$ | NLO | POWHEG v2 (hvq) |
| tW | NLO | POWHEG v2 (ST_wtch) |
| $Z/\gamma^* + \text{jets}$ | NNLO | POWHEG v2 (Zj MiNNLO) |
| t -channel single top | NLO | POWHEG v2 (ST_tch) + MADSPIN |
| s -channel single top | NLO | MG5_AMC@NLO |
| $t\bar{t}W$ | NLO | MG5_AMC@NLO |
| $t\bar{t}Z$ | NLO | MG5_AMC@NLO |
| WW, WZ & ZZ | LO | PYTHIA 8.2 |
| A/H signal | LO | MG5_AMC@NLO |
| η_t signal | LO | MG5_AMC@NLO |

Table 7.2: **Simulated background and signal samples.** An overview of the different background and signal processes considered, as well as the theoretical order in QCD and the ME generator used to simulate them. For all samples, PYTHIA 8.2 is used for showering and hadronization.

| Process | Cross section (pb) | Order | Program / reference |
|---|--------------------|----------------|---------------------|
| $t\bar{t}$ | 833.9 | NNLO+NNLL | Top++ [123] |
| tW | 71.7 | NNLO (approx.) | [127] |
| t -channel single top | 217.0 | NLO | Hathor [174, 175] |
| s -channel single top | 10.3 | NLO | Hathor [174, 175] |
| $t\bar{t}W$ | 0.64 | NLO | MG5_AMC@NLO |
| $t\bar{t}Z$ | 0.75 | NLO | MG5_AMC@NLO |
| $Z/\gamma^* + \text{jets} \rightarrow \ell\ell,$ $m_{\ell\ell} > 10 \text{ GeV}$ | 24.7×10^3 | NNLO | FEWZ [176, 177] |
| WW | 118.7 | NNLO | [178] |
| WZ | 471.3 | NLO | MCFM [179] |
| ZZ | 165.2 | NLO | MCFM [179] |

Table 7.3: **Cross sections for background processes.** The cross sections used for the normalization of background processes relevant for this search, as well as the orders in QCD at which they were computed.

2226 implemented in MADGRAPH 5 and again showered with PYTHIA.

2227 For all signal and background samples, the detector response is simulated with
 2228 GEANT 4 and the full CMS simulation and reconstruction chain as described in
 2229 Sec. 3.6 is performed.

2230 7.2.2 Object definition

2231 **Leptons** All electrons and muons are required to have $p_T > 20 \text{ GeV}$ and $|\eta| < 2.4$
 2232 to be considered for the analysis. Similar to Sec. 5.2.2, electrons in the transition
 2233 region between barrel and endcaps in the ECAL are removed, and additional ID
 2234 critera are applied for both types of leptons.

2235 For electrons, the multivariate classifier (MVA)-based ID described in Ref. [100] is
 2236 used at a working point giving 90 % background rejection. This ID already includes
 2237 an isolation requirement as part of the MVA training, and no further requirement
 2238 is applied.

2239 For muons, the same cut-based ID from Ref. [128] as in Sec. 5.2.2, also at the tight
 2240 working point, is used, and the same I_{rel} requirement using a cone size of $\Delta R < 0.4$
 2241 is applied in addition.

2242 **Jets** Jets are again reconstructed using the anti- k_T algorithm [111] with a distance
 2243 parameter of 0.4. They are required to fulfill $p_T > 20 \text{ GeV}$, $|\eta| < 2.4$, and have a
 2244 minimum distance of $\Delta R > 0.4$ from all leptons passing the above criteria in the
 2245 event.

2246 The DEEPJET algorithm [112], same as in Sec. 5.2.2, is used to identify jets
 2247 originating from the showering and hadronization of b quarks. The medium working
 2248 point of DEEPJET in CMS, corresponding to an identification efficiency of 77 % is
 2249 chosen [129].

2250 **Missing transverse momentum** In the dileptonic decay of $t\bar{t}$, the two neutrinos
 2251 can not be measured experimentally, and escape the detector unseen. However, their
 2252 presence can be inferred from momentum conservation: In a proton-proton collision,
 2253 the longitudinal component of the incoming partons in the hard scattering process is
 2254 unknown, while the transverse component can be assumed to be close to zero. Thus,
 2255 the missing transverse momentum \vec{p}_T^{miss} can be inferred as the negative vectorial sum
 2256 of all reconstructed objects (jets, leptons and photons) [113]. Along with the leptons
 2257 and jets, it will be used to reconstruct the $t\bar{t}$ system.

2258 7.2.3 Event selection

2259 Events are selected with exactly two leptons of opposite electric charge and sorted
 2260 into three channels (ee, e μ and $\mu\mu$) by lepton flavor, similar to Sec. 5.2.3. The two

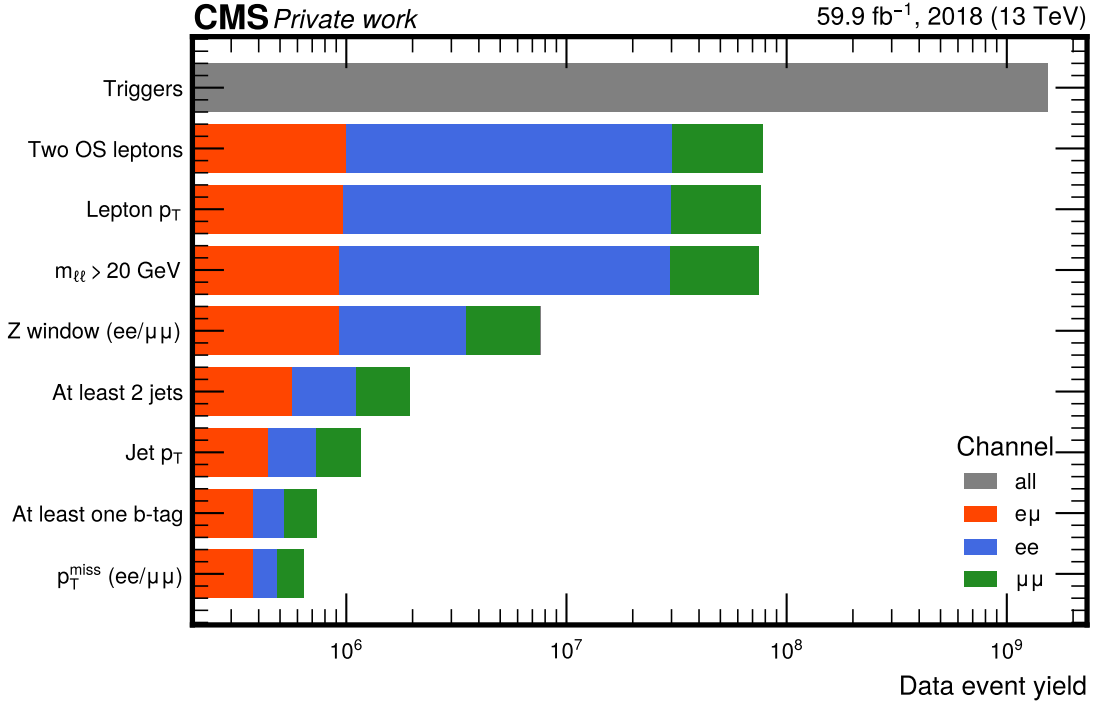


Figure 7.1: **Selection cuts.** Shown is the data yield in 2018 (corresponding to $L_{\text{int}} = 59.9 \text{ fb}^{-1}$) after successively applying all selection cuts. Starting with the requirement of two opposite-sign leptons, the three channels are marked with different colors.

leptons need to fulfill $p_T > 25 \text{ GeV}$ and $p_T > 20 \text{ GeV}$ for the leading and subleading lepton, respectively, and their invariant mass is required to be $m_{ll} > 20 \text{ GeV}$ in order to reject background from $\gamma^* + \text{jets}$ production and low-mass resonances.

In all channels, at least two jets with $p_T > 30 \text{ GeV}$ are required, of which at least one needs to be b-tagged. Furthermore, in the same-flavor lepton channels (ee and $\mu\mu$), additional cuts are applied to reject Z+jets background: Events with $|m_{ll} - m_Z| < 15 \text{ GeV}$, i.e. close to the Z boson mass peak, are discarded (again just as in Sec. 5.2.3), and the magnitude of the missing transverse momentum is required to be $p_T^{\text{miss}} > 40 \text{ GeV}$.

The effect of all selection cuts can be seen in Fig. 7.1.

7.2.4 Experimental corrections

Similar as in Sec. 5.3, several corrections are applied to the MC simulation in order to achieve good agreement with the data. In contrast to the $t\bar{t}$ cross section measurement, where most of these corrections were derived as part of this work, many

2275 of the experimental corrections used in this chapter were provided centrally by the
2276 CMS collaboration. These will only be described very briefly; more details can be
2277 found in the associated references.

2278 **Trigger scale factors** The selection efficiency of the triggers from Tab. 7.1 needs
2279 to be corrected in simulation to the one measured in data. This is done via scale
2280 factors, which were centrally derived as a function of the p_T of the two leptons
2281 using the so-called cross-trigger method: Events are selected using a different set of
2282 triggers - here, a combination of jet and p_T^{miss} triggers - which is assumed to be fully
2283 orthogonal to the lepton triggers used for the main selection. Thus, the event sample
2284 is unbiased with respect to the lepton triggers, and the lepton trigger efficiency can
2285 be measured as the fraction of these events who pass the lepton triggers in addition
2286 to the jet/ p_T^{miss} triggers. This is done independently for all datataking years, and
2287 the resulting scale factor differs from unity by less than 1 % in most cases.

2288 **Lepton scale factors** Differences in the efficiency for a lepton to pass the identifi-
2289 cation and isolation criteria as defined in Sec. 7.2.2 are measured using the tag-and-
2290 probe method, as in Sec. 5.3, and applied to simulation using scale factors binned
2291 in p_T and $|\eta|$ of the lepton. The scale factor typically differs from unity by about
2292 1-5 %, with the magnitude increasing for high $|\eta|$. For more details on this method
2293 see Refs. [100, 128].

2294 **Pileup reweighting** In contrast to the data-driven reweighting method used for
2295 the inclusive $t\bar{t}$ cross section measurement (Sec. 5.3), the mean number of pileup
2296 interactions per bunch crossing in simulation is reweighted to year-dependant dis-
2297 tributions provided centrally by CMS. These have been derived from measurements
2298 of the instantaneous luminosity combined with a total inelastic proton-proton cross
2299 section of $69.2 \text{ mb} \pm 4.6\%$ at $\sqrt{s} = 13 \text{ TeV}$ [87].

2300 **Jet energy corrections** The difference in the jet energy response of the detector
2301 as well as the jet energy resolution in data and simulation was corrected in the same
2302 way as described in Sec. 5.3, using centrally derived jet energy corrections (JECs)
2303 as described in Ref. [130].

2304 **b-tagging scale factors** The identification efficiency of the DEEPJET b-tagging
2305 algorithm was calibrated on events with jets containing a muon, which are likely to
2306 result from the semileptonic decay of a B hadron, using the methodology described
2307 in Ref. [129]. Note that, unlike most CMS analyses using b-tagging, the calibration
2308 done on dileptonic $t\bar{t}$ events presented in the same reference is not used as an input
2309 here, since it was derived in part on the same dataset as used for this search, and
2310 would thus lead to double-counting. However, similar to the discussion in Sec. 5.6,

| | 2016pre | 2016post | 2017 | 2018 |
|----------|------------------|------------------|------------------|------------------|
| ee | 0.96 ± 0.010 | 0.97 ± 0.008 | 0.87 ± 0.006 | 0.88 ± 0.005 |
| e μ | 0.96 ± 0.007 | 0.97 ± 0.005 | 0.88 ± 0.004 | 0.89 ± 0.003 |
| $\mu\mu$ | 0.96 ± 0.009 | 0.97 ± 0.006 | 0.90 ± 0.005 | 0.90 ± 0.004 |

Table 7.4: **Z+jets scale factors.** Ratio of the Z+jets event yields estimated in data using the method described in Sec. 5.3.2 to the prediction by the MC simulation for the four data-taking periods. The results in the e μ channel are the geometric means of those in the ee and $\mu\mu$ channels. Uncertainties are statistical only.

2311 it is expected that the b-tagging efficiency will be constrained from the data during
2312 the likelihood fit.

2313 **ECAL L1 pre-firing** In the 2016 and 2017 data-taking years, the L1 trigger of
2314 the electromagnetic calorimeter was affected by a gradual shift in the timing of the
2315 inputs in the forward region ($|\eta| > 2.0$) [106]. This effect, called L1 pre-firing, is
2316 corrected for using simulation scale factors computed from data.

2317 **Z+jets background normalization** In the same-flavor lepton channels (ee and
2318 $\mu\mu$), Z+jets events again constitute a minor but important background. Since this
2319 analysis is sensitive to small shape effects, it is necessary to precisely model this
2320 background both in shape and normalization. An NNLO Monte Carlo simulation
2321 (see Tab. 7.2) is used for this purpose, which generates up to two partons (including b
2322 quarks) in the final state, as required by the event selection of at least two jets and at
2323 least one b tag. Still, in order to be certain of the Z+jets rate, the same data-driven
2324 estimation as presented in Sec. 5.3.2, using a control region with $|m_{\ell\ell} - m_Z| < 15$ GeV
2325 and a sideband with zero b-tagged jets, is performed. The resulting ratios of Z+jets
2326 yields compared to the prediction of the original simulation can be found in Tab. 7.4.

2327 7.2.5 Reconstruction of the $t\bar{t}$ system

2328 Having identified the relevant objects - leptons, jets and \vec{p}_T^{miss} - in an event, the next
2329 step consists of reconstructing the $t\bar{t}$ system, i.e. the four-momenta of the top and
2330 antitop quark. Due to the presence of the two neutrinos in the dileptonic $t\bar{t}$ decay,
2331 which escape the detector unobserved except for \vec{p}_T^{miss} and thus represent a loss of
2332 information, this is a non-trivial procedure which requires several assumptions on
2333 the kinematic properties. In this work, a variation of the algorithm first presented
2334 in Ref. [180] is used, which is briefly outlined in this section.

2335 The algorithm works in two steps, starting with the assignment of jets to the b
2336 and \bar{b} quarks originating from the $t\bar{t}$ decay. To do so, pairs of jets are selected from

2337 all jets in the event (passing the requirements outlined in Sec. 7.2.2) depending on
 2338 the number n_b of b-tagged jets: For events with $n_b \geq 2$, all (ordered) permutations
 2339 of two b-tagged jets each are considered as candidate pairs, while for events with
 2340 $n_b = 1$, the candidate pairs are formed by pairing the single b-tagged jet with all
 2341 other jets in the event.

2342 From these candidates, the best pair is now chosen based on the invariant masses
 2343 $m_{\ell+b}$ and $m_{\ell-\bar{b}}$ of the b/ \bar{b} candidate and the corresponding (anti)lepton. In each
 2344 event, the candidate pair is chosen that maximizes the product of the truth-level
 2345 likelihoods, as evaluated from MC events, to obtain the measured values of $m_{\ell+b}$
 2346 and $m_{\ell-\bar{b}}$. This pair is then used for the remainder of the reconstruction.

2347 Next, the four-momenta of the top and antitop quark are reconstructed using the
 2348 momentum conservation equations. That is, one demands

$$\begin{aligned} p_t &= p_{W^+} + p_b = p_{\ell^+} + p_{\nu_\ell} + p_b \\ p_{\bar{t}} &= p_{W^-} + p_{\bar{b}} = p_{\ell^-} + p_{\bar{\nu}_\ell} + p_{\bar{b}} \end{aligned} \quad (7.3)$$

2349 where all variables are understood as four-momenta. The lepton and b-quark
 2350 momenta are experimentally measured, while the neutrino momenta are unknowns.
 2351 Demanding them to be massless, i.e. $p_{\nu_\ell}^2 = p_{\bar{\nu}_\ell}^2 = 0$, yields the six components of the
 2352 two neutrino three-momenta as free parameters.

2353 To resolve the ambiguities, several assumptions need to be made. First, it is
 2354 assumed that all of the missing transverse momentum in the event stems from the
 2355 neutrinos, i.e.

$$p_{\nu_\ell,x} + p_{\bar{\nu}_\ell,x} = p_x^{\text{miss}}, \quad p_{\nu_\ell,y} + p_{\bar{\nu}_\ell,y} = p_y^{\text{miss}} \quad (7.4)$$

2356 Additionally, it is assumed that both the top quarks and W bosons are exactly
 2357 on-shell, that is

$$p_{W^+}^2 = m_W^2, \quad p_{W^-}^2 = m_W^2 \quad (7.5)$$

2358 and

$$p_t^2 = m_t^2, \quad p_{\bar{t}}^2 = m_t^2 \quad (7.6)$$

2359 where m_t and m_W are the pole masses of the top quark and W boson, respectively.
 2360 Applying these six constraints leads to a system of quartic equations for the neutrino
 2361 three-momenta \vec{p}_{ν_ℓ} and $\vec{p}_{\bar{\nu}_\ell}$, which was solved in Ref. [181]. From these, the top and
 2362 antitop quark four-momenta can then be calculated. Since the quartic equation
 2363 can in general have up to four solutions, the solution with the lowest value of the
 2364 invariant $t\bar{t}$ mass $m_{t\bar{t}}$ is chosen. This was found in Ref. [182] to minimize the bias
 2365 in $m_{t\bar{t}}$ especially for low- $m_{t\bar{t}}$ events.

2366 In practice, however, this method will not give a real solution even for those $b\bar{b}$

2367 pair candidates which are correctly assigned to the truth-level b quarks. This is
2368 because the experimental inputs to the method - the jet and lepton four-momenta
2369 as well as \vec{p}_T^{miss} - will deviate from their truth-level values within the experimental
2370 resolution of the detectors and object reconstruction. In addition, the constraints
2371 will not be fulfilled exactly: There might be additional p_T^{miss} in the event because
2372 of e.g. neutrinos produced in τ lepton or B hadron decays, and the W bosons and
2373 top quarks might be off-shell with respect to their pole masses by their respective
2374 widths.

2375 To alleviate this, several of the input variables are randomly smeared to model
2376 the experimental resolution. For both the b jets and leptons, the energies are varied
2377 while keeping their masses constant, and the directions of their three-momenta are
2378 varied in a uniformly random direction. For both of these cases, the variations are
2379 randomly sampled from a distribution obtained by comparing the reconstructed and
2380 truth four-momentum in the nominal $t\bar{t}$ MC simulation, as shown in Ref. [172]. Ad-
2381 ditionally, the values of m_W used for the constraints on p_{W+} and p_{W-} are randomly
2382 sampled from a relativistic Breit-Wigner distribution corresponding to the W boson
2383 width Γ_W . This smearing procedure is repeated 100 times per event with different
2384 random values, resulting in up to 100 reconstructed $t\bar{t}$ systems per event, depending
2385 on the number of cases where there is no real solution.

2386 Finally, one unambiguous solution per event is constructed by again using the
2387 invariant lepton-b quark masses and their truth-level likelihoods. For each iteration
2388 of the smearing procedure that yielded a real solution, a weight is defined as the
2389 product of the likelihoods for obtaining the smeared values of $m_{\ell+b}$ and $m_{\ell-\bar{b}}$, i.e.

$$w = \mathcal{P}(m_{\ell+b}) \cdot \mathcal{P}(m_{\ell-\bar{b}}) \quad (7.7)$$

2390 The final solution for the reconstructed top and antitop four-momenta is defined
2391 as the weighted average over all real solutions, using the weight as given in Eq. (7.7).

2392 For $t\bar{t} \rightarrow b\bar{b}\ell\ell\nu\nu$ events passing all previous selection steps, the efficiency of the
2393 full reconstruction algorithm is ca. 90%, as evaluated in MC simulation. To asses
2394 the accuracy of the reconstruction relative to the truth-level top quarks, defined
2395 after parton showering, a per-event relative deviation is defined as

$$\Delta m_{t\bar{t}} = \frac{m_{t\bar{t}}^{\text{reco}} - m_{t\bar{t}}^{\text{gen}}}{m_{t\bar{t}}^{\text{gen}}}, \quad (7.8)$$

2396 where $m_{t\bar{t}}^{\text{reco}}$ and $m_{t\bar{t}}^{\text{gen}}$ stand for the reconstructed and truth-level $m_{t\bar{t}}$, respectively.
2397 The mean and standard deviation of $\Delta m_{t\bar{t}}$ are then the relative bias and resolution
2398 of the reconstruction algorithm. They are evaluated in simulation of dileptonic
2399 $t\bar{t}$ and shown in Fig. 7.2 as a function of truth-level $m_{t\bar{t}}$. The method shows a
2400 bias towards high $m_{t\bar{t}}$ for events with $m_{t\bar{t}}^{\text{gen}} \lesssim 600$ GeV and towards low $m_{t\bar{t}}$ for
2401 $m_{t\bar{t}}^{\text{gen}} \gtrsim 600$ GeV, with resolutions in the range of 17 – 25%. It should be noted here
2402 that this bias relative to the truth level is by itself not problematic for this analysis,

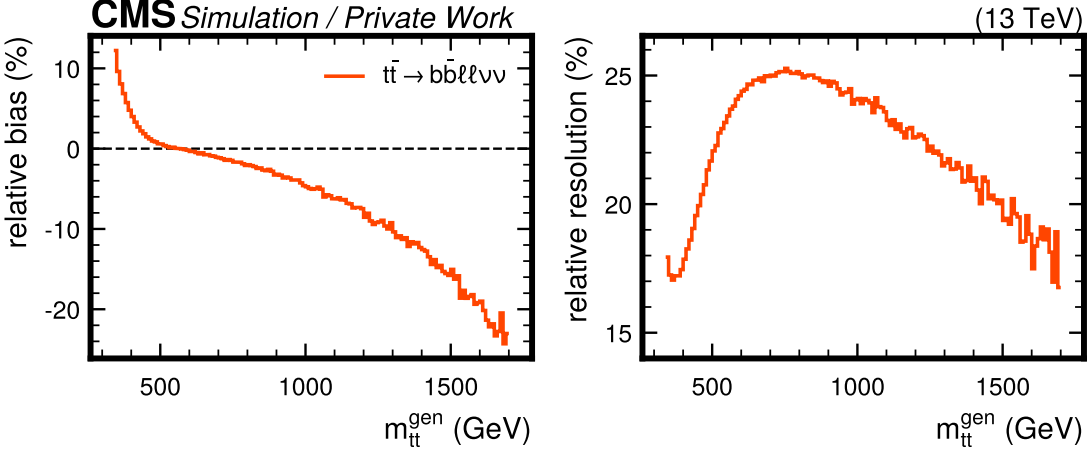


Figure 7.2: **Bias and resolution of $m_{t\bar{t}}$.** Relative bias and resolution of the $t\bar{t}$ reconstruction algorithm, defined in Eq. (7.8), as a function of truth-level $m_{t\bar{t}}$ and evaluated in MC simulation of dileptonic $t\bar{t}$.

2403 since it is expected to be the same in both simulation and data and no unfolding of
 2404 the reconstructed distributions to the truth level is attempted here.

2405 7.2.6 Sensitive observables

2406 To extract the A/H and η_t signals from the background, three sensitive observables
 2407 are considered. The first is simply the invariant $t\bar{t}$ mass $m_{t\bar{t}}$, defined with the
 2408 reconstruction procedure as explained in the last section. As shown in Fig. 2.7,
 2409 an A/H signal is expected to result in a peak-dip structure in $m_{t\bar{t}}$ around the SM
 2410 background, where the zero crossing between peak and dip should be in the vicinity
 2411 of the A/H mass, and the magnitude as well as ratio of the peak and the dip
 2412 depends non-linearly on the coupling modifier. The η_t signal, on the other hand, is
 2413 expected to peak slightly below the $t\bar{t}$ production threshold at $m_{t\bar{t}} \simeq 2m_t - 2$ GeV
 2414 as discussed in Sec. 2.2.3 and shown in Fig. 2.5. In practice, due to the limited
 2415 detector resolution, the exact position of this peak will not be observable, and the
 2416 signal will result in a generic enhancement of the yield for very low values of $m_{t\bar{t}}$.

2417 In addition, the two spin correlation observables c_{hel} and c_{han} , as defined in
 2418 Eq. (2.4) and Eq. (2.10), are used to gain further sensitivity. Both variables are
 2419 again defined using the $t\bar{t}$ system reconstruction as described in the previous sec-
 2420 tion. As discussed in Sec. 2.2.2, they are ideal for separating spin-singlet and spin-
 2421 triplet states, respectively. Thus, A and η_t signals, producing singlet states, will
 2422 have enhanced contributions at high values of c_{hel} , while H signals, producing 3P_0
 2423 triplet states, will be enhanced at low values of c_{han} . This allows not only for better
 2424 discrimination between signal and background, but also to probe the \mathcal{CP} structure

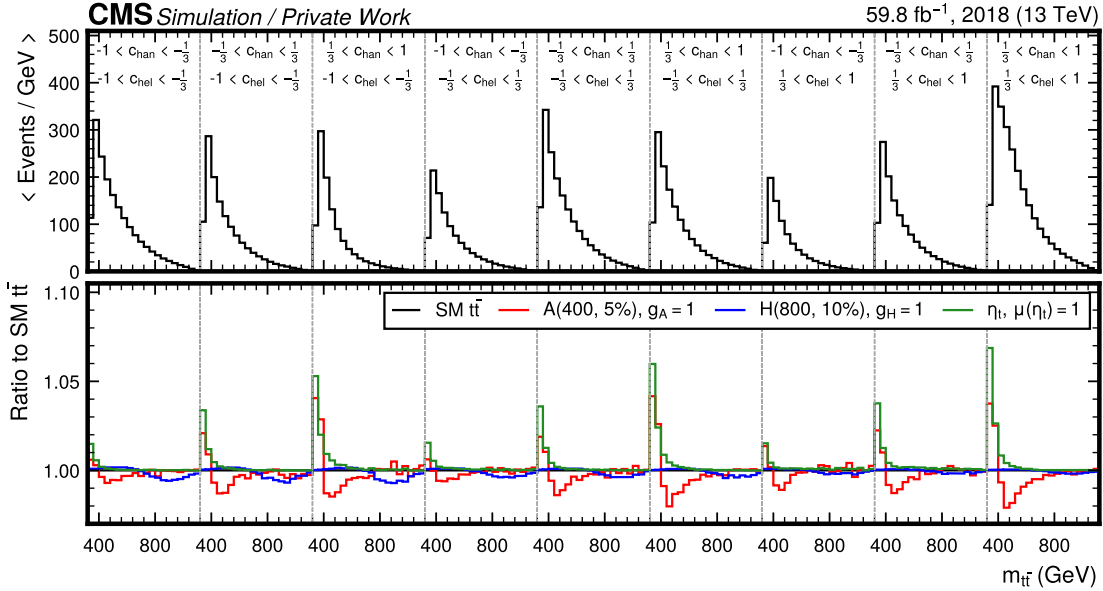


Figure 7.3: **3D template for $m_{t\bar{t}} \times c_{\text{hel}} \times c_{\text{han}}$** for SM $t\bar{t}$ (top) as well as three different example signals (bottom, shown as the ratio to SM $t\bar{t}$), corresponding to the luminosity taken in 2018 only.

of a possible observed signal.

To combine all three variables, three-dimensional templates are created with $20 \times 3 \times 3$ bins in the three observables $m_{t\bar{t}}$, c_{hel} and c_{han} . For $m_{t\bar{t}}$, an irregular binning is chosen to account for the decrease in production cross section at high values. An example can be seen in Fig. 7.3 for SM $t\bar{t}$ and three different signals (A, H and η_t).

7.3 Higher-order corrections in $t\bar{t}$

In this analysis, the SM $t\bar{t}$ background is irreducible - after all, it leads to the exact same final state as the signal. As a result, it is crucial to model it as precisely as possible: a mismodeling of the $t\bar{t}$ kinematic distribution, especially in $m_{t\bar{t}}$, might otherwise be confused for a signal and lead to bias.

The MC simulation used for the SM $t\bar{t}$ background is performed at NLO in QCD using the POWHEG v2 subprocess hvq, as studied also in Chapter 6. On top of this, two different sets of corrections are applied to include missing higher orders, namely NNLO QCD and NLO electroweak (EW) corrections. Both of these are estimated by comparing the MC simulation, which is matched to a parton shower, to fixed-order predictions. The simulation is then reweighted using scale factors binned two-dimensionally in $m_{t\bar{t}}$ and $\cos\theta_t^*$, where the latter is the cosine of the scattering angle of the top quark to the beam axis in the $t\bar{t}$ rest frame. These two

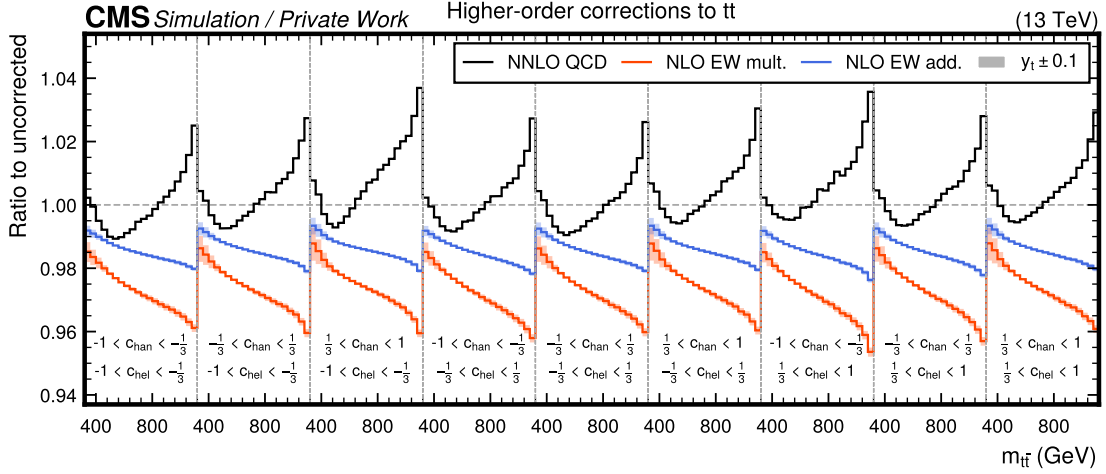


Figure 7.4: **Effect of NNLO QCD and NLO EW corrections** on the 3D $m_{t\bar{t}} \times c_{\text{hel}} \times c_{\text{han}}$ distribution after reconstruction in the form of ratios to the uncorrected distributions. The NNLO QCD corrections are shown as the solid black line, while the NLO EW corrections are shown in orange for the multiplicative scheme and in blue for the additive scheme. The effect of varying y_t by ± 0.1 in the NLO EW corrections is shown as the shaded bands.

variables fully define the kinematics of the top quarks in the $t\bar{t}$ rest frame, save for FSR emissions.

7.3.1 NNLO QCD corrections

The NNLO QCD predictions are obtained with the program MATRIX [126]. They are computed at the level of stable top quarks with a dynamic scale choice of $\sqrt{m_t^2 + p_{T,t}^2}$, where $p_{T,t}$ is the top quark transverse momentum. Fig. 7.4 shows the resulting effect on the 3D $m_{t\bar{t}} \times c_{\text{hel}} \times c_{\text{han}}$ distribution at the detector level as the black line. They are on the order of 1 – 2%.

7.3.2 NLO EW corrections

The NLO corrections in the electroweak coupling α_{EW} are computed with the HATHOR code [174, 183–185] using the same nominal scale choices. Of particular interest here is a class of diagrams which contain an exchange of a virtual SM Higgs boson, an example of which is seen in Fig. 7.5. The matrix element for this diagram is proportional to the square of the SM Higgs-top Yukawa coupling y_t , giving a y_t^2 -dependent correction to $t\bar{t}$ distributions from the interference with LO diagrams. This correction is sizeable mostly for low $m_{t\bar{t}}$ values, and is important for

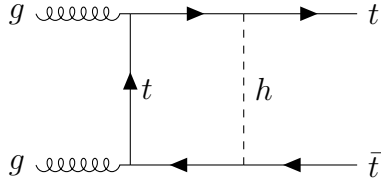


Figure 7.5: **EW correction involving a SM Higgs boson.** An example Feynman diagram for NLO EW corrections to $t\bar{t}$ production involving the exchange of a virtual SM Higgs boson h .

this analysis because the SM Higgs exchange might change the $t\bar{t}$ spin state and thus c_{hel} and c_{han} . To accurately account for this, the correction is derived separately for the different initial states (gg , $q\bar{q}$ and gq) of $t\bar{t}$ production.

The results obtained with HATHOR are accurate only to LO in α_S , i.e. $\mathcal{O}(\alpha_S^2)$, and as of the time of writing no full calculation including both NLO QCD and EW effects exists. Thus, there is an ambiguity on how the NLO-accurate (in QCD) MC simulation and the NNLO-accurate corrections presented in the previous section should be combined with the EW corrections.

Formally, the differential cross section as predicted by Powheg can be decomposed as

$$d\sigma_{\text{POWHEG}} = \alpha_S^2 d\sigma_{\text{LO}} + \alpha_S^3 d\sigma_{\text{NLO}} \quad (7.9)$$

where additional terms beyond $\mathcal{O}(\alpha_S^3)$ due to additional radiation in Powheg and Pythia are not written for simplicity. On the other hand, HATHOR predicts

$$d\sigma_{\text{HATHOR}} = \alpha_S^2 d\sigma_{\text{LO}} + \alpha_S^2 \alpha_{\text{EW}} d\sigma_{\text{EW}}. \quad (7.10)$$

One possible way to combine the calculations is the additive scheme, given by

$$\begin{aligned} d\sigma_{\text{add.}} &= d\sigma_{\text{POWHEG}} + d\sigma_{\text{HATHOR}} - \alpha_S^2 d\sigma_{\text{LO}} \\ &= \alpha_S^2 d\sigma_{\text{LO}} + \alpha_S^3 d\sigma_{\text{NLO}} + \alpha_S^2 \alpha_{\text{EW}} d\sigma_{\text{EW}} \end{aligned} \quad (7.11)$$

which is formally accurate to $\mathcal{O}(\alpha_S^3)$ and $\mathcal{O}(\alpha_S^2 \alpha_{\text{EW}})$. This approach does not include any cross terms of order $\mathcal{O}(\alpha_S^3 \alpha_{\text{EW}})$, which are not fully calculated by either Powheg or HATHOR. However, it is reasonable to assume that these cross terms factorize approximately, leading to the alternative multiplicative scheme [185]

$$\begin{aligned}
 d\sigma_{\text{mult.}} &= d\sigma_{\text{POWHEG}} \times \frac{d\sigma_{\text{HATHOR}}}{\alpha_S^2 d\sigma_{\text{LO}}} \\
 &= \alpha_S^2 d\sigma_{\text{LO}} + \alpha_S^3 d\sigma_{\text{NLO}} + \alpha_S^2 \alpha_{\text{EW}} d\sigma_{\text{EW}} + \alpha_S^3 \alpha_{\text{EW}} \frac{d\sigma_{\text{NLO}} d\sigma_{\text{EW}}}{d\sigma_{\text{LO}}}
 \end{aligned} \tag{7.12}$$

2476 The difference between the two schemes is in the last term of order $\mathcal{O}(\alpha_S^3 \alpha_{\text{EW}})$,
 2477 which is an approximation to the QCD-EW cross terms. In this work, the multi-
 2478 plicative approach is used for all nominal results, while the difference to the additive
 2479 approach is included as a systematic uncertainty. In both cases, the needed term
 2480 $\alpha_S^2 d\sigma_{\text{LO}}$ is computed with MADGRAPH 5.

2481 The effect of both approaches on the 3D $m_{t\bar{t}} \times c_{\text{hel}} \times c_{\text{han}}$ distribution at the
 2482 detector level after parton showering can be seen in Fig. 7.4 for different values of
 2483 y_t . The multiplicative scheme leads to a larger correction of roughly 2 – 4%, while
 2484 the additive scheme only gives 1 – 2%. Notably, the effect of varying y_t modifies not
 2485 only the $m_{t\bar{t}}$ distribution close to the $t\bar{t}$ threshold, but also the distribution of c_{hel} .
 2486 As a result, such a variation in data could potentially be confused for a pseudoscalar
 2487 signal. It is thus important to include it as a systematic uncertainty, as described
 2488 in Sec. 7.5.

2489 7.4 Matrix element reweighting for A/H signals

2490 In order to probe the full phase space of the generic A/H model as described in
 2491 Sec. 7.1, predictions at different A/H masses and widths with a sufficiently small
 2492 spacing are required so that interpolation between the points is possible. However,
 2493 generating a separate MC sample for each mass and width point is computationally
 2494 very expensive.

2495 7.4.1 Principle of the method

2496 As an alternative, it is possible to re-use existing samples for different mass and
 2497 width points via matrix element reweighting. This method works by noting that a
 2498 given MC sample can be seen as a random sample, drawn from a PDF of the form

$$\mathcal{P}(x_i^{\text{ME}}, x_j^{\text{reco}}) = \mathcal{P}^{\text{ME}}(x_i^{\text{ME}}) \cdot \mathcal{P}^{\text{rem}}(x_j^{\text{reco}} | x_i^{\text{ME}}) \tag{7.13}$$

2499 Here, x_i^{ME} are all variables defining the event at the matrix element (ME) level,
 2500 i.e. at the level of the hard interaction, and x_j^{reco} are all variables after detector
 2501 simulation and object reconstruction. For the case of the A/H signals, which are
 2502 generated at LO in QCD, x_i^{ME} is given fully by the four-momenta and helicities of
 2503 the final-state particles (leptons, neutrinos and b quarks) in the hard process. The

2504 x_j^{reco} consist of all possible reconstruction-level variables that are relevant to the
2505 analysis, such as e.g. jet and lepton four-momenta, lepton identification criteria or
2506 $\vec{p}_{\text{T}}^{\text{miss}}$.

2507 $\mathcal{P}^{\text{ME}}(x_i^{\text{ME}})$ refers to the probability density of the ME-level variables as predicted
2508 by the ME generator, which will be proportional to the absolute square of the matrix
2509 element. This function will depend on the chosen scenario of the A/H model, i.e.
2510 $m_{\text{A}/\text{H}}$ and $\Gamma_{\text{A}/\text{H}}$. Meanwhile, the conditional probability density $\mathcal{P}^{\text{rem}}(x_j^{\text{reco}}|x_i^{\text{ME}})$
2511 encodes the effects of all other components of the simulation chain, such as the
2512 parton shower, hadronization, detector simulation and reconstruction. It gives the
2513 probability to observe reconstruction-level variables x_j^{reco} for an event with ME-level
2514 variables x_i^{ME} .

2515 The principal assumption of the method is now that \mathcal{P}^{rem} , and thus the whole
2516 simulation chain except for the matrix element, is independent of the underlying
2517 A/H signal scenario ($m_{\text{A}/\text{H}}$ and $\Gamma_{\text{A}/\text{H}}$). This assumption is certainly true for the
2518 detector simulation and reconstruction, while care must be taken for the parton
2519 shower, which in general needs to be matched to the matrix element and can this
2520 way have a residual dependence. The validity of the assumption will be discussed
2521 in more detail below.

2522 If the assumption is fulfilled, a given A/H MC sample generated with parameters
2523 $m_{\text{A}/\text{H}}^0$ and $\Gamma_{\text{A}/\text{H}}^0$ can now be reweighted to a different A/H scenario with parameters
2524 $\hat{m}_{\text{A}/\text{H}}$ and $\hat{\Gamma}_{\text{A}/\text{H}}$ by applying to each event i a weight

$$w_i = \frac{\mathcal{P}^{\text{ME}}(x_i^{\text{ME}}|\hat{m}_{\text{A}/\text{H}}, \hat{\Gamma}_{\text{A}/\text{H}})}{\mathcal{P}^{\text{ME}}(x_i^{\text{ME}}|m_{\text{A}/\text{H}}^0, \Gamma_{\text{A}/\text{H}}^0)} \quad (7.14)$$

2525 The quantities in the denominator and nominator are the ME-level probability
2526 densities for each event, evaluated at the original and target A/H parameters, respec-
2527 tively. When this weight is inserted into Eq. (7.13), the original probability cancels,
2528 giving the correct probability density for the target scenario $\hat{m}_{\text{A}/\text{H}}$ and $\hat{\Gamma}_{\text{A}/\text{H}}$.

2529 In practice, this method will only work if the MC sample used for the reweighting
2530 has sufficient phase space overlap with the target A/H scenario, i.e. if the two
2531 probabilities in Eq. (7.14) are not too different from each other for the majority of
2532 the events. Otherwise, the weights will become very small in some regions of the
2533 phase space and very large in others, resulting in poor statistics for the reweighted
2534 sample.

2535 The method was implemented by directly evaluating the squared matrix elements
2536 for the different A/H hypotheses, using the standalone reweighting interface pro-
2537 vided by MADGRAPH 5 and the same UFO model as for the signal generation.

2538 7.4.2 Combination of multiple origin samples

2539 For the purpose of this analysis, a set of signal samples for different A/H scenarios
 2540 (as given in Sec. 7.2.1) was already available at the time of starting these studies.
 2541 These samples were used as origin samples for the reweighting. In order to maximize
 2542 the statistics achieved after reweighting for each target A/H scenario, and mitigate
 2543 problems from poor phase space overlap, a subset of the available samples were
 2544 combined after reweighting for each target scenario.

2545 This procedure works as follows: First, a set of several origin samples j with
 2546 different parameters $m_{A/H}$ and $\Gamma_{A/H}$ are all reweighted separately to the same target
 2547 parameters $\hat{m}_{A/H}$ and $\hat{\Gamma}_{A/H}$ with per-event weights $w_{i,j}$ as given in Eq. (7.14). Then,
 2548 the different samples are again weighted with a per-sample weight v_j proportional
 2549 to

$$v_j \propto \langle w_{i,j} \rangle^{-1} = \frac{\sum_i w_{i,j}}{\sum_i w_{i,j}^2} \quad (7.15)$$

2550 where the sums run over all events i in the considered sample j . This expression is
 2551 the inverse of the average ME weight for sample j . It is chosen such that samples
 2552 with large phase space overlap with the target A/H scenario - and thus small ME
 2553 weights $w_{i,j}$ - are assigned a large weight v_j in the combination of samples. Similarly,
 2554 samples with poor phase space overlap, and thus large average ME weights, get
 2555 assigned small weights and contribute less strongly to the combined sample. Finally,
 2556 the total combined sample is normalized to the expected cross section for the target
 2557 scenario, which is calculated independently. It can be shown that this procedure
 2558 minimizes the total statistical error of the combined sample.

2559 In practice, all available masses and parities (A and H) are combined for each
 2560 target A/H mass. Resonance and interference contributions are treated separately
 2561 from each other. Furthermore, it was found that, for the resonance contribution only,
 2562 it is necessary to split the combination of different A/H widths into two halves:
 2563 those with $\Gamma_{A/H}/m_{A/H}$ less or greater than 10%. This is due to an interplay of
 2564 MADGRAPH 5 and the PYTHIA shower leading to a dependency on the A/H width
 2565 in the matrix element, which is not taken into account in the reweighting. For
 2566 $\Gamma_{A/H}/m_{A/H} < 10\%$ (narrow resonance), MADGRAPH 5 includes the intermediate
 2567 A/H particle in the event record, which is then treated by PYTHIA as a unstable
 2568 resonance and its virtuality as predicted by the matrix element is preserved. For
 2569 $\Gamma_{A/H}/m_{A/H} \geq 10\%$ (broad resonance), the A/H particle is not included in the event
 2570 record, and its virtuality is thus not preserved. This leads to slight differences in
 2571 distributions affected by the parton showering. The choice of 10% for the transition
 2572 between the two modes is an arbitrary parameter, and thus not necessarily physical.
 2573 Nonetheless, it was decided in this analysis to not mix the two width ranges in the
 2574 reweighting in order to obtain full closure with a standalone generation.

2575 7.4.3 Validation

2576 The combined reweighting is validated for three masses of $m_{A/H} = 400, 600$ and 800
2577 GeV as well as widths of 2.5 and 10% . For each of these points, the reweighting is
2578 performed as stated above, but leaving out A/H scenarios with the same mass from
2579 the combination of origin samples since otherwise the weights would be trivially
2580 one. The reweighted $m_{t\bar{t}}$ distributions at generator level are then compared to the
2581 standalone samples at the same $m_{A/H}$ and $\Gamma_{A/H}$.

2582 The resulting comparisons and residuals can be seen in Fig. 7.6 for A and H,
2583 separated into the resonance and interference contributions. It can be seen that
2584 the closure between reweighting and standalone generation is excellent within the
2585 statistical uncertainties.

2586 7.5 Systematic uncertainties

2587 Similar to Sec. 5.5, systematic uncertainties affect the distributions of both SM
2588 background and signal processes. They are listed in this section, split into theory
2589 (Sec. 7.5.1) and experimental uncertainties (Sec. 7.5.2).

2590 7.5.1 Theory uncertainties

2591 **Scale uncertainties** Uncertainties due to missing higher orders in the matrix el-
2592 ement as well as the parton shower are included separately for the SM $t\bar{t}$, tW, and
2593 Z/γ^* +jets backgrounds as well as all considered signals by varying the associated
2594 scales by a factor 2 up and down independently, same as in Sec. 5.5. For A and
2595 H, the uncertainties are considered uncorrelated between the resonance and inter-
2596 ference components, which is found to be conservative. For η_t , the renormalization
2597 scale uncertainty is not included since the considered model does not encode any
2598 dependence on either μ_R or α_S .

2599 **PDF uncertainties** For the SM $t\bar{t}$ background, the uncertainty due to the PDF is
2600 again included based on the 100 provided eigenvalues of the used NNPDF 3.1 PDF
2601 set. However, it is not considered sufficient to simply take the envelope of these
2602 variations since this would distort possible shape variations. Instead, a principal
2603 component analysis (PCA) is performed on the final 3D $m_{t\bar{t}} \times c_{\text{hel}} \times c_{\text{han}}$ templates
2604 obtained from the different eigenvalues, thus finding those linear combinations that
2605 have a noticeable shape effect. It is found that only the first eigenvector (correspond-
2606 ing to the largest eigenvalue) is non-negligible, and this variation is considered as
2607 the PDF uncertainty. For more details on this procedure, see Ref. [172]. Independ-
2608 ently of this, another uncertainty based on the value of α_S in the PDF is considered
2609 similarly to Sec. 5.5.

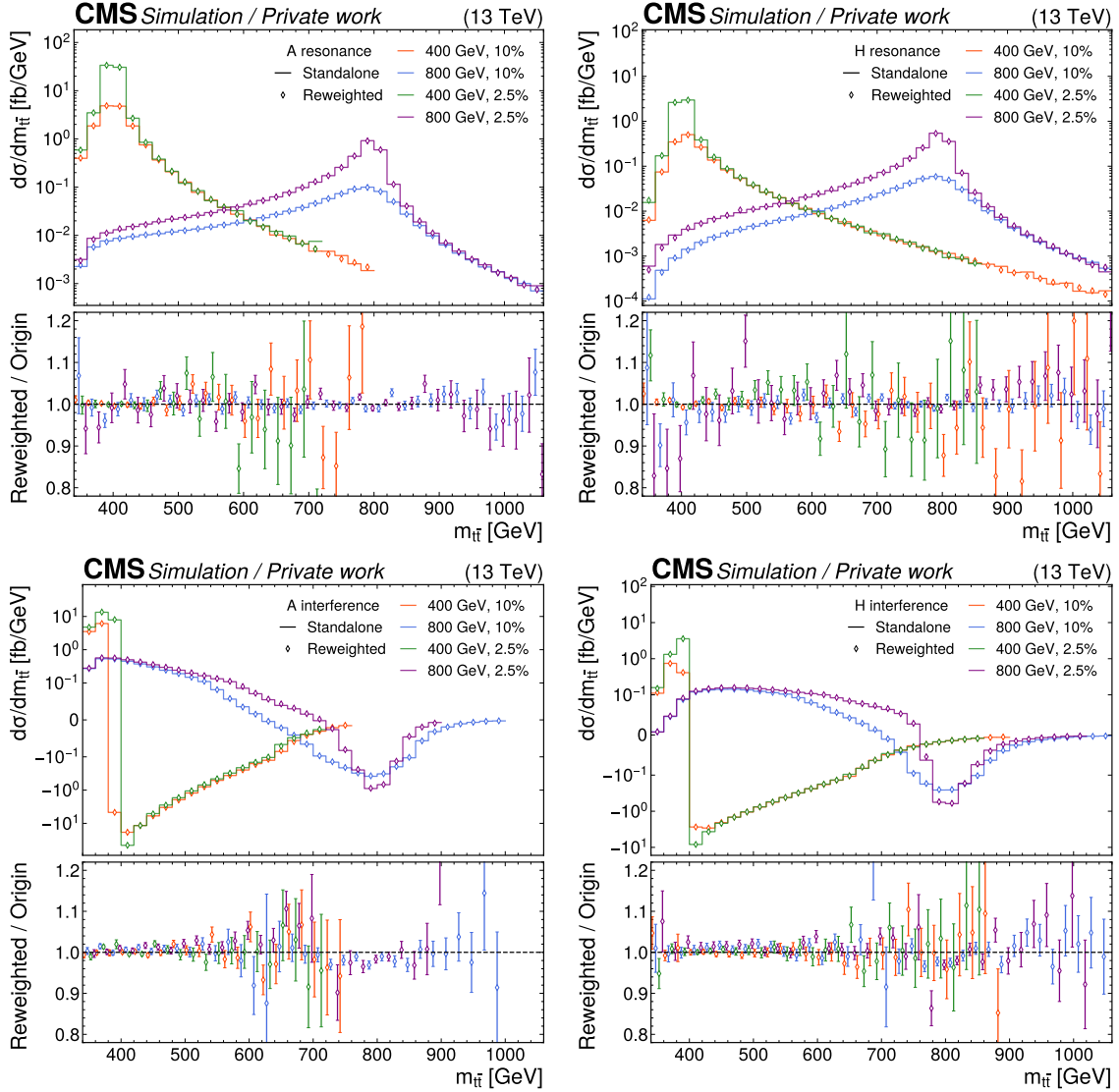


Figure 7.6: Validation of the ME reweighting. Comparison of standalone generated (lines) and reweighted (diamond markers) $m_{t\bar{t}}$ distributions for different values of $m_{A/H}$ and $\Gamma_{A/H}$. From top left to bottom right: A resonance, H resonance, A interference, H interference. The lower panel shows the ratio of reweighted and standalone distributions. The error bars give the combined statistical uncertainty of the reweighted and standalone sample.

EW correction uncertainties As described in Sec. 7.3.2, two independent uncertainties are attached to the NLO electroweak correction of SM $t\bar{t}$: First, the value of the SM top-Higgs Yukawa coupling is allowed to vary in the range $y_t = 1.00^{+0.11}_{-0.11}$, with the range given by the uncertainty of the experimental measurement in Ref. [186]. Second, the difference between the additive and multiplicative application scheme (Eqs. (7.11) and (7.12)) is considered as a separate uncertainty, as recommended in Ref. [185], and symmetrized around the nominal.

Top quark mass uncertainty The top quark mass uncertainty in SM $t\bar{t}$ is estimated by varying it from its nominal value of $m_t = 172.5 \text{ GeV}$ by $\pm 3 \text{ GeV}$ in the POWHEG simulation, and then scaling down the resulting relative deviation by a factor $1/3$, leading to a $\pm 1 \text{ GeV}$ uncertainty. This is done since the variation, obtained from an independent MC sample, is otherwise plagued by large statistical uncertainties. Furthermore, the top mass is also varied in all considered signal samples directly by $\pm 1 \text{ GeV}$ through an ME reweighting method similar to Sec. 7.4. The top mass uncertainties between background and signals are considered as fully correlated.

Further uncertainties in SM $t\bar{t}$ Additionally, separate SM $t\bar{t}$ samples are used to evaluate uncertainties due to ME/PS matching (same as in Sec. 5.5), the underlying event tune [81], and the color reconnection model in PYTHIA [85, 187]. All of these effects are found to be small in the channels considered here.

Background cross section uncertainties For the SM $t\bar{t}$ background, instead of including an explicit cross section uncertainty, the shift in the predicted NNLO+NNLL $t\bar{t}$ cross section due to the ME scales and the top quark mass is correlated with the respective uncertainties. For minor backgrounds, explicit uncertainties of 15% for tW and t-channel single top [188–190], 30% for diboson and $t\bar{t} + X$ [191, 192], and 5% for the data-driven $Z/\gamma^* + \text{jets}$ normalization [193] are considered, which are all based on the precision of relevant cross section measurements.

Background statistical uncertainties Again similar to Sec. 5.5, per-bin background statistical uncertainties for all simulated processes are included following Ref. [139].

7.5.2 Experimental uncertainties

Jet and p_T^{miss} uncertainties The uncertainty on the calibration of the jet p_T detector response is split into five subsources, of which three are considered uncorrelated between years and two (related to the response to jets of different flavor) are correlated. Further subsources as provided by CMS are found to be negligible

for this analysis [130]. Furthermore, the uncertainty in the jet p_T resolution is considered separately, again uncorrelated between years. All jet uncertainties are fully propagated to the calculation of p_T^{miss} , and an additional p_T^{miss} uncertainty based on soft, unclustered hadronic activity is also considered.

b tagging uncertainties Similarly, the uncertainty on the b tagging efficiency is split into 17 subsources, corresponding e.g. to different parton shower modeling, the treatment of leptons in the jet, or the propagation of the jet p_T scale uncertainties [129]. One component represents the statistical uncertainty and is thus considered uncorrelated, while all others are correlated among years. Moreover, an uncertainty on mistagging of light-flavor jets is included, also split into a statistical and a systematic component.

Lepton and trigger uncertainties Uncertainties on the lepton reconstruction, identification, and isolation efficiencies, as measured centrally in CMS using the tag-and-probe method, are considered separately for muons and electrons [100, 128]. For the muons, the uncertainty is split into a statistical component (uncorrelated between the analysis years) and a systematic component (correlated). Similarly, the dilepton trigger efficiency uncertainties are considered uncorrelated between years and lepton flavor channels. Finally, in data taken in 2016 or 2017, an additional uncertainty is assigned due to an inefficiency in the ECAL L1 trigger [106], as described in Sec. 7.2.4.

Luminosity uncertainty The uncertainty on the total integrated luminosity is included following Refs. [87, 194, 195], leading to a total luminosity uncertainty of 1.6%, split into a total of seven components with different correlations between the years.

Pileup uncertainty To estimate the uncertainty on the amount of pileup per pp bunch crossing, the effective inelastic proton-proton cross section used for pileup reweighting in the simulation is varied by 4.6% from its nominal value [196].

7.5.3 Uncertainty smoothing

Several of the considered uncertainty sources, e.g. the top quark mass in SM $t\bar{t}$, are estimated by either comparing to separate MC samples, which causes the relative deviation due to the source to be affected by large statistical noise. A similar problem appears for uncertainties which effectively vary the cuts applied on MC events, such as e.g. the jet p_T scale uncertainties by way of jet acceptances. If left untreated, fitting these noisy shape templates to the data could lead to erroneous constraints in the likelihood fit. To prevent this, the smoothing algorithm LOWESS [197, 198]

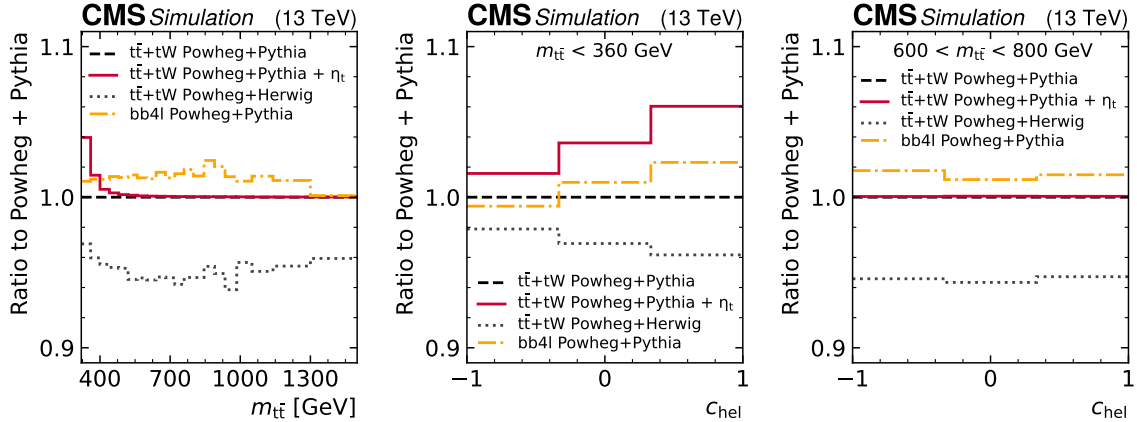


Figure 7.7: **Comparison between MC generators for $t\bar{t} + tW$.** The ratio of the predictions between POWHEG hvq $t\bar{t}$ matched to HERWIG and to PYTHIA as well as between bb4l and $t\bar{t} + tW$ matched to PYTHIA for the inclusive reconstructed $m_{t\bar{t}}$ distribution (left) and the reconstructed c_{hel} distribution, restricted to $m_{t\bar{t}} < 360$ GeV (center) and to $600 < m_{t\bar{t}} < 800$ GeV. The effect of the η_t signal is also shown for comparison. *Figure taken from Ref. [9].*

is applied to the relative deviations for these sources, with the bandwidth used for the smoothing determined separately through cross-validation for each source. For more details on the procedure, see Ref. [28].

7.5.4 Differences between MC generators

It has been observed in previous analyses that the theoretical uncertainties collected in Sec. 7.5.1 do not necessarily cover the differences in the predictions of different MC generators for $t\bar{t}$ [26, 27, 153, 199]. To assess the size of these effects, the standard $t\bar{t}$ prediction as computed using POWHEG hvq matched to PYTHIA is compared to alternate generator setups.

The first of these is the same POWHEG hvq matrix element matched to the multi-purpose event generator HERWIG instead of PYTHIA. The angular-ordered parton shower in HERWIG is used (as opposed to the p_T -ordered dipole shower in PYTHIA) together with the CMS CH3 tune [200]. Furthermore, HERWIG uses a cluster hadronization model [201] instead of the string hadronization model of PYTHIA as described in Sec. 3.4.

Figure 7.7 shows the ratios of the predictions from HERWIG and PYTHIA for the reconstructed $m_{t\bar{t}}$ distribution, as well as for the c_{hel} distribution close to the $t\bar{t}$ threshold (i.e. where the η_t signal is located) and in the $t\bar{t}$ continuum. Besides a significantly lower $t\bar{t}$ acceptance, HERWIG predicts an increase of events at the $t\bar{t}$

threshold similar to η_t . This appears concerning at first glance since, should the data follow the prediction from HERWIG instead of PYTHIA, this enhancement could be confused with an η_t signal if PYTHIA is used as the baseline prediction. However, as seen in Fig. 7.7 in the center, HERWIG at the same predicts a flatter slope in c_{hel} than PYTHIA at the $t\bar{t}$ threshold, equivalent to a dilution of $t\bar{t}$ spin correlations¹. This is in contrast to the η_t signal, in which the $t\bar{t}$ spins are maximally anticorrelated. The inclusion of the spin correlation variable c_{hel} in the analysis thus makes it possible to separate the differences between POWHEG and HERWIG with respect to η_t .

The second alternative generator is **bb41** matched to PYTHIA, as studied extensively in Chapter 6. Here, particularly the off-shell effects included in **bb41** might be of interest for the extraction of η_t since the latter is located below the $t\bar{t}$ threshold. The setup denoted as “**bb41 v2**” in Sec. 6.2, corresponding to Ref. [154], is used, and compared to the sum of the POWHEG **hvq** $t\bar{t}$ and tW predictions for consistency.

A caveat here is presented by the corrections to NNLO QCD and NLO EW as described in Sec. 7.3. These are derived from fixed-order corrections assuming stable top quarks, and are not available for the full $b\bar{b}\ell\ell\nu\nu$ final state. To still be able to apply them to **bb41** predictions, the **bb41** sample is split into a $t\bar{t}$ and a tW part in an ad-hoc way by using the matrix element history projectors implemented in **bb41 v2** [154]. The corrections are then applied to the $t\bar{t}$ part only, in the same manner as to POWHEG **hvq**.

The ratios of the predictions are also shown in Fig. 7.7. It can be seen that **bb41** does not predict major differences in the reconstructed $m_{t\bar{t}}$ spectrum even at its lower edge. However, it results in a significantly steeper slope in reconstructed c_{hel} close to the threshold. This increase in slope is of similar magnitude as the effect expected due to η_t .

The source of this difference is not yet fully understood. **bb41** contains NLO QCD corrections to the top decay which are not present in **hvq** (though they are approximated through the matrix element corrections in PYTHIA). However, NLO corrections to spin correlations are expected to not only be small, but reduce the spin correlation instead of enhancing it [18].

It is possible that the effect instead originates in the $t\bar{t}/tW$ interference: For the tW contribution, where one of the leptons is not actually the decay product of a top quark, $t\bar{t}$ spin correlation is not truly definable. The slope of the reconstructed c_{hel} distribution, obtained under the assumption that the events contain a $t\bar{t}$ system, will thus be arbitrary with no clear *a priori* expectation, and in general different to the slope in SM $t\bar{t}$. The same holds for the $t\bar{t}/tW$ interference. Since **bb41** now gives a true (though effectively LO) prediction of the $t\bar{t}/tW$ interference instead of the ad-hoc treatment of the DR and DS schemes (cf. Sec. 6.3), it is expected that the magnitude of the interference contribution in **bb41** will be different. Thus, it is possible that the total c_{hel} slope, arising from the combination of $t\bar{t}$, tW , and $t\bar{t}/tW$

¹This effect was also seen in the context of Ref. [27].

interference, will be different as well. However, since $t\bar{t}$ and tW are not cleanly separable in **bb41**, however, this hypothesis is difficult to confirm, and such studies are beyond the scope of this analysis.

A third alternative prediction is provided by $t\bar{t}$ + jets production simulated with **MG5_AMC@NLO**, matched to **PYTHIA** with the FxFx scheme [202]. While this prediction is formally also NLO-accurate in QCD in the NWA, and thus comparable to **POWHEG hvq**, it has been observed in past measurements that **MG5_AMC@NLO** does not agree as well with data as **POWHEG** for $t\bar{t}$ production. As a result, **MG5_AMC@NLO** is given less focus compared to the other two predictions in this work.

In this work, **POWHEG hvq** + **PYTHIA** is considered for the nominal background prediction in all cases. A comparison to **POWHEG hvq** + **HERWIG**, **MG5_AMC@NLO** + **PYTHIA**, and **bb41** + **PYTHIA** is shown in Sec. 7.7.3 in the context of measuring the η_t cross section. Furthermore, the effect of including the differences to **POWHEG hvq** + **HERWIG** and **bb41** + **PYTHIA** as two additional shape-based nuisance parameters in the fit is similarly given in Sec. 7.7.3. Note that in Ref. [9], these nuisance parameters were considered as part of the main result in order to be conservative with respect to the total uncertainty.

7.6 Pre-fit distributions

The agreement between the total MC prediction, including all corrections described in Secs. 7.2.4 and 7.3, and the observed data are presented in this section. Shown observables are lepton p_T , η , and $\Delta\phi_{\ell\ell}$ (Fig. 7.8); jet p_T , η , and number of jets (Fig. 7.9); as well as p_T^{miss} , the invariant mass of the two leptons $m_{\ell\ell}$, and the invariant mass of the two leptons and two b-tagged jets $m_{b\bar{b}\ell\ell}$ (Fig. 7.10). All of them are shown after all lepton, jet, b tag and p_T^{miss} requirements, but before the $t\bar{t}$ reconstruction, summed over all analysis years, and separately for the same-flavor (ee and $\mu\mu$) and opposite-flavor ($e\mu$) channels, since the latter have different backgrounds and cuts.

Furthermore, different distributions resulting from the $t\bar{t}$ reconstruction are shown in Fig. 7.11, this time summed also over lepton flavor. They consist of top quark p_T , η , and scattering angle $\cos\theta^*$, as well as the three observables used for the fit $m_{t\bar{t}}$, c_{hel} , and c_{han} .

It can be seen that there is a slight but consistent overprediction of the background normalization compared to the data in almost all distributions. Furthermore, there is a slight slope in the ratio of data and simulation yields in the p_T of leptons, jets or the reconstructed top quarks. This is likely a result of the well-known top quark p_T mismodeling at the LHC, which is not fully removed by NNLO QCD corrections as used here [203, 204]. Further discrepancies are found for high values of $|\eta|$ and for large number of jets, both of which are covered by systematic uncertainties.

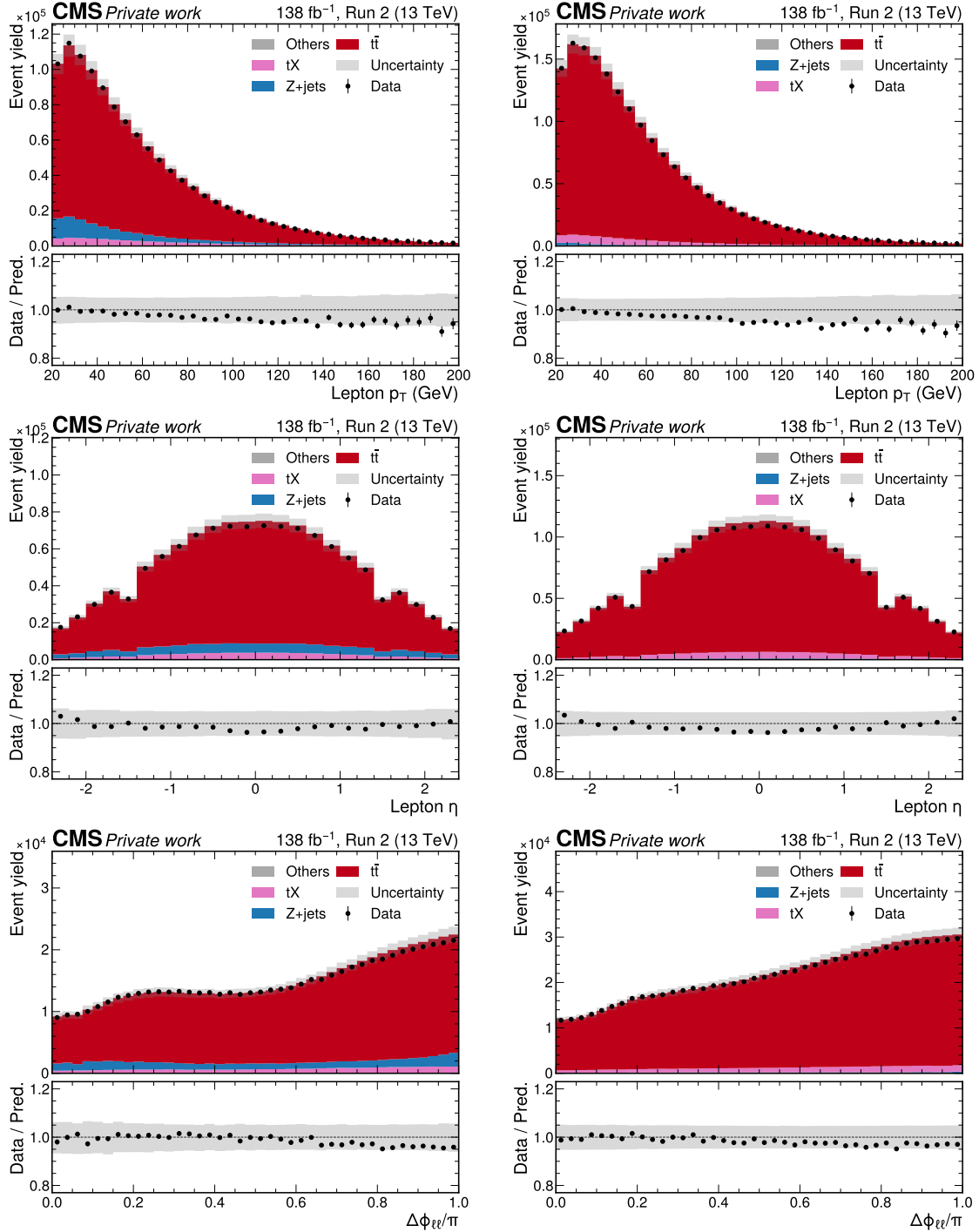


Figure 7.8: Control distributions. Shown are the distributions of p_T of both leptons (top), η of both leptons (center), and the azimuthal angle $\Delta\phi_{\ell\ell}$ between the leptons (bottom) in the $ee/\mu\mu$ (left) and $e\mu$ channels (right). All figures show both data (black dots) and different simulated background processes (colored bars), as well as the total systematic uncertainty (grey band).

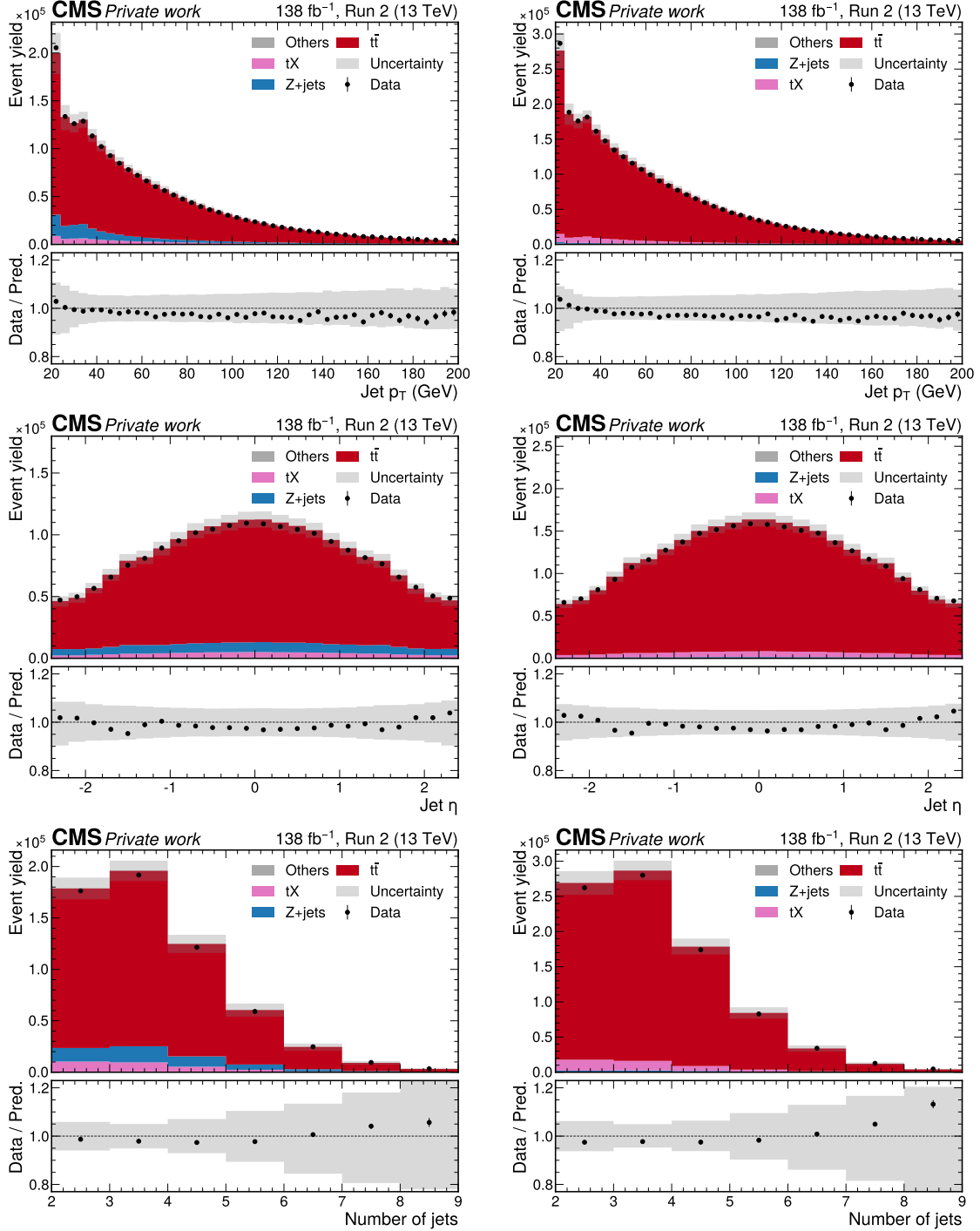


Figure 7.9: Control distributions. Shown are the distributions of p_T of all jets (top), η of all jets (center), and the number of jets (bottom) in the ee/ $\mu\mu$ (left) and e μ channels (right). All figures show both data (black dots) and different simulated background processes (colored bars), as well as the total systematic uncertainty (grey band).

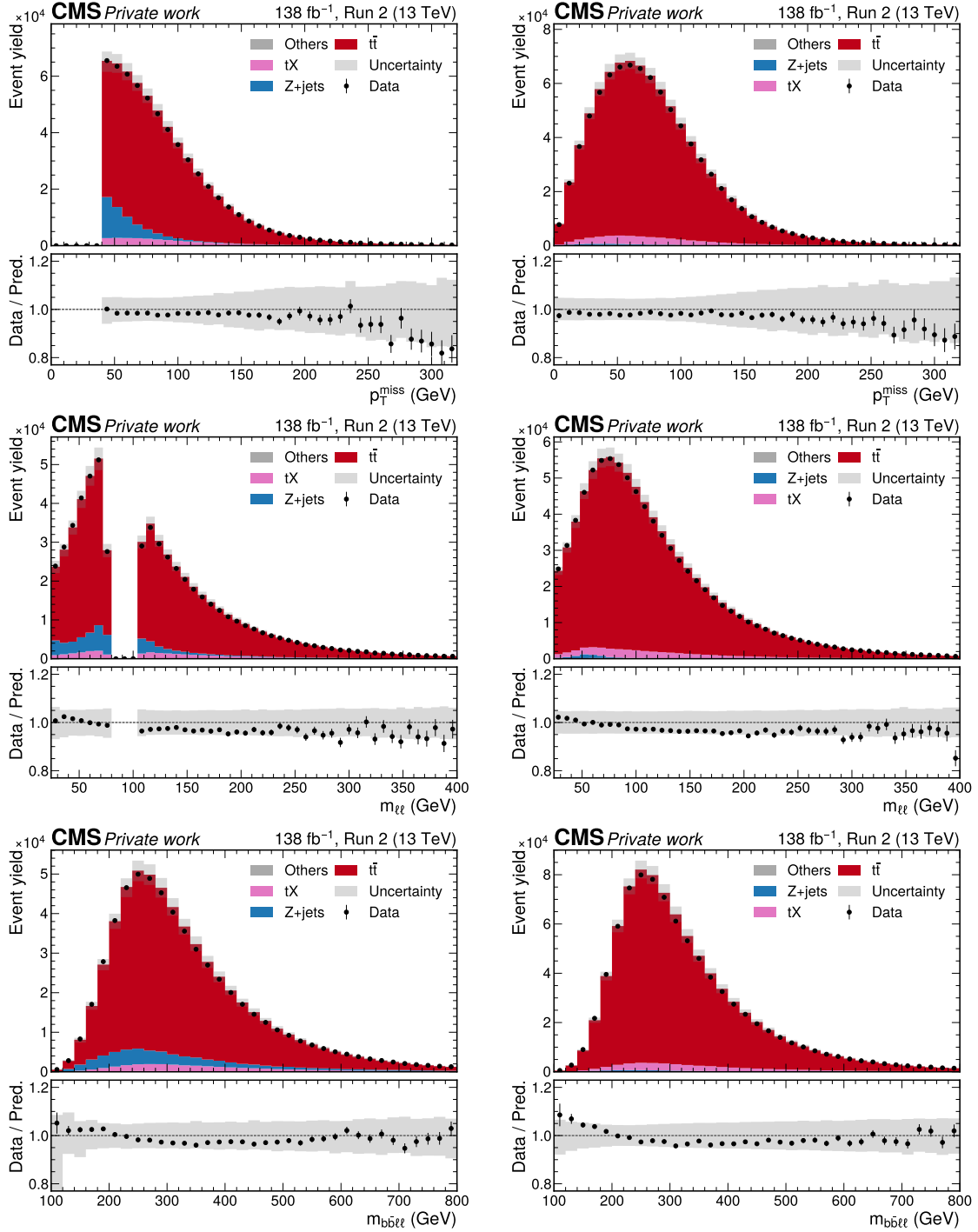


Figure 7.10: Control distributions. Shown are the distributions of p_T^{miss} (top), $m_{\ell\ell}$ (center), and the invariant mass $m_{bb\ell\ell}$ of both b candidates and both leptons (bottom) in the ee/μμ (left) and eμ channels (right). All figures show both data (black dots) and different simulated background processes (colored bars), as well as the total systematic uncertainty (grey band).

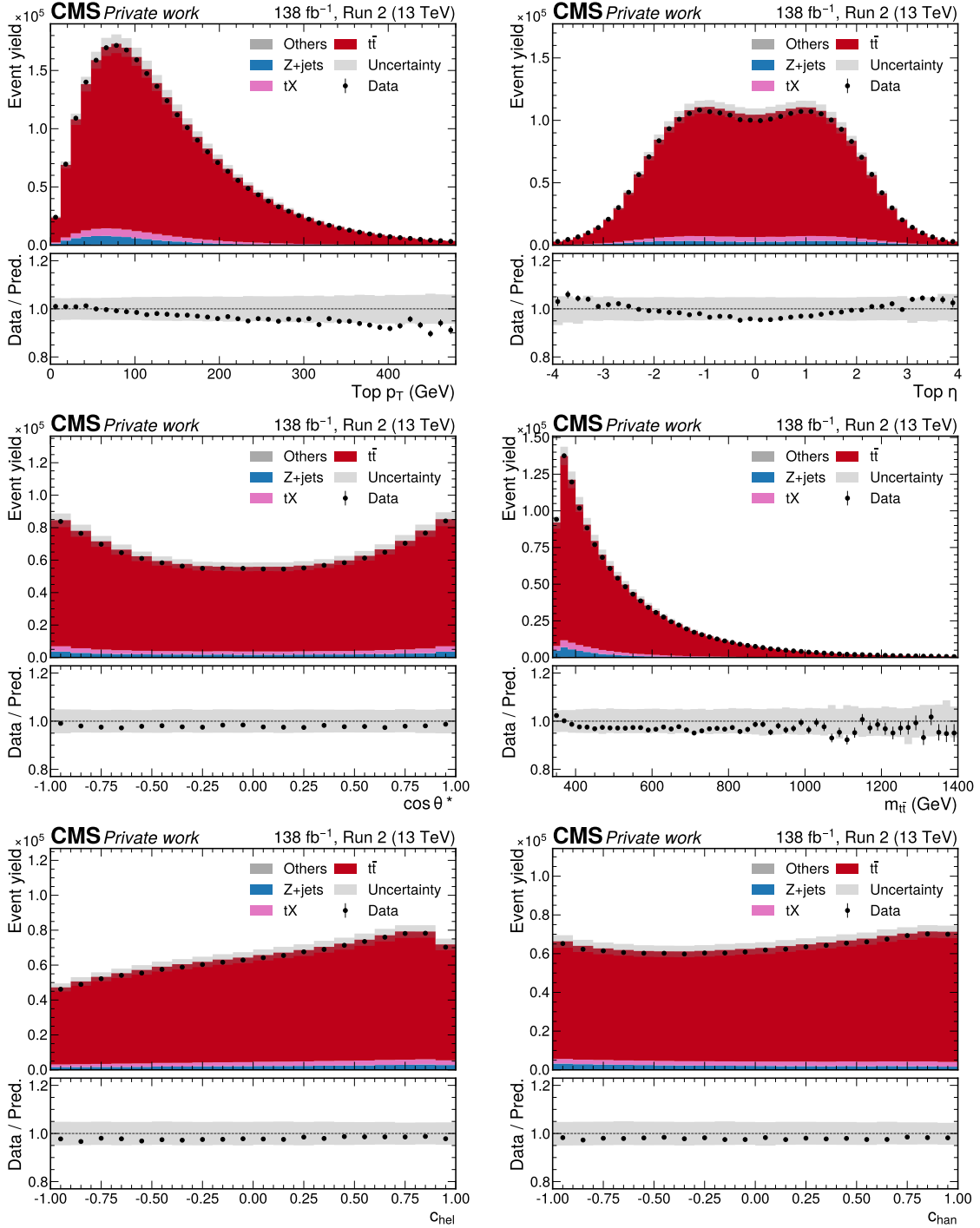


Figure 7.11: Control distributions after $t\bar{t}$ reconstruction. Shown are (from top left to bottom right) the distributions of the top quark p_T , top quark η , $m_{t\bar{t}}$, $\cos \theta^*$, c_{hel} and c_{chan} for the sum of all dilepton channels. All figures show both data (black dots) and different simulated background processes (colored bars), as well as the total systematic uncertainty (grey band).

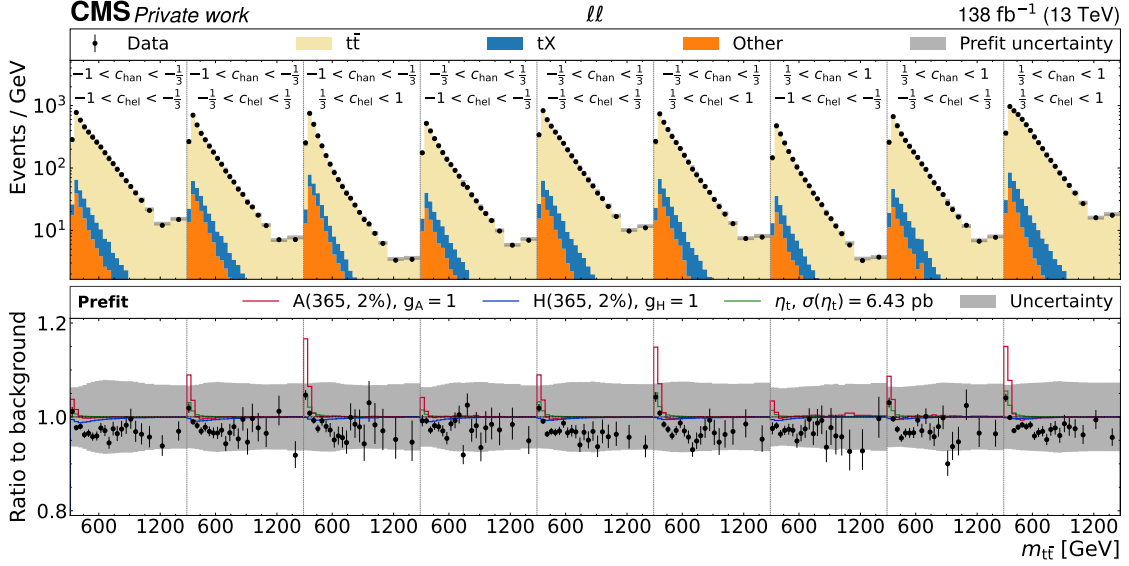


Figure 7.12: **Prefit distributions of $m_{t\bar{t}} \times c_{\text{hel}} \times c_{\text{han}}$.** The unrolled three-dimensional distribution in $m_{t\bar{t}}$, c_{hel} and c_{han} as used for statistical analysis before the fit to the data, summed over all years and lepton flavors. The upper panel shows the sum of the background simulation (colored bars) and the observed data (black dots), while the lower panel shows the ratio of the data to the prediction, with different signals overlaid: A (red) and H (blue), both for $m_{A/H} = 365 \text{ GeV}$ and $\Gamma_{A/H}/m_{A/H} = 2\%$, and η_t (green). *Figure adapted from Ref. [8].*

Finally, the three-dimensional $m_{t\bar{t}} \times c_{\text{hel}} \times c_{\text{han}}$ distribution used for the statistical analysis is shown before the fit, including all systematic uncertainties, in Fig. 7.12. A notable excess of the data compared to the prediction is observed for low values of $m_{t\bar{t}}$, consistent with the excess seen in the one-dimensional $m_{t\bar{t}}$ distribution (Fig. 7.11) and in the related observables $m_{\ell\ell}$ and $m_{b\bar{b}\ell\ell}$ (Fig. 7.10). The excess is stronger for large values of c_{hel} as seen from the multi-dimensional binning, while no trend can be seen by eye regarding c_{han} .

7.7 Interpretation of the excess

7.7.1 Extraction of $t\bar{t}$ bound state effects

The prefit excess visible in Fig. 7.12 is interpreted in terms of a pseudoscalar $t\bar{t}$ bound state by performing a signal+background fit with η_t as the signal, as defined in Sec. 2.2.3. The POI in the fit is $\sigma(\eta_t)$, the cross section of the η_t model, which can be understood as the difference between the data and the fixed-order perturbative

2791 QCD (FO pQCD) background prediction. It is measured to be

$$\sigma(\eta_t) = 8.7 \pm 0.5(\text{stat}) \pm 1.0(\text{syst}) \text{ pb} = 8.7 \pm 1.1 \text{ pb}. \quad (7.16)$$

2792 The statistical and systematic component of the uncertainty are estimated as
2793 described in Sec. 4.4. The significance of the result compared to a background-only
2794 hypothesis, i.e. without a bound state, is more than five standard deviations.

2795 The result is of a similar order of magnitude as the prediction of 6.43 pb given in
2796 Ref. [37], obtained by fitting the results of an NRQCD calculation from Ref. [33],
2797 though this result is not one-to-one comparable since it considers only the range of
2798 $m_{t\bar{t}} \in [338, 350] \text{ GeV}$. It should be noted that the results of Ref. [33] (as well as the
2799 newer ones in Ref. [35]) were obtained by using NLO hard functions for the NRQCD
2800 calculations, and moving to NNLO might give a significant increase in cross section,
2801 by analogy to the difference in NNLO and NLO cross sections for the $t\bar{t}$ continuum.
2802 Furthermore, the NRQCD approach employed in these calculations considers only
2803 the ground state wavefunction of the bound $t\bar{t}$ system, and independent calculations
2804 have shown that including contributions from excited states could increase the cross
2805 section by orders of 15–20% [205, 206].

2806 The postfit $m_{t\bar{t}} \times c_{\text{hel}} \times c_{\text{chan}}$ distribution can be seen in Fig. 7.13. The data,
2807 including the excess at low $m_{t\bar{t}}$, is described well by the η_t model combined with the
2808 FO pQCD background. To illustrate this further, one-dimensional projections of the
2809 $m_{t\bar{t}} \times c_{\text{hel}} \times c_{\text{chan}}$ template into inclusive $m_{t\bar{t}}$, as well as into c_{hel} for both low and high
2810 $m_{t\bar{t}}$, are shown in Fig. 7.14. One can clearly see that the data at the $t\bar{t}$ threshold
2811 shows a stronger slope in data than in the FO pQCD prediction, consistent with the
2812 η_t signal, while no such slope is seen at high $m_{t\bar{t}}$, i.e. in the $t\bar{t}$ continuum.

2813 7.7.2 Parity of the excess

2814 To investigate whether the observed excess is \mathcal{CP} -odd (pseudoscalar) or \mathcal{CP} -even
2815 (scalar) in nature, a simultaneous fit is performed with both η_t and χ_t , as defined in
2816 Sec. 2.2.3, as freely floating signals. These correspond to pure 1S_0 and 3P_0 $t\bar{t}$ states,
2817 respectively, both localized at the $t\bar{t}$ threshold.

2818 The result is shown in Fig. 7.15 in the form of compatibility contours. Consistent
2819 with the result of the η_t -only fit, a non-zero η_t contribution is preferred by the fit by
2820 more than 5 standard deviations. By contrast, the measured χ_t cross section, which
2821 can be seen as the 3P_0 component of the excess, is compatible with zero within
2822 one standard deviation. Based on this, it can be said that the observed excess is
2823 dominated by a pseudoscalar or 1S_0 spin state.

2824 7.7.3 Checks of the result

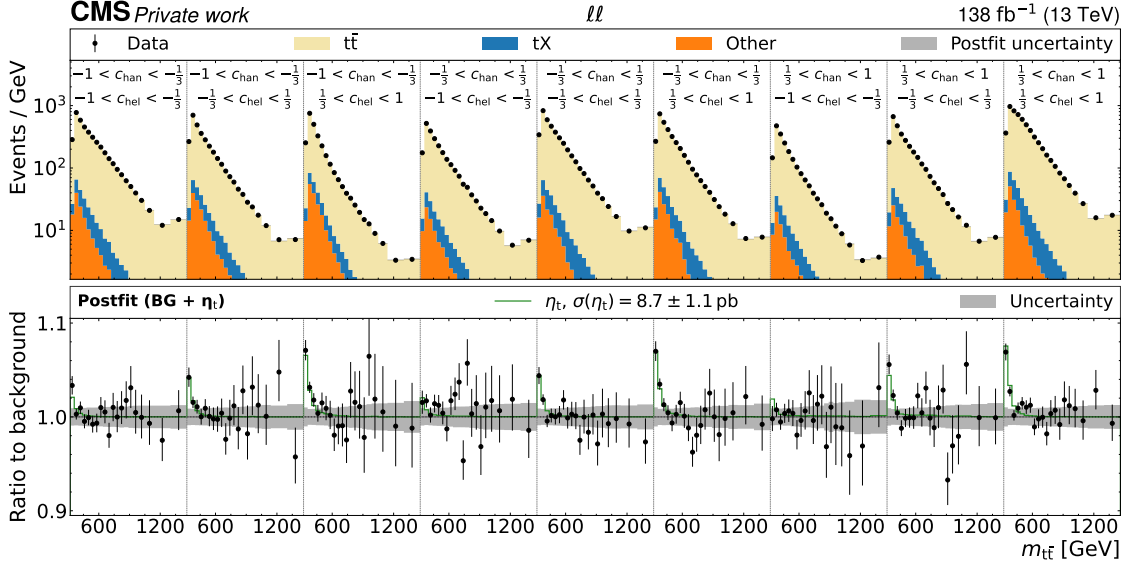


Figure 7.13: **Postfit distributions of $m_{t\bar{t}} \times c_{hel} \times c_{han}$ for the η_t fit.** The unrolled three-dimensional distribution in $m_{t\bar{t}}$, c_{hel} and c_{han} as after the fit to data with η_t as the signal, summed over all years and lepton flavors. The upper panel shows the sum of the background simulation (colored bars) and the observed data (black dots), while the lower panel shows the ratio of the data to the prediction with the postfit η_t signal overlaid. *Figure adapted from Ref. [9].*

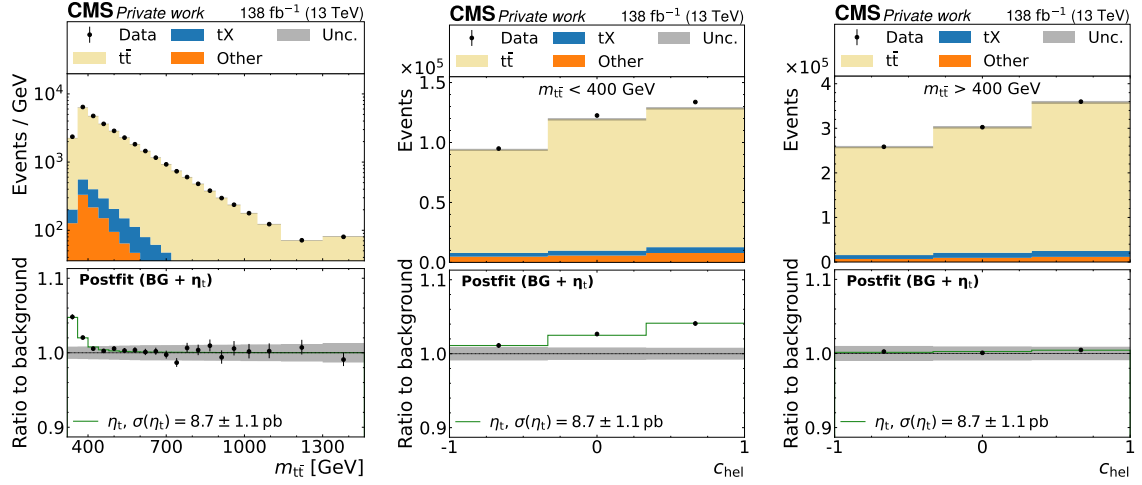


Figure 7.14: **Postfit distributions of $m_{t\bar{t}}$ and c_{hel} for the η_t fit.** One-dimensional distributions of inclusive $m_{t\bar{t}}$ (left), c_{hel} for $m_{t\bar{t}} < 400 \text{ GeV}$ (center), and c_{hel} for $m_{t\bar{t}} > 400 \text{ GeV}$ (right), projected from the $m_{t\bar{t}} \times c_{hel} \times c_{han}$ template in Fig. 7.13 with the same notations. *Figure adapted from Ref. [9].*

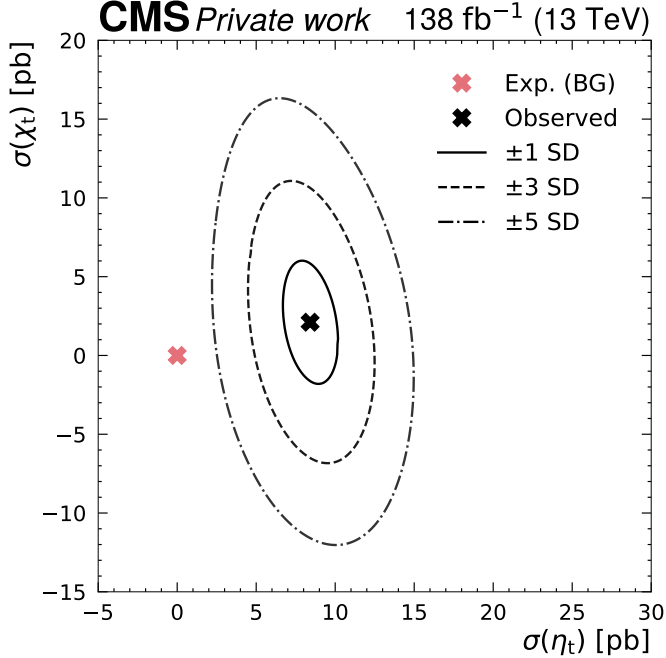


Figure 7.15: **Parity of the excess.** Observed compatibility contours in a simultaneous fit of η_t (corresponding to 1S_0) and χ_t (corresponding to 3P_0). The best-fit point is shown as the black cross, while the BG-only expectation (i.e. $\sigma(\eta_t) = \sigma(\chi_t) = 0$) is marked in pink. *Figure adapted from Ref. [9].*

Nuisance parameter pulls and impacts In Fig. 7.16, nuisance parameter pulls, constraints and impacts for the η_t extraction fit are presented, following the definitions in Sec. 4.4. The most impactful nuisances are all related to the modeling of the $t\bar{t}$ background. In particular, the value of the top Yukawa coupling y_t in the EW corrections is the leading uncertainty. This is notably one of the few uncertainties which can lead to a steeper c_{hel} slope in the $t\bar{t}$ prediction and could thus to some degree be confused for η_t , as discussed in Sec. 7.3.2. Further important modeling uncertainties are the FSR scales in the $t\bar{t}$ parton shower as well as the top quark mass.

On the other hand, experimental nuisances which influence mostly $m_{t\bar{t}}$ like the jet energy scales do not have a large impact on the POI. Regardless, no pulls larger than one prefit standard deviation are observed, indicating that the uncertainty model accommodates the data well.

Fit using $m_{b\bar{b}\ell\ell}$ instead of $m_{t\bar{t}}$ The three observables $m_{t\bar{t}}$, c_{hel} and c_{han} are all obtained from the kinematic reconstruction as described in Sec. 7.2.5. This procedure assumes, among others, that the top quarks are exactly on-shell with

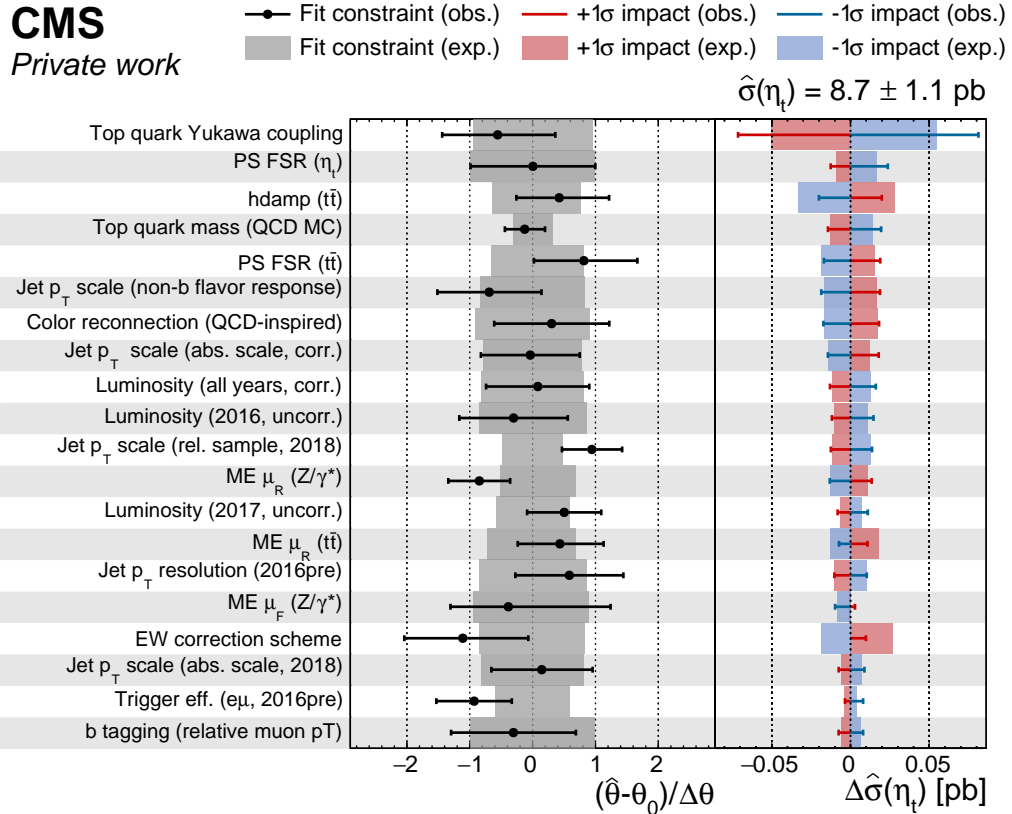


Figure 7.16: **Nuisance parameter pulls and impacts.** Expected and observed pulls, constraints, and impacts on the η_t cross section for the most impactful nuisance parameters in the η_t -only fit. *Figure adapted from Ref. [9].*

2841 a fixed mass of 172.5 GeV. For η_t , which is located below the $t\bar{t}$ threshold, this
 2842 assumption is clearly violated. Since the same kinematic reconstruction procedure
 2843 is applied to simulation and data, this is in principle not a problem as long as
 2844 the virtuality of the top quarks is well described by simulation. However, since the
 2845 modeling of η_t in particular is rather uncertain, it is still important to check whether
 2846 this assumption in the kinematic reconstruction introduces any bias.

This is done by repeating the fit with the observable $m_{t\bar{t}}$ replaced by $m_{b\bar{b}ll}$ (as shown also in Fig. 7.10), thus removing kinematic information obtained via the reconstruction from the fit. The kinematic reconstruction is still performed, however, to obtain c_{hel} and c_{han}^2 .

2851 The resulting $m_{bb\ell\ell} \times c_{\text{hel}} \times c_{\text{chan}}$ postfit distribution can be found in Figs. 7.17

²It has separately been checked that the requirement for events to pass the kinematic reconstruction does not bias the result, either.

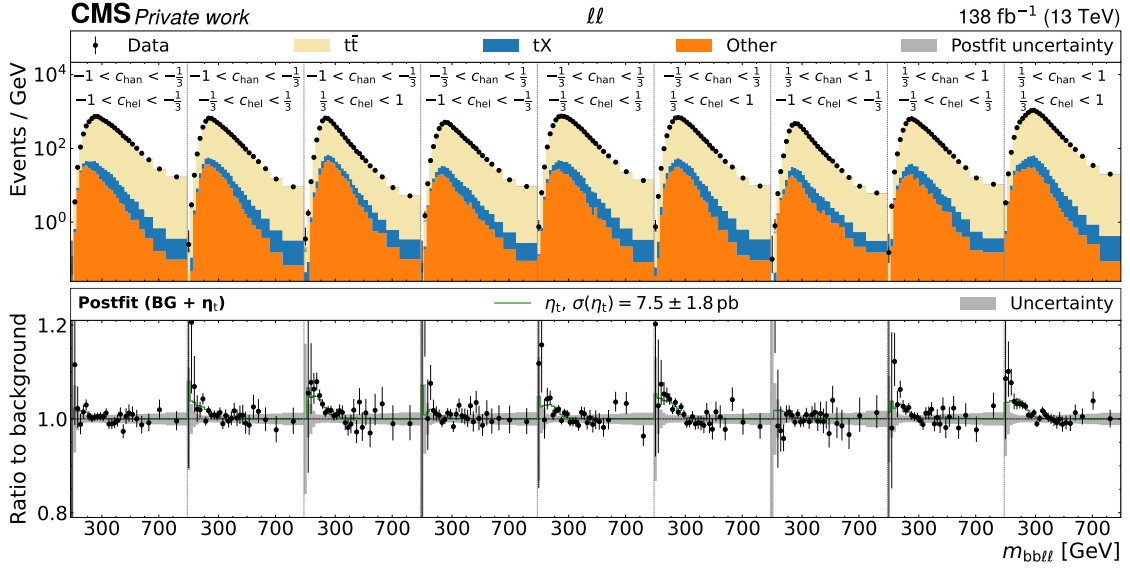


Figure 7.17: **Postfit distributions of $m_{bb\ell\ell} \times c_{hel} \times c_{han}$ for the η_t fit.** The unrolled three-dimensional distribution in $m_{bb\ell\ell}$, c_{hel} and c_{han} after the fit to data with η_t as the signal using $m_{bb\ell\ell}$ instead of $m_{t\bar{t}}$, summed over all years and lepton flavors. The first $m_{bb\ell\ell}$ bin in each $c_{hel} \times c_{han}$ slice is an underflow bin containing events with $m_{bb\ell\ell} < 180 \text{ GeV}$. Otherwise, notations are as in Fig. 7.13.

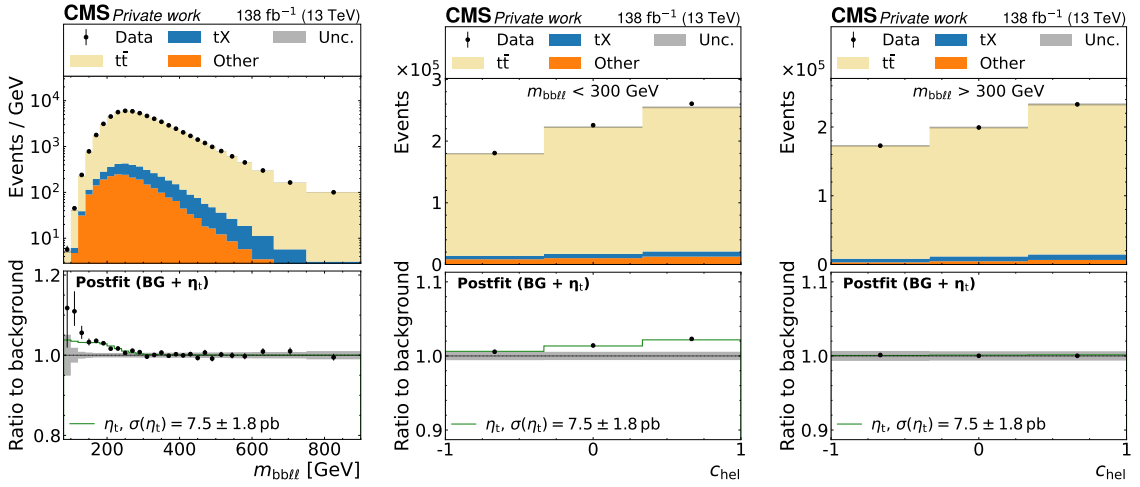


Figure 7.18: **Postfit distributions of $m_{bb\ell\ell}$ and c_{hel} for the η_t fit.** One-dimensional distributions of inclusive $m_{bb\ell\ell}$ (left), c_{hel} for $m_{bb\ell\ell} < 300 \text{ GeV}$ (center), and c_{hel} for $m_{bb\ell\ell} > 300 \text{ GeV}$ (right), projected from a 3D template of $m_{bb\ell\ell} \times c_{hel} \times c_{han}$. The first $m_{bb\ell\ell}$ bin in the left figure is an underflow bin containing events with $m_{bb\ell\ell} < 180 \text{ GeV}$. Otherwise, notations are as in Fig. 7.13. *Figure adapted from Ref. [9].*

and 7.18. It can be seen that the excess is still clearly present, though with a wider spread due to the coarser resolution of $m_{b\bar{b}\ell\ell}$ compared to $m_{t\bar{t}}$. An η_t cross section of $\sigma(\eta_t) = 7.5 \pm 1.8 \text{ pb}$ is extracted, which is in agreement with the nominal result within one standard deviation.

Alternate generator setups The influence of the choice of generator setup for the $t\bar{t}$ prediction is further quantified by repeating the η_t extraction fit with alternate setups. Besides the nominal setup from POWHEG hvq matched to PYTHIA, the three setups introduced in Sec. 7.5.4 are considered: POWHEG hvq matched to HERWIG, MG5_AMC@NLO matched to PYTHIA with the FxFx scheme, and bb41 matched to PYTHIA.

| Generator setup | $\sigma(\eta_t)$ [pb] |
|-------------------------------|-----------------------|
| POWHEG hvq + PYTHIA (nominal) | 8.7 ± 1.1 |
| POWHEG hvq + HERWIG | 8.6 ± 1.1 |
| MG5_AMC@NLO FxFx + PYTHIA | 9.8 ± 1.3 |
| POWHEG bb41 + PYTHIA | 6.6 ± 1.4 |

Table 7.5: **Results for alternate generators.** Results for $\sigma(\eta_t)$ obtained with different simulated event samples for the FO pQCD $t\bar{t}+tW$ prediction.

The results can be found in Tab. 7.5. The results from PYTHIA and HERWIG are fully in agreement with each other, while MG5_AMC@NLO results in a higher η_t cross section by about one standard deviation, and bb41 results in a lower η_t cross section by about ~ 1.5 standard deviations.

As an additional check, the differences between the predictions from POWHEG hvq + HERWIG and POWHEG hvq + PYTHIA as well as between bb41 and $t\bar{t} + tW$ are included in the fit as additional nuisance parameters. In both cases, the POWHEG hvq + PYTHIA prediction is considered the nominal, and the alternate prediction is considered the $+1\sigma$ template. The -1σ template is constructed by symmetrizing the relative difference around the nominal, and intermediate values are obtained by interpolation as usual.

The resulting η_t cross section with these nuisance parameters included is $\sigma(\eta_t) = 8.8^{+1.2}_{-1.4} \text{ pb}^3$. This figure is fully compatible with the nominal result with an asymmetrically increased uncertainty. The reason for the increase can be seen in Fig. 7.19, showing the nuisance parameter pulls and impacts: The nuisance parameter encoding the difference between bb41 and $t\bar{t} + tW$ represents the leading impact on the η_t cross section and is asymmetric. This is understandable from the steeper slope in c_{hel} for bb41 as seen in Fig. 7.7, which is similar to the η_t signal, and is also in agreement with the reduced η_t cross section for a bb41 background prediction shown

³This figure is considered the nominal result in Ref. [9]

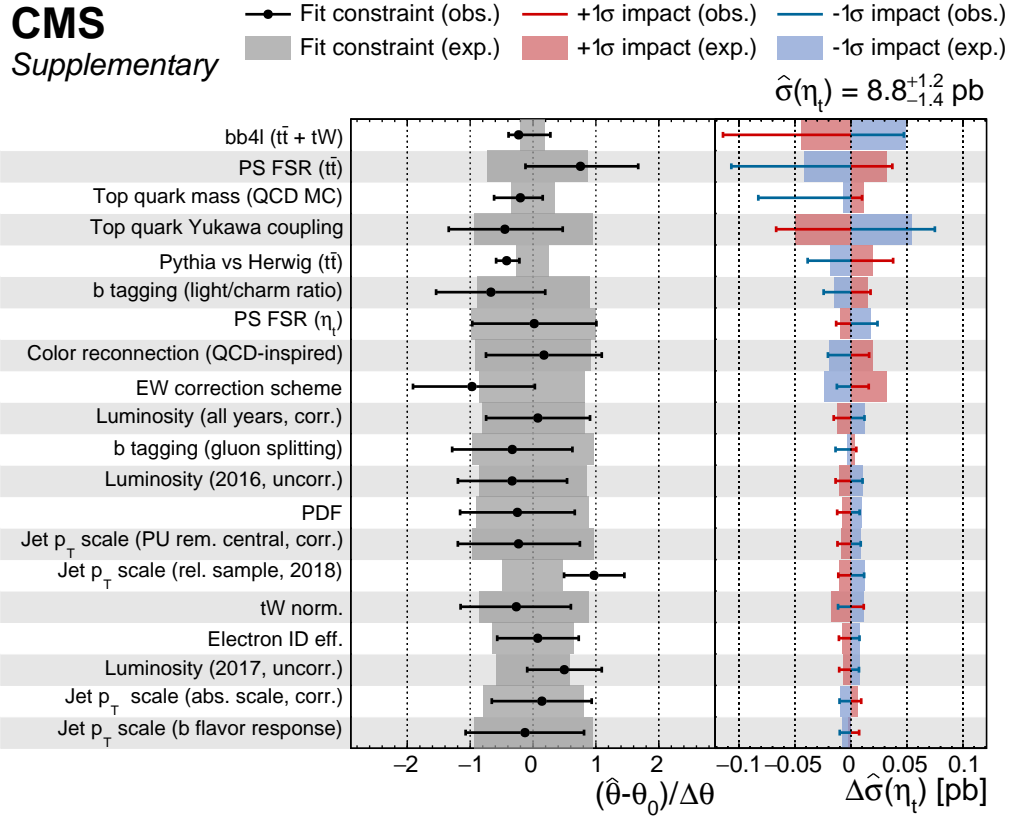


Figure 7.19: **Nuisance parameter pulls and impacts including alternate generators.** Expected and observed pulls, constraints, and impacts on the η_t cross section for the most impactful nuisance parameters in the η_t -only fit where the differences between the predictions from POWHEG hvq + HERWIG and bb4l + PYTHIA compared to POWHEG hvq + PYTHIA are included as additional nuisance parameters. *Figure adapted from Ref. [9].*

in Tab. 7.5. It is furthermore significantly constrained towards zero, i.e. towards the default $t\bar{t} + tW$ prediction, implying that the data prefers the NWA approach over the *a priori* superior bb4l prediction. The reason for this is not readily apparent. One possible cause could be the fact that the NLO EW and NNLO QCD corrections are applied to bb4l in a necessarily ad-hoc manner, and might thus spoil the agreement with the data (cf. Sec. 7.5.4). However, in the scope of this work, this remains speculation.

On the other hand, the nuisance parameter encoding the difference of PYTHIA and HERWIG is less impactful, consistent with the results for HERWIG in Tab. 7.5, and similarly strongly constrained. This is likely because the difference between PYTHIA and HERWIG can be distinguished from η_t based on the combination of $m_{t\bar{t}}$

and c_{hel} information, as expanded upon in Sec. 7.5.4.

7.7.4 Interpretation in terms of A and H

While a $t\bar{t}$ bound state is the conceptually simplest explanation of the enhancement at the $t\bar{t}$ threshold in the sense that it is predicted in the SM and does not invoke any further (BSM) degrees of freedom, it is also possible to perform an interpretation in terms of the generic spin-0 bosons A and H as introduced in Sec. 2.3.1. For this purpose, fits allowing the presence of both A and H at the same time are performed. The two independent POIs are the A/H-top coupling modifiers $g_{A\bar{t}\bar{t}}$ and $g_{H\bar{t}\bar{t}}$, and the interference with the SM is fully taken into account through a parametrization in terms of $g_{A/H\bar{t}\bar{t}}^2$ and $g_{A/H\bar{t}\bar{t}}^4$ (cf. Eq. (2.19)), thus allowing negative A/H contributions with respect to the SM.

A scan is performed over all pairs of considered A/H masses and widths (see Sec. 7.2.1), and the pair with the largest difference in logarithmic likelihood $\Delta \ln L$ is identified as the best-fit point. This results in $m_A = 365 \text{ GeV}$, $\Gamma_A/m_A = 2\%$ for A and $m_H = 925 \text{ GeV}$, $\Gamma_H/m_H = 3\%$ for H. It should be noted here that 365 GeV is the lowest mass point considered in the available signals for A and H, while η_t and χ_t are located at a lower value of 343 GeV. It is possible that considering a lower value of m_A would lead to an even better fit; however, close to the $t\bar{t}$ threshold, modeling the interference with the SM might be difficult due to large corrections at higher orders in QCD [207, 208].

Figure 7.20 shows the postfit $m_{t\bar{t}} \times c_{\text{hel}} \times c_{\text{han}}$ distribution, and Fig. 7.21 shows the allowed region for the two couplings $g_{A\bar{t}\bar{t}}$ and $g_{H\bar{t}\bar{t}}$ as obtained from a likelihood scan. From the latter, the best-fit values and total ranges for the coupling modifiers are found to be

$$g_{A\bar{t}\bar{t}} = 0.79^{+0.04}_{-0.05} \quad \text{and} \quad g_{H\bar{t}\bar{t}} = 1.47^{+0.17}_{-0.30}. \quad (7.17)$$

The same excess close to the $t\bar{t}$ threshold already seen in Sec. 7.7.1 manifests as of a non-zero value of $g_{A\bar{t}\bar{t}}$, which Fig. 7.21 shows is preferred by more than five standard deviations, similar as for the interpretation in terms of η_t . In addition, there is also a preference for a non-zero value of $g_{H\bar{t}\bar{t}}$, though this is significant only at about 2 standard deviations and could thus be a simple statistical fluctuation. It should be noted that both of these values are local significances, i.e. they do not account for the look-elsewhere effect. The source of this preference is again evident from Fig. 7.20: it is due to a mild, broad excess in events compared to the prediction around $m_{t\bar{t}} \approx 900 \text{ GeV}$, which is more pronounced in the low c_{han} bins compared to the others as would be expected for a scalar particle H.

It is important to stress that these results do not constitute any observation of a new BSM particle. Given the experimental resolution in $m_{t\bar{t}}$, as well as the signal mass points available, the $t\bar{t}$ bound state η_t and a BSM pseudoscalar A cannot be

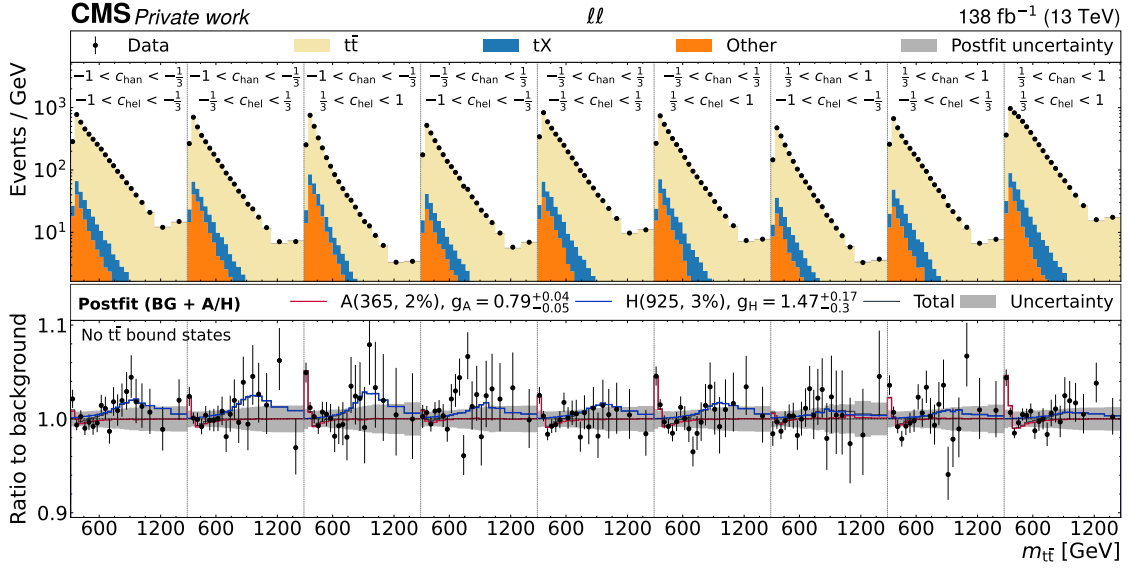


Figure 7.20: **Postfit distributions of $m_{t\bar{t}} \times c_{\text{hel}} \times c_{\text{han}}$ for the A+H fit.** The unrolled three-dimensional distribution in $m_{t\bar{t}}$, c_{hel} and c_{han} as after the fit to data with A and H as signals, summed over all years and lepton flavors. The A/H signals correspond to the best-fit masses and widths of $m_A = 365 \text{ GeV}$, $\Gamma_A/m_A = 2\%$ for A and $m_H = 925 \text{ GeV}$, $\Gamma_H/m_H = 3\%$ for H. The upper panel shows the sum of the background simulation (colored bars) and the observed data (black dots), while the lower panel shows the ratio of the data to the prediction with the postfit A and H signals, as well as their sum, overlaid.

2929 conclusively distinguished.

2930 7.8 Limits on A/H bosons

2931 Having discussed the excess seen at the $t\bar{t}$ threshold and its possible interpretations,
 2932 in this section exclusion limits on A/H bosons in the full considered mass range are
 2933 presented. This is done for two different scenarios: In the first scenario, denoted
 2934 “A/H only”, the SM $t\bar{t}$ background is described by the FO pQCD prediction from
 2935 POWHEG + PYTHIA reweighted to NLO EW and NNLO QCD, same as for the η_t
 2936 extraction in Sec. 7.7.1 and for the A+H fit in Sec. 7.7.4. The observed excess is thus
 2937 expected to manifest in the limits in the form of a weaker observed than expected
 2938 limit for low A/H masses.

2939 In the second scenario, denoted “A/H + η_t ”, the observed excess is assumed to
 2940 originate solely from a $t\bar{t}$ bound state, which is further assumed to be well described
 2941 by the η_t model. Under this assumption, the η_t contribution is added to the $t\bar{t}$

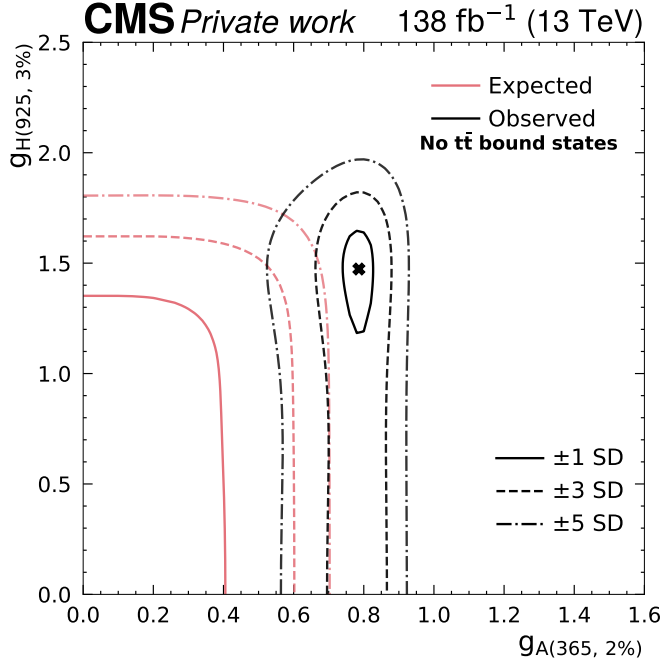


Figure 7.21: **Allowed coupling region in the A+H fit.** The two-dimensional allowed region for the coupling modifiers $g_{A\bar{t}\bar{t}}$ and $g_{H\bar{t}\bar{t}}$ in the A+H fit, for the best-fit A/H masses and widths of $m_A = 365$ GeV, $\Gamma_A/m_A = 2\%$ for A and $m_H = 925$ GeV, $\Gamma_H/m_H = 3\%$ for H, obtained through a scan of the profiled likelihood. The observed region is shown in black, while the SM expectation is shown in pink.

background prediction, with a free-floating normalization as an additional nuisance parameter. A and/or H contributions are then considered as signals on top of this background. It should be stressed that, while Fig. 7.13 shows good agreement of the η_t description with the data, the true cause of the excess can not be fully determined with the available $m_{t\bar{t}}$ resolution. Thus, all limits shown here should be treated with caution for low values of the A/H mass.

In both scenarios, the limits are calculated with the CL_s prescription as introduced in Sec. 4.4. However, a complication is presented by the non-linearity of the A/H signal as a function of $g_{A/H\bar{t}\bar{t}}$, due to which the distribution of the test statistic is not necessarily χ^2 -distributed, and thus the p -values p_{s+b} and p_b cannot be easily computed. To avoid having to perform computationally expensive toy experiments, a *raster scan* method is used in the same way as in Ref. [17]. For a given A/H mass and width point, the coupling modifier $g_{A/H\bar{t}\bar{t}}$ is scanned in the range 0–5. For each value of $g_{A/H\bar{t}\bar{t}}$, the total signal contribution is computed as the sum of the resonant signal, scaling with $g_{A/H\bar{t}\bar{t}}^4$, and the SM-signal interference, scaling with $g_{A/H\bar{t}\bar{t}}^2$. An auxilliary linear signal strength μ is then introduced, so that the total

2958 signal contribution becomes

$$s(\mu) = \mu \left(g_{A/Ht\bar{t}}^4 s_{\text{res}} + g_{A/Ht\bar{t}}^2 s_{\text{int}} \right) \quad (7.18)$$

2959 where s_{res} and s_{int} are the resonance and interference contributions, respectively,
2960 and $g_{A/Ht\bar{t}}$ is held fixed. $\mu = 1$ corresponds to the probed A/H signal, while $\mu = 0$
2961 corresponds to the SM. Intermediate values of μ are in principle unphysical since
2962 they do not correspond to any value of $g_{A/Ht\bar{t}}$.

2963 Since the A/H signal now scales linearly with μ , the usual asymptotic approxima-
2964 tion can be used to obtain the CL_s value for $\mu = 1$. It has been shown as a part of
2965 Ref. [17] that the distribution of the test statistic obtained in this way approximates
2966 well the true test statistic for $g_{A/Ht\bar{t}}$ as evaluated using toy experiments. This pro-
2967 cedure is repeated for all values of $g_{A/Ht\bar{t}}$, and a value of $g_{A/Ht\bar{t}}$ is, as usual, excluded
2968 at 95% confidence level when the CL_s value drops below 0.05.

2969 The resulting observed and expected limits for all considered A and H masses and
2970 six representative width choices are shown in Figs. 7.22 and 7.23 for the “A/H only”
2971 scenario and in Figs. 7.24 and 7.25 for the “A/H + η_t ” scenario. In the “A/H only”
2972 scenario, the excess at the $t\bar{t}$ threshold is visible at low A/H masses as expected. It
2973 is stronger for the pseudoscalar A than for the scalar H, consistent with the results
2974 in Sec. 7.7.2. In the “A/H + η_t ” scenario, the excess is fully absorbed by the η_t
2975 contribution, and the observed and expected limits at low A/H masses agree. It is
2976 notable here that the expected limits change only little between the scenarios even
2977 though, in the “A/H + η_t ” scenario, the cross section of the η_t contribution is freely
2978 floating in the fit. **TODO decide on whether I want to elaborate on this, would
2979 need a plot of the signal templates**

2980 Furthermore, the mild excess for H at high masses as seen in Fig. 7.21 is repro-
2981 duced in the limits on $g_{Ht\bar{t}}$ in both scenarios in the approximate range of $900 < m_H < 1000$ GeV.
2982

2983 7.9 Combination with the $\ell+\text{jets}$ channels

2984 So far, all results in this section have covered only the dilepton decay channel of $t\bar{t}$,
2985 which was analyzed as part of this thesis. In Ref. [8], the results on A/H bosons
2986 are combined with a separate analysis of the $\ell+\text{jets}$ decay channel. The combina-
2987 tion (but not the $\ell+\text{jets}$ analysis) was also performed as part of this thesis, and is
2988 presented in this chapter. The $\ell+\text{jets}$ analysis strategy is roughly outlined in the
2989 following, for a more complete description, see Ref. [8].

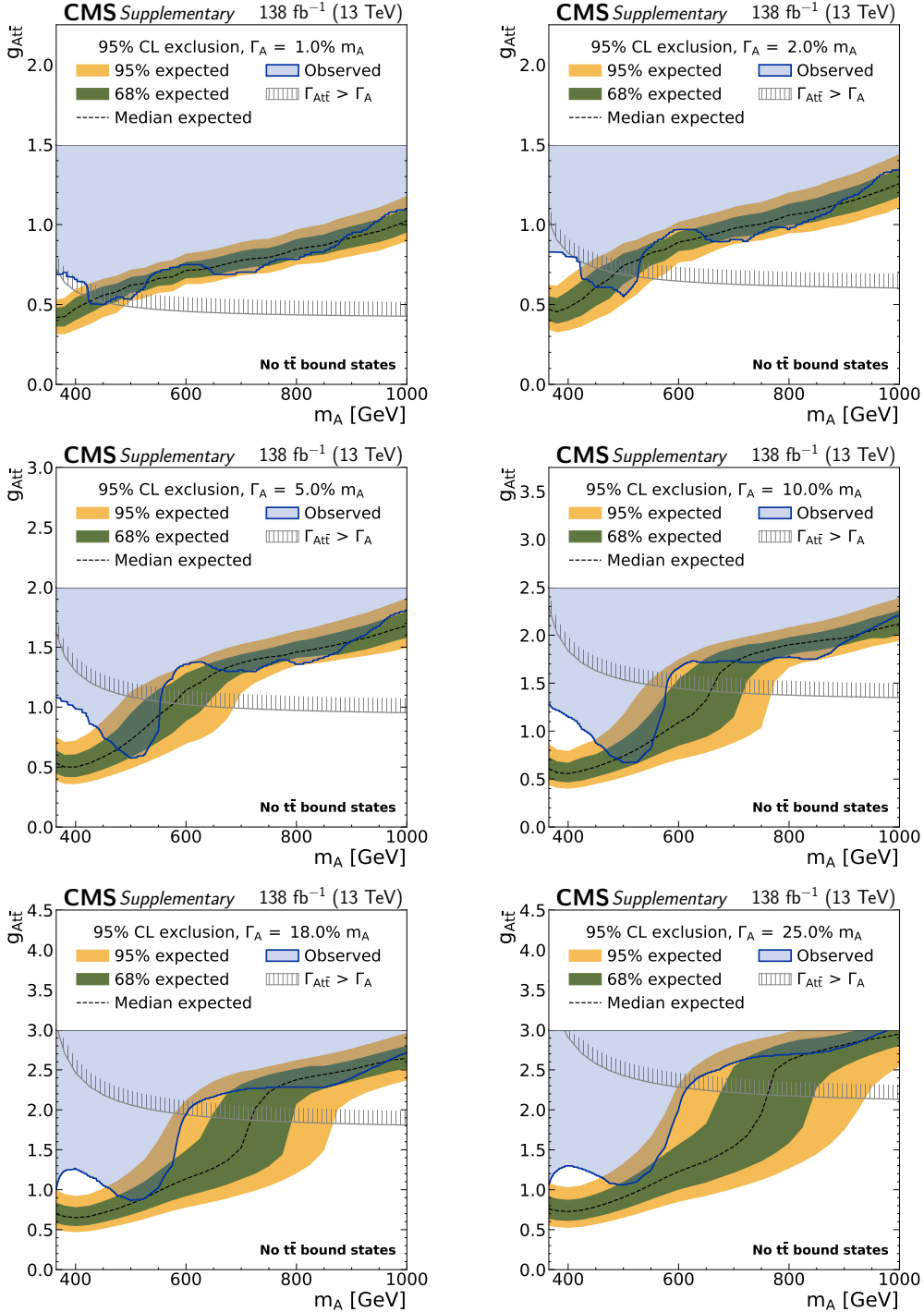


Figure 7.22: **Exclusion limits on $g_{A\bar{t}\bar{t}}$ in the “A only” scenario** in the dilepton channels as a function of the mass of the A boson for relative widths of 1, 2, 5, 10, 18, and 25% (from upper left to lower right). The observed limits are indicated by the blue shaded area, and the inner green band and the outer yellow band indicate the regions containing 68 and 95%, respectively, of the distribution of limits expected under the background-only hypothesis. The unphysical region of phase space in which the partial width $\Gamma_{A\rightarrow\bar{t}\bar{t}}$ becomes larger than the total width of A is indicated by the hatched line.¹³³

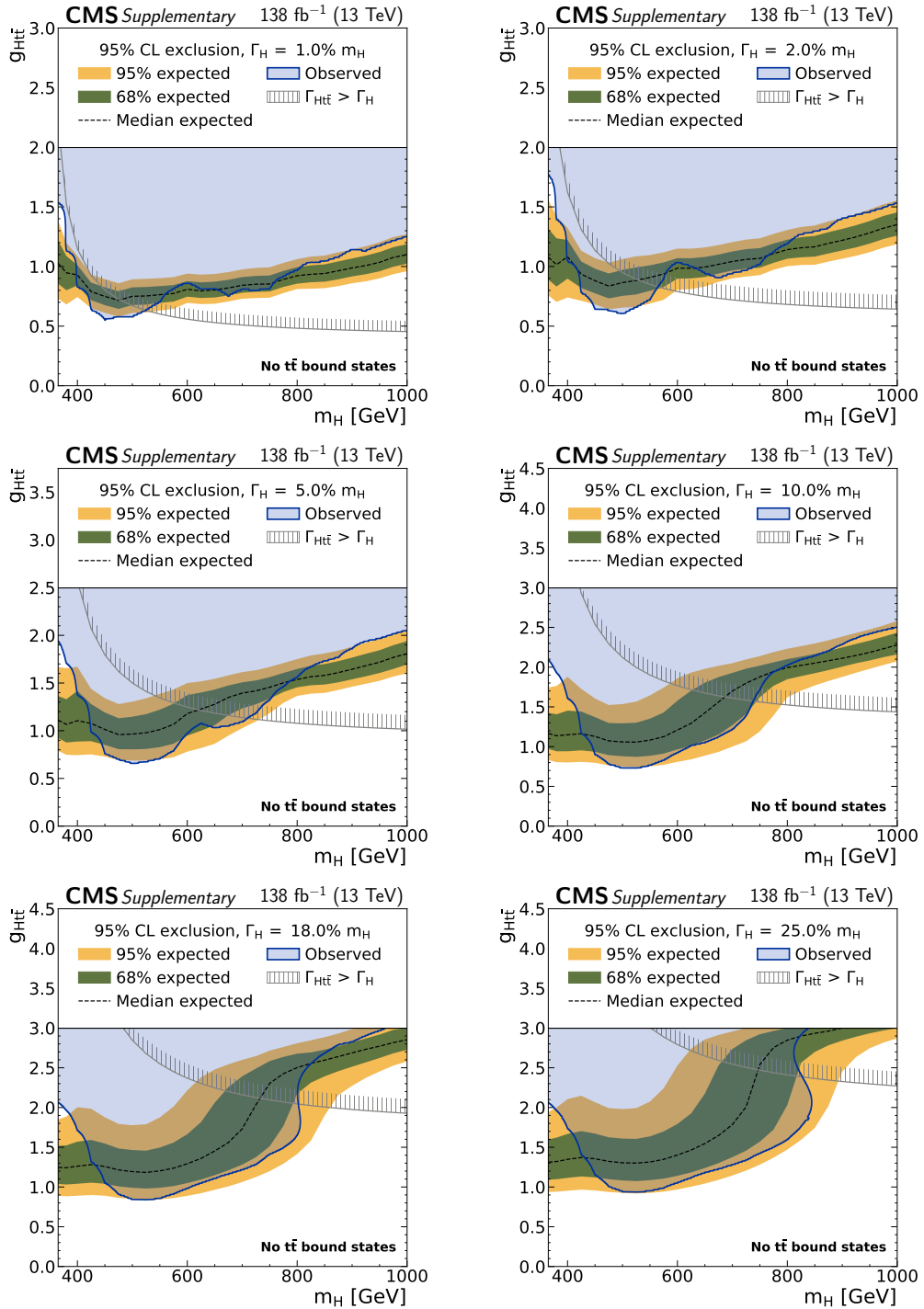


Figure 7.23: **Exclusion limits on g_{Htt} in the “H only” scenario** in the dilepton channels as a function of the mass of the H boson. Notations are equivalent to Fig. 7.22.

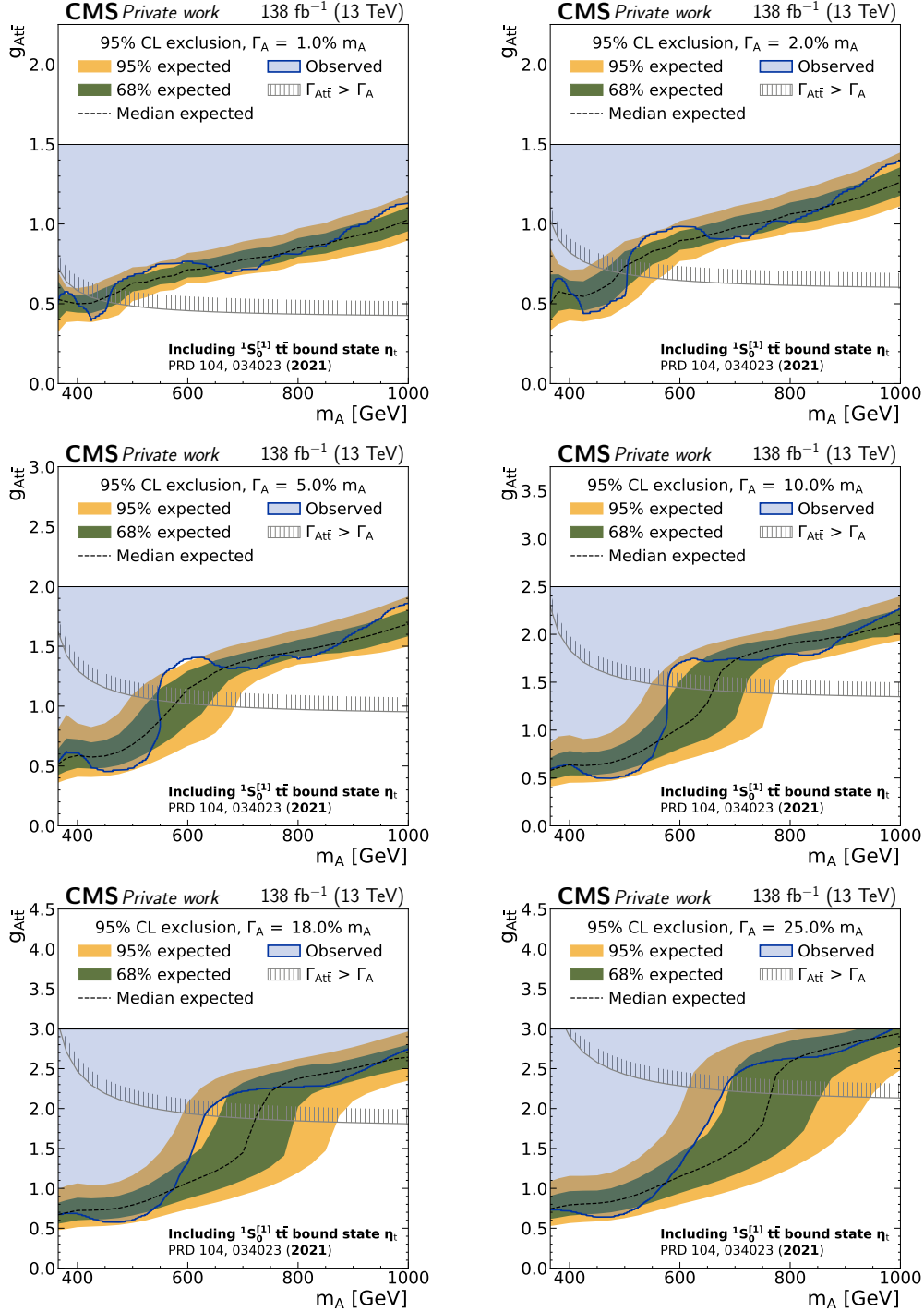


Figure 7.24: **Exclusion limits on $g_{A\bar{t}\bar{t}}$ in the “A + η_t ” scenario** in the dilepton channels as a function of the mass of the A boson. Notations are equivalent to Fig. 7.22.

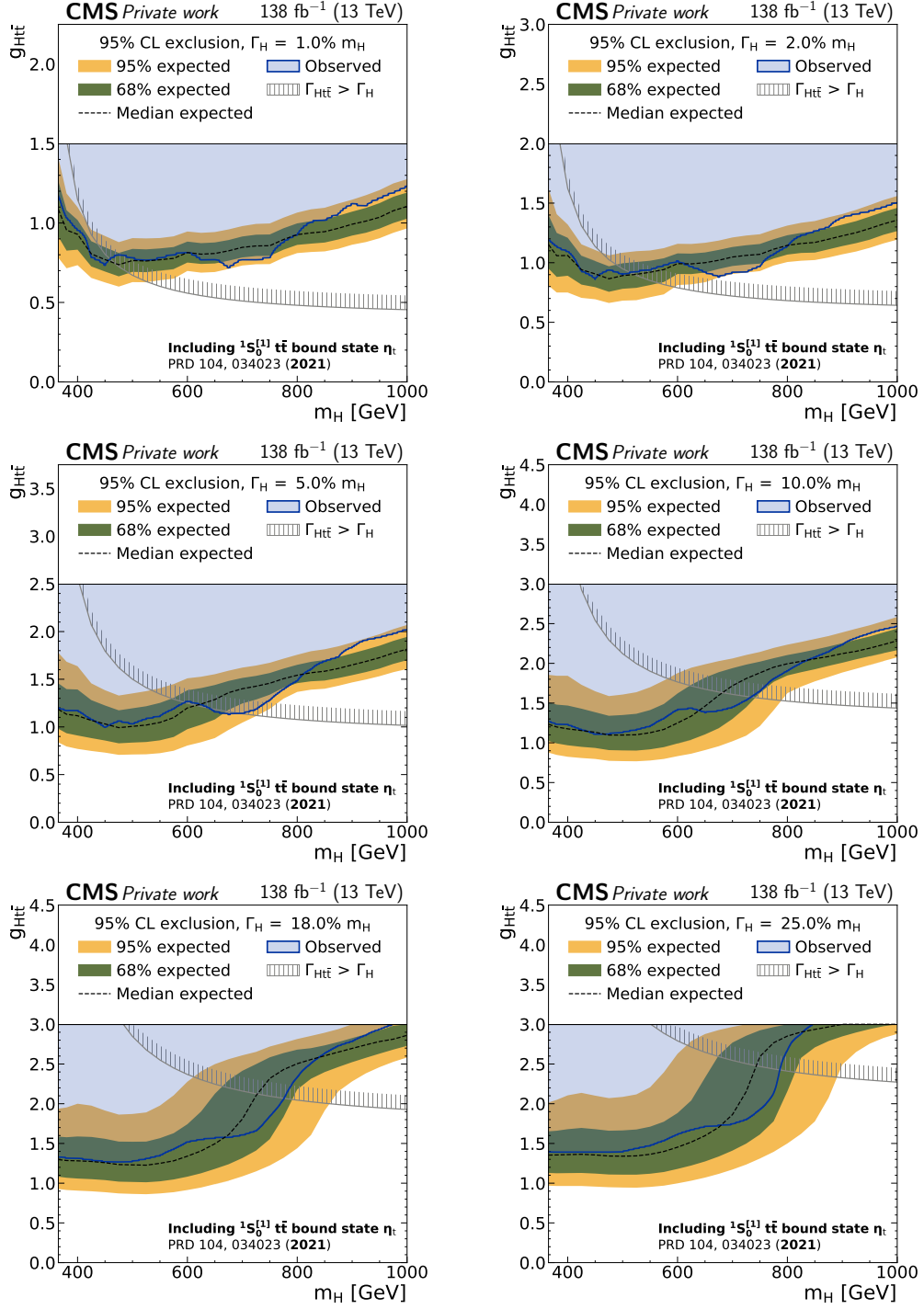


Figure 7.25: **Exclusion limits on g_{Htt} in the “H + η_t ” scenario** in the dilepton channels as a function of the mass of the H boson. Notations are equivalent to Fig. 7.22.

2990 7.9.1 Analysis strategy in the ℓ +jets channel

2991 In the ℓ +jets channel, events with exactly one lepton and at least three jets are
2992 selected, of which at least two need to be b tagged. In addition to the criteria
2993 outlined in Sec. 7.2.2, both the lepton and the jets are required to fulfill $p_T > 30 \text{ GeV}$
2994 to account for the higher single-lepton trigger thresholds. Furthermore, the cut-
2995 based identification criteria for electrons, as described in Ref. [100], are applied
2996 instead of MVA-based criteria. Similar as in the dilepton channel, the events are
2997 categorised by the flavor of the lepton into the e+jets and μ +jets channels.

2998 The algorithm described in Ref. [209] is used to reconstruct the neutrino from the
2999 leptonic top decay. It enforces mass constraints on the W boson and leptonically
3000 decaying top quark and then minimizes the distance $D_\nu = |p_T^\nu - p_T^{\text{miss}}|$ between the
3001 neutrino p_T and the missing transverse momentum. In events with four or more jets,
3002 the same distance D_ν is then also used to assign the jets to the b and \bar{b} candidates
3003 as well as to the decay products of the hadronically decaying W boson. From this,
3004 the $t\bar{t}$ system can then be reconstructed. In events with exactly three jets, where
3005 information has been lost due to either an out-of-acceptance jet or the merger of
3006 two jets into one, additional steps have to be taken. The procedure described in
3007 Ref. [210] is applied to these events, which involves applying an energy correction
3008 factor to the four-momentum of the hadronically decaying top quark, depending on
3009 its reconstructed mass. Since the resolution of this procedure is necessarily worse
3010 than for events where all jets are available, events with three jets and four or more
3011 jets are treated as separate categories in the fit.

3012 A two-dimensional template is constructed from the reconstructed value of $m_{t\bar{t}}$
3013 as well as $|\cos \theta_\ell^*|$, where θ_ℓ^* is the scattering angle of the leptonically decaying top
3014 quark with respect to the direction of flight of the $t\bar{t}$ system in the laboratory frame.
3015 This variable is sensitive to the spin of a possible mediator in $t\bar{t}$ production: For
3016 spin-0 mediators like A/H, the top quarks are emitted isotropically in the $t\bar{t}$ rest
3017 frame, leading to a flat distribution of $|\cos \theta_\ell^*|$, while in the SM $|\cos \theta_\ell^*|$ peaks at
3018 high values. However, it is not sensitive to the \mathcal{CP} structure of the mediator, in
3019 contrast to c_{hel} and c_{han} . Furthermore, the SM prediction changes as a function of
3020 $m_{t\bar{t}}$; close to the $t\bar{t}$ threshold, the difference to a flat spectrum is rather small, while
3021 for high $m_{t\bar{t}}$ the difference is large due to the impact of the $q\bar{q}$ initial state.

3022 The $t\bar{t}$ and tW background predictions as well as the A/H signals are estimated
3023 using the same MC simulation as in the dilepton channels. Additionally, there is a
3024 significant background contribution from QCD multijet production with a fake or
3025 non-prompt lepton as well as EW processes such as W+jets production. These are
3026 difficult to model using MC, and are instead estimated together by a data-driven
3027 approach (cf. Sec. 5.3.2). A sideband in which the b tagging requirement on the
3028 jets is inverted is used for this purpose; details can be found in Ref. [8].

3029 The dilepton and ℓ +jets channels are directly combined by performing a simultaneous
3030 likelihood fit to all categories. Systematic uncertainties related to modeling

of the $t\bar{t}$ and tW backgrounds are treated as fully correlated, while experimental uncertainties as well as uncertainties of the other minor backgrounds can be correlated or uncorrelated as appropriate. Again, both the “A/H only” and “A/H + η_t ” scenarios are considered. For the latter, the ℓ +jets analysis uses a slightly different η_t model, in which the width of the bound state is set to $\Gamma(\eta_t) = 7 \text{ GeV}$ and a cut on the invariant mass $m_{WWb\bar{b}}$ is applied, as described in Sec. 2.2.3. For the sake of consistency, the same model is also used in the dilepton channels when performing the combination only. The resulting impact on the limits from the choice of η_t model is expected to be small.

7.9.2 A/H limits

The resulting observed and expected limits for the combination of both channels are found in Figs. 7.26 to 7.29 for both scenarios. It can be seen that the large excess for low A/H masses is still present in the channel combination in the “A/H only” scenario, and is again stronger for the pseudoscalar A. The mild excess for the scalar H at $m_H \approx 925 \text{ GeV}$, on the other hand, is not confirmed in the channel combination.

To assess the impact of the different channels, the expected limits for the dilepton and ℓ +jets channels alone are also shown in red and orange, respectively. For most of the phase space, the ℓ +jets channel leads to stronger limits than the dilepton channel, which is likely mostly due to the higher branching ratio and thus higher available statistics as well as the better $m_{t\bar{t}}$ resolution in the ℓ +jets channel especially at high $m_{t\bar{t}}$. The difference is large at high A and H masses, where the contribution from the dilepton channels is rather small, while the dilepton channel becomes much more important for low masses, i.e. close to the $t\bar{t}$ threshold. This could be because of the lack of sensitivity of $|\cos \theta_\ell^*|$ close to the $t\bar{t}$ threshold, while c_{hel} and c_{han} do not suffer from such a problem. For H at low masses in particular, the dilepton channel in fact gives stronger limits than ℓ +jets due to the sensitivity of c_{han} to scalar mediators.

7.9.3 Simultaneous A+H exclusion contours

In many possible BSM scenarios, multiple additional spin-0 states are expected at the same time, such as A and H in e.g. the 2HDM (cf. Sec. 2.3.2). Often, the masses of these scalars are close together since they originate from new physics at the same energy scale, in which case their signatures would not easily factorize. It is thus useful for future interpretations of the results to show exclusion contours not only for either A or H, but for the simultaneous presence of both at the same time.

To do so, simultaneous fits are performed with both A and H as freely floating signals as in Sec. 7.7.4. Frequentist exclusion contours are set with the Feldman–Cousins prescription [211, 212], in which the test statistic is numerically evaluated

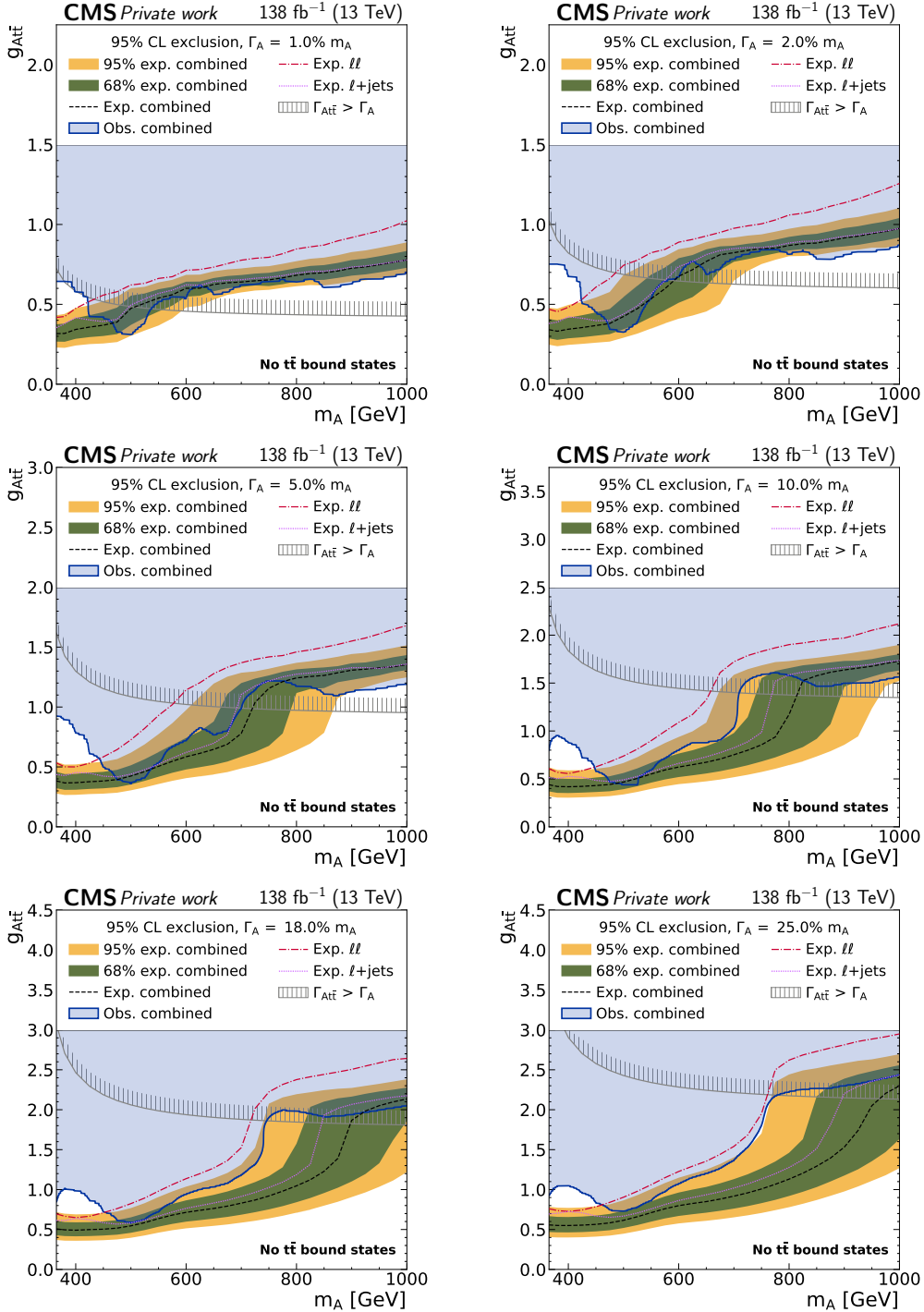


Figure 7.26: **Combined exclusion limits on $g_{A\bar{t}}$ in the “A only” scenario** in the dilepton and ℓ +jets channels as a function of the mass of the A boson. The expected limits in the dilepton and ℓ +jets channels alone are shown as the red and purple lines for comparison. Otherwise, notations are equivalent to Fig. 7.22. *Figure adapted from Ref. [8].*

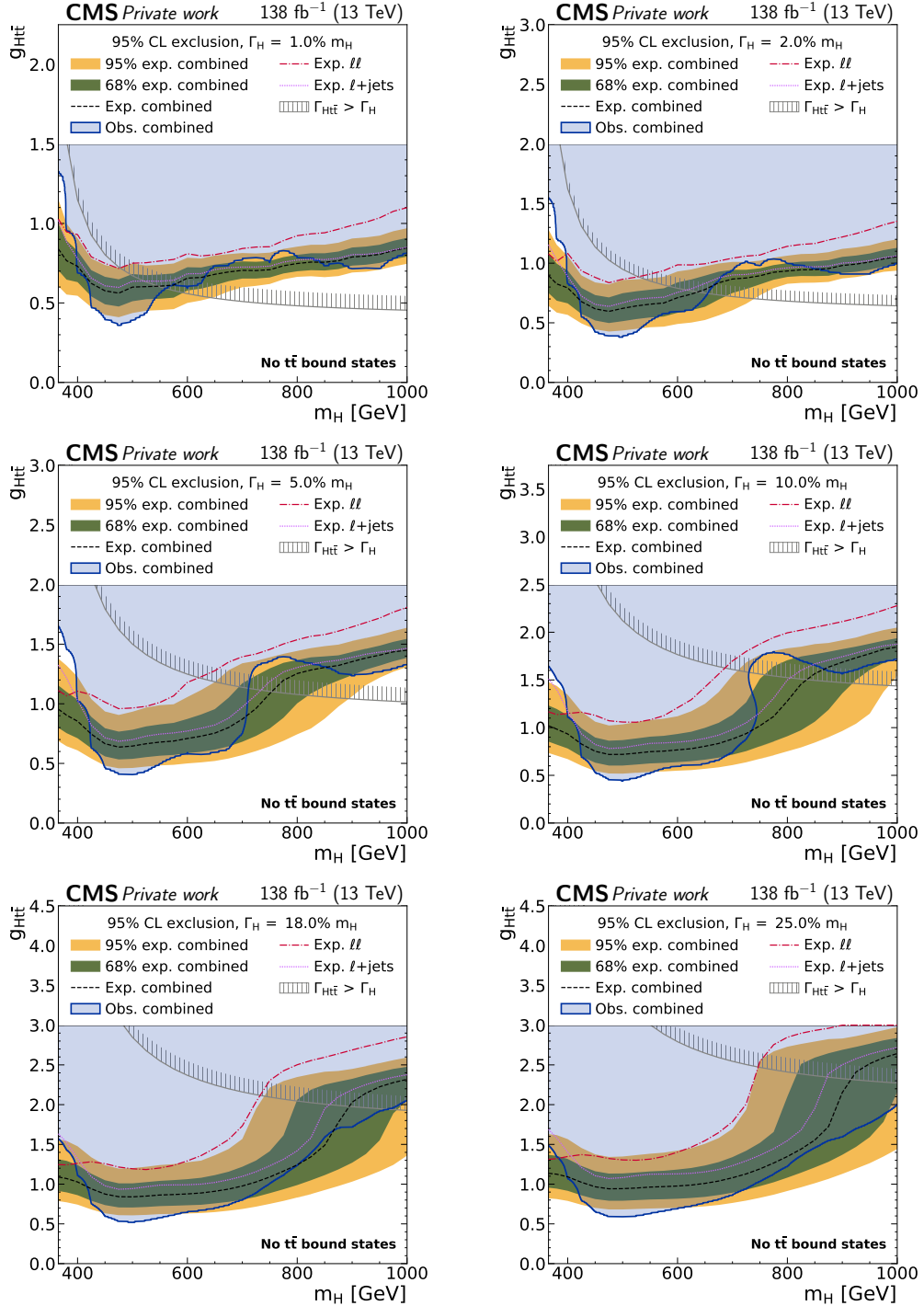


Figure 7.27: **Combined exclusion limits on $g_{Ht\bar{t}}$ in the “H only” scenario** in the dilepton and $\ell+jets$ channels as a function of the mass of the H boson. Notations are equivalent to Fig. 7.26. *Figure adapted from Ref. [8].*

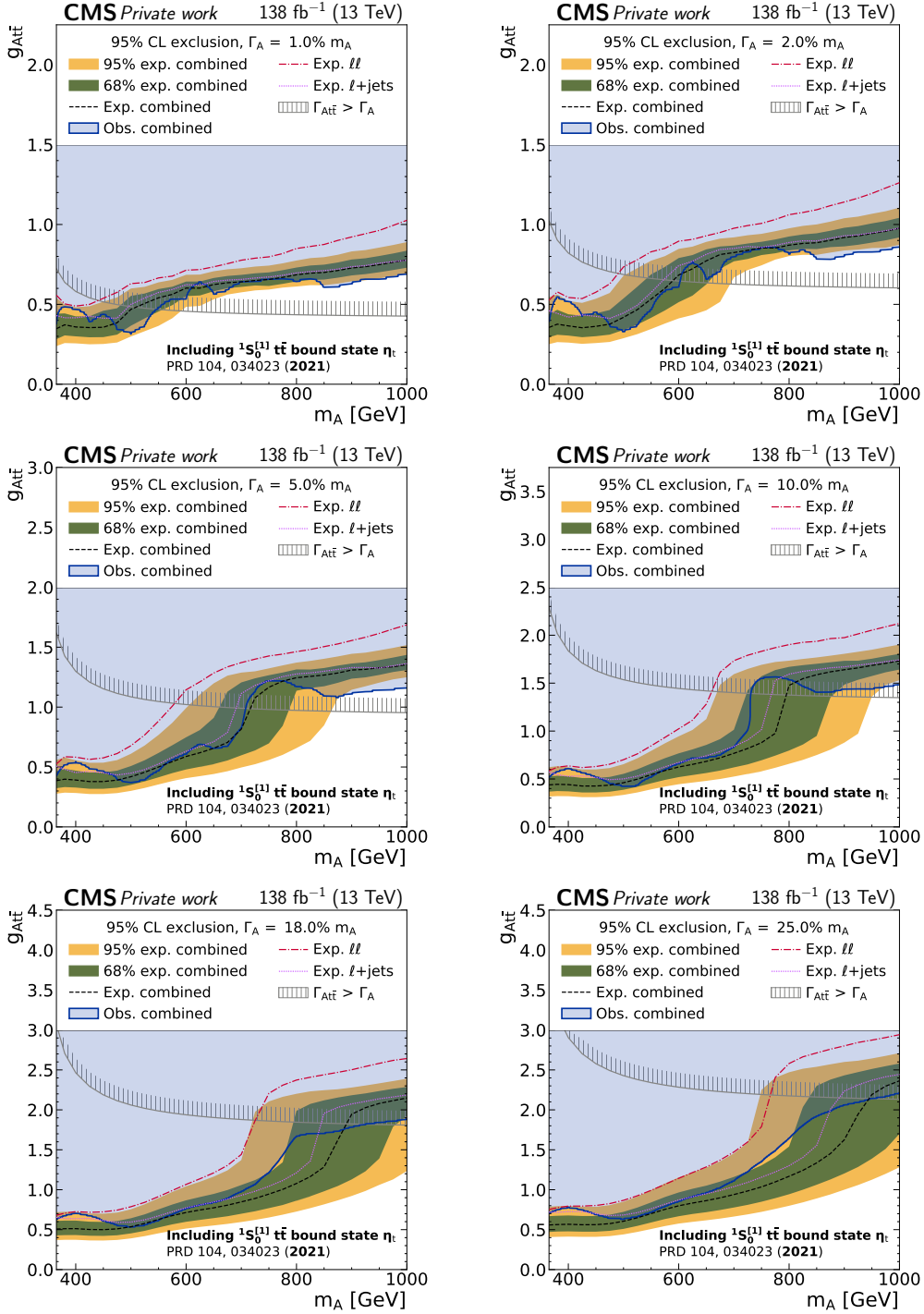


Figure 7.28: **Combined exclusion limits on $g_{A\bar{t}}$ in the “A + η_t ” scenario** in the dilepton and ℓ +jets channels as a function of the mass of the A boson. Notations are equivalent to Fig. 7.26. *Figure adapted from Ref. [8].*

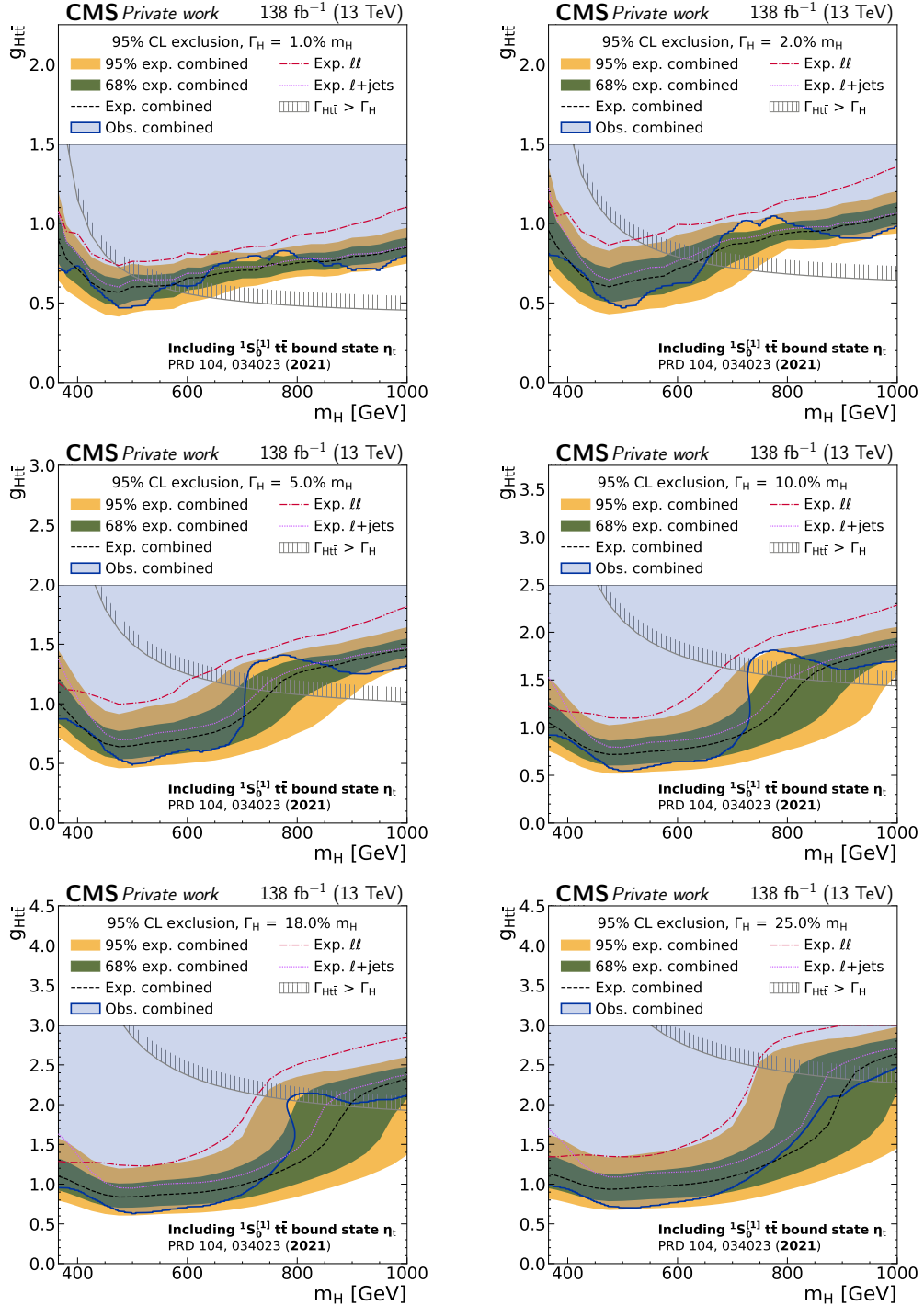


Figure 7.29: **Combined exclusion limits on $g_{Ht\bar{t}}$ in the “H + η_t ” scenario** in the dilepton and $\ell+\text{jets}$ channels as a function of the mass of the H boson. Notations are equivalent to Fig. 7.26. *Figure adapted from Ref. [8].*

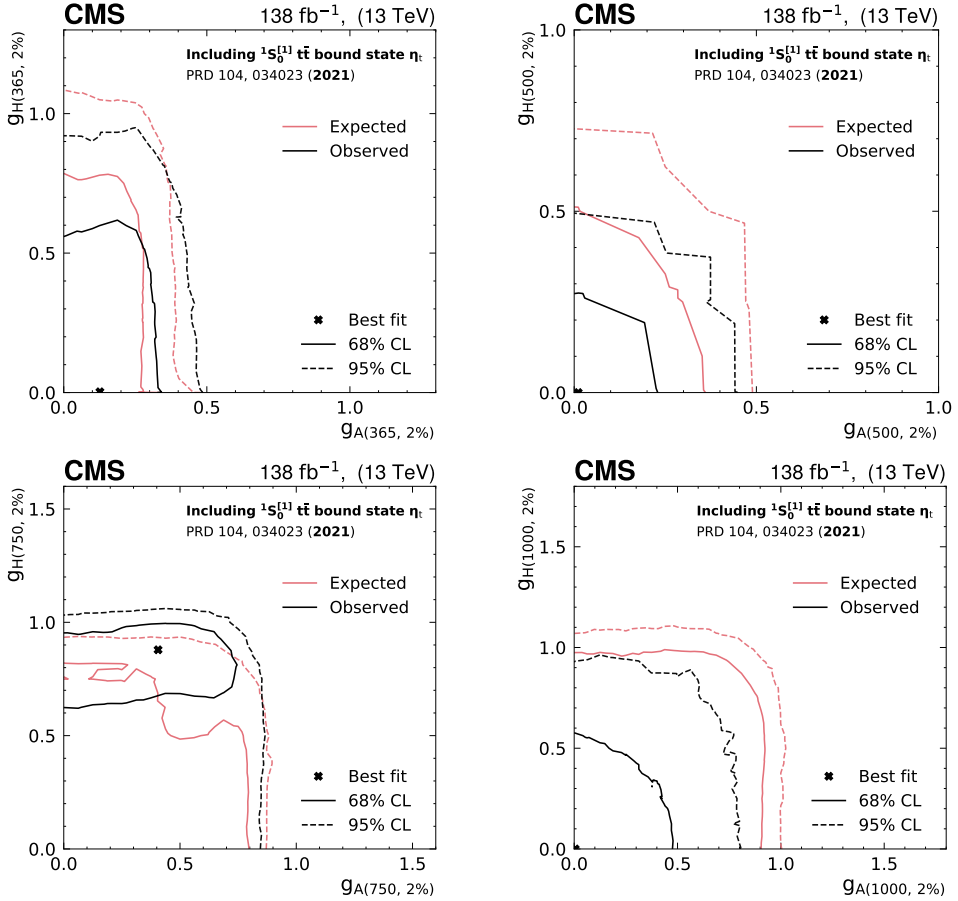


Figure 7.30: **Frequentist 2D exclusion contours for $g_{A\bar{t}\bar{t}}$ and $g_{H\bar{t}\bar{t}}$** for four different signal hypotheses with identical A and H masses of 365 GeV (upper left), 500 GeV (upper right), 750 GeV (lower left) and 1000 GeV (lower right), all assuming a width of 2%. In all cases, η_t production is added to the background. *Figure taken from Ref. [8].*

3069 using toy experiments at each point in the $g_{A\bar{t}\bar{t}}-g_{H\bar{t}\bar{t}}$ plane. This procedure is
 3070 fully correct in the Frequentist sense and does not rely on approximations of the
 3071 test statistic, which are not guaranteed to hold for two non-linear signals, but is
 3072 computationally expensive.

3073 Due to this, combined with the large four-dimensional phase space of possible
 3074 signals, only a few example mass and width points are shown in this work, and only
 3075 for the dilepton and ℓ +jets combination in the “A/H + η_t ” scenario. They can be
 3076 found in Fig. 7.30 for the case of identical A and H masses as well as in Fig. 7.31 for
 3077 differing A and H masses. Alternatively, a coarse scan of the negative log-likelihood
 3078 of the full span is available online as part of the HepData record **TODO ref.**

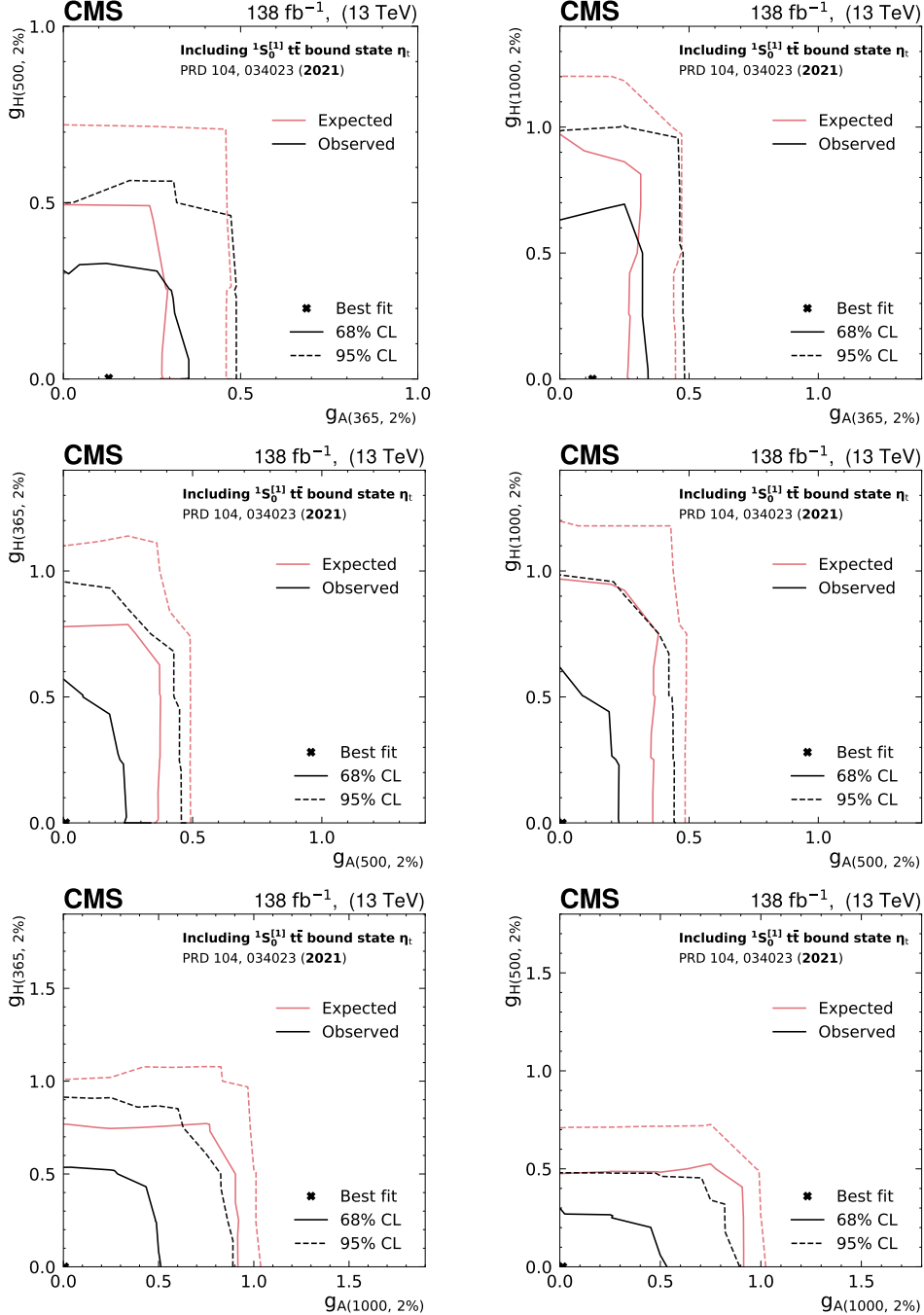


Figure 7.31: **Frequentist 2D exclusion contours for $g_{A t\bar{t}}$ and $g_{H t\bar{t}}$** for six different signal hypotheses with differing A and H masses, corresponding to combinations of 365 GeV, 500 GeV and 1000 GeV, all assuming a width of 2%. In all cases, η_t production is added to the background. *Figure taken from Ref. [8].*

3079 7.10 Comparison to other results

3080 7.10.1 ATLAS $A/H \rightarrow t\bar{t}$ search

3081 In Ref. [171], the ATLAS collaboration presented a similar search for heavy pseu-
3082 doscalar or scalar bosons in $t\bar{t}$ events using the full LHC Run 2 dataset, and observed
3083 no excess at the $t\bar{t}$ threshold. To decide whether that result contradicts the one pre-
3084 sented here, it is necessary to understand the differences between the two analyses.

3085 The ATLAS analysis combines the dilepton and $\ell+jets$ decay channels of $t\bar{t}$, sim-
3086 ilar to the combination presented in Sec. 7.9 for A and H, though the definitions of
3087 the channels are different: In the $\ell+jets$ channel, ATLAS does not consider events
3088 with only three jets as described in Sec. 7.9.1, but instead includes events with only
3089 one b tag in addition to events with two or more b tags. Furthermore, ATLAS
3090 defines an additional category with $\ell+jets$ events in which the decay products of the
3091 hadronically decaying top quark are merged, though this is expected to contribute
3092 mostly at high $m_{t\bar{t}}$.

3093 In the dilepton channels, ATLAS uses a fundamentally different strategy than
3094 the one presented in this work. Instead of performing an explicit $t\bar{t}$ reconstruction,
3095 thus giving access to $m_{t\bar{t}}$ and the spin correlation observables c_{hel} and c_{han} , ATLAS
3096 simply uses the invariant mass $m_{b\bar{b}\ell\ell}$ of the visible decay products as well as $\Delta\phi_{\ell\ell}$,
3097 the azimuthal distance between the two leptons in the laboratory frame. The former
3098 can be considered a proxy for $m_{t\bar{t}}$, though with significant smearing due to the loss
3099 of information from the two neutrinos, as also studied in Sec. 7.7.3. The latter has
3100 indirect sensitivity to the $t\bar{t}$ spin correlation, but this sensitivity is intermixed with
3101 kinematic information due to the boosts of the leptons from their top quark parents.
3102 As a result, it is known to be hard to model accurately and affected by theoretical
3103 uncertainties [24, 213].

3104 Combining these properties, it is expected that the dilepton channels in the AT-
3105 LAS analysis give only subdominant sensitivity compared to the $\ell+jets$ channels. In
3106 this work, while the situation is similar for high $m_{t\bar{t}}$, the dilepton channels contribute
3107 significantly close to the $t\bar{t}$ threshold. Furthermore, the direct use of spin corre-
3108 lation information means that the effect of many systematic uncertainties which only
3109 affect the kinematics is lessened greatly, as elaborated on in Sec. 7.7.3. It has been
3110 checked internally that adopting the strategy employed by ATLAS for the dilepton
3111 channels in this work would lead to a greatly lessened sensitivity at the $t\bar{t}$ threshold,
3112 and likely no claims of a significant excess.

3113 A further cause of differences could be the different treatment of systematic uncer-
3114 tainties. ATLAS considers additional nuisance parameters for the modeling of the $t\bar{t}$
3115 continuum regarding the choice of parton shower (PYTHIA vs. HERWIG), the choice
3116 of calculation for the top quark decay (POWHEG vs. MADSPIN), and the choice
3117 of PDF in the calculation of the NNLO QCD and NLO EW corrections. The first
3118 of these has been studied here in Sec. 7.7.3, and found to not influence the results

3119 strongly in the dilepton channels due to the effect of c_{hel} . However, the important
3120 uncertainties due to the top quark Yukawa coupling and the EW correction scheme
3121 are not included in the ATLAS result, since the EW corrections are calculated in a
3122 different manner. In an effort to be as conservative as possible, ATLAS moreover
3123 treats several significant uncertainties as decorrelated between different bins of the
3124 angular variables $\cos\theta^*$ and $\Delta\phi_{\ell\ell}$, which could reduce the sensitivity gained from
3125 these variables.

3126 Since ATLAS does not consider an explicit signal model for a $t\bar{t}$ bound state,
3127 the expected sensitivities to η_t cannot be directly compared. Instead, the closest
3128 considered signal is the generic pseudoscalar A at a mass of 400 GeV, higher than the
3129 minimum of 365 GeV considered here. Since a non-negligible excess is still present
3130 at that value in this work both in the dilepton channels alone (Fig. 7.22) and in
3131 the combination with $\ell+\text{jets}$ (Fig. 7.26), while no such excess is visible in Fig. 15 of
3132 Ref. [171], the choice of signals is not the cause of the differences on its own. However,
3133 the shape difference between A at 400 GeV including the SM interference and η_t is
3134 not negligible. It is thinkable that, if the excess truly originates from a $t\bar{t}$ bound state
3135 manifesting as a narrow peak at the $t\bar{t}$ threshold, fitting the non-matching A signal
3136 to the data will worsen the issues due to modeling and systematic uncertainties as
3137 described in the previous paragraphs, though this is partly speculation.

3138 Even with all this information, it is not fully clear whether the result of this work
3139 and the ATLAS result in Ref. [171] should be considered in conflict with each other
3140 or not. Together with the cross-checks performed in Sec. 7.7.3, it seems likely that
3141 the $t\bar{t}$ kinematic reconstruction in the dilepton channels, in particular the access to
3142 spin correlation, is the most important difference. To decisively answer the question
3143 of consistency, it would be desirable for ATLAS to repeat their analysis with a
3144 similar strategy in the dilepton channels, as well as with a dedicated signal model
3145 for a $t\bar{t}$ bound state.

3146 7.10.2 Other $t\bar{t}$ measurements

3147 While this work constitutes the first time that an excess consistent with a $t\bar{t}$ bound
3148 state has been observed with a large significance, there have been hints for such
3149 an effect in other $t\bar{t}$ measurements. First, several measurements of unfolded $t\bar{t}$
3150 differential cross sections have observed excesses in data compared to MC predictions
3151 of the $t\bar{t}$ continuum at low invariant masses, such as $m_{t\bar{t}}$ in dilepton events [214],
3152 $m_{\ell\ell}$ in $e\mu$ events [215], and $m_{t\bar{t}}$ in $\ell+\text{jets}$ events [199]. The significances of these
3153 excesses vary depending on the MC generator the data is compared to, and are also
3154 strongly influenced by systematic uncertainties for the two $m_{t\bar{t}}$ measurements.

3155 Secondly, the measurements of quantum entanglement in $t\bar{t}$ pairs in the dilepton
3156 channel presented in Refs. [26, 27] measure as a sensitive observable the value of
3157 D , i.e. the slope of c_{hel} (cf. Sec. 2.2.1), for low $m_{t\bar{t}}$ events. This is very similar
3158 in spirit to the observables $m_{t\bar{t}}$ and c_{hel} used in the dilepton channel of this work,

3159 though the measurement is only performed one-dimensionally in c_{hel} instead of the
3160 3D $m_{t\bar{t}} \times c_{\text{hel}} \times c_{\text{han}}$ template used here. In both Refs. [26, 27], a smaller (i.e. more
3161 negative) value of D is observed in data compared to MC $t\bar{t}$ continuum predictions,
3162 though the significance is only at the level of one SD. This can be interpreted as
3163 a hint for the presence of an additional pseudoscalar contribution from a $t\bar{t}$ bound
3164 state, consistent with the results of this work.

3165 7.11 Summary and Outlook

3166 In this chapter, a generic search for spin-0 states in $t\bar{t}$ events with the full data of
3167 LHC Run 2 was presented, targeting the dilepton decay channel of $t\bar{t}$. In addition
3168 to the invariant mass $m_{t\bar{t}}$, it uses the spin correlation variables c_{hel} and c_{han} to probe
3169 the spin and \mathcal{CP} structure of $t\bar{t}$ and possible new particles.

3170 A statistically significant excess was observed in data for low $m_{t\bar{t}}$ events, close
3171 to the $t\bar{t}$ production threshold, showing spin correlations consistent with a pseu-
3172 doscalar state. This excess is interpreted as a pseudoscalar $t\bar{t}$ quasi-bound state η_t ,
3173 which is expected to be present in the SM according to NRQCD calculations. A
3174 simplified model for the production of η_t is used to measure its cross section, yielding
3175 $\sigma(\eta_t) = 8.7 \pm 1.1 \text{ pb}$. Several cross-checks of this result, relaxing assumptions on the
3176 $t\bar{t}$ kinematic reconstruction as well as considering alternate MC generator setups,
3177 validate the observed excess. This result represents the first observation of η_t .

3178 Alternatively, the excess could be interpreted as an additional pseudoscalar boson
3179 A , with mass close to the $t\bar{t}$ threshold. While the explanation as a $t\bar{t}$ bound state
3180 might be favored *a priori* as it is part of the SM and does not invoke any new
3181 physics, experimentally the two interpretations cannot be distinguished with the
3182 current resolution. In addition to the interpretation of the excess, exclusion limits
3183 are set on new pseudoscalar or scalar bosons A/H through their coupling strengths
3184 to the top quark, allowing for either one or both of these bosons simultaneously.
3185 They are presented for two scenarios, where the observed excess is either assumed
3186 to be fully described by the bound state η_t or fully by the new boson A . These limits
3187 are further combined with a separate analysis targeting the $\ell+\text{jets}$ decay channel of
3188 $t\bar{t}$.

3189 It is clear that much remains to be studied about the excess observed in this
3190 work. Firstly, the interpretation in terms of η_t presented here is performed only
3191 in the dilepton channels. In the preliminary results of Ref. [8], the combination
3192 with the $\ell+\text{jets}$ channels was also performed for the measurement of the η_t cross
3193 section; however, since the $\ell+\text{jets}$ analysis used was not optimized for signals at the
3194 $t\bar{t}$ threshold, little sensitivity could be gained compared to the dilepton channels
3195 alone. Instead, a separate $\ell+\text{jets}$ analysis optimized for a $t\bar{t}$ bound state should be
3196 performed in the future. In particular, spin correlation variables analogous to c_{hel}
3197 and c_{han} could be defined also in the $\ell+\text{jets}$ channel, as has already been done in

3198 Ref. [25] through ML-based identification of the decay products of the hadronically
3199 decaying top quark.

3200 By contrast, in the dilepton channel, the most pressing targets of improvement are
3201 the kinematic reconstruction and the $t\bar{t}$ modeling uncertainties. For the former, it
3202 would again be useful to investigate ML-based reconstruction techniques, for which
3203 several proof-of-concept studies have already been performed [172, 216], in a realistic
3204 setup. For the latter, the differences between different generator setups, as briefly
3205 studied in Sec. 7.5.4, needs to be understood more deeply. It would be ideal to cover
3206 the difference between predictions by a set of well-motivated nuisance parameters
3207 with clear physical meaning, as has been recently used by CMS in the measurement
3208 of the W boson mass [68, 217]. Extending this approach to the $t\bar{t}$ process however
3209 requires many theoretical advancements, and is likely to lie far in the future for now.
3210 In a similar fashion, it will be required to obtain a more precise prediction for the $t\bar{t}$
3211 bound state itself. A possible approach here, involving the reweighting of $t\bar{t}$ events
3212 by the ratio of Green’s functions, is presented in Ref. [39], though this remains to
3213 be validated.

3214 To sidestep the issue of imperfect modeling of both η_t and the $t\bar{t}$ continuum,
3215 one could attempt to observe the $t\bar{t}$ bound state in other decay channels, the most
3216 promising being the decay $\eta_t \rightarrow \gamma\gamma$ to two photons. This final state is experimentally
3217 extremely clean and does not require MC modeling of the $\gamma\gamma$ background. Instead,
3218 a possible signal could be extracted using a parametric fit of a peak over a falling
3219 background, similar to the measurement of the SM Higgs boson in the $h \rightarrow \gamma\gamma$
3220 channel. The most important obstacle in such a project would be the small branching
3221 ratio of η_t to $\gamma\gamma$. Extrapolations of the partial width to $\gamma\gamma$ from $b\bar{b}$ and $c\bar{c}$ bound
3222 states [218], combined with an expected total width of $\Gamma(\eta_t) \approx 2m_t$, predict a
3223 branching ratio of $\approx 2 \times 10^{-5}$, though this is a rough estimate that could be wrong
3224 by as much as an order of magnitude. If this prediction holds, it might be possible
3225 to observe this decay channel with the full statistics collected in Runs 2 and 3 of
3226 the LHC. Moreover, a measurement of the ratio of branching fractions to $\gamma\gamma$ and $t\bar{t}$
3227 could help distinguish a bound state from possible BSM scenarios.

3228 It is further necessary, of course, to repeat the analysis presented here with the
3229 data of LHC Run 3, ideally combining the results. While the η_t cross section, and
3230 similarly A/H limits at low masses, are dominated by systematic effects, especially
3231 the sensitivity at high A and H masses is limited by the statistics of the data. The
3232 increase in center-of-mass energy from 13 to 13.6 TeV will also help increase the
3233 cross section of high-mass signals, together making it possible to extend the probed
3234 A/H mass range to higher values.

3235 Furthermore, concerning the limits on A and H derived here, the next step is
3236 to include these generic exclusion limits into concrete bounds on BSM models of
3237 interest. A particular such model, the production of heavy Axion-Like Particles
3238 coupling to top quarks, is studied on a phenomenological basis in the following
3239 chapter.

3240 **8 Investigation of Axion-Like Particles**
3241 **decaying to $t\bar{t}$**

3242 **8.1 Introduction**

3243 Following the results of Chapter 7 including the interpretations as generic scalar or
3244 pseudoscalar bosons and $t\bar{t}$ bound states, this chapter is dedicated to Axion-Like
3245 Particles decaying to $t\bar{t}$. As explained in Sec. 2.3.3, the coupling structure of ALPs
3246 to top quarks is identical to those of the generic pseudoscalar A, such as e.g. in
3247 the 2HDM, if the basis for the ALP is chosen appropriately (cf. Eq. (2.23)). The
3248 difference comes from the gluon interaction term, which is absent for the model used
3249 for A in Chapter 7, and which results in an additional diagram where the ALP is
3250 produced through a contact interaction with the gluons.

3251 If the coefficient $c_{\tilde{G}}$ of the ALP-gluon interaction term in Eq. (2.23) vanishes, the
3252 forms of the Lagrangians for ALP and A become identical, and the limits for A
3253 shown in Chapter 7 can be directly recasted. This is done in Sec. 8.2. If on the
3254 other hand $c_{\tilde{G}} \neq 0$, the kinematic distributions of the ALP will differ from those of
3255 A, and the experimental results are not easily translatable. This case is addressed in
3256 the scope of this work through an phenomenological study on simulation only. The
3257 technical setup of this study is described in Sec. 8.3, after which the distributions
3258 of ALP and A are compared for different benchmark points in Sec. 8.4. Projected
3259 exclusion limits for the $c_{\tilde{G}} \neq 0$ case are presented in Sec. 8.5, and a short summary
3260 is given in Sec. 8.6.

3261 The results of this chapter have been originally published in *JHEP* as Ref. [10].
3262 Since the results of Chapter 7 (Refs. [8, 9]) were not yet public at the time, the
3263 previous CMS result from Ref. [17] was used as a baseline. For this thesis, the
3264 translation of limits in Sec. 8.2 has been updated to reflect the results of Chapter 7.

3265 All results presented in this chapter have been obtained as part of this thesis,
3266 except for the comparison to other final states in Sec. 8.5, which was performed by
3267 the coauthors of Ref. [10] as indicated.

3268 **8.2 Translation of experimental limits**

3269 In the basis of Eq. (2.23), the ALP Lagrangian is identical in form to the Lagrangian
3270 of the generic pseudoscalar A given in Eq. (2.18) as long as the gluon interaction

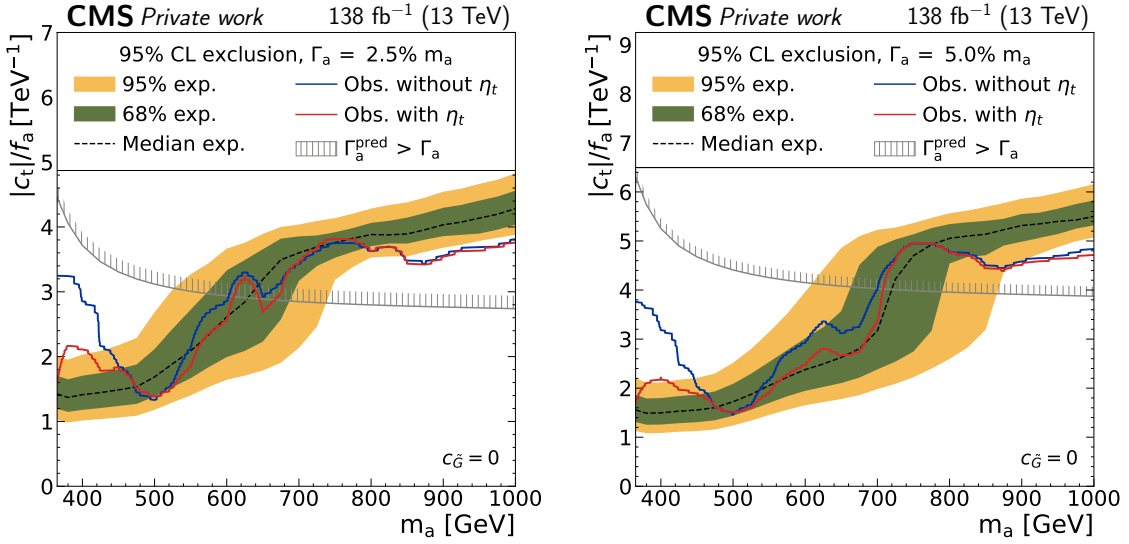


Figure 8.1: **ALP limits for $c_{\tilde{G}} = 0$.** Expected and observed limits on the ALP-top coupling c_t/f_a as a function of the ALP mass for the case $c_{\tilde{G}} = 0$ for the combined dilepton and $\ell+\text{jets}$ decay channels, translated from the results of Chapter 7. The expected limit (black line) is shown without contribution from $t\bar{t}$ bound states in the background modeling, while the observed limit is shown both without $t\bar{t}$ bound states (blue) and with η_t included in the background (red). *Figure adapted from Ref. [10].*

3271 coefficient $c_{\tilde{G}}$ vanishes. For this case, one finds by comparing the coefficients that
3272 the phenomenology will be identical if

$$\frac{c_t}{f_a} = \frac{g_{A t \bar{t}}}{v} \quad (8.1)$$

3273 where $v = 246$ GeV is the SM Higgs vacuum expectation value. Thus, the exper-
3274imental results of Chapter 7, particularly the limits on $g_{A t \bar{t}}$ from the combination of
3275dilepton and $\ell+\text{jets}$ decay channels as presented in Sec. 7.9.2, can be recasted into
3276limits on the ALP coupling c_t/f_a for the case $c_{\tilde{G}} = 0$. This is shown in Fig. 8.1 for
3277two different (fixed) ALP widths. The observed limits are shown with and without
3278a $t\bar{t}$ bound state contribution as modeled by η_t in the background modeling, corre-
3279sponding to the two scenarios in Fig. 7.26 and Fig. 7.28, and the same excess as in
3280Chapter 7 is seen for at low ALP masses when the η_t contribution is not included.

3281 In a similar fashion, the best-fit point for A as presented in Eq. (7.17) can be
3282translated to an ALP for the case of $c_{\tilde{G}} = 0$, giving

$$m_a = 365 \text{ GeV}, \quad \Gamma_a/m_a = 2\%, \quad \text{and} \quad \frac{c_t}{f_a} = 3.2 \pm 0.2 \text{ TeV}^{-1}.$$

This represents a third alternative interpretation of the excess besides a $t\bar{t}$ bound state or a generic pseudoscalar A . The same caveats as for the A interpretation, as outlined in Sec. 7.7.4, apply; in particular, the mass of 365 GeV is the lowest mass point considered in the signal samples, and it is possible that lower masses closer to the $t\bar{t}$ threshold would result in a better fit.

8.3 Phenomenological setup

The remainder of this chapter is dedicated to exploring an ALP decaying to $t\bar{t}$ for the case $c_{\tilde{G}} \neq 0$, for which the results of Chapter 7 are not easily translatable since the distributions are expected to differ in shape. Due to time constraints, it was not possible as part of this work to investigate this case experimentally in the same fashion as done in Chapter 7. Instead, a phenomenological study is performed on MC simulation only, using a setup that approximates the workflow in Chapter 7.

To do so, MC samples for the signal are generated at LO in QCD with MADGRAPH 5 for two different ALP masses (400 GeV and 800 GeV). For the ALP, an UFO model taken from Ref. [219] is used and modified to include the top quark loop form factor including finite mass effects, according to the expressions given in Ref. [220]. Both possible production diagrams, as shown in Fig. 2.8, as well as their interference with the SM are considered. A similar ME reweighting technique as in Sec. 7.4 is used to obtain samples for different widths and $c_{\tilde{G}}$ values. For the generic pseudoscalar A as well as the SM $t\bar{t}$ background, the same generators as in Sec. 7.2.1 are used (MADGRAPH 5 and POWHEG v2 hvq, respectively). For all samples, the NNPDF 3.1 PDF set [65] is used, and PYTHIA 8.2 is used to simulate initial and final state radiation [76].

Only the dilepton decay channel of $t\bar{t}$ is considered, and no detector simulation is performed. Instead, the truth-level top quarks and leptons after parton showering are used, and a Gaussian smearing is applied to $m_{t\bar{t}}$ randomly on a per-event basis, the standard deviation of which is chosen so that the resolution of the resulting distribution matches that observed in full detector simulation. Since this study was performed before the results of Chapter 7 were public, its predecessor Ref. [17] is used to extract the resolution by fitting to the $m_{t\bar{t}}$ distributions displayed therein. The result is $\sigma(m_{t\bar{t}})/m_{t\bar{t}} = 15\%$, which is somewhat lower than the widths found using the full detector simulation in Sec. 7.2.5 (c.f. Fig. 7.2). However, it should be cautioned that since the true $m_{t\bar{t}}$ smearing in the full detector simulation is not perfectly Gaussian, the results are not one-to-one comparable.

The experimental acceptance and efficiency, defined as the fraction of $t\bar{t} \rightarrow \ell\ell$ (ℓ being electrons, muons or leptonically decaying taus) events to survive all trigger and selection requirements, is estimated to be 10.6% for both signal and $t\bar{t}$ background, also based on Ref. [17]. This is lower compared to the updated analysis presented in Chapter 7, where values of 15–16% are achieved, varying slightly with the data-

3322 taking period. Thus, the projections in this chapter should be considered somewhat
3323 conservative.

3324 Since the ALP always has a \mathcal{CP} -odd coupling to top quarks (cf. Eq. (2.23)), it
3325 is expected to decay to a $t\bar{t}$ system in the 1S_0 state, identically to A. This is true
3326 irrespective of the gluon coupling $c_{\tilde{G}}$ since the latter only affects the production, not
3327 the decay, and the ALP as a colorless, spinless particle has no internal degrees of
3328 freedom. Thus, $m_{t\bar{t}}$ and c_{hel} are good discriminating variables, again similar to A,
3329 while c_{han} (optimal for \mathcal{CP} -even couplings) does not offer much additional discrim-
3330 ination and is not considered here. For simplicity, instead of a multi-dimensional
3331 binning in $m_{t\bar{t}}$ and c_{hel} like in Chapter 7, a one-dimensional binning in $m_{t\bar{t}}$ only is
3332 used, and events are required to have $c_{\text{hel}} > 0.6$ to enhance the ALP signal over the
3333 background.

3334 A simplified version of the likelihood model from Chapter 7 is used, implemented
3335 in `pyhf` [120], in order to estimate projected significances and limits. Only sources
3336 of systematic uncertainty arising from theory are considered, namely:

- 3337 • Missing higher orders in the matrix element, estimated from varying renor-
3338 malization and factorization scale by factors of 2,
- 3339 • The PDF uncertainty, estimated as the envelope of 100 pseudo-Hessian NNPDF 3.1
3340 replicas [65],
- 3341 • The total $t\bar{t}$ background production cross section, taken as a log-normal un-
3342 certainty of 6% following Ref. [17],
- 3343 • The top quark mass in the $t\bar{t}$ background, varied in the range $m_t = 172.5 \pm$
3344 1 GeV.

3345 It is clear that this simple treatment of systematic uncertainties can only give a
3346 rough estimate of the full likelihood as used in Chapter 7, which is sensitive mostly to
3347 the differences in shapes induced by the various systematic sources. In particular,
3348 like in the experimental result, the variation in the top quark mass is important
3349 especially for ALPs with masses close to the $t\bar{t}$ threshold.

3350 To illustrate the dependence on the likelihood model, the significances in the fol-
3351 lowing results will be quoted for three different setups including different systematic
3352 uncertainties, namely all of the above, all of the above except for the top quark
3353 mass, and statistical uncertainties only. By comparing to the expected significance
3354 given in Ref. [17] for the best-fit point of the pseudoscalar A, it is found that the
3355 full setup overestimates the uncertainty, while the setup without the top quark mass
3356 slightly underestimates it.

| $c_t/f_a [\text{TeV}^{-1}]$ | $c_{\tilde{G}}/f_a [\text{TeV}^{-1}]$ | A | $(\sigma^{\text{tot}} - \sigma^{\text{SM}}) [\text{pb}]$ |
|-----------------------------|---------------------------------------|------|--|
| 3.0 | +0.015 | 0.95 | +6.7 |
| 3.0 | -0.015 | 0.43 | -2.7 |
| 1.0 | +0.025 | 0.75 | -1.7 |
| 1.0 | -0.025 | 0.87 | +2.0 |

Table 8.1: **Benchmark points for comparing ALP and A.** In addition to the ALP couplings c_t/f_a and $c_{\tilde{G}}/f_a$ for the benchmark points, also the difference in integrated cross section to the SM is shown, as well as a value of $g_{A\bar{t}\bar{t}}$ corresponding to a generic pseudoscalar A with the same integrated cross section.

3357 8.4 Comparison of ALP and A

3358 To investigate the differences and possible discrimination between ALP and A, four
 3359 different ALP benchmark points with $c_{\tilde{G}} \neq 0$ are defined for a mass of 400 GeV and
 3360 a width of 2.5%. Each of the benchmarks is compared to a generic pseudoscalar A
 3361 with its coupling $g_{A\bar{t}\bar{t}}$ chosen such that the total integrated cross section of ALP and
 3362 A are identical, i.e. that they can not be distinguished by cross section information
 3363 alone. The chosen couplings and resulting cross sections can be found in Tab. 8.1.

3364 The expected $m_{t\bar{t}}$ distributions, including the smearing and acceptance described
 3365 in Sec. 8.3, for the four benchmark points are shown in Fig. 8.2, together with the
 3366 expected statistical uncertainty for both Run 2 and the HL-LHC.

3367 It can be seen that the shapes of the distributions differ qualitatively for the differ-
 3368 ent benchmarks: For example, the case $c_t/f_a = 3.0 \text{ TeV}^{-1}$ and $c_{\tilde{G}}/f_a = 0.015 \text{ TeV}^{-1}$
 3369 (top left) shows a clear peak-dip structure similar to the A case, and as a result will
 3370 likely not be distinguishable from it. In contrast, e.g. the case $c_t/f_a = 1.0 \text{ TeV}^{-1}$
 3371 and $c_{\tilde{G}}/f_a = -0.025 \text{ TeV}^{-1}$ (bottom right) shows a dip-peak structure instead, which
 3372 cannot be reproduced by the A. This is possible because of the relative sign of the
 3373 two couplings in this case, i.e. $c_t c_{\tilde{G}} < 0$, which flips the sign of the interference
 3374 between the gluon interaction diagram in Fig. 2.8 and the SM.

3375 By comparing the distributions to the expected statistical uncertainty, one can
 3376 already estimate roughly whether discrimination of the signals with respect to the
 3377 SM or with respect to each other is possible. To quantify this further, the expected
 3378 significance to reject the SM-only hypothesis under the benchmark scenarios are
 3379 reported in Tab. 8.2. They are computed with the likelihood model as defined in
 3380 Sec. 8.3, and quoted both for the three different described uncertainty setups as
 3381 well as for three different eras of the LHC, corresponding to different (expected)
 3382 integrated luminosities: full Run 2 (138 fb^{-1}), Run 2+3 (300 fb^{-1}), and the HL-
 3383 LHC (3 ab^{-1}). For the latter case, all systematic uncertainties are halved to account

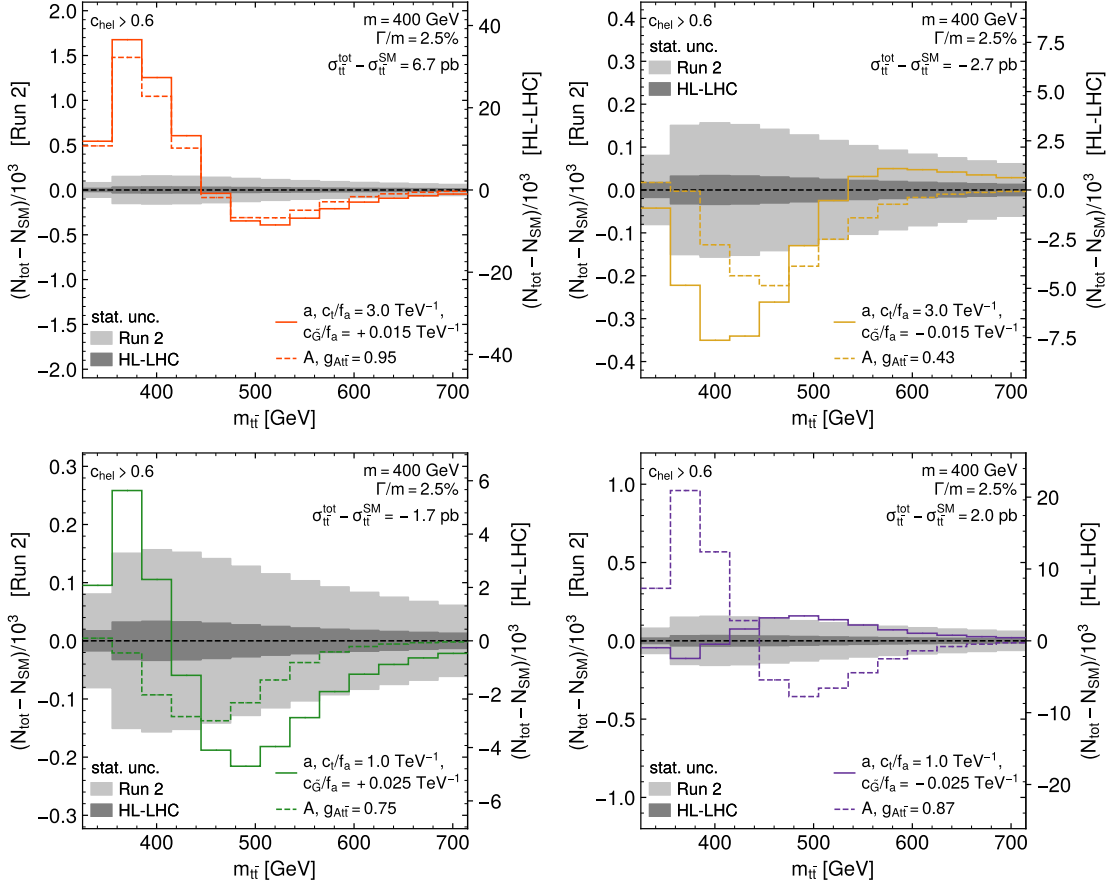


Figure 8.2: **Expected $m_{t\bar{t}}$ distributions for $pp \rightarrow a/A \rightarrow t\bar{t}$.** Shown are both ALP and A at a mass of 400 GeV for four benchmark points, with the SM subtracted. The couplings for A and a are adjusted such that the inclusive cross section is identical. The grey bands show the expected statistical uncertainty for Run 2 and HL-LHC. *Figure taken from Ref. [10].*

for the expected increase in data reconstruction quality and reduction in theoretical uncertainty.

Tab. 8.2 shows that all considered benchmark scenarios can be expected to be distinguished from the SM with $> 5\sigma$ significance if the top quark mass uncertainty is not considered in the model, that is, if experimentally it can be significantly reduced from the estimate used in this study.

If one such signal would be discovered in the future, it would be important to ascertain the particle it originates from. The $m_{t\bar{t}}$ distribution could then be used to distinguish between an ALP, exhibiting both couplings to top quarks and gluons, and the more restrictive case of A, in which only a top quark coupling is allowed. To quantify this, Tab. 8.3 now shows, for the four benchmark points, the expected

| | | ^a | Significance (a vs. SM) | | |
|-----|----------|--------------|----------------------------|----------|------------|
| | | | all syst. | no m_t | stats only |
| 3.0 | $+0.015$ | Run 2 | 3.9 | > 10 | > 10 |
| | | Run 2+3 | 5.2 | > 10 | > 10 |
| | | HL-LHC | > 10 | > 10 | > 10 |
| 3.0 | -0.015 | Run 2 | 2.1 | 2.2 | 4.4 |
| | | Run 2+3 | 3.0 | 3.0 | 6.5 |
| | | HL-LHC | 8.7 | 8.8 | > 10 |
| 1.0 | $+0.025$ | Run 2 | 1.1 | 2.6 | 4.0 |
| | | Run 2+3 | 1.4 | 3.2 | 5.9 |
| | | HL-LHC | 3.9 | 8.2 | > 10 |
| 1.0 | -0.025 | Run 2 | 0.7 | 1.7 | 2.8 |
| | | Run 2+3 | 0.9 | 2.2 | 4.1 |
| | | HL-LHC | 2.3 | 5.5 | > 10 |

Table 8.2: **Significances for detecting an ALP** with a mass of 400 GeV and a width of 2.5% for the benchmark scenarios considered in Fig. 8.2. Three different treatments of the uncertainties as defined in Sec. 8.3 are shown. For the HL-LHC projection, all systematic uncertainties are scaled by a factor of 0.5.

significances for rejecting the A hypothesis assuming that the corresponding ALP model is realized in nature. Again, the three different uncertainty models and three LHC eras are shown in the same fashion. It can be seen that for all benchmarks, the HL-LHC data would make it possible to distinguish the two scenarios with $> 5\sigma$ significance in the case of an observation.

8.5 Projected limits for ALPs

In case that no (additional) signal is seen in either Run 3 or at the HL-LHC, one would quantify the exclusion of ALP models based on limits in the plane of c_t/f_a and $c_{\tilde{G}}/f_a$. Projections for such expected 95% exclusion limits are presented in Fig. 8.3 for the three different considered luminosities as well as for ALP masses of 400 and 800 GeV, again computed with the same likelihood model. All systematic uncertainties save for the top quark mass are considered here, same as in the “no m_t ” column in Tabs. 8.2 and 8.3.

The figures show that strong limits can be set for values of $|c_{\tilde{G}}|/f_a \gtrsim 0.05 \text{ TeV}^{-1}$ where the gluon-ALP interaction dominates and leads to signals with large cross sections, while the limits are weaker close to $c_{\tilde{G}} = 0$. Notably, the smallest signals are obtained for slightly negative values of $c_{\tilde{G}}/f_a$ due to destructive interference between the two production diagrams, leading to a slight tilt of the curve in the

| c_t/f_a [TeV $^{-1}$] | a | $c_{\tilde{G}}/f_a$ [TeV $^{-1}$] | A $g_{A t\bar{t}}$ | Luminosity | Significance (a vs. A) | | |
|--------------------------|--------|------------------------------------|-------------------------|------------|------------------------------|----------|------------|
| | | | | | all syst. | no m_t | stats only |
| 3.0 | +0.015 | 0.95 | | Run 2 | 1.3 | 1.9 | 3.3 |
| | | | | Run 2+3 | 1.8 | 2.3 | 4.9 |
| | | | | HL-LHC | 5.3 | 5.7 | > 10 |
| 3.0 | −0.015 | 0.43 | | Run 2 | 1.2 | 1.9 | 3.3 |
| | | | | Run 2+3 | 1.7 | 2.4 | 4.9 |
| | | | | HL-LHC | 5.0 | 6.0 | > 10 |
| 1.0 | +0.025 | 0.75 | | Run 2 | 1.5 | 2.3 | 2.7 |
| | | | | Run 2+3 | 2.0 | 3.1 | 3.9 |
| | | | | HL-LHC | 5.8 | 8.8 | > 10 |
| 1.0 | −0.025 | 0.87 | | Run 2 | 3.7 | 9.0 | > 10 |
| | | | | Run 2+3 | 4.6 | > 10 | > 10 |
| | | | | HL-LHC | > 10 | > 10 | > 10 |

Table 8.3: **Significances for the discrimination of an ALP and A** for the benchmark scenarios considered in Fig. 8.2. The uncertainties are treated as in Tab. 8.2.

³⁴¹³ left panel of Fig. 8.3. Of the four considered benchmark points for a 400 GeV ALP,
³⁴¹⁴ all can be safely expected to be excluded with HL-LHC data, while those with
³⁴¹⁵ $c_t/f_a = 3 \text{ TeV}^{-1}$ might already be excluded by the combination of Run 2 and 3.

³⁴¹⁶ As part of the work of the coauthors in Ref. [10], the projected limits for Run 2
³⁴¹⁷ were compared with limits derived from existing analyses in other search channels,
³⁴¹⁸ using the tool `HiggsTools` [221]. These are reproduced briefly in the following in
³⁴¹⁹ order to provide a point of reference; details can be found in Ref. [10]. The following
³⁴²⁰ search channels were found to be of relevance:

- ³⁴²¹ • $pp \rightarrow a \rightarrow \gamma\gamma$, from a generic narrow-resonance search in ATLAS [222],
- ³⁴²² • ³⁴²³ $pp \rightarrow a \rightarrow Zh$, from a search for pseudoscalars decaying into a Z boson and a SM Higgs boson in ATLAS [223],
- ³⁴²⁴ • ³⁴²⁵ $pp \rightarrow t\bar{t}a \rightarrow t\bar{t}t\bar{t}$, from the CMS measurement of the four-top production cross section [224],
- ³⁴²⁶ • ³⁴²⁷ interference effects between the ALP effective Lagrangian and SM Effective Field Theory (SMEFT), which would induce non-zero Wilson coefficients of SMEFT operators in electroweak precision observables such as e.g. the W boson mass, leading to indirect limits [225].

³⁴³⁰ The comparison of all these limits to the projected limits from $pp \rightarrow a \rightarrow t\bar{t}$ de-
³⁴³¹ rived in this work is shown in Fig. 8.4 in the c_t - $c_{\tilde{G}}$ plane for a 400 GeV ALP.

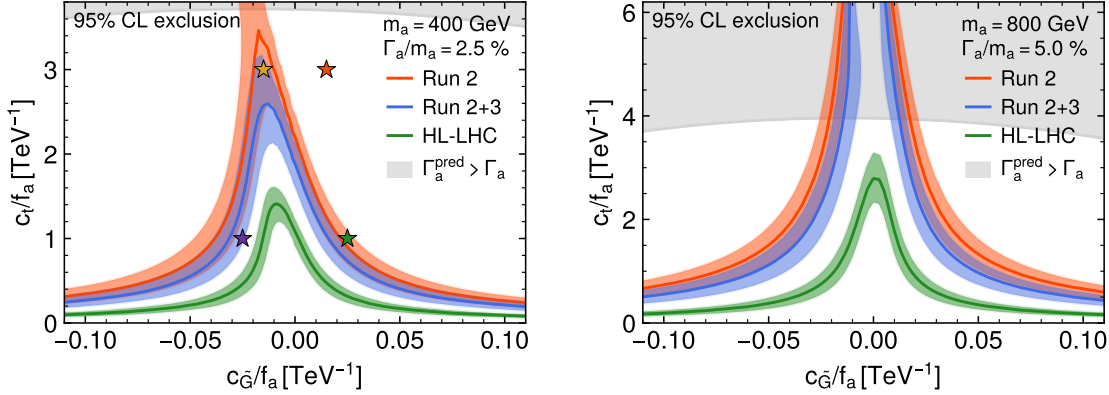


Figure 8.3: **Projected ALP limits.** Projected 95% exclusion limits in the plane of $c_{\tilde{G}}/f_a$ and c_t/f_a for a mass of 400 GeV and a width of 2.5% (left) as well as 800 GeV and 5.0% (right). The limits are shown for three different integrated luminosities, corresponding to Run 2, Run 2+3, and the HL-LHC, where for the latter the systematic uncertainties are halved. *Figure taken from Ref. [10].*

For almost all points, $\text{pp} \rightarrow a \rightarrow t\bar{t}$ leads to stronger limits than all other direct search channels. Furthermore, for $|c_{\tilde{G}}|/f_a \gtrsim 0.03 \text{ TeV}^{-1}$ the projected limits are also stronger than the indirect ones from ALP-SMEFT interference, while this is not the case for smaller $|c_{\tilde{G}}|/f_a$. It should however be noted here that the indirect limits are subject to more assumptions, in particular, that the ALP is the only new physics contribution at the ALP scale ($\approx f_a$). For a more detailed discussion, see again Ref. [10].

8.6 Summary and Outlook

In this chapter, the $t\bar{t}$ final state is found to be an excellent channel for searching for heavy ALPs coupling to top quarks. Depending on the value of the explicit gluon-ALP coupling $c_{\tilde{G}}$, two scenarios are considered. For $c_{\tilde{G}} = 0$, the results of the experimental search for a generic pseudoscalar presented in Chapter 7 of this work, including the excess observed there, are directly translated into limits on the ALP-top coupling c_t/f_a .

For $c_{\tilde{G}} \neq 0$, on the other hand, a phenomenological study targeting the dilepton decay channel of $t\bar{t}$ is performed on simulation only, comparing ALPs to a generic pseudoscalar A which does not couple directly to gluons. It is found that ALP and A can lead to drastically different $m_{t\bar{t}}$ distributions depending on the coupling values, and could possibly be distinguished at the HL-LHC if a signal is observed. Furthermore, projected expected limits in the plane of the ALP couplings c_t/f_a and

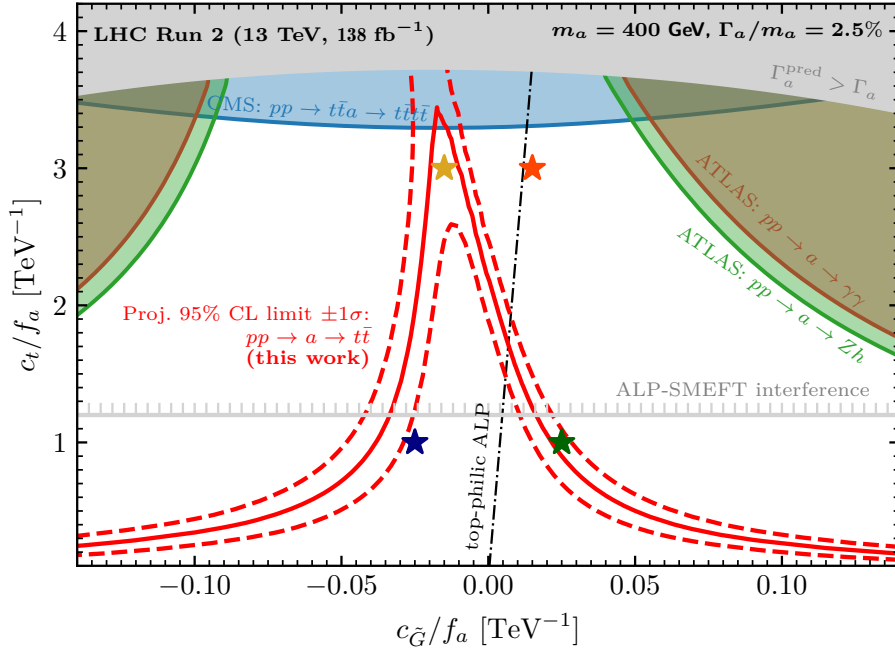


Figure 8.4: **Comparison of limits from different search channels.** 95% exclusion limits in the plane of $c_{\tilde{G}}/f_a$ and c_t/f_a for a mass of 400 GeV and a width of 2.5% (left) from different search channels. The projected limits from this work are overlaid in red. *Figure taken from Ref. [10].*

3452 $c_{\tilde{G}}/f_a$ are set for different integrated luminosities. They are more sensitive than
3453 other possible direct search channels in almost the whole parameter space.

3454 The obvious continuation of this work would be to include the ALP signals for
3455 the $c_{\tilde{G}} \neq 0$ case into an experimental search like the one performed in Chapter 7.
3456 For the purpose of this thesis, this was not possible within the time constraints, and
3457 needs to be postponed to the future. Alternatively, one could investigate how the
3458 parameter space considered in this work - in particular, the very large ALP mass
3459 and comparatively strong top coupling - match to possible UV completions of the
3460 ALP effective Lagrangian and, if such models exist, whether they can still solve the
3461 strong \mathcal{CP} problem.

3462 9 Summary and Conclusions

3463 In this work, several aspects of top quark pair ($t\bar{t}$) production with the CMS detector
3464 at the Large Hadron Collider (LHC) were studied. First, a measurement of the
3465 inclusive $t\bar{t}$ production cross section at a center-of-mass energy of $\sqrt{s} = 13.6$ TeV was
3466 performed, using 1.21 fb^{-1} of early LHC Run 3 data. By combining the dilepton and
3467 $\ell+\text{jets}$ decay channels of $t\bar{t}$ for the first time and categorizing the events by their
3468 number of b-tagged jets, the analysis is capable of constraining lepton and b tagging
3469 efficiencies directly *in situ*.

3470 The result is $\sigma_{t\bar{t}} = 882 \pm 23 \text{ (stat+syst)} \pm 20 \text{ (lumi)} \text{ pb}$, compatible with the SM
3471 prediction within one standard deviation. The measurement became public only
3472 two months after datataking, constituting the first physics result of LHC Run 3, and
3473 despite the small considered luminosity is of comparable precision with previous $\sigma_{t\bar{t}}$
3474 measurements. At the time, it served as an important validation of the quality of
3475 CMS Run 3 data.

3476 Second, off-shell $t\bar{t}$ production as well as interference between $t\bar{t}$ and tW produc-
3477 tion was studied in simulation using the Monte Carlo (MC) generator **bb41**, which
3478 generates the full $pp \rightarrow b\bar{b}\ell\ell\nu\nu$ amplitude at next-to-leading order (NLO) in quan-
3479 tum chromodynamics (QCD). In this work, **bb41** matched to the parton shower in
3480 PYTHIA is implemented and validated in the CMS software stack for the first time
3481 and compared to several other $t\bar{t}$ MC generators. Good agreement between **bb41**
3482 and unfolded ATLAS data is found for the variable $m_{b\ell}^{\min\max}$, which is sensitive to
3483 the $t\bar{t}/tW$ interference, and significant shifts in the reconstructed top mass lineshape
3484 compared to other generators are observed. Additionally, a brief investigation of the
3485 matching procedure between **bb41** and PYTHIA is presented. These studies repre-
3486 sent the starting point for future precision $t\bar{t}$ analyses in CMS using **bb41**, such as
3487 measurements of the top mass and width.

3488 Finally, a search for spin-0 states decaying to $t\bar{t}$ in the dilepton channel has
3489 been presented. The search uses the full CMS Run 2 dataset, corresponding to
3490 138 fb^{-1} and $\sqrt{s} = 13$ TeV, and employs the invariant $t\bar{t}$ mass ($m_{t\bar{t}}$) as well as two
3491 $t\bar{t}$ spin correlation obserables to gain sensitivity to the \mathcal{CP} structure of possible
3492 new states. An excess compared to the $t\bar{t}$ continuum prediction is observed for
3493 low $m_{t\bar{t}}$ events, consistent with spin correlations as expected from a pseudoscalar
3494 state. This excess is interpreted as a pseudoscalar $t\bar{t}$ bound state η_t , as predicted
3495 by several calculations in non-relativistic QCD (NRQCD). The production cross
3496 section of η_t is measured using a simplified η_t model, resulting in $\sigma(\eta_t) = 8.7 \pm$
3497 1.1 pb , which is of the same order of magnitude as NRQCD-based estimates. The

9 Summary and Conclusions

3498 uncertainty is dominated by its systematic component, in particular the challenging
3499 modeling of the $t\bar{t}$ continuum. Several detailed cross-checks, such as bypassing
3500 the experimental $t\bar{t}$ reconstruction as well as using different MC generators, are
3501 discussed, and all confirm the presence of the excess. The significance of the result
3502 exceeds five standard deviations.

3503 Alternatively, the same search is interpreted in terms of new, generic pseudoscalar
3504 (A) or scalar (H) particles coupling to top quarks, as expected e.g. in Two-Higgs
3505 Doublet models (2HDMs). The interference between the new particles and the SM
3506 is taken into account. Besides an interpretation of the same excess at low $m_{t\bar{t}}$,
3507 exclusion limits on the couplings to the top quark are presented in two scenarios,
3508 assuming the excess to be either fully described by A and H or fully by a $t\bar{t}$ bound
3509 state. These limits are combined with a similar search in the $\ell+$ jets decay channels
3510 of $t\bar{t}$, and exclusion regions are also provided for the simultaneous presence of A and
3511 H.

3512 For a third interpretation, Axion-Like Particles (ALPs) decaying to $t\bar{t}$ are con-
3513 sidered. It is found that in the case of vanishing tree-level couplings between ALP
3514 and gluons $c_{\tilde{G}}$, the results for the generic pseudoscalar A are directly translatable,
3515 and experimental limits on the coupling between ALP and top quark are presented.
3516 The more generic case of $c_{\tilde{G}} \neq 0$ is studied using simulated events, and projected
3517 significances and exclusion limits on such ALPs decaying to $t\bar{t}$ are derived for var-
3518 ious phases of the LHC. It is found that at the high-luminosity LHC, ALPs and
3519 other pseudoscalars as e.g. in the 2HDM could be distinguishable based on their
3520 $m_{t\bar{t}}$ distribution. The resulting projected limits are expected to improve on limits
3521 from other final states in large areas of phase space.

3522 Branching out from the different aspects of this work, many directions of further
3523 study could be pursued. The most pressing one is certainly a further investigation
3524 of the excess at the $t\bar{t}$ production threshold observed here. Besides the outstand-
3525 ing confirmation or refutation from the ATLAS experiment, it would be of great
3526 interest to attempt to determine the origin of the excess - in particular, whether it
3527 is purely the result of a SM bound state or whether it originates in BSM physics
3528 - though this will likely be challenging. Searches at the same invariant mass in
3529 other decay channels, in particular $\gamma\gamma$, as well as measurements of other kinematic
3530 distributions for low $m_{t\bar{t}}$ events could represent first steps towards this goal. It is
3531 also in general important to improve the experimental $t\bar{t}$ reconstruction techniques
3532 e.g. with modern machine learning approaches, which would also greatly contribute
3533 to precision measurements of top quark properties. From the theoretical side, more
3534 precise calculations of the $t\bar{t}$ threshold region are required, for which this work will
3535 hopefully serve as a motivation.

3536 It is not every day that such an excess is observed in high energy physics. One can
3537 only hope that, regardless of its origin, its study will produce many further results
3538 of great interest.

3539

A Bibliography

- 3540 [1] ATLAS Collaboration, “Observation of a new particle in the search for the
3541 standard model Higgs boson with the ATLAS detector at the LHC”, *Phys.*
3542 *Lett. B*, vol. 716, p. 1, 2012. DOI: 10.1016/j.physletb.2012.08.020. arXiv:
3543 1207.7214 [hep-ex].
- 3544 [2] CMS Collaboration, “Observation of a new boson at a mass of 125 GeV with
3545 the CMS experiment at the LHC”, *Phys. Lett. B*, vol. 716, p. 30, 2012. DOI:
3546 10.1016/j.physletb.2012.08.021. arXiv: 1207.7235 [hep-ex].
- 3547 [3] CMS Collaboration, “Observation of a new boson with mass near 125 GeV
3548 in pp collisions at $\sqrt{s} = 7$ and 8 TeV”, *JHEP*, vol. 06, p. 081, 2013. DOI:
3549 10.1007/JHEP06(2013)081. arXiv: 1303.4571 [hep-ex].
- 3550 [4] CMS Collaboration, “The CMS Experiment at the CERN LHC”, *JINST*,
3551 vol. 3, S08004, 2008. DOI: 10.1088/1748-0221/3/08/S08004.
- 3552 [5] CMS Collaboration, “First measurement of the top quark pair production
3553 cross section in proton-proton collisions at $\sqrt{s} = 13.6$ TeV”, *JHEP*, vol. 08,
3554 p. 204, 2023. DOI: 10.1007/JHEP08(2023)204. arXiv: 2303.10680 [hep-ex].
- 3555 [6] CMS Collaboration, “Simulation of on- and off-shell $t\bar{t}$ production with the
3556 Monte Carlo generator b_bbar_4l at CMS”, CERN, Geneva, Tech. Rep.,
3557 2023. [Online]. Available: <https://cds.cern.ch/record/2884265>.
- 3558 [7] T. Ježo, J. M. Lindert, P. Nason, C. Oleari, and S. Pozzorini, “An NLO+PS
3559 generator for $t\bar{t}$ and Wt production and decay including non-resonant and
3560 interference effects”, *Eur. Phys. J. C*, vol. 76, p. 691, 2016. DOI: 10.1140/
3561 epjc/s10052-016-4538-2. arXiv: 1607.04538 [hep-ph].
- 3562 [8] CMS Collaboration, “Search for heavy pseudoscalar and scalar bosons de-
3563 caying to top quark pairs in proton-proton collisions at $\sqrt{s} = 13$ TeV”, CMS
3564 Physics Analysis Summary CMS-PAS-HIG-22-013, 2024. [Online]. Available:
3565 <https://cds.cern.ch/record/2911775>.
- 3566 [9] CMS Collaboration, “Observation of a pseudoscalar excess at the top quark
3567 pair production threshold”, 2025. arXiv: 2503.22382 [hep-ex].
- 3568 [10] A. Anuar et al., “ALP-ine quests at the LHC: hunting axion-like particles
3569 via peaks and dips in $t\bar{t}$ production”, *JHEP*, vol. 24, p. 197, 2024. DOI: 10.
3570 1007/JHEP12(2024)197. arXiv: 2404.19014 [hep-ph].
- 3571 [11] R. L. Workman et al., “Review of Particle Physics”, *PTEP*, vol. 2022, p. 083C01,
3572 2022. DOI: 10.1093/ptep/ptac097.

- 3573 [12] P. W. Higgs, “Broken symmetries, massless particles and gauge fields”, *Phys.*
3574 *Lett.*, vol. 12, pp. 132–133, 1964. DOI: 10.1016/0031-9163(64)91136-9.
- 3575 [13] F. Englert and R. Brout, “Broken Symmetry and the Mass of Gauge Vector
3576 Mesons”, *Phys. Rev. Lett.*, vol. 13, J. C. Taylor, Ed., pp. 321–323, 1964. DOI:
3577 10.1103/PhysRevLett.13.321.
- 3578 [14] CDF Collaboration, “Observation of top quark production in $\bar{p}p$ collisions”,
3579 *Phys. Rev. Lett.*, vol. 74, pp. 2626–2631, 1995. DOI: 10.1103/PhysRevLett.
3580 74.2626. arXiv: hep-ex/9503002.
- 3581 [15] D0 Collaboration, “Observation of the top quark”, *Phys. Rev. Lett.*, vol. 74,
3582 pp. 2632–2637, 1995. DOI: 10.1103/PhysRevLett.74.2632. arXiv: hep-
3583 ex/9503003.
- 3584 [16] Y. Kats and D. Uzan, “Prospects for measuring quark polarization and spin
3585 correlations in $b\bar{b}$ and $c\bar{c}$ samples at the LHC”, *JHEP*, vol. 03, p. 063, 2024.
3586 DOI: 10.1007/JHEP03(2024)063. arXiv: 2311.08226 [hep-ph].
- 3587 [17] CMS Collaboration, “Search for heavy Higgs bosons decaying to a top quark
3588 pair in proton-proton collisions at $\sqrt{s} = 13$ TeV”, *JHEP*, vol. 04, p. 171, 2020,
3589 [Erratum: JHEP 03, 187 (2022)]. DOI: 10.1007/JHEP04(2020)171. arXiv:
3590 1908.01115 [hep-ex].
- 3591 [18] W. Bernreuther, A. Brandenburg, Z. G. Si, and P. Uwer, “Top quark pair
3592 production and decay at hadron colliders”, *Nucl. Phys. B*, vol. 690, pp. 81–
3593 137, 2004. DOI: 10.1016/j.nuclphysb.2004.04.019. arXiv: hep-ph/
3594 0403035.
- 3595 [19] F. Maltoni, C. Severi, S. Tentori, and E. Vryonidou, “Quantum detection of
3596 new physics in top-quark pair production at the LHC”, *JHEP*, vol. 03, p. 099,
3597 2024. DOI: 10.1007/JHEP03(2024)099. arXiv: 2401.08751 [hep-ph].
- 3598 [20] K. Cheng, T. Han, and M. Low, “Optimizing entanglement and Bell inequality
3599 violation in top antitop events”, *Phys. Rev. D*, vol. 111, no. 3, p. 033004,
3600 2025. DOI: 10.1103/PhysRevD.111.033004. arXiv: 2407.01672 [hep-ph].
- 3601 [21] A. Czarnecki, M. Jezabek, and J. H. Kuhn, “Lepton Spectra From Decays
3602 of Polarized Top Quarks”, *Nucl. Phys. B*, vol. 351, pp. 70–80, 1991. DOI:
3603 10.1016/0550-3213(91)90082-9.
- 3604 [22] W. Bernreuther, A. Brandenburg, Z. G. Si, and P. Uwer, “Spin properties of
3605 top quark pairs produced at hadron colliders”, *Acta Phys. Polon. B*, vol. 34,
3606 K. Fialkowski, M. Jezabek, and M. Rozanska, Eds., pp. 4477–4490, 2003.
3607 arXiv: hep-ph/0304244.

- 3608 [23] CMS Collaboration, “Measurements of t t-bar spin correlations and top quark
3609 polarization using dilepton final states in pp collisions at sqrt(s) = 8 TeV”,
3610 *Phys. Rev. D*, vol. 93, no. 5, p. 052007, 2016. DOI: 10.1103/PhysRevD.93.
3611 052007. arXiv: 1601.01107 [hep-ex].
- 3612 [24] CMS Collaboration, “Measurement of the top quark polarization and t̄t spin
3613 correlations using dilepton final states in proton-proton collisions at $\sqrt{s} =$
3614 13 TeV”, *Phys. Rev. D*, vol. 100, no. 7, p. 072002, 2019. DOI: 10.1103/
3615 PhysRevD.100.072002. arXiv: 1907.03729 [hep-ex].
- 3616 [25] CMS Collaboration, “Measurements of polarization and spin correlation and
3617 observation of entanglement in top quark pairs using lepton+jets events from
3618 proton-proton collisions at $\sqrt{s} = 13$ TeV”, *Phys. Rev. D*, vol. 110, no. 11,
3619 p. 112016, 2024. DOI: 10.1103/PhysRevD.110.112016. arXiv: 2409.11067
3620 [hep-ex].
- 3621 [26] CMS Collaboration, “Observation of quantum entanglement in top quark
3622 pair production in proton–proton collisions at $\sqrt{s} = 13$ TeV”, *Rept. Prog.*
3623 *Phys.*, vol. 87, no. 11, p. 117801, 2024. DOI: 10.1088/1361-6633/ad7e4d.
3624 arXiv: 2406.03976 [hep-ex].
- 3625 [27] ATLAS Collaboration, “Observation of quantum entanglement with top quarks
3626 at the ATLAS detector”, *Nature*, vol. 633, no. 8030, pp. 542–547, 2024. DOI:
3627 10.1038/s41586-024-07824-z. arXiv: 2311.07288 [hep-ex].
- 3628 [28] A. A. Anuar, “Top Quark Spin and Polarization Properties in Searches for
3629 New Phenomena with the CMS Detector at the LHC”, PhD thesis, DESY,
3630 Hamburg, 2019.
- 3631 [29] W. Bernreuther, P. Galler, Z.-G. Si, and P. Uwer, “Production of heavy Higgs
3632 bosons and decay into top quarks at the LHC. II: Top-quark polarization and
3633 spin correlation effects”, *Phys. Rev. D*, vol. 95, no. 9, p. 095012, 2017. DOI:
3634 10.1103/PhysRevD.95.095012. arXiv: 1702.06063 [hep-ph].
- 3635 [30] W. Bernreuther, D. Heisler, and Z.-G. Si, “A set of top quark spin correlation
3636 and polarization observables for the LHC: Standard Model predictions and
3637 new physics contributions”, *JHEP*, vol. 12, p. 026, 2015. DOI: 10.1007/
3638 JHEP12(2015)026. arXiv: 1508.05271 [hep-ph].
- 3639 [31] V. S. Fadin, V. A. Khoze, and T. Sjöstrand, “On the threshold behaviour
3640 of heavy top production”, *Z. Phys. C*, vol. 48, p. 613, 1990. DOI: 10.1007/
3641 BF01614696.
- 3642 [32] Y. Kiyo, J. H. Kuhn, S. Moch, M. Steinhauser, and P. Uwer, “Top-quark
3643 pair production near threshold at LHC”, *Eur. Phys. J. C*, vol. 60, pp. 375–
3644 386, 2009. DOI: 10.1140/epjc/s10052-009-0892-7. arXiv: 0812.0919
3645 [hep-ph].

- [33] Y. Sumino and H. Yokoya, “Bound-state effects on kinematical distributions of top quarks at hadron colliders”, *JHEP*, vol. 09, p. 034, 2010, [Erratum: JHEP 06, 037 (2016)]. DOI: 10.1007/JHEP09(2010)034. arXiv: 1007.0075 [hep-ph].
- [34] W.-L. Ju, G. Wang, X. Wang, X. Xu, Y. Xu, and L. L. Yang, “Top quark pair production near threshold: single/double distributions and mass determination”, *JHEP*, vol. 06, p. 158, 2020. DOI: 10.1007/JHEP06(2020)158. arXiv: 2004.03088 [hep-ph].
- [35] M. V. Garzelli, G. Limatola, S. Moch, M. Steinhauser, and O. Zenaiev, “Updated predictions for toponium production at the LHC”, Dec. 2024. arXiv: 2412.16685 [hep-ph].
- [36] F. Maltoni, C. Severi, S. Tentori, and E. Vryonidou, “Quantum tops at circular lepton colliders”, *JHEP*, vol. 09, p. 001, 2024. DOI: 10.1007/JHEP09(2024)001. arXiv: 2404.08049 [hep-ph].
- [37] B. Fuks, K. Hagiwara, K. Ma, and Y.-J. Zheng, “Signatures of toponium formation in LHC run 2 data”, *Phys. Rev. D*, vol. 104, no. 3, p. 034023, 2021. DOI: 10.1103/PhysRevD.104.034023. arXiv: 2102.11281 [hep-ph].
- [38] J. A. Aguilar-Saavedra, “Toponium hunter’s guide”, *Phys. Rev. D*, vol. 110, no. 5, p. 054032, 2024. DOI: 10.1103/PhysRevD.110.054032. arXiv: 2407.20330 [hep-ph].
- [39] B. Fuks, K. Hagiwara, K. Ma, and Y.-J. Zheng, “Simulating toponium formation signals at the LHC”, *Eur. Phys. J. C*, vol. 85, no. 2, p. 157, 2025. DOI: 10.1140/epjc/s10052-025-13853-3. arXiv: 2411.18962 [hep-ph].
- [40] T. Barnes, S. Godfrey, and E. S. Swanson, “Higher charmonia”, *Phys. Rev. D*, vol. 72, p. 054026, 2005. DOI: 10.1103/PhysRevD.72.054026. arXiv: hep-ph/0505002.
- [41] CMS Collaboration, “Search for dark matter produced in association with a single top quark or a top quark pair in proton-proton collisions at $\sqrt{s} = 13$ TeV”, CERN, Geneva, Tech. Rep., 2024. [Online]. Available: <https://cds.cern.ch/record/2895470>.
- [42] T. D. Lee, “A Theory of Spontaneous T Violation”, *Phys. Rev. D*, vol. 8, G. Feinberg, Ed., pp. 1226–1239, 1973. DOI: 10.1103/PhysRevD.8.1226.
- [43] G. C. Branco, P. M. Ferreira, L. Lavoura, M. N. Rebelo, M. Sher, and J. P. Silva, “Theory and phenomenology of two-Higgs-doublet models”, *Phys. Rept.*, vol. 516, pp. 1–102, 2012. DOI: 10.1016/j.physrep.2012.02.002. arXiv: 1106.0034 [hep-ph].

- 3682 [44] H. E. Haber and G. L. Kane, “The Search for Supersymmetry: Probing
3683 Physics Beyond the Standard Model”, *Phys. Rept.*, vol. 117, pp. 75–263,
3684 1985. DOI: 10.1016/0370-1573(85)90051-1.
- 3685 [45] J. E. Kim, “Light Pseudoscalars, Particle Physics and Cosmology”, *Phys.
3686 Rept.*, vol. 150, pp. 1–177, 1987. DOI: 10.1016/0370-1573(87)90017-2.
- 3687 [46] R. D. Peccei and H. R. Quinn, “CP Conservation in the Presence of In-
3688 stantons”, *Phys. Rev. Lett.*, vol. 38, pp. 1440–1443, 1977. DOI: 10.1103/
3689 PhysRevLett.38.1440.
- 3690 [47] R. D. Peccei and H. R. Quinn, “Constraints Imposed by CP Conservation in
3691 the Presence of Instantons”, *Phys. Rev. D*, vol. 16, pp. 1791–1797, 1977. DOI:
3692 10.1103/PhysRevD.16.1791.
- 3693 [48] S. Weinberg, “A New Light Boson?”, *Phys. Rev. Lett.*, vol. 40, pp. 223–226,
3694 1978. DOI: 10.1103/PhysRevLett.40.223.
- 3695 [49] F. Wilczek, “Problem of Strong P and T Invariance in the Presence of
3696 Instantons”, *Phys. Rev. Lett.*, vol. 40, pp. 279–282, 1978. DOI: 10.1103/
3697 PhysRevLett.40.279.
- 3698 [50] L. Di Luzio, M. Giannotti, E. Nardi, and L. Visinelli, “The landscape of
3699 QCD axion models”, *Phys. Rept.*, vol. 870, pp. 1–117, 2020. DOI: 10.1016/
3700 j.physrep.2020.06.002. arXiv: 2003.01100 [hep-ph].
- 3701 [51] J. M. Pendlebury et al., “Revised experimental upper limit on the electric
3702 dipole moment of the neutron”, *Phys. Rev. D*, vol. 92, no. 9, p. 092003, 2015.
3703 DOI: 10.1103/PhysRevD.92.092003. arXiv: 1509.04411 [hep-ex].
- 3704 [52] C. Abel et al., “Measurement of the Permanent Electric Dipole Moment
3705 of the Neutron”, *Phys. Rev. Lett.*, vol. 124, no. 8, p. 081803, 2020. DOI:
3706 10.1103/PhysRevLett.124.081803. arXiv: 2001.11966 [hep-ex].
- 3707 [53] J. E. Kim, “Weak Interaction Singlet and Strong CP Invariance”, *Phys. Rev.
3708 Lett.*, vol. 43, p. 103, 1979. DOI: 10.1103/PhysRevLett.43.103.
- 3709 [54] M. A. Shifman, A. I. Vainshtein, and V. I. Zakharov, “Can Confinement En-
3710 sure Natural CP Invariance of Strong Interactions?”, *Nucl. Phys. B*, vol. 166,
3711 pp. 493–506, 1980. DOI: 10.1016/0550-3213(80)90209-6.
- 3712 [55] M. Dine, W. Fischler, and M. Srednicki, “A Simple Solution to the Strong
3713 CP Problem with a Harmless Axion”, *Phys. Lett. B*, vol. 104, pp. 199–202,
3714 1981. DOI: 10.1016/0370-2693(81)90590-6.
- 3715 [56] A. R. Zhitnitsky, “On Possible Suppression of the Axion Hadron Interac-
3716 tions”, *Sov. J. Nucl. Phys.*, vol. 31, p. 260, 1980.
- 3717 [57] H. Georgi, D. B. Kaplan, and L. Randall, “Manifesting the Invisible Axion at
3718 Low-energies”, *Phys. Lett. B*, vol. 169, pp. 73–78, 1986. DOI: 10.1016/0370-
3719 2693(86)90688-X.

- [58] V. A. Rubakov, “Grand unification and heavy axion”, *JETP Lett.*, vol. 65, pp. 621–624, 1997. DOI: 10.1134/1.567390. arXiv: hep-ph/9703409.
- [59] B. Holdom and M. E. Peskin, “Raising the Axion Mass”, *Nucl. Phys. B*, vol. 208, pp. 397–412, 1982. DOI: 10.1016/0550-3213(82)90228-0.
- [60] S. Dimopoulos, A. Hook, J. Huang, and G. Marques-Tavares, “A collider observable QCD axion”, *JHEP*, vol. 11, p. 052, 2016. DOI: 10.1007/JHEP11(2016)052. arXiv: 1606.03097 [hep-ph].
- [61] T. Gherghetta, N. Nagata, and M. Shifman, “A Visible QCD Axion from an Enlarged Color Group”, *Phys. Rev. D*, vol. 93, no. 11, p. 115010, 2016. DOI: 10.1103/PhysRevD.93.115010. arXiv: 1604.01127 [hep-ph].
- [62] M. E. Peskin and D. V. Schroeder, *An Introduction to quantum field theory*. Reading, USA: Addison-Wesley, 1995, ISBN: 978-0-201-50397-5, 978-0-429-50355-9, 978-0-429-49417-8. DOI: 10.1201/9780429503559.
- [63] G. Altarelli and G. Parisi, “Asymptotic Freedom in Parton Language”, *Nucl. Phys. B*, vol. 126, pp. 298–318, 1977. DOI: 10.1016/0550-3213(77)90384-4.
- [64] P. Skands, “Introduction to QCD”, in *Theoretical Advanced Study Institute in Elementary Particle Physics: Searching for New Physics at Small and Large Scales*, 2013, pp. 341–420. DOI: 10.1142/9789814525220_0008. arXiv: 1207.2389 [hep-ph].
- [65] R. D. Ball et al., “Parton distributions from high-precision collider data”, *Eur. Phys. J. C*, vol. 77, p. 663, 2017. DOI: 10.1140/epjc/s10052-017-5199-5. arXiv: 1706.00428 [hep-ph].
- [66] F. Maltoni and T. Stelzer, “MadEvent: Automatic event generation with MadGraph”, *JHEP*, vol. 02, p. 027, 2003. DOI: 10.1088/1126-6708/2003/02/027. arXiv: hep-ph/0208156.
- [67] M. D. Schwartz, *Quantum Field Theory and the Standard Model*. Cambridge University Press, Mar. 2014, ISBN: 978-1-107-03473-0, 978-1-107-03473-0.
- [68] F. J. Tackmann, “Beyond Scale Variations: Perturbative Theory Uncertainties from Nuisance Parameters”, Nov. 2024. arXiv: 2411.18606 [hep-ph].
- [69] P. Nason and B. Webber, “Next-to-Leading-Order Event Generators”, *Ann. Rev. Nucl. Part. Sci.*, vol. 62, pp. 187–213, 2012. DOI: 10.1146/annurev-nucl-102711-094928. arXiv: 1202.1251 [hep-ph].
- [70] J. Alwall et al., “The automated computation of tree-level and next-to-leading order differential cross sections, and their matching to parton shower simulations”, *JHEP*, vol. 07, p. 079, 2014. DOI: 10.1007/JHEP07(2014)079. arXiv: 1405.0301 [hep-ph].

- 3756 [71] C. Degrande, C. Duhr, B. Fuks, D. Grellscheid, O. Mattelaer, and T. Reiter, “UFO - The Universal FeynRules Output”, *Comput. Phys. Commun.*, vol. 183, pp. 1201–1214, 2012. doi: 10.1016/j.cpc.2012.01.022. arXiv: 1108.2040 [hep-ph].
- 3760 [72] P. Nason, “A new method for combining NLO QCD with shower Monte Carlo algorithms”, *JHEP*, vol. 11, p. 040, 2004. doi: 10.1088/1126-6708/2004/11/040. arXiv: hep-ph/0409146.
- 3763 [73] S. Frixione, P. Nason, and C. Oleari, “Matching NLO QCD computations with parton shower simulations: The POWHEG method”, *JHEP*, vol. 11, p. 070, 2007. doi: 10.1088/1126-6708/2007/11/070. arXiv: 0709.2092 [hep-ph].
- 3767 [74] S. Alioli, P. Nason, C. Oleari, and E. Re, “A general framework for implementing NLO calculations in shower Monte Carlo programs: The POWHEG BOX”, *JHEP*, vol. 06, p. 043, 2010. doi: 10.1007/JHEP06(2010)043. arXiv: 1002.2581 [hep-ph].
- 3771 [75] S. Frixione, G. Ridolfi, and P. Nason, “A positive-weight next-to-leading-order Monte Carlo for heavy flavour hadroproduction”, *JHEP*, vol. 09, p. 126, 2007. doi: 10.1088/1126-6708/2007/09/126. arXiv: 0707.3088 [hep-ph].
- 3774 [76] T. Sjöstrand et al., “An introduction to PYTHIA8.2”, *Comput. Phys. Commun.*, vol. 191, p. 159, 2015. doi: 10.1016/j.cpc.2015.01.024. arXiv: 1410.3012 [hep-ph].
- 3777 [77] C. Bierlich et al., “A comprehensive guide to the physics and usage of PYTHIA 8.3”, *SciPost Phys. Codeb.*, vol. 2022, p. 8, 2022. doi: 10.21468/SciPostPhysCodeb.8. arXiv: 2203.11601 [hep-ph].
- 3780 [78] J. Bellm et al., “HERWIG7.0/HERWIG++3.0 release note”, *Eur. Phys. J. C*, vol. 76, p. 196, 2016. doi: 10.1140/epjc/s10052-016-4018-8. arXiv: 1512.01178 [hep-ph].
- 3783 [79] M. Bähr et al., “HERWIG++ physics and manual”, *Eur. Phys. J. C*, vol. 58, p. 639, 2008. doi: 10.1140/epjc/s10052-008-0798-9. arXiv: 0803.0883 [hep-ph].
- 3786 [80] P. Skands, S. Carrazza, and J. Rojo, “Tuning PYTHIA 8.1: the Monash 2013 Tune”, *Eur. Phys. J. C*, vol. 74, no. 8, p. 3024, 2014. doi: 10.1140/epjc/s10052-014-3024-y. arXiv: 1404.5630 [hep-ph].
- 3789 [81] CMS Collaboration, “Extraction and validation of a new set of CMS Pythia 8 tunes from underlying-event measurements”, *Eur. Phys. J. C*, vol. 80, p. 4, 2020. doi: 10.1140/epjc/s10052-019-7499-4. arXiv: 1903.12179 [hep-ex].

- 3793 [82] B. Andersson, G. Gustafson, G. Ingelman, and T. Sjostrand, “Parton Frag-
3794 mentation and String Dynamics”, *Phys. Rept.*, vol. 97, pp. 31–145, 1983. DOI:
3795 10.1016/0370-1573(83)90080-7.
- 3796 [83] T. Sjostrand, “Jet Fragmentation of Nearby Partons”, *Nucl. Phys. B*, vol. 248,
3797 pp. 469–502, 1984. DOI: 10.1016/0550-3213(84)90607-2.
- 3798 [84] S. Argyropoulos and T. Sjöstrand, “Effects of color reconnection on $t\bar{t}$ final
3799 states at the LHC”, *JHEP*, vol. 11, p. 043, 2014. DOI: 10.1007/JHEP11(2014)
3800 043. arXiv: 1407.6653 [hep-ph].
- 3801 [85] J. R. Christiansen and P. Z. Skands, “String Formation Beyond Leading
3802 Colour”, *JHEP*, vol. 08, p. 003, 2015. DOI: 10.1007/JHEP08(2015)003.
3803 arXiv: 1505.01681 [hep-ph].
- 3804 [86] CMS Collaboration, “Pileup mitigation at CMS in 13 TeV data”, *JINST*,
3805 vol. 15, no. 09, P09018, 2020. DOI: 10.1088/1748-0221/15/09/P09018.
3806 arXiv: 2003.00503 [hep-ex].
- 3807 [87] CMS Collaboration, “Precision luminosity measurement in proton-proton
3808 collisions at $\sqrt{s} = 13$ TeV in 2015 and 2016 at CMS”, *Eur. Phys. J. C*,
3809 vol. 81, no. 9, p. 800, 2021. DOI: 10.1140/epjc/s10052-021-09538-2.
3810 arXiv: 2104.01927 [hep-ex].
- 3811 [88] S. Agostinelli et al., “GEANT4 — a simulation toolkit”, *Nucl. Instrum. Meth.*
3812 *A*, vol. 506, p. 250, 2003. DOI: 10.1016/S0168-9002(03)01368-8.
- 3813 [89] “LHC Design Report Vol.1: The LHC Main Ring”, O. S. Bruning et al., Eds.,
3814 Jun. 2004. DOI: 10.5170/CERN-2004-003-V-1.
- 3815 [90] ATLAS Collaboration, “The ATLAS Experiment at the CERN Large Hadron
3816 Collider”, *JINST*, vol. 3, S08003, 2008. DOI: 10.1088/1748-0221/3/08/
3817 S08003.
- 3818 [91] LHCb Collaboration, “The LHCb Detector at the LHC”, *JINST*, vol. 3,
3819 S08005, 2008. DOI: 10.1088/1748-0221/3/08/S08005.
- 3820 [92] ALICE Collaboration, “The ALICE experiment at the CERN LHC”, *JINST*,
3821 vol. 3, S08002, 2008. DOI: 10.1088/1748-0221/3/08/S08002.
- 3822 [93] I. Zurbano Fernandez et al., “High-Luminosity Large Hadron Collider (HL-
3823 LHC): Technical design report”, vol. 10/2020, I. Béjar Alonso, O. Brüning,
3824 P. Fessia, L. Rossi, L. Tavian, and M. Zerlauth, Eds., Dec. 2020. DOI: 10.
3825 23731/CYRM-2020-0010.
- 3826 [94] CMS Collaboration, “Technical Proposal for the Phase-II Upgrade of the
3827 CMS Detector”, Geneva, Tech. Rep., 2015. DOI: 10.17181/CERN.VU8I.D59J.
3828 [Online]. Available: <https://cds.cern.ch/record/2020886>.

- 3829 [95] CMS Collaboration, “Development of the CMS detector for the CERN LHC
3830 Run 3”, *JINST*, vol. 19, P05064, 2024. DOI: 10.1088/1748-0221/19/05/
3831 P05064. arXiv: 2309.05466 [physics.ins-det].
- 3832 [96] CMS Collaboration, *CMS Detector Slice*, 2016. [Online]. Available: <https://cds.cern.ch/record/2120661>.
- 3834 [97] CMS Collaboration, “Description and performance of track and primary-
3835 vertex reconstruction with the CMS tracker”, *JINST*, vol. 9, P10009, 2014.
3836 DOI: 10.1088/1748-0221/9/10/P10009. arXiv: 1405.6569 [physics.ins-
3837 det].
- 3838 [98] W. Adam et al., “The CMS Phase-1 Pixel Detector Upgrade”, *JINST*, vol. 16,
3839 no. 02, P02027, 2021. DOI: 10.1088/1748-0221/16/02/P02027. arXiv:
3840 2012.14304 [physics.ins-det].
- 3841 [99] “The CMS electromagnetic calorimeter project: Technical Design Report”,
3842 Tech. Rep., 1997.
- 3843 [100] CMS Collaboration, “Electron and photon reconstruction and identification
3844 with the CMS experiment at the CERN LHC”, *JINST*, vol. 16, no. 05,
3845 P05014, 2021. DOI: 10.1088/1748-0221/16/05/P05014. arXiv: 2012.06888
3846 [hep-ex].
- 3847 [101] “The CMS hadron calorimeter project: Technical Design Report”, Tech. Rep.,
3848 1997.
- 3849 [102] “CMS Technical Design Report for the Phase 1 Upgrade of the Hadron
3850 Calorimeter”, Tech. Rep., Sep. 2012. DOI: 10.2172/1151651.
- 3851 [103] “The CMS muon project: Technical Design Report”, Tech. Rep., 1997.
- 3852 [104] N. Pozzobon, “The CMS Muon System performance during the LHC Run-2”,
3853 CERN, Geneva, Tech. Rep., 2019. DOI: 10.1088/1748-0221/14/11/C11031.
3854 [Online]. Available: <https://cds.cern.ch/record/2701333>.
- 3855 [105] V. Khachatryan et al., “The CMS trigger system”, *JINST*, vol. 12, no. 01,
3856 P01020, 2017. DOI: 10.1088/1748-0221/12/01/P01020. arXiv: 1609.02366
3857 [physics.ins-det].
- 3858 [106] CMS Collaboration, “Performance of the CMS Level-1 trigger in proton-
3859 proton collisions at $\sqrt{s} = 13$ TeV”, *JINST*, vol. 15, no. 10, P10017, 2020.
3860 DOI: 10.1088/1748-0221/15/10/P10017. arXiv: 2006.10165 [hep-ex].
- 3861 [107] W. Adam et al., “The CMS high level trigger”, *Eur. Phys. J. C*, vol. 46,
3862 pp. 605–667, 2006. DOI: 10.1140/epjc/s2006-02495-8. arXiv: hep-ex/
3863 0512077.
- 3864 [108] S. Varghese, “CMS High Level Trigger Performance for Run 3”, *PoS*, vol. EPS-
3865 HEP2023, p. 517, 2023. DOI: 10.22323/1.449.0517.

- 3866 [109] CMS Collaboration, “Particle-flow reconstruction and global event descrip-
3867 tion with the CMS detector”, *JINST*, vol. 12, P10003, 2017. DOI: 10.1088/
3868 1748-0221/12/10/P10003. arXiv: 1706.04965 [physics.ins-det].
- 3869 [110] D. Bertolini, P. Harris, M. Low, and N. Tran, “Pileup Per Particle Identifica-
3870 tion”, *JHEP*, vol. 10, p. 059, 2014. DOI: 10.1007/JHEP10(2014)059. arXiv:
3871 1407.6013 [hep-ph].
- 3872 [111] M. Cacciari, G. P. Salam, and G. Soyez, “The anti- k_t jet clustering algo-
3873 rithm”, *JHEP*, vol. 04, p. 063, 2008. DOI: 10.1088/1126-6708/2008/04/063.
3874 arXiv: 0802.1189 [hep-ph].
- 3875 [112] E. Bols, J. Kieseler, M. Verzetti, M. Stoye, and A. Stakia, “Jet Flavour
3876 Classification Using DeepJet”, *JINST*, vol. 15, no. 12, P12012, 2020. DOI:
3877 10.1088/1748-0221/15/12/P12012. arXiv: 2008.10519 [hep-ex].
- 3878 [113] CMS Collaboration, “Performance of missing transverse momentum recon-
3879 struction in proton-proton collisions at $\sqrt{s} = 13$ TeV using the CMS detec-
3880 tor”, *JINST*, vol. 14, no. 07, P07004, 2019. DOI: 10.1088/1748-0221/14/
3881 07/P07004. arXiv: 1903.06078 [hep-ex].
- 3882 [114] G. Cowan, K. Cranmer, E. Gross, and O. Vitells, “Asymptotic formulae for
3883 likelihood-based tests of new physics”, *Eur. Phys. J. C*, vol. 71, p. 1554, 2011,
3884 [Erratum: Eur.Phys.J.C 73, 2501 (2013)]. DOI: 10.1140/epjc/s10052-011-
3885 1554-0. arXiv: 1007.1727 [physics.data-an].
- 3886 [115] S. S. Wilks, “The large-sample distribution of the likelihood ratio for testing
3887 composite hypotheses”, *Annals Math. Statist.*, vol. 9, no. 1, pp. 60–62, 1938.
3888 DOI: 10.1214/aoms/1177732360.
- 3889 [116] A. Wald, “Tests of statistical hypotheses concerning several parameters when
3890 the number of observations is large”, *Trans. Am. Math. Soc.*, vol. 54, no. 3,
3891 pp. 462–482, 1942. DOI: 10.1090/S0002-9947-1943-0012401-3.
- 3892 [117] T. Junk, “Confidence level computation for combining searches with small
3893 statistics”, *Nucl. Instrum. Meth. A*, vol. 434, p. 435, 1999. DOI: 10.1016/
3894 S0168-9002(99)00498-2. arXiv: hep-ex/9902006.
- 3895 [118] A. L. Read, “Presentation of search results: The CL_s technique”, *J. Phys. G*,
3896 vol. 28, p. 2693, 2002. DOI: 10.1088/0954-3899/28/10/313.
- 3897 [119] CMS Collaboration, “The CMS Statistical Analysis and Combination Tool:
3898 Combine”, *Comput. Softw. Big Sci.*, vol. 8, no. 1, p. 19, 2024. DOI: 10.1007/
3899 s41781-024-00121-4. arXiv: 2404.06614 [physics.data-an].
- 3900 [120] L. Heinrich, M. Feickert, G. Stark, and K. Cranmer, “Pyhf: Pure-Python
3901 implementation of HistFactory statistical models”, *Journal of Open Source
3902 Software*, vol. 6, no. 58, p. 2823, 2021. DOI: 10.21105/joss.02823. [Online].
3903 Available: <https://doi.org/10.21105/joss.02823>.

- 3904 [121] CMS Collaboration, “First measurement of the top quark pair production
 3905 cross section in proton-proton collisions at $\sqrt{s} = 13.6\text{TeV}$ ”, CMS Physics
 3906 Analysis Summary CMS-PAS-TOP-22-012, 2022. [Online]. Available: <https://cds.cern.ch/record/2834110>.
- 3908 [122] ATLAS Collaboration, “Measurement of the $t\bar{t}$ cross section and its ratio to
 3909 the Z production cross section using pp collisions at $\sqrt{s} = 13.6\text{ TeV}$ with the
 3910 ATLAS detector”, *Phys. Lett. B*, vol. 848, p. 138376, 2024. DOI: 10.1016/
 3911 j.physletb.2023.138376. arXiv: 2308.09529 [hep-ex].
- 3912 [123] M. Czakon and A. Mitov, “TOP++: A program for the calculation of the top-
 3913 pair cross-section at hadron colliders”, *Comput. Phys. Commun.*, vol. 185,
 3914 p. 2930, 2014. DOI: 10.1016/j.cpc.2014.06.021. arXiv: 1112.5675
 3915 [hep-ph].
- 3916 [124] J. Campbell, T. Neumann, and Z. Sullivan, “Single-top-quark production
 3917 in the t -channel at NNLO”, *JHEP*, vol. 02, p. 040, 2021. DOI: 10.1007/
 3918 JHEP02(2021)040. arXiv: 2012.01574 [hep-ph].
- 3919 [125] S. Camarda et al., “DYTURBO: Fast predictions for Drell–Yan processes”,
 3920 *Eur. Phys. J. C*, vol. 80, p. 251, 2020. DOI: 10.1140/epjc/s10052-020-
 3921 7757-5. arXiv: 1910.07049 [hep-ph].
- 3922 [126] M. Grazzini, S. Kallweit, and M. Wiesemann, “Fully differential NNLO com-
 3923 putations with MATRIX”, *Eur. Phys. J. C*, vol. 78, p. 537, 2018. DOI: 10.
 3924 1140/epjc/s10052-018-5771-7. arXiv: 1711.06631 [hep-ph].
- 3925 [127] N. Kidonakis and N. Yamanaka, “Higher-order corrections for tW production
 3926 at high-energy hadron colliders”, *JHEP*, vol. 05, p. 278, 2021. DOI: 10.1007/
 3927 JHEP05(2021)278. arXiv: 2102.11300 [hep-ph].
- 3928 [128] CMS Collaboration, “Performance of the CMS muon detector and muon
 3929 reconstruction with proton-proton collisions at $\sqrt{s} = 13\text{ TeV}$ ”, *JINST*, vol. 13,
 3930 no. 06, P06015, 2018. DOI: 10.1088/1748-0221/13/06/P06015. arXiv:
 3931 1804.04528 [physics.ins-det].
- 3932 [129] CMS Collaboration, “Identification of heavy-flavour jets with the CMS de-
 3933 tector in pp collisions at 13 TeV”, *JINST*, vol. 13, no. 05, P05011, 2018. DOI:
 3934 10.1088/1748-0221/13/05/P05011. arXiv: 1712.07158 [physics.ins-
 3935 det].
- 3936 [130] CMS Collaboration, “Jet energy scale and resolution in the CMS experiment
 3937 in pp collisions at 8 TeV”, *JINST*, vol. 12, P02014, 2017. DOI: 10.1088/1748-
 3938 0221/12/02/P02014. arXiv: 1607.03663 [hep-ex].
- 3939 [131] CDF Collaboration, “Measurement of $\sigma \cdot B(W \rightarrow e\nu)$ and $\sigma \cdot B(Z^0 \rightarrow e^+e^-)$
 3940 in $p\bar{p}$ Collisions at $\sqrt{s} = 1.8\text{ TeV}$ ”, *Phys. Rev. Lett.*, vol. 76, pp. 3070–3075,
 3941 1996. DOI: 10.1103/PhysRevLett.76.3070. arXiv: hep-ex/9509010.

- [3942] [132] CDF Collaboration, “Measurement of the W boson mass with the Collider
[3943] Detector at Fermilab”, *Phys. Rev. D*, vol. 64, p. 052001, 2001. DOI: 10.1103/
[3944] PhysRevD.64.052001. arXiv: hep-ex/0007044.
- [3945] [133] CMS Collaboration, “Search for dark matter particles produced in association
[3946] with a top quark pair at $\sqrt{s} = 13$ TeV”, *Phys. Rev. Lett.*, vol. 122, no. 1,
[3947] p. 011803, 2019. DOI: 10.1103/PhysRevLett.122.011803. arXiv: 1807.06522 [hep-ex].
- [3949] [134] CMS Collaboration, “Luminosity monitoring with z counting in early 2022
[3950] data”, CMS Detector Performance Note CMS-DP-2023-003, 2023. [Online].
[3951] Available: <https://cds.cern.ch/record/2851655>.
- [3952] [135] CMS Collaboration, “Luminosity measurement in proton-proton collisions at
[3953] 13.6 TeV in 2022 at CMS”, CERN, Geneva, CMS Physics Analysis Summary,
[3954] 2024. [Online]. Available: <http://cds.cern.ch/record/2890833>.
- [3955] [136] M. Cacciari, S. Frixione, M. L. Mangano, P. Nason, and G. Ridolfi, “The $t\bar{t}$
[3956] cross-section at 1.8 and 1.96 TeV: A study of the systematics due to parton
[3957] densities and scale dependence”, *JHEP*, vol. 04, p. 068, 2004. DOI: 10.1088/
[3958] 1126-6708/2004/04/068. arXiv: hep-ph/0303085.
- [3959] [137] J. Butterworth et al., “PDF4LHC recommendations for LHC Run II”, *J.
[3960] Phys. G*, vol. 43, p. 023001, 2016. DOI: 10.1088/0954-3899/43/2/023001.
[3961] arXiv: 1510.03865 [hep-ph].
- [3962] [138] CMS Collaboration, “Investigations of the impact of the parton shower tuning
[3963] in PYTHIA 8 in the modelling of $t\bar{t}$ at $\sqrt{s} = 8$ and 13 TeV”, CMS Physics
[3964] Analysis Summary CMS-PAS-TOP-16-021, 2016. [Online]. Available: <https://cds.cern.ch/record/2235192>.
- [3966] [139] R. Barlow and C. Beeston, “Fitting using finite Monte Carlo samples”, *Comput.
[3967] Phys. Commun.*, vol. 77, p. 219, 1993. DOI: 10.1016/0010-4655(93)
[3968] 90005-W.
- [3969] [140] CMS Collaboration, “Measurement of the $t\bar{t}$ production cross section, the
[3970] top quark mass, and the strong coupling constant using dilepton events in
[3971] pp collisions at $\sqrt{s} = 13$ TeV”, *Eur. Phys. J. C*, vol. 79, p. 368, 2019. DOI:
[3972] 10.1140/epjc/s10052-019-6863-8. arXiv: 1812.10505 [hep-ex].
- [3973] [141] ATLAS Collaboration, “Measurement of the $t\bar{t}$ production cross-section in the
[3974] lepton+jets channel at $\sqrt{s} = 13$ TeV with the ATLAS experiment”, *Phys.
[3975] Lett. B*, vol. 810, p. 135797, 2020. DOI: 10.1016/j.physletb.2020.135797.
[3976] arXiv: 2006.13076 [hep-ex].
- [3977] [142] CMS Collaboration, “Measurement of the $t\bar{t}$ production cross section in the
[3978] all-jet final state in pp collisions at $\sqrt{s} = 7$ TeV”, *JHEP*, vol. 05, p. 065,
[3979] 2013. DOI: 10.1007/JHEP05(2013)065. arXiv: 1302.0508 [hep-ex].

- 3980 [143] CMS Collaboration, “Measurement of the $t\bar{t}$ production cross section in the
 3981 all-jets final state in pp collisions at $\sqrt{s} = 8$ TeV”, *Eur. Phys. J. C*, vol. 76,
 3982 p. 128, 2016. DOI: [10.1140/epjc/s10052-016-3956-5](https://doi.org/10.1140/epjc/s10052-016-3956-5). arXiv: [1509.06076](https://arxiv.org/abs/1509.06076)
 3983 [[hep-ex](#)].
- 3984 [144] CMS Collaboration, “Measurements of the $t\bar{t}$ production cross section in
 3985 lepton+jets final states in pp collisions at 8 TeV and ratio of 8 to 7 TeV cross
 3986 sections”, *Eur. Phys. J. C*, vol. 77, p. 15, 2017. DOI: [10.1140/epjc/s10052-016-4504-z](https://doi.org/10.1140/epjc/s10052-016-4504-z). arXiv: [1602.09024](https://arxiv.org/abs/1602.09024) [[hep-ex](#)].
- 3988 [145] CMS Collaboration, “Measurement of the $t\bar{t}$ production cross section in the
 3989 $e\mu$ channel in proton-proton collisions at $\sqrt{s} = 7$ and 8 TeV”, *JHEP*, vol. 08,
 3990 p. 029, 2016. DOI: [10.1007/JHEP08\(2016\)029](https://doi.org/10.1007/JHEP08(2016)029). arXiv: [1603.02303](https://arxiv.org/abs/1603.02303) [[hep-ex](#)].
- 3991 [146] CMS Collaboration, “Measurement of the top quark pair production cross
 3992 section in dilepton final states containing one τ lepton in pp collisions at
 3993 $\sqrt{s} = 13$ TeV”, *JHEP*, vol. 02, p. 191, 2020. DOI: [10.1007/JHEP02\(2020\)191](https://doi.org/10.1007/JHEP02(2020)191).
 3994 arXiv: [1911.13204](https://arxiv.org/abs/1911.13204) [[hep-ex](#)].
- 3995 [147] CMS Collaboration, “Measurement of differential $t\bar{t}$ production cross sections
 3996 in the full kinematic range using lepton+jets events from proton-proton col-
 3997 lisions at $\sqrt{s} = 13$ TeV”, *Phys. Rev. D*, vol. 104, p. 092013, 2021. DOI:
 3998 [10.1103/PhysRevD.104.092013](https://doi.org/10.1103/PhysRevD.104.092013). arXiv: [2108.02803](https://arxiv.org/abs/2108.02803) [[hep-ex](#)].
- 3999 [148] CMS Collaboration, “Measurement of the inclusive $t\bar{t}$ production cross sec-
 4000 tion in proton-proton collisions at $\sqrt{s} = 5.02$ TeV”, *JHEP*, vol. 04, p. 144,
 4001 2022. DOI: [10.1007/JHEP04\(2022\)144](https://doi.org/10.1007/JHEP04(2022)144). arXiv: [2112.09114](https://arxiv.org/abs/2112.09114) [[hep-ex](#)].
- 4002 [149] M. Czakon, P. Fiedler, and A. Mitov, “Total top-quark pair-production cross
 4003 section at hadron colliders through $\mathcal{O}(\alpha_S^4)$ ”, *Phys. Rev. Lett.*, vol. 110,
 4004 p. 252004, 2013. DOI: [10.1103/PhysRevLett.110.252004](https://doi.org/10.1103/PhysRevLett.110.252004). arXiv: [1303.6254](https://arxiv.org/abs/1303.6254) [[hep-ph](#)].
- 4006 [150] R. Tarrach, “The Pole Mass in Perturbative QCD”, *Nucl. Phys. B*, vol. 183,
 4007 pp. 384–396, 1981. DOI: [10.1016/0550-3213\(81\)90140-1](https://doi.org/10.1016/0550-3213(81)90140-1).
- 4008 [151] M. C. Smith and S. S. Willenbrock, “Top quark pole mass”, *Phys. Rev. Lett.*,
 4009 vol. 79, pp. 3825–3828, 1997. DOI: [10.1103/PhysRevLett.79.3825](https://doi.org/10.1103/PhysRevLett.79.3825). arXiv:
 4010 [hep-ph/9612329](https://arxiv.org/abs/hep-ph/9612329).
- 4011 [152] A. H. Hoang, “What is the Top Quark Mass?”, *Ann. Rev. Nucl. Part. Sci.*,
 4012 vol. 70, pp. 225–255, 2020. DOI: [10.1146/annurev-nucl-101918-023530](https://doi.org/10.1146/annurev-nucl-101918-023530).
 4013 arXiv: [2004.12915](https://arxiv.org/abs/2004.12915) [[hep-ph](#)].
- 4014 [153] ATLAS Collaboration, “Probing the quantum interference between singly
 4015 and doubly resonant top-quark production in pp collisions at $\sqrt{s} = 13$ TeV
 4016 with the ATLAS detector”, *Phys. Rev. Lett.*, vol. 121, p. 152002, 2018. DOI:
 4017 [10.1103/PhysRevLett.121.152002](https://doi.org/10.1103/PhysRevLett.121.152002). arXiv: [1806.04667](https://arxiv.org/abs/1806.04667) [[hep-ex](#)].

- 4018 [154] T. Ježo, J. M. Lindert, and S. Pozzorini, “Resonance-aware NLOPS matching
4019 for off-shell $t\bar{t} + tW$ production with semileptonic decays”, *JHEP*, vol. 10,
4020 p. 008, 2023. DOI: 10.1007/JHEP10(2023)008. arXiv: 2307.15653 [hep-ph].
- 4021 [155] T. Ježo and P. Nason, “On the treatment of resonances in next-to-leading
4022 order calculations matched to a parton shower”, *JHEP*, vol. 12, p. 065, 2015.
4023 DOI: 10.1007/JHEP12(2015)065. arXiv: 1509.09071 [hep-ph].
- 4024 [156] <https://powhegbox.mib.infn.it>.
- 4025 [157] S. Frixione, E. Laenen, P. Motylinski, and B. R. Webber, “Angular correla-
4026 tions of lepton pairs from vector boson and top quark decays in Monte Carlo
4027 simulations”, *JHEP*, vol. 04, p. 081, 2007. DOI: 10.1088/1126-6708/2007/
4028 04/081. arXiv: hep-ph/0702198.
- 4029 [158] E. Re, “Single-top Wt -channel production matched with parton showers us-
4030 ing the powheg method”, *Eur. Phys. J. C*, vol. 71, p. 1547, 2011. DOI: 10.
4031 1140/epjc/s10052-011-1547-z. arXiv: 1009.2450 [hep-ph].
- 4032 [159] S. Frixione, E. Laenen, P. Motylinski, B. R. Webber, and C. D. White,
4033 “Single-top hadroproduction in association with a W boson”, *JHEP*, vol. 07,
4034 p. 029, 2008. DOI: 10.1088/1126-6708/2008/07/029. arXiv: 0805.3067
4035 [hep-ph].
- 4036 [160] T. M. P. Tait, “The tW^- mode of single top production”, *Phys. Rev. D*,
4037 vol. 61, p. 034001, 1999. DOI: 10.1103/PhysRevD.61.034001. arXiv: hep-
4038 ph/9909352.
- 4039 [161] J. M. Campbell, R. K. Ellis, P. Nason, and E. Re, “Top-pair production and
4040 decay at NLO matched with parton showers”, *JHEP*, vol. 04, p. 114, 2015.
4041 DOI: 10.1007/JHEP04(2015)114. arXiv: 1412.1828 [hep-ph].
- 4042 [162] S. Ferrario Ravasio, T. Ježo, P. Nason, and C. Oleari, “A theoretical study of
4043 top-mass measurements at the LHC using NLO+PS generators of increasing
4044 accuracy”, *Eur. Phys. J. C*, vol. 78, p. 458, 2018. DOI: 10.1140/epjc/
4045 s10052-018-5909-7. arXiv: 1906.09166 [hep-ph].
- 4046 [163] C. Bierlich et al., “Robust independent validation of experiment and the-
4047 ory: Rivet version 3”, *SciPost Phys.*, vol. 8, p. 026, 2020. DOI: 10.21468/
4048 SciPostPhys.8.2.026. arXiv: 1912.05451 [hep-ph].
- 4049 [164] M. Cacciari and G. P. Salam, “Pileup subtraction using jet areas”, *Phys. Lett.*
4050 *B*, vol. 659, pp. 119–126, 2008. DOI: 10.1016/j.physletb.2007.09.077.
4051 arXiv: 0707.1378 [hep-ph].
- 4052 [165] M. Cacciari, G. P. Salam, and G. Soyez, “The Catchment Area of Jets”,
4053 *JHEP*, vol. 04, p. 005, 2008. DOI: 10.1088/1126-6708/2008/04/005. arXiv:
4054 0802.1188 [hep-ph].

- 4055 [166] ATLAS Collaboration, “Studies of $t\bar{t}/tW$ interference effects in $b\bar{b}\ell^+\ell^-\nu\bar{\nu}'$
 4056 final states with POWHEG and MG5_AMC@NLO setups”, ATLAS PUB
 4057 Note ATL-PHYS-PUB-2021-042, 2021. [Online]. Available: <https://cds.cern.ch/record/2792254>.
 4058
- 4059 [167] D. Boer et al., “Gluons and the quark sea at high energies: Distributions,
 4060 polarization, tomography”, Aug. 2011. arXiv: 1108.1713 [nucl-th].
 4061
- 4062 [168] H. Brooks and P. Skands, “Coherent showers in decays of colored resonances”,
 4063 *Phys. Rev. D*, vol. 100, no. 7, p. 076 006, 2019. DOI: 10.1103/PhysRevD.100.
 4064 076006. arXiv: 1907.08980 [hep-ph].
 4065
- 4066 [169] ATLAS Collaboration, “Measurement of the top-quark mass using a leptonic
 4067 invariant mass in pp collisions at $\sqrt{s} = 13$ TeV with the ATLAS detector”,
 4068 *JHEP*, vol. 06, p. 019, 2023. DOI: 10.1007/JHEP06(2023)019. arXiv: 2209.
 4069 00583 [hep-ex].
 4070
- 4071 [170] ATLAS Collaboration, “Search for Heavy Higgs Bosons A/H Decaying to
 4072 a Top Quark Pair in pp Collisions at $\sqrt{s} = 8$ TeV with the ATLAS De-
 4073 tector”, *Phys. Rev. Lett.*, vol. 119, no. 19, p. 191 803, 2017. DOI: 10.1103/
 4074 PhysRevLett.119.191803. arXiv: 1707.06025 [hep-ex].
 4075
- 4076 [171] ATLAS Collaboration, “Search for heavy neutral Higgs bosons decaying into
 4077 a top quark pair in 140 fb^{-1} of proton-proton collision data at $\sqrt{s} = 13$
 4078 TeV with the ATLAS detector”, *JHEP*, vol. 08, p. 013, 2024. DOI: 10.1007/
 4079 JHEP08(2024)013. arXiv: 2404.18986 [hep-ex].
 4080
- 4081 [172] J. Rübenach, “Search for Heavy Higgs Bosons in Conjunction with Neural-
 4082 Network-Driven Reconstruction and Upgrade of the Fast Beam Condition
 4083 Monitor at the CMS Experiment”, PhD thesis, DESY, Hamburg, May 2023.
 4084
- 4085 [173] CMS Collaboration, “Simulation of the silicon strip tracker pre-amplifier in
 4086 early 2016 data”, CMS Detector Performance Note CMS-DP-2020-045, 2020.
 4087 [Online]. Available: <https://cds.cern.ch/record/2740688>.
 4088
- 4089 [174] M. Aliev, H. Lacker, U. Langenfeld, S. Moch, P. Uwer, and M. Wiedermann,
 4090 “HATHOR: Hadronic top and heavy quarks cross section calculator”, *Comput.
 4091 Phys. Commun.*, vol. 182, p. 1034, 2011. DOI: 10.1016/j.cpc.2010.12.040.
 4092 arXiv: 1007.1327 [hep-ph].
 4093
- 4094 [175] P. Kant et al., “HatHor for single top-quark production: Updated predictions
 4095 and uncertainty estimates for single top-quark production in hadronic col-
 4096 lisions”, *Comput. Phys. Commun.*, vol. 191, pp. 74–89, 2015. DOI: 10.1016/
 4097 j.cpc.2015.02.001. arXiv: 1406.4403 [hep-ph].
 4098
- 4099 [176] K. Melnikov and F. Petriello, “Electroweak gauge boson production at hadron
 4100 colliders through $\mathcal{O}(\alpha_S^2)$ ”, *Phys. Rev. D*, vol. 74, p. 114 017, 2006. DOI: 10.
 4101 1103/PhysRevD.74.114017. arXiv: hep-ph/0609070.
 4102

- 4093 [177] Y. Li and F. Petriello, “Combining QCD and electroweak corrections to dilepton production in FEWZ”, *Phys. Rev. D*, vol. 86, p. 094034, 2012. DOI: 10.1103/PhysRevD.86.094034. arXiv: 1208.5967 [hep-ph].
- 4094
- 4095
- 4096 [178] T. Gehrmann et al., “ W^+W^- Production at Hadron Colliders in Next to Next to Leading Order QCD”, *Phys. Rev. Lett.*, vol. 113, no. 21, p. 212001, 2014. DOI: 10.1103/PhysRevLett.113.212001. arXiv: 1408.5243 [hep-ph].
- 4097
- 4098
- 4099 [179] J. M. Campbell and R. K. Ellis, “MCFM for the Tevatron and the LHC”, *Nucl. Phys. B Proc. Suppl.*, vol. 205-206, J. Blümlein, S.-O. Moch, and T. Riemann, Eds., pp. 10–15, 2010. DOI: 10.1016/j.nuclphysbps.2010.08.011. arXiv: 1007.3492 [hep-ph].
- 4100
- 4101
- 4102
- 4103 [180] CMS Collaboration, “Measurement of the differential cross section for top quark pair production in pp collisions at $\sqrt{s} = 8$ TeV”, *Eur. Phys. J. C*, vol. 75, no. 11, p. 542, 2015. DOI: 10.1140/epjc/s10052-015-3709-x. arXiv: 1505.04480 [hep-ex].
- 4104
- 4105
- 4106
- 4107 [181] L. Sonnenschein, “Analytical solution of ttbar dilepton equations”, *Phys. Rev. D*, vol. 73, p. 054015, 2006, [Erratum: Phys.Rev.D 78, 079902 (2008)]. DOI: 10.1103/PhysRevD.78.079902. arXiv: hep-ph/0603011.
- 4108
- 4109
- 4110 [182] I. Korol, “Measurement of double differential $t\bar{t}$ production cross sections with the CMS detector”, CERN-THESIS-2016-060, DESY-THESIS-2016-011, Ph.D. dissertation, Universität Hamburg, 2016. DOI: 10.3204/DESY-THESIS-2016-011.
- 4111
- 4112
- 4113
- 4114 [183] J. H. Kühn, A. Scharf, and P. Uwer, “Electroweak corrections to top-quark pair production in quark-antiquark annihilation”, *Eur. Phys. J. C*, vol. 45, p. 139, 2006. DOI: 10.1140/epjc/s2005-02423-6. arXiv: hep-ph/0508092.
- 4115
- 4116
- 4117 [184] J. H. Kühn, A. Scharf, and P. Uwer, “Electroweak effects in top-quark pair production at hadron colliders”, *Eur. Phys. J. C*, vol. 51, p. 37, 2007. DOI: 10.1140/epjc/s10052-007-0275-x. arXiv: hep-ph/0610335.
- 4118
- 4119
- 4120 [185] J. H. Kühn, A. Scharf, and P. Uwer, “Weak interactions in top-quark pair production at hadron colliders: An update”, *Phys. Rev. D*, vol. 91, p. 014020, 2015. DOI: 10.1103/PhysRevD.91.014020. arXiv: 1305.5773 [hep-ph].
- 4121
- 4122
- 4123 [186] CMS Collaboration, “Combined measurements of Higgs boson couplings in proton-proton collisions at $\sqrt{s} = 13$ TeV”, *Eur. Phys. J. C*, vol. 79, no. 5, p. 421, 2019. DOI: 10.1140/epjc/s10052-019-6909-y. arXiv: 1809.10733 [hep-ex].
- 4124
- 4125
- 4126
- 4127 [187] CMS Collaboration, “CMS pythia 8 colour reconnection tunes based on underlying-event data”, *Eur. Phys. J. C*, vol. 83, no. 7, p. 587, 2023. DOI: 10.1140/epjc/s10052-023-11630-8. arXiv: 2205.02905 [hep-ex].
- 4128
- 4129

- [188] ATLAS Collaboration, “Measurement of the inclusive cross-sections of single top-quark and top-antiquark t -channel production in pp collisions at $\sqrt{s} = 13$ TeV with the ATLAS detector”, *JHEP*, vol. 04, p. 086, 2017. DOI: 10.1007/JHEP04(2017)086. arXiv: 1609.03920 [hep-ex].
- [189] CMS Collaboration, “Measurement of the single top quark and antiquark production cross sections in the t channel and their ratio in proton-proton collisions at $\sqrt{s} = 13$ TeV”, *Phys. Lett. B*, vol. 800, p. 135 042, 2020. DOI: 10.1016/j.physletb.2019.135042. arXiv: 1812.10514 [hep-ex].
- [190] CMS Collaboration, “Measurement of the production cross section for single top quarks in association with W bosons in proton-proton collisions at $\sqrt{s} = 13$ TeV”, *JHEP*, vol. 10, p. 117, 2018. DOI: 10.1007/JHEP10(2018)117. arXiv: 1805.07399 [hep-ex].
- [191] CMS Collaboration, “Measurement of the cross section for top quark pair production in association with a W or Z boson in proton-proton collisions at $\sqrt{s} = 13$ TeV”, *JHEP*, vol. 08, p. 011, 2018. DOI: 10.1007/JHEP08(2018)011. arXiv: 1711.02547 [hep-ex].
- [192] ATLAS Collaboration, “Measurement of the $t\bar{t}Z$ and $t\bar{t}W$ cross sections in proton-proton collisions at $\sqrt{s} = 13$ TeV with the ATLAS detector”, *Phys. Rev. D*, vol. 99, p. 072 009, 2019. DOI: 10.1103/PhysRevD.99.072009. arXiv: 1901.03584 [hep-ex].
- [193] ATLAS Collaboration, “Measurements of top-quark pair to Z-boson cross-section ratios at $\sqrt{s} = 13, 8, 7$ TeV with the ATLAS detector”, *JHEP*, vol. 02, p. 117, 2017. DOI: 10.1007/JHEP02(2017)117. arXiv: 1612.03636 [hep-ex].
- [194] CMS Collaboration, “CMS luminosity measurement for the 2017 data-taking period at $\sqrt{s} = 13$ TeV”, CMS Physics Analysis Summary CMS-PAS-LUM-17-004, 2018. [Online]. Available: <https://cds.cern.ch/record/2621960>.
- [195] CMS Collaboration, “CMS luminosity measurement for the 2018 data-taking period at $\sqrt{s} = 13$ TeV”, CMS Physics Analysis Summary CMS-PAS-LUM-18-002, 2019. [Online]. Available: <https://cds.cern.ch/record/2676164>.
- [196] CMS Collaboration, “Measurement of the inelastic proton-proton cross section at $\sqrt{s} = 13$ TeV”, *JHEP*, vol. 07, p. 161, 2018. DOI: 10.1007/JHEP07(2018)161. arXiv: 1802.02613 [hep-ex].
- [197] W. S. Cleveland, “Robust locally weighted regression and smoothing scatterplots”, *Journal of the American Statistical Association*, vol. 74, no. 368, pp. 829–836, 1979. DOI: 10.1080/01621459.1979.10481038.
- [198] W. S. Cleveland and S. J. Devlin, “Locally weighted regression: An approach to regression analysis by local fitting”, *Journal of the American Statistical Association*, vol. 83, no. 403, pp. 596–610, 1988. DOI: 10.1080/01621459.1988.10478639.

- 4169 [199] CMS Collaboration, “Measurement of differential cross sections for the pro-
4170 duction of top quark pairs and of additional jets in lepton+jets events from
4171 pp collisions at $\sqrt{s} = 13$ TeV”, *Phys. Rev. D*, vol. 97, no. 11, p. 112003, 2018.
4172 DOI: [10.1103/PhysRevD.97.112003](https://doi.org/10.1103/PhysRevD.97.112003). arXiv: 1803.08856 [hep-ex].
- 4173 [200] CMS Collaboration, “Development and validation of HERWIG 7 tunes from
4174 CMS underlying-event measurements”, *Eur. Phys. J. C*, vol. 81, no. 4, p. 312,
4175 2021. DOI: [10.1140/epjc/s10052-021-08949-5](https://doi.org/10.1140/epjc/s10052-021-08949-5). arXiv: 2011.03422 [hep-
4176 ex].
- 4177 [201] B. R. Webber, “A QCD Model for Jet Fragmentation Including Soft Gluon
4178 Interference”, *Nucl. Phys. B*, vol. 238, pp. 492–528, 1984. DOI: [10.1016/0550-3213\(84\)90333-X](https://doi.org/10.1016/0550-3213(84)90333-X).
- 4180 [202] R. Frederix and S. Frixione, “Merging meets matching in MC@NLO”, *JHEP*,
4181 vol. 12, p. 061, 2012. DOI: [10.1007/JHEP12\(2012\)061](https://doi.org/10.1007/JHEP12(2012)061). arXiv: 1209.6215
4182 [hep-ph].
- 4183 [203] CMS Collaboration, “Measurement of differential cross sections for top quark
4184 pair production using the lepton+jets final state in proton-proton collisions
4185 at 13 TeV”, *Phys. Rev. D*, vol. 95, no. 9, p. 092001, 2017. DOI: [10.1103/PhysRevD.95.092001](https://doi.org/10.1103/PhysRevD.95.092001). arXiv: 1610.04191 [hep-ex].
- 4187 [204] CMS Collaboration, “Measurements of $t\bar{t}$ differential cross sections in proton-
4188 proton collisions at $\sqrt{s} = 13$ TeV using events containing two leptons”, *JHEP*,
4189 vol. 02, p. 149, 2019. DOI: [10.1007/JHEP02\(2019\)149](https://doi.org/10.1007/JHEP02(2019)149). arXiv: 1811.06625
4190 [hep-ex].
- 4191 [205] F. J. Llanes-Estrada, “Ensuring that toponium is glued, not nailed”, Nov.
4192 2024. arXiv: 2411.19180 [hep-ph].
- 4193 [206] D. d’Enterria and K. Kang, “Exclusive photon-fusion production of even-
4194 spin resonances and exotic QED atoms in high-energy hadron collisions”,
4195 Mar. 2025. arXiv: 2503.10952 [hep-ph].
- 4196 [207] A. Djouadi, J. Ellis, A. Popov, and J. Quevillon, “Interference effects in $t\bar{t}$
4197 production at the LHC as a window on new physics”, *JHEP*, vol. 03, p. 119,
4198 2019. DOI: [10.1007/JHEP03\(2019\)119](https://doi.org/10.1007/JHEP03(2019)119). arXiv: 1901.03417 [hep-ph].
- 4199 [208] A. Djouadi, J. Ellis, and J. Quevillon, “Discriminating between Pseudoscalar
4200 Higgs and Toponium States at the LHC and Beyond”, Dec. 2024. arXiv:
4201 2412.15138 [hep-ph].
- 4202 [209] B. A. Betchart, R. Demina, and A. Harel, “Analytic solutions for neutrino
4203 momenta in decay of top quarks”, *Nucl. Instrum. Meth. A*, vol. 736, p. 169,
4204 2014. DOI: [10.1016/j.nima.2013.10.039](https://doi.org/10.1016/j.nima.2013.10.039). arXiv: 1305.1878 [hep-ph].

- [210] R. Demina, A. Harel, and D. Orbaker, “Reconstructing $t\bar{t}$ events with one lost jet”, *Nucl. Instrum. Meth. A*, vol. 788, p. 128, 2015. DOI: 10.1016/j.nima.2015.03.069. arXiv: 1310.3263 [hep-ex].
- [211] G. J. Feldman and R. D. Cousins, “Unified approach to the classical statistical analysis of small signals”, *Phys. Rev. D*, vol. 57, p. 3873, 1998. DOI: 10.1103/PhysRevD.57.3873. arXiv: physics/9711021.
- [212] R. D. Cousins and V. L. Highland, “Incorporating systematic uncertainties into an upper limit”, *Nucl. Instrum. Meth. A*, vol. 320, pp. 331–335, 1992. DOI: 10.1016/0168-9002(92)90794-5.
- [213] ATLAS Collaboration, “Measurement of the $t\bar{t}$ production cross-section and lepton differential distributions in $e\mu$ dilepton events from pp collisions at $\sqrt{s} = 13$ TeV with the ATLAS detector”, *Eur. Phys. J. C*, vol. 80, no. 6, p. 528, 2020. DOI: 10.1140/epjc/s10052-020-7907-9. arXiv: 1910.08819 [hep-ex].
- [214] CMS Collaboration, “Differential cross section measurements for the production of top quark pairs and of additional jets using dilepton events from pp collisions at $\sqrt{s} = 13$ TeV”, *JHEP*, vol. 02, p. 064, 2025. DOI: 10.1007/JHEP02(2025)064. arXiv: 2402.08486 [hep-ex].
- [215] ATLAS Collaboration, “Inclusive and differential cross-sections for dilepton $t\bar{t}$ production measured in $\sqrt{s} = 13$ TeV pp collisions with the ATLAS detector”, *JHEP*, vol. 07, p. 141, 2023. DOI: 10.1007/JHEP07(2023)141. arXiv: 2303.15340 [hep-ex].
- [216] J. A. Raine, M. Leigh, K. Zoch, and T. Golling, “Fast and improved neutrino reconstruction in multineutrino final states with conditional normalizing flows”, *Phys. Rev. D*, vol. 109, no. 1, p. 012005, 2024. DOI: 10.1103/PhysRevD.109.012005. arXiv: 2307.02405 [hep-ph].
- [217] CMS Collaboration, “High-precision measurement of the W boson mass with the CMS experiment at the LHC”, Dec. 2024. arXiv: 2412.13872 [hep-ex].
- [218] S.-J. Jiang, B.-Q. Li, G.-Z. Xu, and K.-Y. Liu, “Study on Toponium: Spectrum and Associated Processes”, Dec. 2024. arXiv: 2412.18527 [hep-ph].
- [219] I. Brivio et al., “ALPs Effective Field Theory and Collider Signatures”, *Eur. Phys. J. C*, vol. 77, no. 8, p. 572, 2017. DOI: 10.1140/epjc/s10052-017-5111-3. arXiv: 1701.05379 [hep-ph].
- [220] J. Bonilla, I. Brivio, M. B. Gavela, and V. Sanz, “One-loop corrections to ALP couplings”, *JHEP*, vol. 11, p. 168, 2021. DOI: 10.1007/JHEP11(2021)168. arXiv: 2107.11392 [hep-ph].

- [221] H. Bahl et al., “HiggsTools: BSM scalar phenomenology with new versions of HiggsBounds and HiggsSignals”, *Comput. Phys. Commun.*, vol. 291, p. 108 803, 2023. DOI: [10.1016/j.cpc.2023.108803](https://doi.org/10.1016/j.cpc.2023.108803). arXiv: 2210.09332 [hep-ph].
- [222] ATLAS Collaboration, “Search for resonances decaying into photon pairs in 139 fb^{-1} of pp collisions at $\sqrt{s}=13 \text{ TeV}$ with the ATLAS detector”, *Phys. Lett. B*, vol. 822, p. 136 651, 2021. DOI: [10.1016/j.physletb.2021.136651](https://doi.org/10.1016/j.physletb.2021.136651). arXiv: 2102.13405 [hep-ex].
- [223] ATLAS Collaboration, “Search for heavy resonances decaying into a Z or W boson and a Higgs boson in final states with leptons and b -jets in 139 fb^{-1} of pp collisions at $\sqrt{s} = 13 \text{ TeV}$ with the ATLAS detector”, *JHEP*, vol. 06, p. 016, 2023. DOI: [10.1007/JHEP06\(2023\)016](https://doi.org/10.1007/JHEP06(2023)016). arXiv: 2207.00230 [hep-ex].
- [224] CMS Collaboration, “Observation of four top quark production in proton-proton collisions at $\sqrt{s} = 13 \text{ TeV}$ ”, *Phys. Lett. B*, vol. 847, p. 138 290, 2023. DOI: [10.1016/j.physletb.2023.138290](https://doi.org/10.1016/j.physletb.2023.138290). arXiv: 2305.13439 [hep-ex].
- [225] A. Biekötter, J. Fuentes-Martín, A. M. Galda, and M. Neubert, “A global analysis of axion-like particle interactions using SMEFT fits”, *JHEP*, vol. 09, p. 120, 2023. DOI: [10.1007/JHEP09\(2023\)120](https://doi.org/10.1007/JHEP09(2023)120). arXiv: 2307.10372 [hep-ph].